

An Electrochemical Investigation of the Chemical Diffusivity in Liquid Metal Alloys

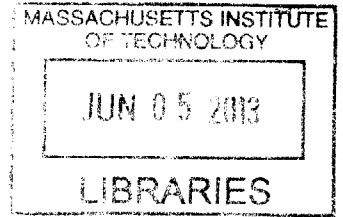
by

Salvador A. Barriga

A.S., Modesto Junior College (2004)

B.A., University of California, Berkeley (2006)

ARCHIVES



Submitted to the Department of Materials Science and Engineering
in partial fulfillment of the requirements for the degree of

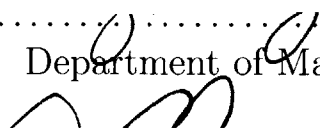
Doctor of Philosophy

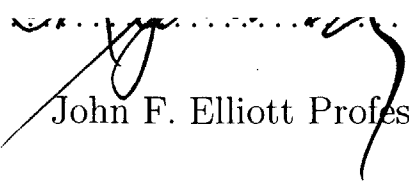
at the


MASSACHUSETTS INSTITUTE OF TECHNOLOGY

June 2013

© Massachusetts Institute of Technology 2013. All rights reserved.

Author
Department of Materials Science and Engineering

May 24, 2013

Certified by

Donald R. Sadoway
John F. Elliott Professor of Materials Chemistry
Thesis Supervisor

Accepted by

Gerbrand Ceder
Chair, Department Committee on Graduate Theses

An Electrochemical Investigation of the Chemical Diffusivity in Liquid Metal Alloys

by

Salvador A. Barriga

Submitted to the Department of Materials Science and Engineering
on May 24, 2013, in partial fulfillment of the
requirements for the degree of
Doctor of Philosophy

Abstract

The liquid metal battery has been shown to be a viable candidate for grid-scale energy storage, due to its fast kinetics and ability to be constructed from economically feasible materials. Various of the liquid metal couples that form high stable voltages, such as the calcium chemistries, are rate limited because they tend to form solid intermetallic compounds with high melting points. In order to understand and better engineer these batteries, the kinetic properties of these liquid alloys, in particular the chemical diffusivity, must be known accurately so that it can be used as input in computational simulations to avoid the nucleation of any solids. Unfortunately, the dominant experimental methods for measuring diffusion in liquid metals today are unreliable because the measurement timescales are on the order of days, require long capillaries susceptible to buoyancy-driven flow from temperature fluctuations, and composition analysis must be done *ex-situ* as a solid. To counter all these problems, a new and novel method for measuring the chemical diffusivity of metals in liquid alloys derived from electrochemical principles is presented in this thesis. This new method has the advantage of operating in shorter times scales of minutes rather than days, and requires the use of small capillaries which collectively minimize the effect of convectively-driven flow caused from temperature gradients. This new method was derived by solving the same boundary conditions required by the galvanostatic intermittent titration technique for solid-state electrodes. To verify the validity of the new theoretical derivation, the method was used to measure the chemical diffusivity of calcium in liquid bismuth within the temperature range of 550 - 700 °C using a three-electrode setup with a ternary molten salt electrolyte. Three compositions were studied (5% Ca-Bi, 10% Ca-Bi, and 15% Ca-Bi) for comparison. The chemical diffusion coefficient was found to range between $(6.77 \pm 0.21) \times 10^{-5} \text{ cm}^2/\text{s}$ - $(10.9 \pm 0.21) \times 10^{-5} \text{ cm}^2/\text{s}$ at 5% Ca-Bi, $(4.95 \pm 0.65) \times 10^{-5} \text{ cm}^2/\text{s}$ - $(7.93 \pm 0.37) \times 10^{-5} \text{ cm}^2/\text{s}$ at 10% Ca-Bi, and $(6.22 \pm 1.2) \times 10^{-5} \text{ cm}^2/\text{s}$ - $(10.2 \pm 0.26) \times 10^{-5} \text{ cm}^2/\text{s}$ at 15% Ca-Bi which, to our knowledge, are the first successful measurements of calcium diffusivity in the liquid state. Arrhenius fits with good correlations revealed the activation energy for diffusion to be $(21.4 \pm 1.7) \text{ kJ/mol}$, $(23.0 \pm 2.4) \text{ kJ/mol}$, and $(17.7 \pm 5.9) \text{ kJ/mol}$ as

the calcium concentration increased, which are in excellent agreement with literature published values and lie in the same range of 15-30 kJ/mol that is reported for most liquid metals. The chemical diffusivity value was then used as input in finite element simulations to model how convection affects the overall transport inside a 20-Ah liquid bismuth electrode under the influence of different thermal boundary conditions. Also, a phase field model was created to simulate the motion of the two interfaces inside a liquid metal battery during operation, which to our knowledge, is the first time phase field has been extended beyond two phases. Experimental kinetic values can then be used as input in these numerical models to help characterize and optimize the entire battery.

Thesis Supervisor: Donald R. Sadoway

Title: John F. Elliott Professor of Materials Chemistry

Acknowledgments

First and foremost, I would like to thank my advisor Professor Donald R. Sadoway for his superb mentoring and healthy discussions we've had throughout the years. Without his wisdom, I would not be who I am today, and I will forever be grateful for the unique opportunity I've had to learn and grow under him. I also want to thank Dr. Adam Powell for teaching me everything about numerical simulations and for all the engaging scientific discussing throughout my time at MIT, and Professor Chris Schuh for being part of my thesis committee.

Also, I would like to thank Ms. Hilary Sheldon for all of her hard work she did for me and the group, whether it was scheduling a room or ordering complicated stuff, I could of never achieved all of those things without her assistance, so thank you Hilary for simplifying my life during my stay with the group.

I have been extremely fortunate to be surrounded by great people, in particular Dr. Dane Boysen and Dr. Hojong Kim. Without their mentoring and support, I would of never succeed in tackling such a difficult problem for my dissertation. Dr. Dane Boysen taught me to be ambitious and determined, and to always question the facts. Dr. Hojong Kim shaped me into the experimentalist I am today, he taught me the art of working with molten salt systems, and paved the ground work on calcium-based chemistries that I was able to use as a test bed for my theoretical work. I would also like to thank Dr. Brice Chung and Dr. Takanari Ouchi for all of their support, patience, and willingness to always help out.

I would also like to thank my fellow students and colleagues I've had the pleasure to work with and discuss science: Dr. Aislin Sirk, Dr. David Bradwell, Dr. Ken Avery, Ms. Jocelyn Newhouse, Mr. Brian Spatocco, Dr. Sophie Poizeau, Mr. John Rogosic, Ms. Camille Martinez, Dr. Kai Jiang, Dr. Luis Ortiz, Dr. Paul Burke, Dr. Weifeng Wei, Dr. Kangli Wang, Dr. Xiaohui Ning, Dr. Alina Tomaszowska, Dr. Sebastian

Osswald, and Mr. Mike Parent.

Also, I would like to thank my funding sources throughout the years: Xerox fellowship, the Chesonis foundation, TOTAL, and Arpa-E.

Throughout my time at MIT I was also involved part-time at MIT Lincoln Laboratory working on after-pulse measurements of avalanche photodiodes. This is where I learned all the MATLAB skills I used to analyze my dissertation work, so for this I would to thank Dr. Erik Duerr and Dr. Katherine Jensen for teaching me the confidence to learn and apply MATLAB.

I would like to thank my roommates Matthew Smith, Thomas Fellows, and Brian Beliveau for the time we lived together and for treating me like family. I am extremely grateful to have shared a living space with these three individuals whom I'm proud to call some of my closest friends. Miguel Padilla and Justin Jeet have been like brothers to me since we first met at Modesto Junior College, thank you two for everything. A big thanks to Rahul Malik and Reece Daniel for being amazing friends, and for all the battery discussions we handled throughout the years. Many thanks to my MIT classmates and other friends for making my social life that much better, which include Billy Woodford, Kevin Huang, Matthew Gerding, Alex Scott, Joe Sullivan, Joan Mao, Mandy Woo, Becky Smith, Danny Ubilla, and Sam Crawford.

A very special thanks to my mother Nedelia T. Aguilar, whom this thesis is dedicated to, and my brother Ricardo A. Barriga for their tremendous support. There really are no words to describe my appreciation, thank you very much for being the perfect family to me.

Contents

1	Introduction	21
1.1	Grid Scale Energy Storage	21
1.1.1	Current Energy Storage Technologies	22
1.2	From Hall-Hérault to Liquid Metal Batteries	23
1.2.1	Hall-Hérault Process	23
1.3	Liquid Metal Batteries	25
1.3.1	Calcium Chemistries	33
1.4	LMB Operating Principles	36
1.4.1	Thermodynamics	36
1.4.2	Kinetic Processes	37
1.4.3	LMB Limitations and Efficiencies	39
1.5	Liquid Structure Background	41
1.5.1	Pure Liquid Metals and Semi Metals	43
1.5.2	Liquid Alloys	48
1.6	Interest in Liquid Diffusion	52
1.7	Sensitivity Analysis - Impact of Chemical Diffusivity to the Transport in LMBs	52
1.8	Conclusion	55
2	Diffusion - Theory and Experiment	57
2.1	Fundamentals of Diffusion	57
2.1.1	Probability Associated With Diffusion	58
2.2	Diffusion in Liquid Metals	60

2.2.1	Theoretical Models	60
2.2.2	Experimental Techniques for Measuring Diffusivity	62
2.3	Conclusion	75
3	Theoretical Derivation of Chemical Diffusivity in Liquid Alloys	77
3.1	Chemical Diffusivity of A in the A B Binary Liquid Alloy	78
3.1.1	Surface Concentration Solution	79
3.1.2	Composition Relation to Potential	81
3.1.3	Chemical Diffusivity Equation	83
3.2	Chemical Diffusivity Derivation of A in the $A_{y+\delta}B$ Binary Solid Inter-metallic Compound	84
3.3	Difference Between Liquid and Solid-State Diffusivity Equations	85
3.4	Conclusion	86
4	Electrochemical Experiments and Procedure for Measuring the Chemical Diffusivity in Liquid Alloys	89
4.1	Experimental Setup	89
4.1.1	Materials Selection	89
4.1.2	Electrochemical System	91
4.2	Electrochemical Pulse Sequences	93
4.2.1	Initial Composition Titration	93
4.2.2	Determination of \tilde{D}	93
4.3	Conclusion	97
5	Results and Data Analysis	99
5.1	Application of the Chemical Diffusion Equation (eq. 3.18)	99
5.2	Sources of Error	100
5.2.1	Uncertainty in Voltage Measurements	100
5.2.2	Differential Error Analysis	101
5.3	Calculated Chemical Diffusivities of Calcium in Bismuth	104
5.3.1	5% Calcium in Bismuth	105

5.3.2	10% Calcium in Bismuth	106
5.3.3	15% Calcium in Bismuth	107
5.4	$\frac{dE_i}{d\sqrt{t}}$ vs Temperature	108
5.5	Average Diffusion Coefficients	115
5.6	Diffusion Activation Energies	118
5.6.1	Diffusion Activation Energies	120
5.7	Conclusion	123
6	Transport Phenomena Simulations	125
6.1	Brief Introduction to Finite Element Analysis (FEA)	126
6.2	Conservation Equations	128
6.3	Thermal Simulation Results	133
6.3.1	Argonne National Laboratory Cell Geometry	133
6.3.2	MIT Cell Geometry	137
6.4	Electrode Mixing Simulations	140
6.4.1	Uniform Temperature Gradient	140
6.4.2	Nonuniform Temperature Gradient	141
6.4.3	Dimensionless Numbers	143
6.4.4	Induced Velocity as a Function of Geometry	146
6.5	Phase Field Simulations	146
6.5.1	Phase Field Theory	146
6.5.2	Derivation of Custom Source Term	149
6.5.3	Phase Field Modification for Three Phases	150
6.5.4	Results	150
6.6	Conclusion	153
7	Conclusion	155
A	Energy Storage Technologies	157
A.1	Pumped-Hydro Storage	157
A.2	Sodium-Sulfur (NaS) Battery	157

A.3	Lead-Acid Battery	158
A.4	Lithium-Ion Battery	158
A.5	Flywheels	158
B	Error Function Related Equations	159
C	Sensitivity Analysis on $\frac{dx_A}{d\sqrt{t}}$	161
D	Experiment Preparation	163
D.1	Electrolyte	163
D.2	Electrodes	164
D.2.1	Reference Electrodes	164
D.2.2	Working Electrode	166
D.2.3	Counter Electrode	166
E	Supplementary Data	167
E.1	5% Ca-Bi: Electrode Potential Pulse Sequence and Temperature . . .	168
E.2	10% Ca-Bi: Electrode Potential Pulse Sequence and Temperature . .	169
E.3	15% Ca-Bi: Electrode Potential Pulse Sequence and Temperature . .	170
E.4	5% Ca-Bi: Potential Variation With Time	171
E.5	10% Ca-Bi: Potential Variation With Time	173
E.6	15% Ca-Bi: Potential Variation With Time	175
E.7	5% Ca-Bi: Reference Electrode	177
E.8	10% Ca-Bi: Reference Electrode	178
E.9	15% Ca-Bi: Reference Electrode	179
E.10	5% Ca-Bi: Counter Electrode	180
E.11	10% Ca-Bi: Counter Electrode	181
E.12	15% Ca-Bi: Counter Electrode	182
F	MATLAB Data Analysis Scripts	183
G	Conservation Equations	225

List of Figures

1-1	Power cost (\$/kW) versus energy cost (\$/kWh) [2].	22
1-2	Paul Héroult operating the first aluminum electrolysis cell.	24
1-3	A schematic of the Hall-Héroult process to produce aluminum. The electrolyte dissolves the alumina, allowing the O^{2-} anions to travel to the top graphite anode and bubble away as CO_2 gas while simultaneously reducing Al^{3+} cations at the bottom cathode during electrolysis. The operating temperature is $960^\circ C$. [9]	25
1-4	Thermally Regenerative Galvanic Cell System created at Argonne National Laboratory [10].	26
1-5	Efficiencies for Thermally Regenerative Bimetallic Cells [10].	26
1-6	Sodium-bismuth secondary cell with liquid electrolyte and improved design. [10].	28
1-7	Ambipolar electrolysis cell, composed of magnesium and antimony as electrodes with a magnesium antimonide molten electrolyte [11].	30
1-8	Schematic of alloying electrochemical cell. (a) Discharging of cell, cation A is oxidized at its electrode electrolyte interface resulting in the reaction $A \rightarrow A^+ + e^-$ (b) After the cation A^+ travels through the electrolyte, it is reduced at the bottom electrode-electrolyte interface resulting in $A^+ + e^- \rightarrow A(\text{in B})$	31
1-9	Periodic table of the elements. On the left we have the negative electrode candidates suitable to build a LMB composed of alkali and alkaline earth metals. On the right we have the positive electrode candidates located under the chalcogens and pnictogens.	33

1-10	Calcium-antimony phase diagram [16].	35
1-11	Calcium-bismuth phase diagram [17].	35
1-12	Over 1 A/cm ² current density induced during potentiostatic step of 0.7 V.	41
1-13	Radial distribution function schematic.	43
1-14	Both the solid (a) and liquid (b) contain the same number of atoms, the only difference is the number of nearest neighbors surrounding the A atom. In (a) it has six, while (b) has five [30].	44
1-15	Radial distribution function comparison for (a) liquid mercury and (b) solid mercury [32].	45
1-16	Coordination number comparison between solid and liquid metals [30].	46
1-17	Table showing the the variation of material properties [30]	47
1-18	The energy distribution curves of photoemitted electrons from solid (300 K) and liquid (820 K) Bi at a photon energy of 21.2 eV. [36] . .	48
1-19	Relative intensities of X-ray scattering from lead, bismuth and five alloys. Composition is in wt%. The monotonic curves represent the calculated independent scattering [37].	49
1-20	Summary of diffraction and density results [37].	49
1-21	Bismuth-lead phase diagram	50
1-22	Chemical diffusivity of bismuth in lead measured using the capillary- reservoir method [39].	51
1-23	Sensitivity analysis on a 5cm thick electrode. The chemical diffusivity was varied over three orders of magnitude.	54
2-1	Probability distribution function at various times.	58
2-2	A schematic illustration of the sodium- β'' -alumina electrochemical cell used in the diffusivity measurements of sodium in tin [83].	63
2-3	A schematic drawing showing the boundary and the initial conditions of the diffusion problem as well as a schematic illustration of the com- position profile for $t > 0$ [83].	64

2-4	Curve of open circuit potential against time at 440 °C. The decay curve calculated with $D = 2.6 \times 10^{-5} \text{ cm}^2/\text{s}$ agrees with the experimental decay curve [83].	66
2-5	The conceptual change of the concentrations of solute M in liquid metal (solid line) and M^{n+} ion in LiCl-KCl melts (dotted line) during constant current electrolysis. $c_{M^{n+}}^*$ is the initial concentration in the electrolyte, and c_M^* is the initial concentration in the liquid metal [84].	68
2-6	Typical chronopotentiograms using a liquid Cd electrode containing La in LiCl-KCl-2.0 wt % LaCl_3 melts at 723 K. The applied current was (a) 65 mA, (b) 60 mA, (c) 55 mA [84].	69
2-7	Schematic of capillary-reservoir apparatus used by Meyer [60] to measure the diffusion of liquid sodium.	70
2-8	Effect of capillary diameter on concentration-penetration profiles for the interdiffusion of Bi in liquid Sn at 700 °C [76]	72
2-9	(a) Initial concentration profile. (b) Concentration profile after melting. (c) Freezing interface of metal thread. (d) Concentration profiles at capillary axis and wall. [52]	73
2-10	Schematic representation of the shear cell: (1) intermediate disk with radioactive alloy; (2) filling reservoir: A , configuration of the cell during the heating of the system; B , the radioactive isotope is put into contact with the long capillary; C , at the end of the diffusion run, each capillary is sectioned into 20 beads. [102]	74
3-1	Schematic of alloying cell. Current is passed between the negative electrode and positive electrode, while the potential is measured versus the reference electrode A_{RE} . The electrode-electrolyte interface is at $z = 0$ and the bottom of the electrode is $z = l$	78
3-2	Boundary conditions, (a) initial molar concentration at $t = 0$, and (b) fluxes during galvanostatic pulse.	79

3-3	GITT pulse (a) Applied current density j_0 at $t = 0$. (b) Evolution of electrode potential.	79
3-4	EMF data of calcium in bismuth between 600-800°C [17].	81
4-1	Experiment test vessel.	90
4-2	Cell layout. The outer perimeter is the alumina crucible, and it is not drawn to scale.	91
4-3	Three-electrode cell schematic. Current is passed between the counter electrode and working electrode, while the working electrode potential is measured with respect to the reference electrode.	91
4-4	Experiment setup	93
4-5	Calcium-Bismuth phase diagram [17].	94
4-6	Titration to composition. A) Potentionstatic cleaning of working electrode. B) Coulometric titration to composition. C) Open circuit relaxation.	94
4-7	Custom four pulse sequence used for determining chemical diffusivity. Each individual pulse changes the calcium composition by 0.25% x_{Ca}	95
4-8	Typical pulse sequence applied at 5%, 10%, and 15% - mol Ca-Bi. Each individual pulse changes the calcium composition by 0.25% x_{Ca}	96
5-1	Four-pulse sequence used in determining the chemical diffusivity of calcium in bismuth at roughly 575 °C. The temperature fluctuations during the pulse sequence are superimposed to aid in the analysis.	100
5-2	Potential versus calcium mole fraction. 5% Ca-Bi, 575°C.	101
5-3	$\frac{dE_i}{dx_{Ca}}$ plotted for each pulse. In theory these values should be the same, but deviations in temperature and other environmental changes will induce small deviations.	102
5-4	$\frac{dE_i}{dx_{Ca}}$ error bars are the standard deviation of the four values. This is assumed valid because in theory they should be equal.	102
5-5	Chemical diffusion coefficients at 5% Ca-Bi.	105
5-6	Chemical diffusion coefficients at 10% Ca-Bi.	106

5-7	Chemical diffusion coefficients at 15% Ca-Bi.	107
5-8	Electrode potential dependence with the square root of time. The longer pulse shown in blue corresponds to the smallest applied current density which was 5 mA/cm ²	109
5-9	Top: Linear fits to electrode potential variation with square root of time. Bottom: Residual plot from the fits and data showing random scatter averaged at zero, signifying good fits.	110
5-10	Top: Linear fits to electrode potential variation of pulse 1 with square root of time. Bottom: Residual plot from the linear fit and data. . .	111
5-11	Top: Linear fit to simulated electrode potential variation of pulse 1 with square root of time. Bottom: Residual plot from the linear fit and data.	111
5-12	Top: Linear fits to simulated electrode potential variation of pulse 1 with square root of time. Bottom: Residual plot from the linear fit and data. The residual fit in red has both upper and lower bounds, and the slope in that region is $\frac{dE_i}{d\sqrt{t}} = -8.56 \times 10^{-5} \text{ V s}^{-1/2}$	112
5-13	Potential variation with square root of time plotted as a function of temperature. The error bars is the standard deviation of the values assuming they only rely on current density.	114
5-14	Average chemical diffusion coefficient at 5% Ca-Bi.	116
5-15	Average chemical diffusion coefficient at 10% Ca-Bi.	116
5-16	Average chemical diffusion coefficient at 15% Ca-Bi.	117
5-17	Averaged chemical diffusivity values.	117
5-18	Natural log of chemical diffusivity versus inverse temperature for 5% Ca-Bi.	120
5-19	Natural log of chemical diffusivity versus inverse temperature for 10% Ca-Bi.	121
5-20	Natural log of chemical diffusivity versus inverse temperature for 15% Ca-Bi.	122

6-1	Simple quadratic mesh on a rectangular geometry. Each square is called an element, 48 elements make up this geometry. Each point of intersection makes up a node, so there are 63 nodes on the geometry.	127
6-2	Cell schematic of the geometry used at Argonne National Laboratory by Cairns [10].	134
6-3	Radial cross-section of simplified Argonne National Laboratory cell design used in the simulations.	135
6-4	Thermal boundary conditions for the 20Ah Argonne National Laboratory cell geometry.	136
6-5	Joule heating generated as a function of cell radius for three different current densities.	137
6-6	Radial cross-section of simplified MIT cell design used in the simulations.	139
6-7	Radial schematic with thermal boundary conditions for liquid electrode.	140
6-8	Concentration and fluid velocity profile after titrating calcium for an hour into a liquid electrode with a one degree per centimeter thermal gradient.	141
6-9	New boundary conditions to compare the mixing behavior.	142
6-10	Concentration and fluid velocity profile after titrating calcium for an hour into a liquid electrode with the modified boundary conditions seen in figure 6-9.	142
6-11	Cell schematic used in the phase field model with the appropriate conserved order parameter values.	151
6-12	Heaviside function used to differentiate the volume fractions of the different phases.	151
6-13	The density from equation 6.42 self-segregates with the help of Heaviside step functions.	151
6-14	Simulation of three phases and two boundaries simultaneous moving at a time $t = 2$ s.	152

6-15	Simulation of three phases and two boundaries simultaneous moving at a time $t = 50$ s. Compared to figure 6-14, the bismuth electrode has grown at the expense of the calcium-magnesium.	152
6-16	Mass loss of each component as a function of time calculated using an integration coupling variable over the entire system. The variation was less than 1% signifying mass conservation.	153
C-1	Sensitivity analysis at various current densities $j_0 = 5, 10, 15, 20$ [mA/cm ²].	162
D-1	Pre-melted salts inside quartz crucibles before	164
D-2	Arcmelter used to prepare the reference electrodes.	165
D-3	Calcium and bismuth metals inside arc-melter.	165
D-4	35-mol% Ca-Bi alloy premelted inside the arc-melter.	166
E-1	5%: Electrode potential and temperature with time.	168
E-2	10%: Electrode potential and temperature with time.	169
E-3	15%: Electrode potential and temperature with time.	170
E-4	5%: Potential versus square root of time.	172
E-5	10%: Potential versus square root of time.	174
E-6	15%: Potential versus square root of time.	176
E-7	5%: Reference electrode stability.	177
E-8	10%: Reference electrode stability.	178
E-9	15%: Reference electrode stability.	179
E-10	5%: Counter electrode stability.	180
E-11	10%: Counter electrode stability.	181
E-12	15%: Counter electrode stability.	182
G-1	Control volume $V(t)$ with surface area $S(t)$ that can change with time. The surface normal vector ($\hat{\mathbf{n}}$), surface velocity \mathbf{v}_S , and fluid velocity (\mathbf{v}) all vary with surface position and time.	225

List of Tables

1.1	Table showing the theoretical cell potential between A B couples [2].	33
1.2	Prices for selected metals [2].	34
1.3	Table showing the theoretical energy cost for A B couples in \$/kWh [2].	34
1.4	Nernst-Planck transport component with description.	38
4.1	Electrode dimensions.	90
4.2	Pulse sequence parameters at 5%, 10%, and 15% Ca-Bi.	96
5.1	Chemical diffusion coefficients of Ca in 5% a Ca-Bi liquid alloy. Errors are shown to one significant figure.	106
5.2	Chemical diffusion coefficients of Ca in 10% Ca-Bi. Errors are shown to one significant figure.	107
5.3	Chemical diffusion coefficients of Ca in 15% Ca-Bi. Errors are shown to one significant figure.	108
5.4	Rate of change of electrode potential versus square root of time at 5% Ca-Bi.	113
5.5	Rate of change of electrode potential versus square root of time at 10% Ca-Bi.	113
5.6	Rate of change of electrode potential versus square root of time at 15% Ca-Bi.	114
5.7	Averaged chemical diffusion coefficients. Errors are shown to one significant figure and are the standard deviation of the averaged values.	115
5.8	Natural log of averaged chemical diffusivity for 5% Ca-Bi liquid alloy.	120
5.9	Natural log of averaged chemical diffusivity for 10% Ca-Bi liquid alloy.	121

5.10	Natural log of averaged chemical diffusivity for 15% Ca-Bi liquid alloy.	121
5.11	Activation energy for diffusion of Ca in Ca-Bi liquid alloy along with the diffusion prefactor values and propagated uncertainties.	122
6.1	Physical examples of common FEA matrix variables.	127
6.2	Cell dimensions used in the thermal simulation of the cell design shown in figure 6-3.	135
6.3	Simulated power for the three radii of interest.	136

Chapter 1

Introduction

The main motivation behind the research presented in this thesis was driven by the need for grid scale energy storage, and the potential of using liquid metal batteries (LMBs) to asses that need. In this chapter I briefly discuss the potential of using LMBs for storing energy at the grid scale, as well as the fundamentals of how the LMB operates, and the importance of how knowledge of the chemical diffusivity leads to optimizing the kinetic performance of LMBs.

1.1 Grid Scale Energy Storage

The deployment of large scale energy storage is one approach to meet our increasing demands on todays electric power grid. The lack of grid storage capacity requires that power generation is safely adjusted to meet fluctuating consumer demands, and needs to be achieved economically. Solar and wind power are renewable alternatives to fossil fuels, but their intermittent power generation resulting from environmental conditions make them unreliable and incapable of following fluctuations in consumer demand [1]. Now, this doesn't mean they are bad candidates and should never be used because of nature's mercurial personality, but that we should find ways to store the energy generated by these intermittent sources. An example of an alternative technology is the liquid metal battery [2]. It has the potential to store energy at the grid-scale and increase grid efficiency by storing energy during off-peak hours, and

returning it during peak time. In this mode, the production of electricity does not need to be ramped up drastically to meet consumption, hence reducing the need of conventional generators while allowing for a more economical and stable production of electricity. Analytical studies on energy storage applications such as frequency stability, peak shaving, and transmission line upgrade deferral, have demonstrated the need for large energy storage systems, but the current leading technologies are not economically feasible [3].

1.1.1 Current Energy Storage Technologies

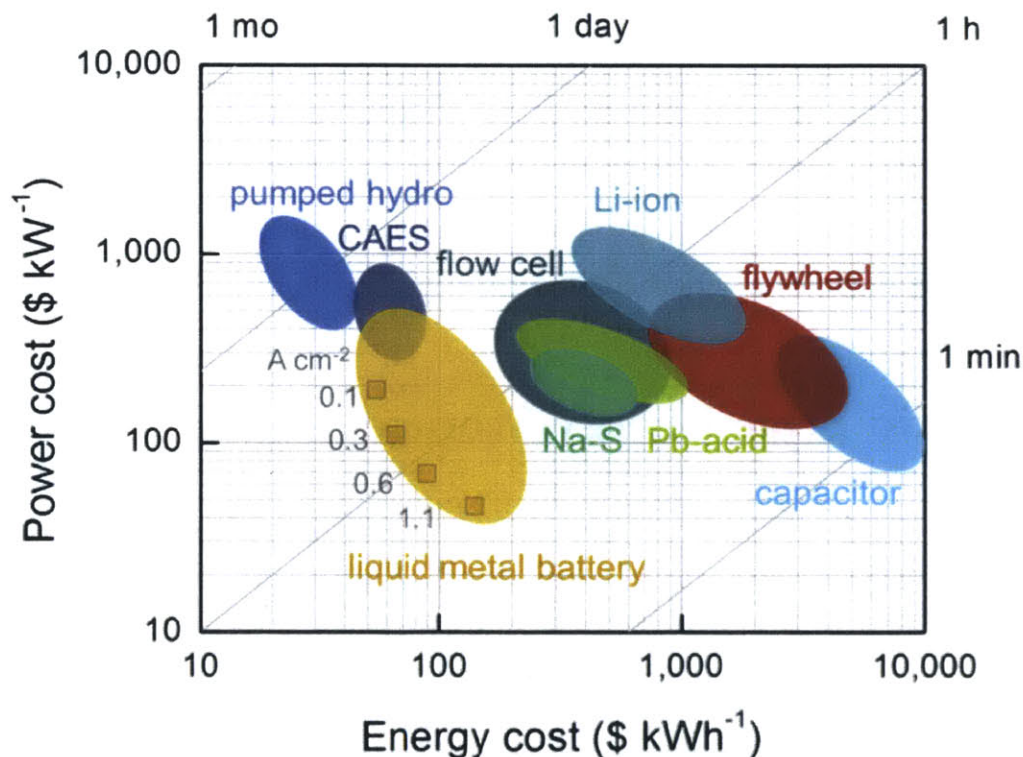


Figure 1-1: Power cost (\$/kW) versus energy cost (\$/kWh) [2].

Energy can be stored in many forms. Batteries and fuel cells store energy in chemical bonds, capacitors in electric fields, while flywheels store energy mechanically. In order to make grid-scale energy storage possible, it must be done economically by incorporating cheap, abundant materials. Current modern battery technologies are

designed for portable electronics and transportation, which require expensive electronics, high specific volume and mass power/energy densities. Large-scale batteries are not bound by the same mass and volume requirements; therefore, chemistries other than lithium can be considered with the following metrics [4]:

- The storage system must have a capital cost of less than \$150/kWh.
- Deliver energy for longer than 4 hours.
- Have an energy efficiency greater than 80%.
- Cycle longer than 3000 times.

Some of the leading energy storage technologies are outlined in appendix A. From here on we will focus only on the LMB storage technology.

1.2 From Hall-Héroult to Liquid Metal Batteries

Aluminum is an abundant and cheap metal, which is no surprise given how much of it we use daily. It's used by the automotive industry, we use it to wrap left overs with, and to contain beverages. To meet our high demands, in 2010 we produced 40.8 million metric tons of aluminum [5], the enabler being molten-salt electrolysis.

1.2.1 Hall-Héroult Process

The molten-salt electrolysis method is The Hall-Héroult process, where the electrolyte is a molten bath of cryolite (NaAlF_3) with dissolved alumina (Al_2O_3) at 960 °C [6]. Cryolite is the only molten salt known to dissolve alumina, and it is so corrosive, the only material capable of sustaining it for long periods of time is solid cryolite. Figure 1-3 is a schematic of the process; a cathode sits at the bottom of the electrolyte, reducing Al^{3+} ions to molten aluminum metal that is syphoned out as it is produced. A graphite anode above the electrolyte oxidizes O^{2-} anions to produce CO_2 gas, consuming the graphite anode making it an irreversible process [6]. The overall reaction is [7]

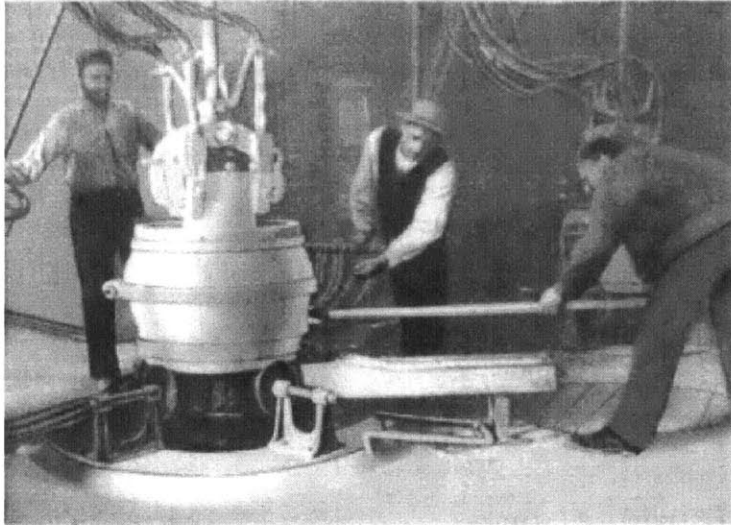
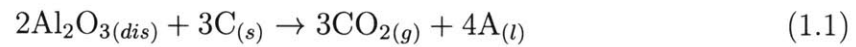


Figure 1-2: Paul Héroult operating the first aluminum electrolysis cell.



The electrolysis process consumes GWh amounts of electrical energy and operates at current densities of $0.7\text{A}/\text{cm}^2$ with current efficiencies above 90% [8]. The immiscibility between the electrolyte and aluminum contributes to the high current efficiency, and demonstrates that a large-scale electrolysis can remain stable when two high-temperature, self-segregated liquids are in contact.

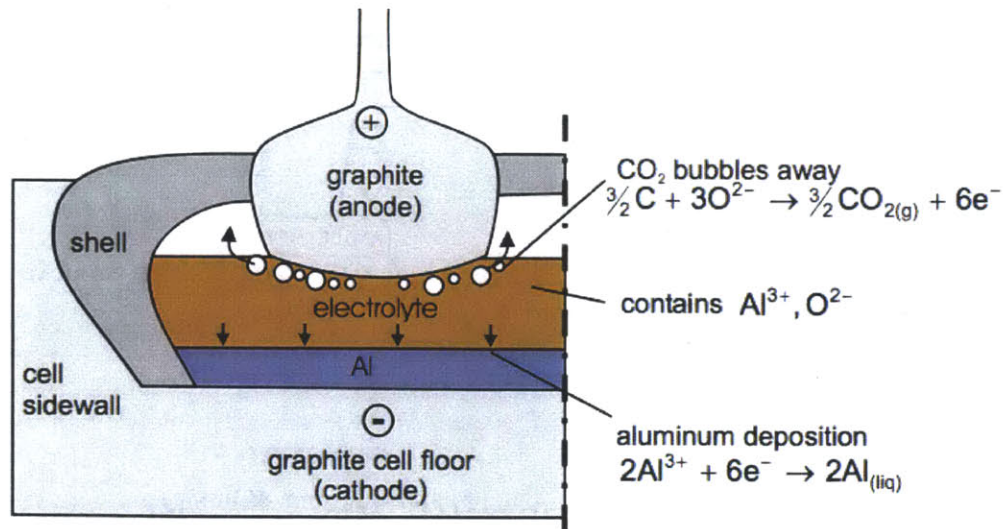


Figure 1-3: A schematic of the Hall-Héroult process to produce aluminum. The electrolyte dissolves the alumina, allowing the O^{2-} anions to travel to the top graphite anode and bubble away as CO_2 gas while simultaneously reducing Al^{3+} cations at the bottom cathode during electrolysis. The operating temperature is 960°C . [9]

1.3 Liquid Metal Batteries

In the 1960s and 1970s, Argonne National Laboratory investigated the possibility of making a battery out of a molten salt and liquid metal electrodes [10]. Cairns *et al.* demonstrated the first concept of such a battery, called a thermally regenerative galvanic cell system (fig. 1-4). The system consists of a galvanic cell to generate electricity, and a heat exchanger to balance the heat between the galvanic cell and the regenerator. The regenerator is used to vaporize the anode metal at temperature T_2 , which then condenses at a lower temperature T_1 at the top of the galvanic cell.

The vapor metal oxidizes at the top electrode-electrolyte interface undergoing the chemical reaction $\text{A} \rightarrow \text{A}^+ + \text{e}^-$, allowing for the anion A^+ to migrate down to the cathode alloy and react to produce $\text{A}^+ + \text{e}^- + \text{C} \rightarrow \text{AC}$ (in C). A main disadvantage of this system is the low overall efficiency, defined as the ratio of integrated power over time to the total heat in, which is always less than the Carnot-cycle efficiency. Cairns defines the overall efficiency as the product of the Carnot efficiency, Gibbs free energy efficiency, and the heat-exchanger efficiency given by

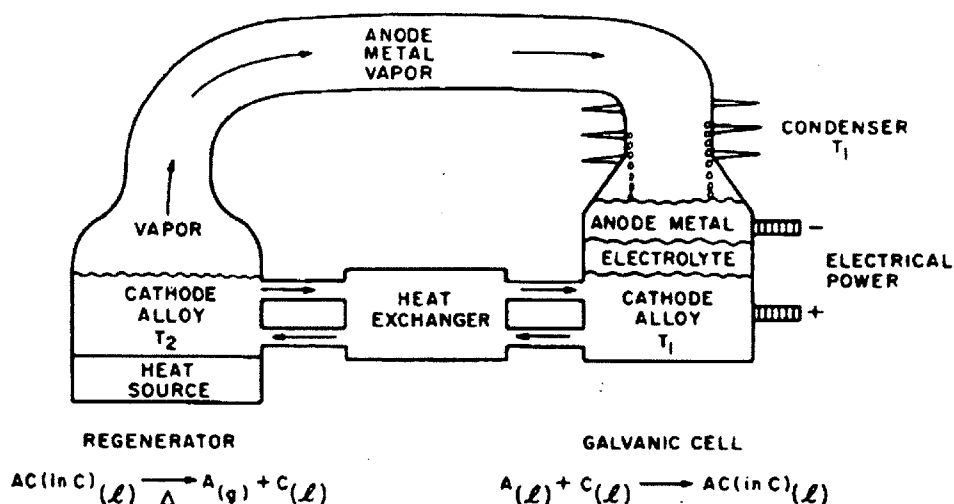


Figure 1-4: Thermally Regenerative Galvanic Cell System created at Argonne National Laboratory [10].

$$\text{Eff}_S = \text{Eff}_C \cdot \text{Eff}_G \cdot \text{Eff}_h. \quad (1.2)$$

The table in figure 1-5 was taken from Cairns report to show the predicted overall efficiency of some selected thermally regenerative cells, which are on the low side.

System	Li-Sn	Na-Sn	Na-Pb	Na-Bi
Regeneration temperature, T_2 , °K	1323	1073	1100	1310
Condenser temperature, T_1 , °K	1005	785	795	859
Regeneration pressure, P, Torr	0.75	5.3	6.38	4.9
Carnot-cycle efficiency, Eff_C , %	24	27	27	38
Gibbs free-energy efficiency, Eff_G , %	60	60	60	60
Heat-exchange efficiency, Eff_h , %	75	75	75	75
Overall efficiency, Eff_S , %	11	12	12	12

^aComputed for 20 m/o anode metal in cathode metal.

Figure 1-5: Efficiencies for Thermally Regenerative Bimetallic Cells [10].

We can conclude from the information that one needs a very high regeneration temperature of around 1500°C, and a low cell temperature of 700°C. This will be extremely difficult to achieve due to the energy requirements and minimal material selection that are stable at extreme temperatures. The requirements that need to be satisfied in order to make these galvanic cells possible are:

- Anode metal should have a low electronegativity.
- Cathode metal should have a high electronegativity.
- Both cathode and anode should form intermetallic compounds with large negative free energies of formation.
- Anode and cathode metals should melt below the desired cell-operating temperature (500-800K).
- The anode, cathode, and intermetallic should have low solubilities in the electrolyte at the cell-operating temperature.
- The electrolyte should have a low melting point, low vapor pressure, and high ionic conductance at the cell-temperature.
- The electrolyte should contain a large concentration of the anode metal cation.
- All cell components should be inert with containment materials to minimize corrosion.

And for the regenerator, the requirements are:

- The anode metal needs to be much more volatile than the cathode metal to ease separation.
- The intermetallic compound should not be super stable, and should decompose readily at the regeneration temperatures.
- The vapor liquid look should not intersect the solid-liquid equilibrium line on the phase diagram at the pressure of the operating temperature.
- The regenerator should operate such that it maximizes the anode vapor pressure.
- The regenerator should be inert.

It might seem impossible to find candidates that can meet the stringent requirements mentioned above. One can also see how the problem could be minimized if we can get rid of the generator and heat exchanger, which will allow one to focus on just the galvanic cell part. This is what the team did at Argonne National Laboratory when they switched cell designs to the schematic shown in figure 1-6. The cell enclosure was made of stainless steel, and it contained six cooling lines to keep the silicone rubber gasket that was sealing the cell from melting. The top current collector was a 1.5 mm-thick stainless steel spiral made to hold the liquid sodium upon charging. It contained electric ring heaters on the top and bottom to heat the cell to temperature, and it was predominantly insulated for obvious reasons.

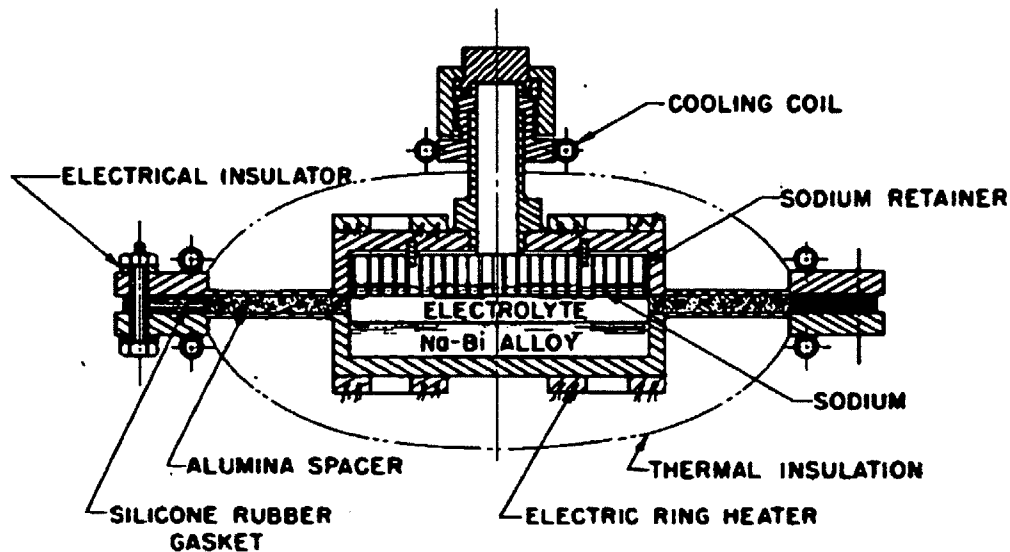


Figure 1-6: Sodium-bismuth secondary cell with liquid electrolyte and improved design. [10].

The main advantage of this cell was that it did not need a heat exchanger, regenerator, nor condenser to operate, making the regenerator restrictions mentioned above inapplicable. This enabled the use of stronger interacting alloys which can form more stable intermetallic compounds with higher cell voltages. The new cell worked in a similar fashion, metal A atoms oxidize at the top electrode-electrolyte interface producing $A \rightarrow A^+ + e^-$ while it is simultaneously reduced at the bottom electrode-electrolyte interface $A^+ + e^- \rightarrow A_{C(l)}$. $A_{C(l)}$ is the liquid alloy $A||C$

stable during electrolysis that does not form an intermetallic, a requirement for the thermally regenerative cells first tested [10].

The main disadvantage for this cell was not the physics behind its operating principles – it was the geometry. The cell was designed with cooling lines near the silicone rubber gaskets to keep them from melting. This creates huge thermal gradients, which then forces the heaters to output more power to keep the cell components at temperature¹. Unfortunately, this work was discontinued shortly after these reports were written due to funding issues, and not much attention was devoted to research in molten salts.

It wasn't until the mid 2000s when similar type of work resurfaced at MIT independent to what was done at Argonne National Laboratory. Bradwell *et al.* [11] used the concept of the aluminum smelter as a model for an energy storage system. The problem was aimed at finding compatible materials that could substitute in for the irreversible part of aluminum electrolysis, which is the production of carbon dioxide at the anode. The energy storage system created was dubbed the liquid metal battery (LMB), designed to self-segregate when liquid at high temperatures, and have high charge transfer interfacial kinetics with low overpotentials. What makes this battery unique is the ability to cycle many times at high rates while retaining a high charge capacity, making it a bidirectional process. The liquid state of matter of the two electrodes and electrolyte allows the current density to be limited only by the mass transport of the active species, eliminating metrics related to solid electrodes such as electrochemical shock caused by diffusion-induced stresses [12–14].

Ambipolar Cell

The first liquid metal battery created at MIT was called the ambipolar cell. It was composed of liquid magnesium as the cathode, liquid antimony as the anode, and a molten magnesium antimonide electrolyte [9]. This clever setup allowed for the simultaneous reduction and oxidation of two metal species, known as ambipolar

¹For part of my thesis, I created two dimensional FEA thermal models using this cell type to estimate the required operating power, the results are outlined in chapter 6

electrochemical reaction. The key lies in selecting an electrolyte which can dissolve the reaction product Mg_3Sb_2 . Upon dissolution, the compound breaks down into its respective ionic species:

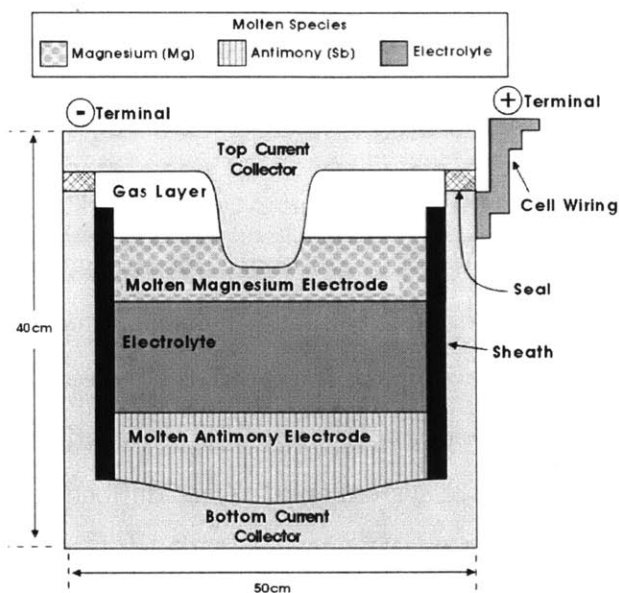
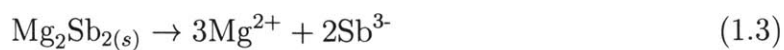


Figure 1-7: Ambipolar electrolysis cell, composed of magnesium and antimony as electrodes with a magnesium antimonide molten electrolyte [11].

Upon charging the cell, the dissolved intermetallic in the electrolyte is consumed by the following reaction at the cathode



And at the anode the following reaction takes place



making the overall reaction



The opposite happens when the cell discharges, the above reaction is reversed causing the electrolyte to grow making it a bidirectional process. The Gibbs free energy of formation ΔG_{rxn} for Mg_3Sb_2 is what drives the cell to discharge, and can be calculated using an Ellingham diagram. The corresponding cell voltage from the free energy can then be obtained using the following relation

$$E_{\text{rxn}} = -\frac{\Delta G_{\text{rxn}}}{z_i F}, \quad (1.7)$$

where z_i is the number of electrons involved in the chemical reaction, and F is the Faraday constant (96,485C/mol).

Overall this cell proved difficult to operate as a battery, but not as a recycling method. Bradwell extended the electrochemical principle behind the ambipolar cell to extract cadmium and tellurium from dissolved cadmium telluride in a molten salt [15], which enabled an alternative method for recycling the cadmium telluride used in solar cells. Besides this novel application, the ambipolar process served as the fundamental basis for the current LMB used, the alloying cell.

Alloying Cell

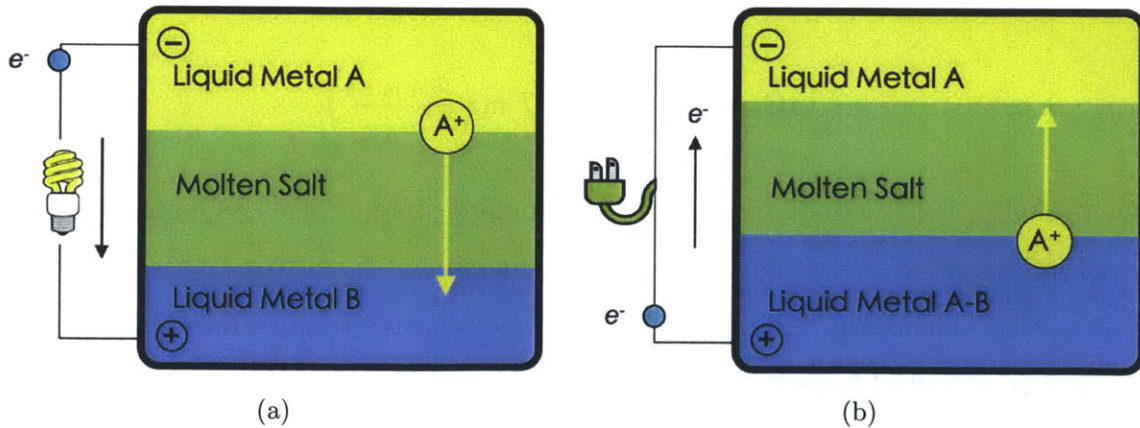
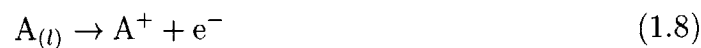


Figure 1-8: Schematic of alloying electrochemical cell. (a) Discharging of cell, cation A is oxidized at its electrode electrolyte interface resulting in the reaction $A \rightarrow A^+ + e^-$ (b) After the cation A^+ travels through the electrolyte, it is reduced at the bottom electrode-electrolyte interface resulting in $A^+ + e^- \rightarrow A(\text{in B})$

Figure 1-8 is an illustration of the alloying cell. The liquid phase helps the in-

terfacial kinetics to occur extremely fast compared to mass transport, making it a reversible reaction. Electric potentials of reversible systems can be modeled using the Nernst equation and a voltage can be obtained for the following chemical reaction

Anode:



Cathode:



Overall:



For the overall reaction 1.10, the Gibbs free energy is

$$\Delta G_{\text{rxn}} = \Delta G_{\text{rxn}}^{\circ} + RT \ln \left(\frac{a_{(A \text{ in } B)}}{a_A} \right) \quad (1.11)$$

where $\Delta G_{\text{rxn}}^{\circ}$ is the Gibbs free energy in standard state, R the gas constant, T the absolute temperature, a_A the activity of pure component A, and $a_{(A \text{ in } B)}$ is the activity of A in the B electrode. Using equation (1.7) we can rewrite the Gibbs free energy as an electric potential between the two electrodes as

$$\Delta E_{\text{rxn}} = \Delta E_{\text{rxn}}^{\circ} - \frac{RT}{z_i F} \ln \left(\frac{a_A}{a_{(A \text{ in } B)}} \right), \quad (1.12)$$

where E_{rxn}° is the electric potential of the reaction in standard conditions (unit activity).

H																	He
Li	Be	Negative electrode candidates										B	C	N	O	F	Ne
Na	Mg																Ar
K	Ca	Sc	Ti	V	Cr	Mn	Fe	Co	Ni	Cu							Kr
Rb	Sr	Y	Zr	Nb	Mo	Tc	Ru	Rh	Pd	Ag	Cd	In	Sn	Sb	Te	I	Xe
Cs	Ba		Hf	Ta	W	Re	Os	Ir	Pt	Au	Hg	Tl	Pb	Bi	Po	At	Rn

Figure 1-9: Periodic table of the elements. On the left we have the negative electrode candidates suitable to build a LMB composed of alkali and alkaline earth metals. On the right we have the positive electrode candidates located under the chalcogens and pnictogens.

1.3.1 Calcium Chemistries

Economics will ultimately govern which alloys can be used as electrode couples in LMBs. Keeping this in mind, we set forth to discover cheap abundant materials with the theoretical potential to form high stable voltages. The first place to look is at the periodic table while keeping the requirements in mind that were outlined earlier in this section. Knowing that we have to limit ourselves to cheap materials, an examination of the A||B elements on figure 1-9 was done to select suitable candidates. This was achieved by comparing the theoretical potentials in table 1.1 with the cost per mol in table 1.2 to calculate the energy cost (\$/kWh). These results are outlined in table 1.3.

B \ A	Li	Na	K	Mg	Ca
Sn	0.64	0.33	-	0.27	0.64
Pb	0.55	0.33	0.33	0.17	0.6
Sb	0.92	0.73	0.77	0.45	0.99
Bi	0.82	0.65	0.67	0.32	0.85

Table 1.1: Table showing the theoretical cell potential between A||B couples [2].

One might be inclined to conclude the Ca||Sb couple to be the optimal choice

Metal	\$/mol
Li	0.43
Na	0.057
Mg	0.069
Ca	0.14
Sn	3.2
Pb	0.52
Sb	1.8
Bi	4.9

Table 1.2: Prices for selected metals [2].

B \ A	Li	Na	K	Mg	Ca
Sn	210	370	-	480	190
Pb	64	64	630	180	36
Sb	89	93	330	180	69
Bi	240	300	550	560	220

Table 1.3: Table showing the theoretical energy cost for A||B couples in \$/kWh [2].

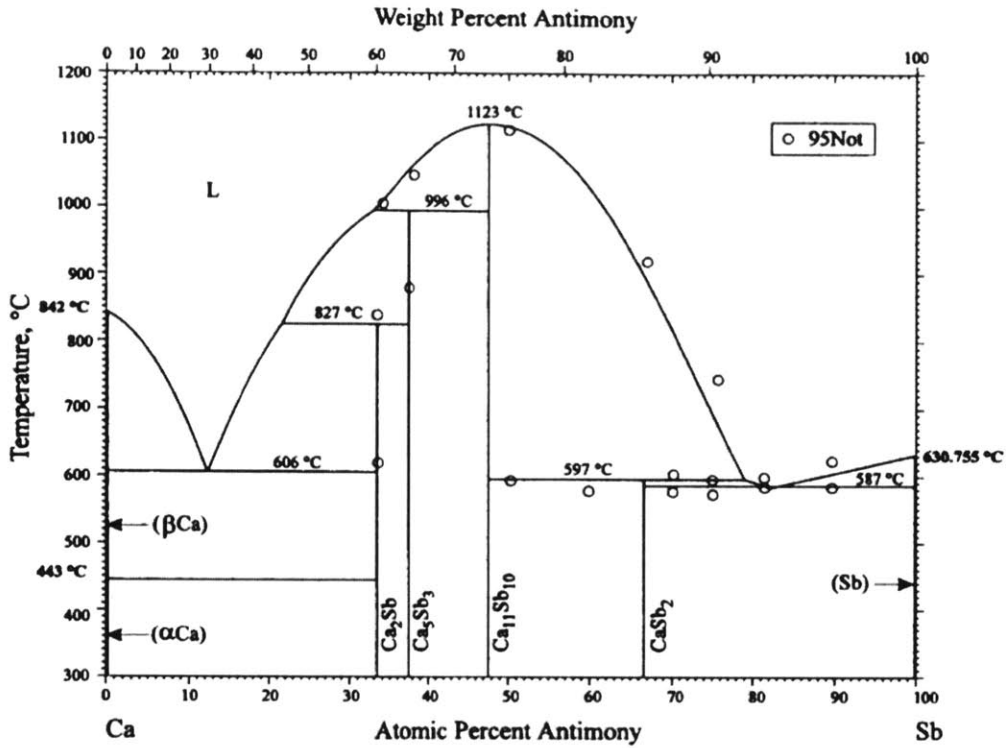


Figure 1-10: Calcium-antimony phase diagram [16].

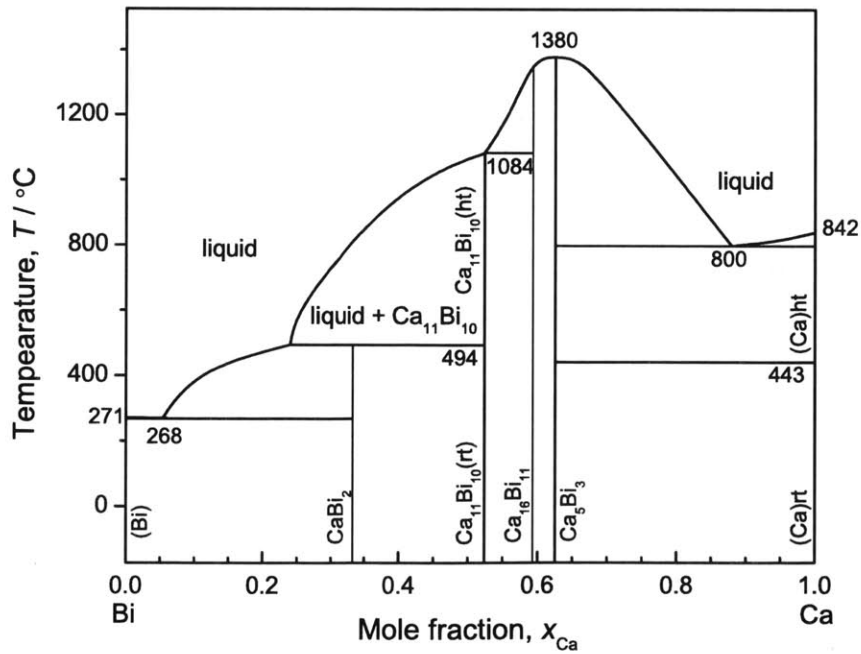


Figure 1-11: Calcium-bismuth phase diagram [17].

because it yields the highest cell voltage (0.99V) and is the cheapest (\$220/kWh), but this is not necessarily the case. The phase diagram for this couple (fig. 1-10) reveals the liquid temperature for this system to be over 600°C, which will require a greater amount of energy to keep it at that temperature. The operating temperature is another critical constraint when it comes to engineering LMBs, therefore a system (electrodes and electrolyte) that can be liquid at significant lower temperatures needs to be selected.

Another couple of interest is Ca||Bi, which is the chemistry I used to do the electrochemical experiments presented in this thesis. The phase diagram (fig. 1-11) for this system reveals nice high temperature intermetallics, but more exiting, it shows the wide liquid composition range in the bismuth-rich side to be at a significant lower temperature than that of Ca||Sb.

1.4 LMB Operating Principles

1.4.1 Thermodynamics

Equation 1.7 was used to convert the Gibbs free energy of the cell ΔG_{rxn} (eq 1.11) to an equivalent cell voltage ΔE_{rxn} (eq 1.12) one can measure during equilibrium. This cell voltage is directly related to the activity of an electrode surface, which for species i is defined as

$$a_i = \gamma_i x_i. \tag{1.13}$$

Equation 1.13 is the product of the activity coefficient, γ_i , and the species mole fraction, x_i . The activity coefficient is the parameter describing how binary systems will energetically interact at the atomic level. In an ideal solution, the interaction energies between all the permutations of A and B atoms are assumed identical, so the activity coefficient is defined as one. In a regular solution, such as the chemistries we use for LMBs, this is not the case and the activity will deviate from ideality depending on the interatomic interactions between the alloying atoms.

Binary alloys can deviate ways away from ideal behavior if the interaction energy between similar atoms ($\epsilon_{AA}, \epsilon_{AA}$) and dissimilar ones ($\epsilon_{AB} = \epsilon_{BA}$) are significantly different. Its deviation depends on the following two cases [18]:

1. $\epsilon_{AA} > \epsilon_{AB} < \epsilon_{BB}$.
2. $\epsilon_{AA} < \epsilon_{AB} > \epsilon_{BB}$.

The first case describes the atomic interactions of identical components to be greater than the energy between the two alloying components. This will make the mixture unstable, and will phase separate due to their immiscible nature. The Gibbs free energies for these type of binary couples are positive, meaning one must add extreme energies to make such reactions possible. This is the preferred interatomic interactions desired between the electrolyte and liquid metal, and the material housing the LMB because it will help minimize corrosion and contamination.

The second case describes a binary system where the energy of attraction between dissimilar atoms A and B is greater than that of identical constituents. This is a system favoring compound formation and mixing, so the activity will negatively deviate from the ideal solution behavior. These interatomic interactions are essential for LMBs because binary alloys that are 'happier' together than when separated are desired. This 'happiness' factor is the Gibbs free energy of formation, and first order approximations of the expected voltage can be calculated from Ellingham diagrams [19] using the free energy of interest in equation 1.7.

1.4.2 Kinetic Processes

The total flux, \mathbf{J}_i , of species i in an LMB is described by the Nernst-Planck equation [20],

$$\mathbf{J}_i = -D_i \nabla c_i - \frac{z_i F}{RT} D_i c_i \nabla \phi + c_i \mathbf{v} \quad (1.14)$$

where D_i is the diffusion coefficient (cm^2/s) of the i^{th} species, c_i is the species concentration (moles/cm^3), F is the Faraday constant, R is the gas constant, T is the

operating temperature (K), and \mathbf{v} the fluid velocity (cm/s). The three terms in the Nernst-Planck equation describe the forms of transport found in most liquid systems which are summarized in table 1.4.

Part	Equation	Description
Diffusion	$-D_i \nabla c_i$	Also known as Fickian diffusion, this type of transport results from local concentration gradients.
Migration	$-\frac{n_i F}{RT} D_i c_i \nabla \phi$	Describes the motion of charged species, such as electrolyte components, under the influence of an electric field ($\nabla \phi$).
Convection	$c_i \mathbf{v}$	Transport due to the collective motion of atoms under the influence of a force.

Table 1.4: Nernst-Planck transport component with description.

Historically, the influence of convection has been neglected when it comes to studying transport mechanisms in liquid alloys. This is due to the existence of only one closed-form solution to the momentum equations which account for convection, which is solved on the surface of a rotating disc electrode [21]. Any other set of boundary conditions will require lots of computational power (and patience) to generate solutions for the boundary conditions of interest, so it's easier to instead design the experiment such as to minimize the influence of it. Any significant buoyant forces become a problem under temperature variations because they cause the density to become unstable and possibly induce convection. This topic is further discussed in the simulation chapter of this thesis.

As mentioned in section 1.4.1, the binary couples of interest are the ones with high negative Gibbs free energy of formation, so LMBs can be built with suitable power and energy density applicable for grid-scale storage. The higher the open circuit voltage, the more energy efficient LMBs can be made because overpotentials become significant less of an issue.

1.4.3 LMB Limitations and Efficiencies

Voltage Overpotentials

The reason overpotentials become less problematic if the open circuit voltage is high can be seen in the components of the cell voltage, defined as

$$V_{\text{cell}} = V_{\text{ocv}} + \eta_{\text{mt}} + \eta_{\text{ct}} + \eta_{\text{ohm}}. \quad (1.15)$$

V_{ocv} is the theoretical open circuit voltage, η_{mt} is the mass transport overpotential associated with the Nernst-Planck equation. η_{ct} is the charge transfer overpotential at an electrode/electrolyte interface during a Faradaic process. It's essentially the extra voltage needed to drive the chemical reaction forward or reverse, which is described by the Butler-Volmer equation [21],

$$j = j_0 \left(e^{-\alpha f \eta_{\text{ct}}} - e^{(1-\alpha) f \eta_{\text{ct}}} \right), \quad (1.16)$$

where j is the current density (mA/cm²), j_0 is the exchange current density (mA/cm²), α is the transfer coefficient², and $f = F/RT$. The Butler-Volmer equation can be simplified in the limits of both high and low overpotentials. The last overpotential affecting the cell performance is the ohmic contribution, η_{ohm} . This is purely due to resistive heating in the cell components, primarily the electrolyte, during current flow. This overpotential is calculated using Ohms law

$$\eta_{\text{ohm}} = i R_{\Omega}, \quad (1.17)$$

where R_{Ω} is the combined electronic and ionic resistance in the electrolyte, and it's a function of the cell geometry.

Coulombic Efficiency

Electrochemical side reactions inside a LMB can lead to the loss of current during battery operation. This current, commonly known as the self-discharge current, will

²The value of α ranges between 0 and 1, and 0.5 for a reversible reaction.

reduce the overall coulombic efficiency of the battery, resulting in reduced energy efficiency. The coulombic efficiency is defined as the ratio of the discharged (Q_d) to charged (Q_c) number of coulombs in a cycle, written as

$$\text{Eff}_Q = \frac{Q_d}{Q_c} = \frac{\int i_d t_d dt}{\int i_c t_c dt}. \quad (1.18)$$

i_d and i_c are the discharge and charge currents, and t_d and t_c are the discharge and charge time respectively. What this current loss really signifies is the internal discharging of the battery where the electrons do not flow through the external circuit load, and instead are involved in side reactions.

Energy Efficiency

Perhaps the most important efficiency metric is the energy efficiency (Eff_U) which describes the overall energy round-trip efficiency. This parameter is defined as the product of the coulombic efficiency to the voltage efficiency given by,

$$\text{Eff}_U = \text{Eff}_Q \cdot \text{Eff}_V, \quad (1.19)$$

where the voltage efficiency is defined as the ratio of the discharge voltage, $V_{\text{cell, d}}$, to the charging voltage, $V_{\text{cell, c}}$ which can be computed from the governing voltages and overpotentials during operation.

Electrolyte Kinetic Limitations

The interfacial chemical reactions of an alloying cell are kinetically limited by mass transport of the electroactive species in the electrolyte, and once reduced by the transport within the electrode itself. The three entities governing transport phenomena are diffusion, migration, and convection, which can be modeled by the Nernst-Planck equation (eq 1.14). There is no convective influence in solid-state batteries which drastically simplifies the math, but this assumption cannot be made when characterizing the performance of liquid electrodes. One tends to neglect any kinetic limitations from the electroactive species in the electrolyte because most ionic diffusion coeffi-

cients vary over various orders of magnitude [22–24]. This assumption is true for the calcium-bismuth system studied in this thesis because of the large current densities induced (over 1 mA/cm^2) under potentiostatic conditions, as seen in figure 1-12.

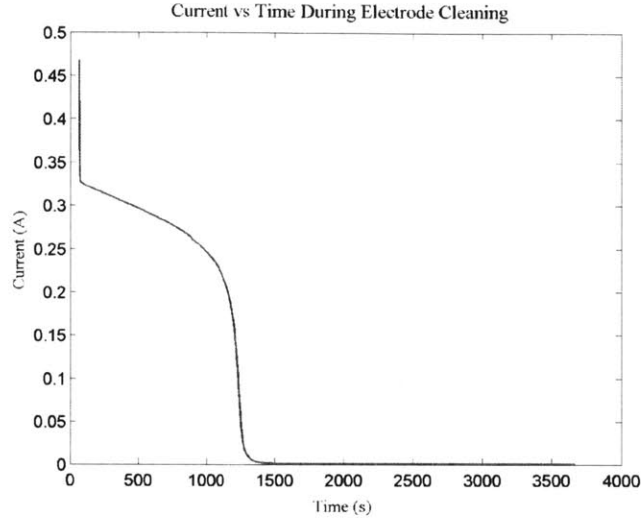


Figure 1-12: Over 1 A/cm^2 current density induced during potentiostatic step of 0.7 V .

The important fundamental material parameters that play a critical role to the onset of natural convection under a thermal gradient are density, diffusivity, and viscosity. The focus of this thesis involves chemical diffusivity measurements of calcium in bismuth, but before I begin talking about diffusion and only diffusion for the remainder of this document, I’d like to take a moment to discuss the structure of liquid metals.

1.5 Liquid Structure Background

In 1855, Adolph Fick [25] published the fundamental laws that mathematically described diffusion in liquids. He realized how the same phenomena causing a substance to diffuse was the same that caused heat to flow in a material, and electrons to flow in a conductor. This was a significant contribution to science, but questions still remained about the atomic structure of liquids. Questions such as “what type of interatomic interactions dominate when liquids mix, and how does it affect the rate

of diffusion?”, and “does liquid structure resemble that of the solid phase?” There was no way to answer such questions without knowledge of the atomic structure of materials.

Ten years after Fick’s discoveries, James Clerk Maxwell published his work on electromagnetism titled *A Dynamical Theory of the Electromagnetic Field* [26], where he presented the four equations which describe the interaction between electricity and magnetism. He proved to the world how light was an electromagnetic wave with a fixed speed that could be calculated from the two fundamental constants in electromagnetism, the permeability and permittivity of free space. This proved powerful because we now had a method to mathematically predict how electromagnetic waves would behave under certain conditions. Thirty years after Maxwell’s achievements the full potential of his theoretical work on electromagnetic theory was finally unleashed with the discovery of the X-ray.

In 1895 Wilhelm Conrad Röntgen was studying the effects of electric discharge inside vacuum tubes. His work led to the discovery of X-ray radiation which was published in his famous paper *On A New Kind of Rays* [27], and subsequently won him the first Nobel Prize in physics in 1901. In 1912, William Lawrence Bragg and William Henry Bragg derived Bragg’s law of diffraction after noting how crystalline solids formed distinct patterns of reflected X-rays. This work allowed us to use X-rays for imaging solids at the atomic scale, which paved the way for developing methods to understand liquid structure.

In 1915, Peter J. W. Debye [28] made a significant contribution in understanding liquid diffraction by demonstrating how electrons surrounding atomic nuclei must diffract electromagnetic waves. Throughout the years more contributions were made to the field of liquid diffraction in an effort to better understand the structure, but the overall progress was rather slow. In 1925 Debye furthered our understanding of liquid diffraction by introducing a probability function which described the chances atoms would be near each other within an interatomic distance. Two years later, Zernike and Prins [29] derived the well known radial distribution function $\rho(r)$ that is widely used today. The radial distribution function is a continuous function that describes

the probability per unit volume of an atom being a distance r from a central atom. It calculates the average number of nearest neighbors around a central atom between the interatomic distances r and $r + dr$, and it's most commonly written as $4\pi r\rho(r)dr$. Figure 1-13 shows the region of integration of the radial distribution function.

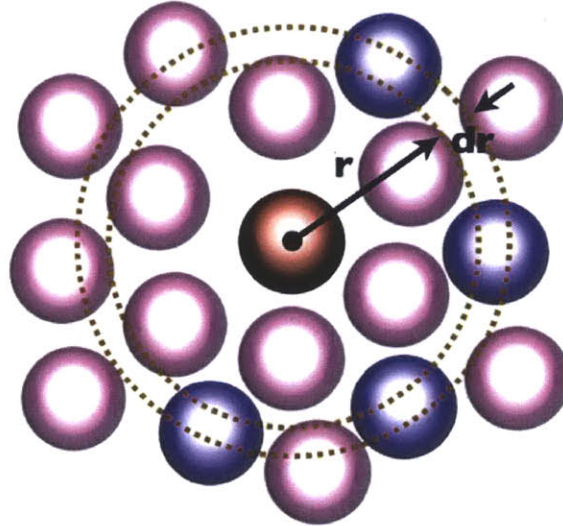


Figure 1-13: Radial distribution function schematic.

1.5.1 Pure Liquid Metals and Semi Metals

The difference in the number of nearest neighbors between a liquid and solid are graphically represented in Figure 1-14. In (a), every atoms is surrounded by exactly six atoms, but in (b) the atom labeled A is only surrounded by five. The atom to the left of the A in (b) looks to be surrounded by seven, and a couple atoms above it's only surrounded by six. From here we can see how the number of nearest neighbors for liquids is a statistical average making it impossible for long-range order atomic interactions to exist.

In fact, Frank [31] reasoned how a liquid metal was structurally different than its solid counterpart, and used the principle of supercooling to argue his point. He believed supercooling existed because the difference in atomic structure between the two phases giving rise to an energy difference with the solid lattice having the highest energy. He proposed a liquid pseudo-structure with five-fold symmetry consisting of

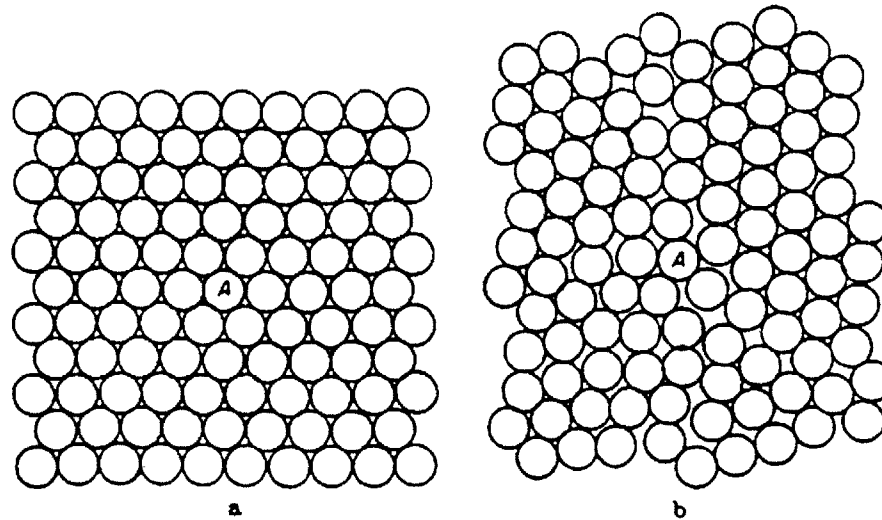


Figure 1-14: Both the solid (a) and liquid (b) contain the same number of atoms, the only difference is the number of nearest neighbors surrounding the A atom. In (a) it has six, while (b) has five [30].

an atom surrounded by twelve nearest neighbors, which yielded a configuration with a higher binding energy. As a result, the five-fold symmetry prohibited the liquid from exhibiting long-range lattice interactions.

Since the number of nearest neighbors changes upon melting for most metals (fig. 1-16), the radial distribution function should also change. In fact, figure 1-15 portrays very well the difference in the radial distribution function between a liquid and solid gathered from X-ray diffraction experiments. Solids always conform to a crystal lattice, so atoms are surrounded by a well defined number of nearest neighbors. In a liquid, atoms do not have a constant number of surrounding atoms, instead they will vary over time making the radial distribution function appear as an average rather than a step function.³

Interesting trends in coordination changes have been observed for metals and semi-metals conforming to different crystal structures. These trends change some of the material properties, most notably the electrical conductivity as shown in figure 1-17. For example, solid mercury has a rhombohedral structure with six nearest neighbors, which is more complex when compared to cubic lattices. When mercury melts, it

³In reality, there will be a finite width to the radial distribution function of a solid due to lattice defects and vibrations.

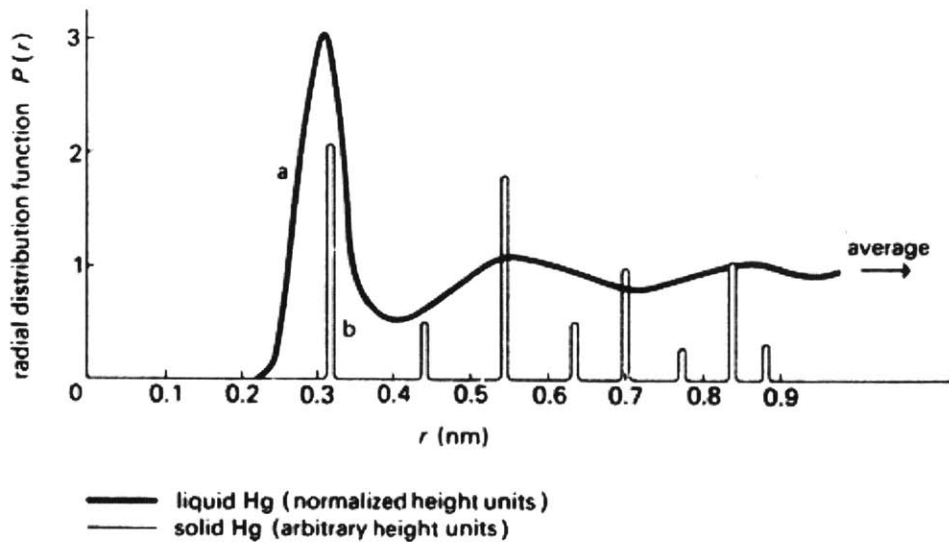


Figure 1-15: Radial distribution function comparison for (a) liquid mercury and (b) solid mercury [32].

gains six more nearest neighbors making it a more compact and simpler structure. The opposite effect was observed when metals with face-centered cubic structures melted. The liquid phase usually has a smaller coordination number than the solid phase, while body-centered cubic metals such as sodium and potassium observed virtually no change in coordination (see Figure 1-16).

Semimetals such as Sn, Sb, Bi, Ga, Ge undergo the largest change in entropy [33] upon melting due to their drastic changes in both material and electronic structure. Property changes most notable are magnetic susceptibility [34], and heat capacity dependence on temperature c_p . At the atomic level, one can see how this will reduce vibrational frequency modes, specially if the nature of the bond changes upon melting, so the heat capacity will be significantly affected. The electronic bandstructure changes the most for these semimetals compared to metals, especially in Bi, which was measured using nuclear magnetic resonance (NMR) by Knight *et al.* [34]. The NMR study showed a strong correlation between the arrangement of nearest neighbors and the electronic structure because of the notable shift observed in the NMR line. Since the NMR shift is directly related to the magnetic susceptibility, it will also estimate the change in the density of states at the Fermi level. Other techniques such as the Hall Effect [35] show a large difference in the free electron value between

<i>Metal</i>	<i>Solid</i>		<i>Liquid</i>		
	<i>Coordination No.</i>	<i>Distance Å</i>	<i>Coordination No.</i>	<i>Distance Å</i>	<i>Temp. °C</i>
Hg	6 + 6	3.0 + 3.47	12	3.30	20
Cd	6 - 6	2.97 + 3.29	8 + 4	3.06 + 4.0	350
Zn	6 - 6	2.66 + 2.90	11	2.94	480
Au	12	2.88	11	2.86	~ 1100
Pb	12	3.49	8 + 4	3.40 - 4.37	375
Al	12	2.86	10.6	2.96	700
Tl	6 + 6	3.40 - 3.45	8 + 4	3.30 + 4.22	375
In	4 - 8	3.24 - 3.37	8 + 4	3.17 + 3.88	165
			8 + 4	3.30 - 4.0	160
			8	3.36	390
Na	8	3.72	8	4.385	100
			8	3.90	400
			9.28	3.79	100
			8.95	3.79	400
K	8	4.62 *	8	4.64; 9.0	70
				4.85; 9.2	395
Rb	8	4.87 *	Analogous with f.c.c.		
			Analogous with f.c.c.		
Li	8	3.31 *	Analogous with f.c.c.		
			9.8	3.24	
		3.02 *			
Sn	4 - 2 + 4	3.15 - 3.76	10	3.20	280
			10	3.38	480
Ga	1 + 6	2.71 + 2.79	11	2.77	20
Bi	3 - 3	3.09 + 3.46	7 - 8	3.32	340
Ge	4	2.43	8	2.70	1000

* Values from W. HUME-ROTHERY, Institute of Metals Monograph, No. 1, London, 1947

Figure 1-16: Coordination number comparison between solid and liquid metals [30].

<i>Property</i>	<i>True Metals</i>	<i>Meta-Metals</i>	<i>Semi-Metals</i>	<i>Non-Metals</i>
Coordination number	12 or 8	6 + 6, 4 + 8	< 6	Low
κ Electrical conductivity	$3 \times 10^4 \rightarrow 7 \times 10^5$	$10^4 \rightarrow 10^6$	$10^{-3} \rightarrow 10^4$	$< 10^{-6}$
χ Magnetic susceptibility	Para, ferro.	Weakly dia.	Weak \rightarrow strong dia.	dia.
$\delta_{\text{solid}} = \frac{\Delta\kappa}{\Delta T}$	85	90-120	150-400	< 70
$\kappa_{\text{Liquid}} - \kappa_{\text{solid}}$	← Weakly - ve →		← - ve →	
δ_m	65	65	- ve	< 40
Liquid coordination number	8-11	8-11	7.5-11	Variable
δ_{Liquid}	75	75	80-180	< 50
Elements	Li, Na, K, Rb, Cs, Cu, Ag, Au, Mg, Ca, Al, Co, Ni, Ti, Pb	Zn, Cd, Hg, In	C, Sn, Si, Ge, Sb, Bi, Te, Ga, Se, P	P, S, Se, F, Cl, Br, I

Figure 1-17: Table showing the the variation of material properties [30]

the solid and liquid, and photoelectron spectroscopy [36], used for probing the band structure in condensed matter, agrees with the notable trend of these semimetals showing significant structural changes upon melting (fig. 1-18).

Bismuth also has the property of increasing its density upon melting, which came as no surprise when Sharrah [37] and Chamberlain [38] used X-ray and neutron diffraction to show how on average each bismuth atom gained two more nearest neighbors upon melting (from six to eight) making it a more compact structure. It is also believed that this is due to bismuth having mixed metallic and directional bonds [33] in the solid state, but not in the liquid state, where most of the directional bonds are lost and electrons are allowed to pass more freely into the conduction band.

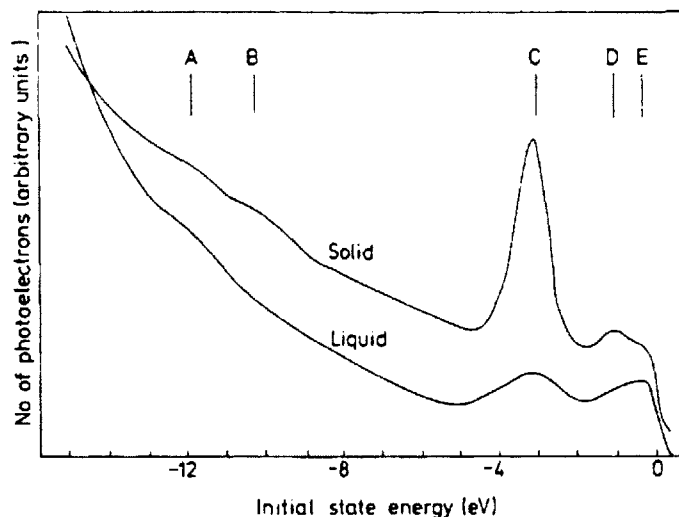


Figure 1-18: The energy distribution curves of photoemitted electrons from solid (300 K) and liquid (820 K) Bi at a photon energy of 21.2 eV. [36]

1.5.2 Liquid Alloys

These interesting changes in the properties of metals and semimetals led to asking questions about the atomic interactions between dissimilar⁴ metals such as bismuth and lead. If two metals with different solid crystal structures are alloyed at various compositions in the liquid state, say one gains and the other loses nearest neighbors upon melting, what happens to the material properties of the alloy? How does the diffusion coefficient vary in these liquid metals as a function of composition and temperature? Can the alloy material characteristics be predicted by numerically combining the component properties measured with techniques such as diffraction, optical, magnetic, and resistivity measurements? To begin answering these type of questions, Sharrah [37] performed X-ray diffraction experiments on bismuth in lead as a function of composition.

The XRD spectra in figure 1-19 shows bismuth and lead to be a little similar because both contain eight nearest neighbors at approximately the same distance (3.4 Å for lead, 3.32 Å for bismuth) but lead has another four slightly less than 1 Å radially away from the initial eight making it 12 total. The results show the

⁴Liquid Bi and Pb have different number of nearest neighbors when measured with diffraction methods.

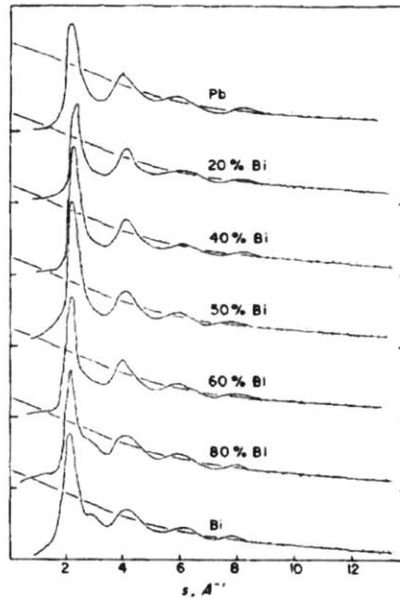


Figure 1-19: Relative intensities of X-ray scattering from lead, bismuth and five alloys. Composition is in wt%. The monotonic curves represent the calculated independent scattering [37].

		$T^{\circ}\text{C}$	s at intensity maxima and minima, \AA^{-1}						r at density maxima, \AA		Mean number of nearest neighbors	
			max.	min.	max.	min.	max.	min.	max.	1st		2nd
Pb	x^{1h}	375	2.2 ^a	3.1 ^a	3.9 ^a	5.0 ^a	5.9 ^a	6.8 ^a	...	3.40	6.4 ^a	8+4
Pb	n^7	390	2.0 ^a	3.0 ^a	4.1 ^a	3.4	6.4	12±1
Pb	x^4	3.4 ^a	6.2 ^a	11
Pb	n^5	350	2.3	3.1	4.2	5.2	6.1	7.0	8.2	3.40	6.6	9.4
Pb	x	331	2.2	3.2	4.1	5.2	6.0	7.4	8.2	3.39	6.8	12.1
Pb	n	350	2.2	3.3	4.1	5.2	6.1	7.1	8.1	3.38	6.7	11.7
10% Bi	n	330	2.2	3.2	4.1	5.0	6.0	7.0	8.0	3.40	6.7	11.0
20% Bi	x	266	2.2	3.4	4.1	5.1	6.1	7.5	8.2	3.39	6.4	12.5
25% Bi	n	260	2.2	3.2	4.1	5.1	6.1	7.0	8.0	3.39	6.7	11.8
40% Bi	x	200	2.2	3.4	4.1	5.4	6.1	7.5	8.2	3.36	6.5	12.2
50% Bi	x	154	2.2	3.4	4.1	5.3	6.0	7.0	8.0	3.41	6.8	12.1
55.5% Bi	n	170	2.2	3.3	4.1	5.0	6.1	7.0	8.0	3.38	6.7	11.7
55.5% Bi	x^{1c}	130	3.45	6.8 ^a	...
60% Bi	x	154	2.1	3.4	4.0	5.2	6.0	7.2	8.0	3.39	6.8	11.5
80% Bi	x	216	2.1	3.5	4.2	5.3	6.0	7.2	8.0	3.35	6.6	10.9
90% Bi	n	260	2.1	3.3	4.1	5.1	6.2	7.3	8.0	3.37	6.7	8.3
Bi	x	285	2.1	3.4	4.1	5.5	6.2	7.2	8.0	3.35	6.7	7.6
Bi	n	300	2.1	3.4	4.1	5.3	6.1	7.3	8.0	3.36	6.7	7.8
Bi	n^6	300	2.2	3.3	4.2	5.3	6.2	7.2	8.2	3.35	6.8	7.7
Bi	n^6	3.2 ^a	6.5 ^a	7-7.5
Bi	n^7	310	2.0 ^a	3.3 ^a	4.2 ^a	5.2 ^a	6.4 ^a	7.6 ^a	...	3.2	6.7	8 to 4A
Bi	x^{1A}	340	2.1 ^a	3.5 ^a	4.1 ^a	5.4 ^a	5.9 ^a	7.1 ^a	8.0 ^a	3.32	6.6 ^a	7-8
Bi	x^{10}	280	2.1	3.1	3.9	4.8	5.6	3.55	5.9 ^a	10.5

^a Estimated from graphs given in reference.

Figure 1-20: Summary of diffraction and density results [37].

lead-bismuth alloy maintained a coordination number of 12 when alloyed up to 60 – mol% bismuth (fig. 1-20) before decreasing asymptotically to that of pure bismuth. There really is no way of predicting such behavior from the phase diagram (fig. 1-21) or chemical diffusivity experiments. Figure 1-22 shows the chemical diffusivity of bismuth reaching an asymptotic value over the range of composition where the number of nearest neighbors decrease from 12 to eight. This is baffling because in the lead-rich region, the density decreased upon melting and the results showed a coordination of 12 with a mean distance shorter than that of the crystal. This led him to suggest a liquid structure model having the symmetry of a pentagonal dodecahedron, which also described the lack of long range order in a liquid. These results are not surprising because lead has a coordination number of 12 at a distance of 3.49 Å in the solid state, and when it melts, it switches to an 8 + 4 coordination at the average distances of 3.40 Å + 4.37 Å. This will cause the average local volume occupied by the same number of nearest neighbors to increase, which in return will decrease the density.

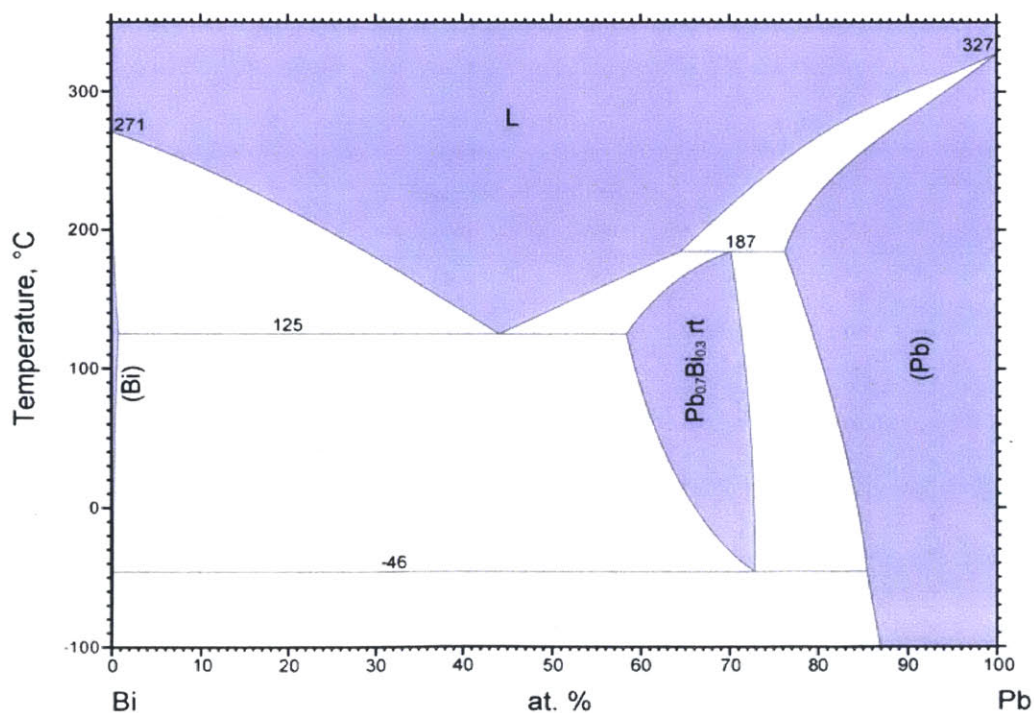


Figure 1-21: Bismuth-lead phase diagram

It is difficult to guess what the trend in chemical diffusivity will be as a function

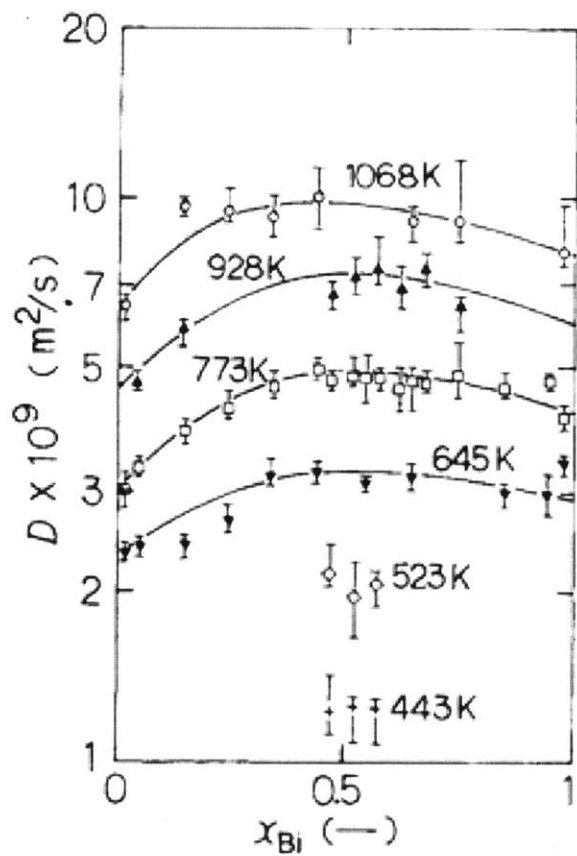


Figure 1-22: Chemical diffusivity of bismuth in lead measured using the capillary-reservoir method [39].

of composition of a liquid alloy by looking at XRD data, therefore it is of extreme importance to measure it experimentally.

1.6 Interest in Liquid Diffusion

Since the mid-20th century, liquid metals have been of interest to the scientific community, not only out of curiosity, but because of their applications. Their high thermal conductivity made them applicable as coolants for atomic reactors [40–42] in the nuclear industry. Also, because nuclear reactor waste is recycled from liquid metals [43,44], an accurate knowledge of the transport properties could help optimize the reprocessing rate. The diffusivity in liquid alloys also plays a critical role in the kinetics of solidification because it dictates how the microstructure will evolve [45]. Other applications where diffusion plays an important role include soldering [46], welding [47], diffusion bonding such as transient liquid phase bonding [48], and the latest being Liquid Metal Batteries (LMBs) [2,4,9,11]. The boom of the electronic industry furthered the interest of obtaining more efficient ways to measure this liquid diffusivity because the interactions between the liquid soldering alloy and copper substrates have tendencies to form intermetallic compounds [49] leading to the degradation of solder joints over time. Over the years many techniques such as the shear cell [50–59], capillary [39,52,58,60–71,71–77], neutron scattering [78–80], radiotracers [81], pulsed ion beam [82] and electrochemical [83,84] were developed and selectively applied to different liquid alloy systems.

1.7 Sensitivity Analysis - Impact of Chemical Diffusivity to the Transport in LMBs

The definition of a liquid is a material having a definitive volume, but lacks shape, usually settling at the bottom and taking shape of whatever is containing it. This simple definition might not mean much, but if one dives deeper into its root, it can be concluded that liquid atoms exert very strong atomic interactions, possibly stronger

than that of solids if the metal densifies upon melting. Since most of the material properties for liquid metals are very similar to their solid state, it made it easy to treat the liquid as a solid, with the exception of mechanical deformation. The force required to shear a liquid is orders of magnitude smaller than that required for a solid, therefore causing the fluid to flow upon stressing. The rate of deformation, or fluid flow, is proportional to the shear force by a constant known as the viscosity. Deformation cause by shearing will depend on the atomic properties of the metal in question, which inherently depend on temperature. This ‘deformation’ implies permanent relocation of atoms, making the viscosity a function of self-diffusion. Similar to the viscosity, the diffusion coefficients in liquid metals have been shown to be orders of magnitude higher than solids.

In order to understand the transport properties of liquid metals, the atomic interactions between atoms have to be well understood. Frost [30] was first to propose how the properties of a liquid metal alloy as a function of composition resemble that of its solid phase. He came to the conclusion after comparing the latent heats of fusion to the latent heat of vaporization for certain metals, and noticing that of fusion being much smaller, indicating the material properties of liquids would be more similar to the solid state than the gas state. Also, the electrical and thermal conductivity of liquid metals was shown to drop by about half its value upon melting when compared to its solid state, so he concluded that the structure of liquid metals was not very different than its solid since these material properties rely heavily on the arrangement of atoms within their lattice.

We know LMBs are composed of three liquid layers separated by immiscibility and difference in density. The liquid state allows the battery to operate at higher than normal kinetic rates when compared to standard solid-state batteries, but have also proven difficult to characterize as they scale-up in size. To begin optimizing the performance of the LMBs, the chemical diffusivity must be known as a function of temperature and composition because it dictates how the concentration profile will transiently evolve in the electrode. This allows one to compute specific operating conditions that maximize the energy capacity per cycle for a specific LMB. The

chemical diffusivities for a very limited number of liquid metal couples have been measured before using various experimental techniques and have shown to range between 10^{-4} cm²/s and 10^{-6} cm²/s [39,58,75–77,85–89]. Even though the chemical diffusivity database for liquid alloy couples is sparse, it still spans three orders of magnitude, which makes it difficult to form educated guesses on desired values. One such desired value is the chemical diffusion of calcium in liquid bismuth because it is a promising electrode LMB candidate due to its high voltage and earth abundance [17]. To our knowledge, the diffusion coefficient of calcium in the liquid state has never been measured in any host liquid metal. This can be attributed to the extreme difficulty of working with calcium because of its affinity to oxidize and react violently with other materials.

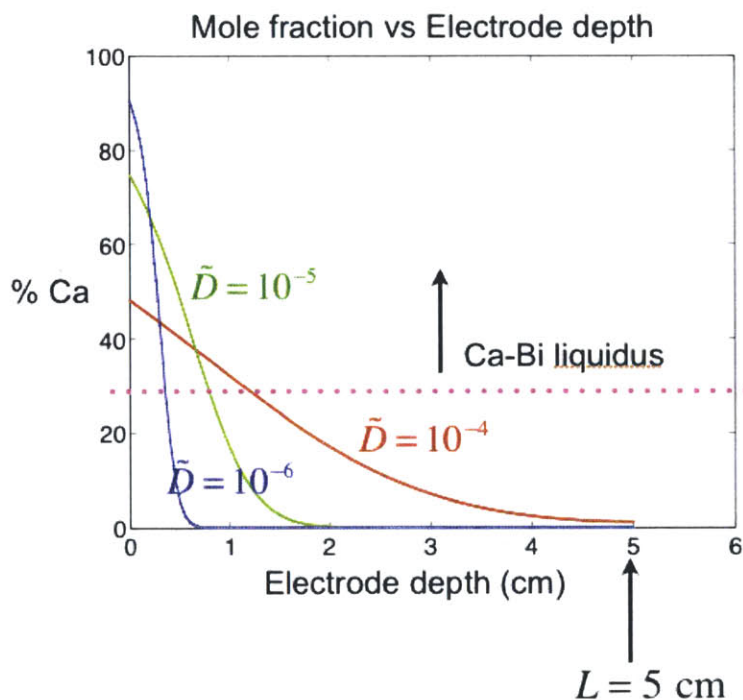


Figure 1-23: Sensitivity analysis on a 5cm thick electrode. The chemical diffusivity was varied over three orders of magnitude.

The true impact of the chemical diffusivity on the transport in a liquid electrodes can be seen by simulating a galvanostatic process. Figure 1-23 shows the simulated diffusion profiles at six hours after titrating calcium with a constant current density of

250 mA/cm² in the absence of convection⁵ at 600°C. The LMB will begin to experience rate limitations when the electrode surface concentration surpasses the liquidus composition of 23 – mol % calcium because the system will become unstable and start to nucleate the Ca₁₁Bi₁₀ intermetallic compound. Once the compound is formed, the LMB cannot be operated at high rates because the kinetics of the system will be hindered by the slower diffusivity of calcium in the intermetallic. Also, the intermetallic will grow as a function of time eventually forming a solid layer between the electrolyte and electrode, completely eliminating the liquid-liquid interface. Therefore it is imperative to operate the battery within current densities and times that will keep the electrode surface concentration from exceeding the critical composition. The battery can in theory be operated beyond the 23 – mol % because the alloy still maintains a high voltage [17] up to the composition of 60 – mol % Ca when measured with respect to pure calcium, but will have to be operated at much lower current densities. The chemical diffusivity also dictates how the penetration depth of the titrated species will vary, hence we can optimize the electrode thickness for a particular galvanostatic application.

1.8 Conclusion

During the 1950's theoretical advances were made in understanding the electronic properties of liquid metals so that we can use that knowledge to better comprehend their structure, just as we had done with solid metals. Solids are easier to characterize because the atoms periodically arrange themselves to form a crystal lattice, therefore we can use experimental tools such as X-ray diffraction to decipher its structure. A huge advantage to studying solid metals was the ability to mathematically describe their material properties with either the theory of electronic structure or dislocation theory. Contrast to solid metals, liquid metals have no long-range order, therefore exhibit random atomic fluctuations making them extremely difficult to study.

Historically, liquid diffusion coefficients have been difficult to experimentally mea-

⁵Convection scales with the Rayleigh number, smaller capillaries yield smaller velocity fields.

sure, having an uncertainty of up to 50 pct [90]. This is due to the extreme temperatures needed to keeping the metals liquid, which make it very difficult to handle and maintain at a constant temperature. If the temperature fluctuates, the liquid density's dependence on temperature will induce convection which will affect the transport and enhance the diffusivity value, therefore it is imperative to maintain experimental conditions that will allow one to keep a constant temperature throughout the entire duration of the measurement.

Chapter 2

Diffusion - Theory and Experiment

This chapter focuses on the fundamental concept of diffusion and various techniques used throughout the years to measure such phenomena in liquid systems.

2.1 Fundamentals of Diffusion

In 1905 Einstein published his famous paper on Brownian Motion [91], describing how diffusion leads to the homogenization of spherical particles in a mixture. This diffusive process, most commonly known as a *random walk*, is a stochastic Markov process that is independent of the history and relies solely on the current state. Einstein derived the well known Stokes-Einstein equation using the drag force in Stokes law [92] to describe the diffusion of spherical particles of radius r through a continuous medium with viscosity η , given by

$$D = \frac{k_{\text{B}}T}{6\pi\eta r}, \quad (2.1)$$

where D is the diffusion coefficient, k_{B} is Boltzmann's constant, and T is the absolute temperature. Equation 2.1 is intended to be used for a system of noninteracting particles which is a fundamental assumption in the derivation of Stokes law.

2.1.1 Probability Associated With Diffusion

Figure 2-1 is a generic illustration of a probability function $p(\mathbf{r})$ decaying with time, and the general form can be derived using the Central Limit Theorem [93]. $p(\mathbf{r})$ is defined to be the probability distribution function for a displacement \mathbf{r} , and $P_N(\mathbf{R})$ is the probability distribution function for the position after N steps¹. If independent and identically displacements are assumed during the random walk, the probability distribution can be written as

$$P_{N+1}(\mathbf{R}) = \int p(\mathbf{r}) \cdot P_N(\mathbf{R} - \mathbf{r}) d\mathbf{r}. \quad (2.2)$$

Other assumptions require the displacement steps to be isotropic, defined as $\langle \mathbf{r} \rangle = \int \mathbf{r} p(\mathbf{r}) d\mathbf{r} = 0$, and for the length scale l to be finite satisfying the condition $\langle \mathbf{r}^2 \rangle = d \langle \mathbf{r}_i^2 \rangle = l^2 < \infty$.

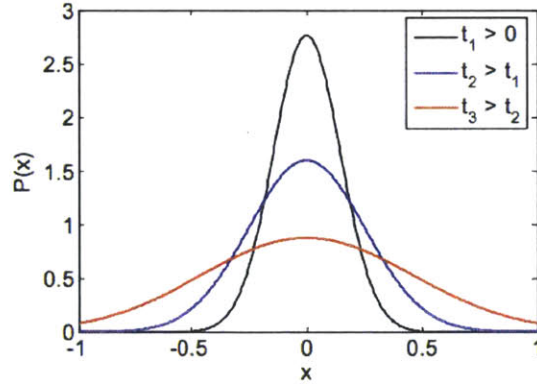


Figure 2-1: Probability distribution function at various times.

$p(\mathbf{r})$ is localized at the scale l which is much less than the scale describing the dynamical spreading of the distribution function. With this, we can Taylor expand $P_N(\mathbf{R} - \mathbf{r})$ inside the integral,

$$P_{N+1}(\mathbf{R}) = \int \left[P_N(\mathbf{R}) - \mathbf{r} \cdot \nabla P_N(\mathbf{r}) + \mathbf{r} \cdot (\nabla \nabla P_N(\mathbf{r})) \cdot \frac{1}{2} \mathbf{r} \right] p(\mathbf{r}) d\mathbf{r}. \quad (2.3)$$

¹After $N = 1$ steps, they equal each other $p(\mathbf{r}) = P_1(\mathbf{R})$

We can further simplify equation 2.3 by writing the gradient operators as infinite sums²

$$P_{N+1}(\mathbf{R}) = \int \left[P_N(\mathbf{R}) - \sum_{i=0}^d r_i \frac{\partial R_N}{\partial R_i}(R) + \frac{1}{2} \sum_{i=1}^d \sum_{j=1}^d r_i r_j \frac{\partial^2 P_N}{\partial R_i \partial R_j}(R) \right] p(\mathbf{r}) d\mathbf{r} \quad (2.4)$$

which simplifies to

$$P_{N+1}(\mathbf{R}) \cong \int P_N(\mathbf{R}) p(\mathbf{r}) d\mathbf{r} - \sum_{i=1}^d \left(\int r_i p(\mathbf{r}) d\mathbf{r} \right) \frac{\partial R_N}{\partial R_i}(R) \quad (2.5)$$

$$+ \frac{1}{2} \sum_i \sum_j \int (r_i r_j p(\mathbf{r}) d\mathbf{r}) \frac{\partial^2 P_N}{\partial R_i \partial R_j}(R) + \dots$$

$$\cong P_N(\mathbf{r}) + \frac{1}{2} \sum_{i=1}^d \sum_{j=1}^d \langle r_i r_j \rangle \frac{\partial^2 P_N}{\partial R_i \partial R_j}(R). \quad (2.6)$$

(...) represents higher order terms from the Taylor expansion that are negligible. Since the displacement vector varies with time τ , we can rearrange equation 2.6 and use the following substitution $\langle r_i r_j \rangle = \delta_{ij} \frac{l^2}{d}$ to get

$$\frac{P_{N+1}(\mathbf{R}) - P_N(\mathbf{R})}{\tau} = \left(\frac{l^2}{2d\tau} \right) \nabla_R^2 P_N(\mathbf{R}) = \frac{\partial P_N(\mathbf{R})}{\partial t}. \quad (2.7)$$

Atomic Diffusion

As noted above, $P_N(\mathbf{R})$ is the probability associated with one random walk after N steps at time τ . The probability associated with M random walks then is the concentration (c), which is the product of the two, $c(\mathbf{R}, t = N\tau) = M P_N(\mathbf{R})$. This can be used in conjunction with the differential form of equation 2.7 to get

$$\frac{\partial c}{\partial t} = D \nabla^2 c, \quad (2.8)$$

² $\mathbf{r} \cdot \nabla P_N(\mathbf{r}) = \sum_{i=1}^d r_i \frac{\partial R_N}{\partial R_i}(\mathbf{R})$ and $\mathbf{r} \cdot (\nabla \nabla P_N(\mathbf{r})) \cdot \frac{1}{2} \mathbf{r} = \frac{1}{2} \sum_{i=1}^d \sum_{j=1}^d r_i r_j \frac{\partial^2 P_N}{\partial R_i \partial R_j}(\mathbf{R})$

where $D = l^2/2d\tau$ is the diffusion coefficient, and d the space dimension of the system.

2.2 Diffusion in Liquid Metals

In general, this thesis focuses on the chemical diffusivity of component A (\tilde{D}_A) in the A||B liquid alloy, which describes how component A diffuses under the influence of a gradient in its concentration. The following sections talk about both diffusion in liquid metals, the first focuses on theoretical models, and the second section on experimental methods used to measure the diffusion coefficients in liquid metals.

2.2.1 Theoretical Models

Free Volume Model

In 1959, Cohen and Turnbull [94] published a theoretical model for the diffusion constant (D) in liquids that is best described by hard-spheres. Their model was related to the *free volume* v_f of the liquid because their derivation originated from the statistical ordering of the spherical atoms, which can fluctuate and create enough free volume for diffusion to occur. They called the inverse of the viscosity the fluidity ($\phi = 1/\eta$) and related it to the diffusion coefficient using the Stokes-Einstein relation

$$D = \frac{k_B T \phi}{3\pi a_0}, \quad (2.9)$$

where a_0 is the diameter of a spherical molecule. They used the fluidity description because of the features observed experimentally, such as its negligible dependence on temperature, and strong dependence on pressure. In fact, because the fluidity decreases with increasing pressure, the authors reasoned how the fluidity was related to the molecular average free volume, defined as

$$v_f = \bar{v} - v_0, \quad (2.10)$$

with \bar{v} being the average volume of a spherical molecule in the liquid and v_0 the van

der Waals molecular volume. Their view focused on diffusion occurring due to atomic volume fluctuations, which is an activated process. Using a probability function that described the chance free volume will form, they obtained the expression

$$D = ga^*u \exp(-\gamma v^*/v_f) \quad (2.11)$$

for the diffusion coefficient, where g is a geometrical constant, a^* is approximately the molecular diameter, u is the average particle velocity, γ is a correction factor for the free volume overlap, and v^* is the critical volume that needs to be exceeded for diffusion to happen.

Equation 2.11 accurately predicts diffusivities for simple liquids if the product γv^* is approximately that of the molecular volume [94]. Their model eliminates the need to characterize liquid diffusion as an activated process of Arrhenius behavior because the average molecular velocity u is proportional to the square root of temperature (\sqrt{T}), and v_f increases linearly with temperature [18]. The authors showed how the equation was able to predict the self-diffusion coefficients for simple metals, such as Na, Hg, Ag, but was 30% off when predicting the self-diffusion of tin [94]. To conclude, their theoretical description of liquid diffusion agrees well when it is used to describe van der Waals-type liquids such as hydrocarbons, but it lacks the ability to describe diffusion in more complicated systems such as liquid metals, or in my case, liquid metals mixed with semimetals.

Thermodynamic Models

R. A. Swalin [95] proposed a liquid diffusion model around the same time as Cohen, that originated from the theory of fluctuations due to the belief that diffusion resulted from small atomic movements caused by density fluctuations. His theory assumes there being no activation energy for diffusion to occur, with the implication that thermodynamic properties contribute to solute diffusion, given by

$$D = 1.29 \times 10^{-8} \frac{T^2}{\Delta H_v \alpha^2}, \quad (2.12)$$

where ΔH_v is the enthalpy of vaporization, and α is related to the interatomic potential's dependence on separation distance. Although he claims the theory to be non-Arrhenius, his data shows linear behavior when plotting $\ln(D)$ vs $1/T$ with an activation energy proportional to temperature, $Q = 2RT$. Nachtrieb [52] was first to point out the main discrepancy behind Swalin's theory, by explaining how Swalin made an error in his derivation by assuming the partition functions for both activated and ground states could be cancelled on the basis that they are equal. This throws away the terms containing the free energy functions, which indirectly makes it a non-activated process. This theoretical effort still served to be valuable because it emphasized on the importance of very small atomic displacements.

2.2.2 Experimental Techniques for Measuring Diffusivity

Electrochemical Methods

Rickert [96] was the first to investigate diffusion in liquid metals using electrochemical techniques. Unfortunately it did not involve only liquid metals because his work focused on the diffusivity of oxygen, a nonmetal, in copper and silver. Several other authors have since studied oxygen diffusion in liquid metals [97–100]. Our interest lies purely in the electrochemical measurement of the chemical diffusivity within binary liquid alloys, an area not well investigated. Just recently in 2011, a paper was published by Murakami [84] claiming to be the first to use electrochemical methods for measuring the diffusion coefficient in liquid binary alloys. This is not necessarily true because in 1984, Oakeson [83] electrochemically measured the chemical diffusivity of sodium in liquid tin. Oakeson's method used sodium- β'' -alumina as the electrolyte because of its superb ability to conduct sodium ions at an efficient fast rate which proved suitable for studying the kinetic properties of liquid alloys. Figure 2-2 is the schematic of their electrochemical cell used in these experiments.

Oakeson used both equilibrium and transient methods to measure the chemical diffusivity. The equilibrium method consisted of solving Fick's second law (eq. 2.8) with

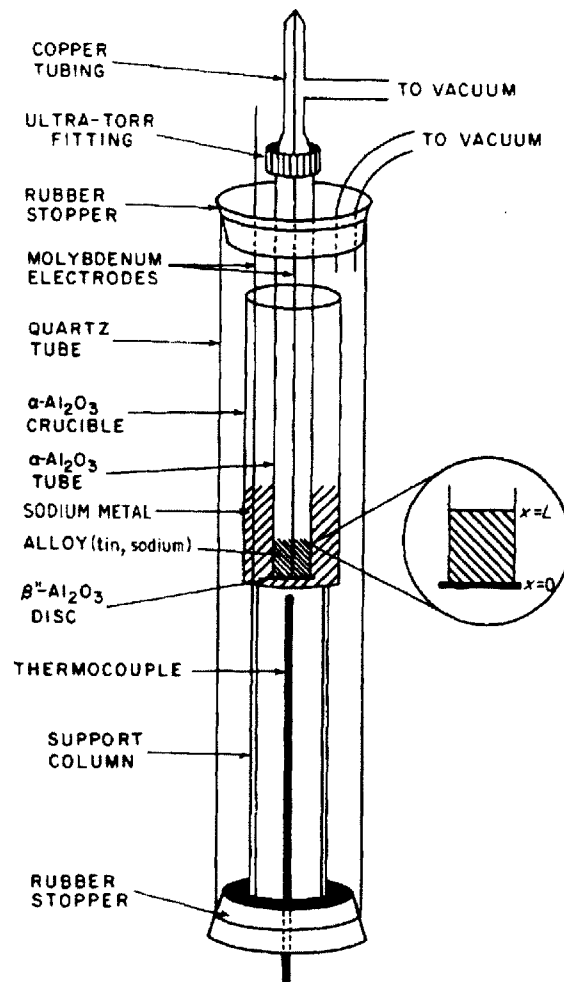


Figure 2-2: A schematic illustration of the sodium- β'' -alumina electrochemical cell used in the diffusivity measurements of sodium in tin [83].

the following boundary conditions³

$$c(x, 0) = c_0 \quad 0 \leq x \leq l \quad (2.13)$$

$$c(0, t) = c^0 \quad t > 0 \quad (2.14)$$

$$\frac{\partial c}{\partial x}(l, t) = 0 \quad t > 0 \quad (2.15)$$

to get the following infinite series solution [83]:

$$c(x, t) = c^0 + \sum_{m=0}^{\infty} \frac{4(c_0 - c^0)}{\pi(2m+1)} \sin \left[\left(m + \frac{1}{2} \right) \frac{\pi x}{l} \right] \exp \left[- \left(m + \frac{1}{2} \right)^2 \frac{\pi^2 D t}{l^2} \right]. \quad (2.16)$$

Their procedure included the application of a constant voltage for a time t_1 to generate generate the concentration profile shown in figure 2-3.

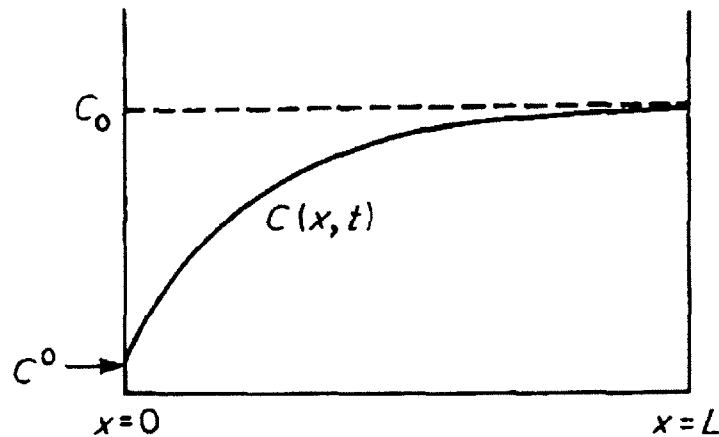


Figure 2-3: A schematic drawing showing the boundary and the initial conditions of the diffusion problem as well as a schematic illustration of the composition profile for $t > 0$ [83].

The applied voltage was removed after time t_1 (around an hour), and the concentration was allowed to equilibrate. The new average composition is given by

³The length in the equations l is the same as the schematic length L .

$$\bar{c}(t_1) = \frac{1}{l} \int_0^l c(x, t_1) dx \quad (2.17)$$

which can be applied to equation 2.16 to obtain the full solution. The authors assumed Henrian⁴ behavior, and wrote the concentration of sodium as a function of voltage using the Nernst equation to get

$$\begin{aligned} \bar{c}(t_1) &= \frac{c_{\text{Sn}}}{\gamma_{\text{Na}}} \exp\left(-\frac{F\bar{E}(t_1)}{RT}\right) \\ &= c^0 + \sum_{m=0}^{\infty} \frac{8(c_0 - c^0)}{\pi^2(2m+1)} \exp\left[-\left(\frac{2m+1}{2l}\right)^2 \frac{\pi^2 Dt_1}{l^2}\right]. \end{aligned} \quad (2.18)$$

By applying a constant voltage for the time t_1 , and keeping the first couple of terms in the series solution, the authors calculated the diffusion coefficient of sodium in tin.

Their transient method involved examining the relaxation behavior of the cell potential after removal of the external applied voltage. The initial concentration is given by equation 2.16 evaluated at t_1 . There is no flux of sodium into the cell during the evolution of the potential, so the end boundary conditions are simply

$$\frac{\partial c}{\partial x}(0, t) = \frac{\partial c}{\partial x}(l, t) = 0. \quad (2.19)$$

Solving Fick's second law with these boundary conditions gives the following solution,

$$\begin{aligned} c(x, t) &= \frac{1}{l} \int_0^l f(\zeta) d\zeta + \\ &\quad \frac{2}{l} \sum_{n=1}^{\infty} \cos\left(\frac{n\pi x}{l}\right) \exp\left[-\frac{n^2 \pi^2 Dt}{l^2}\right] \int_0^l \cos\left(\frac{n\pi \zeta}{l}\right) f(\zeta) d\zeta, \end{aligned} \quad (2.20)$$

where $f(\zeta) = c(x, t_1)$ (equation 2.16 evaluated at t_1). Equation 2.20 is evaluated at the surface, then related to the cell voltage using equation 2.18. The chemical

⁴They wrote the activity of sodium as $a_{\text{Na}} = \gamma_{\text{Na}} \frac{c_{\text{Na}}}{c_{\text{Na}} + c_{\text{Sn}}} \cong \gamma_{\text{Na}} \frac{c_{\text{Na}}}{c_{\text{Sn}}}$

diffusivity was calculated by fitting a curve to the data (fig. 2-4).

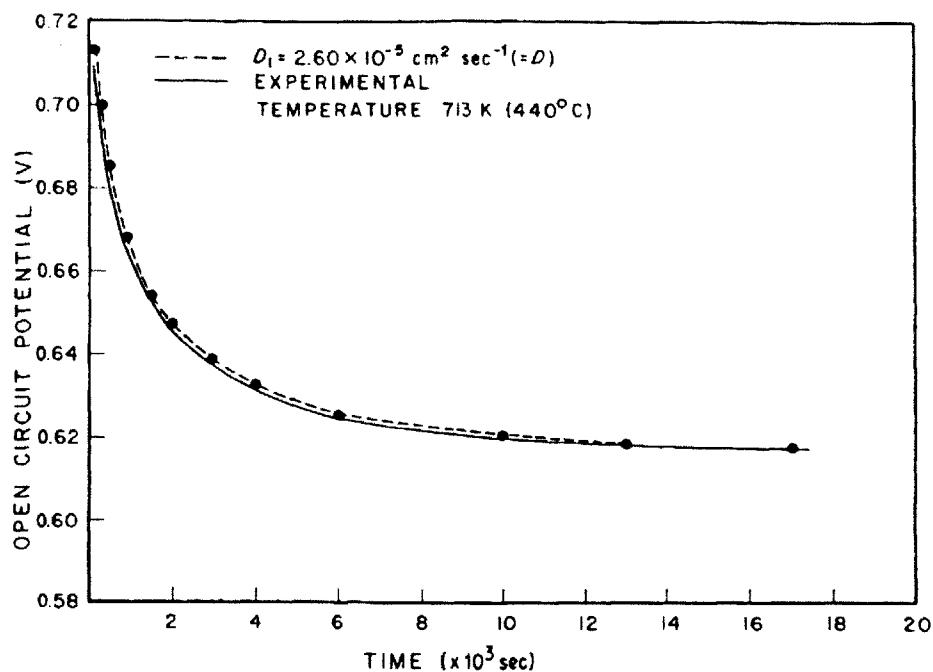


Figure 2-4: Curve of open circuit potential against time at 440 °C. The decay curve calculated with $D = 2.6 \times 10^{-5} \text{ cm}^2/\text{s}$ agrees with the experimental decay curve [83].

Both methods proved that one could fit the derived concentration-voltage relations to the experimental data and extrapolate the diffusion coefficients, but both did not agree well with each other. The transient method gave consistent higher diffusivity values compared to the equilibrium method, which they attributed to the relaxation being influenced by the faradaic activity at the liquid metal/ β'' -alumina interface, particularly the electrical double-layer effect. This is not necessarily true because the electrical double-layer only influences the signal within the first milliseconds. Also, the authors failed to use a reference electrode in their measurements, so the measured voltages could possibly have been influenced by changes in activity at the counter electrode from polarization effects. They used a cell diameter of 2 cm, but failed to mention the length l or the effect of convection. Convective transport probably did affect their measurements because the sodium, which is seven times less dense than tin, is being introduced from the bottom of the cell. This coupled with thermal gradients will induce convection, but it's difficult to say because they did not provide

details on the thermal stability during the experiments.

Murakami [84] used a chronopotentiometry method to measure the diffusivity of rare-earths (La, Pr, Nd, Gd, Y, and Sc) in liquid cadmium, driven by the application of optimizing the pyrometallurgical reprocessing kinetics of spent nuclear fuels. They started with a known concentration of rare-earth metal M (c_M^*) in liquid cadmium, then applied a constant anodic current to oxidize the rare-earth metal $M_{(\text{in Cd liq})} \rightarrow M^{n+} + ne^-$ into a LiCl-KCl melt. Figure 2-5 is an illustration of the concentration profile during the chronopotentiostatic pulse, and a solution for the concentration equation is obtained when Fick's second law is solved using the following boundary conditions⁵:

$$D \frac{\partial c_M}{\partial x}(0, t) = \frac{I}{nFA} \quad (2.21)$$

$$c_M(x, 0) = c_M^* \quad (2.22)$$

$$c_M(\infty, t) = c_M^*. \quad (2.23)$$

The derived solution is

$$c_M(x, t) = c_M^* - \frac{I}{nFAD} \left[2 \left(\frac{Dt}{\pi} \right)^{\frac{1}{2}} \exp\left(-\frac{x^2}{4Dt}\right) - x \operatorname{erf}\left(\frac{x}{2\sqrt{Dt}}\right) \right], \quad (2.24)$$

but evaluating it at $x = 0$ reduces to

$$c_M(t) = c_M^* - \frac{2I\sqrt{\tau}}{nFA\sqrt{\pi D}}. \quad (2.25)$$

The concentration will decrease during the application of a current until $c_M(t)$ reaches zero, which happens at time $t = \tau$. At this transition time τ , equation 2.25 simplifies to

⁵ I is the applied current, A is the electrode surface area, and F the Faraday constant in equation 2.21

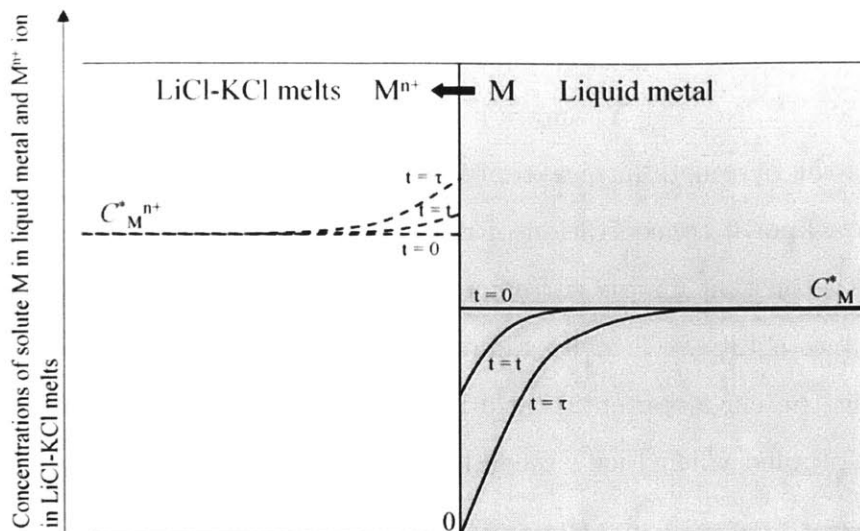


Figure 2-5: The conceptual change of the concentrations of solute M in liquid metal (solid line) and M^{n+} ion in LiCl-KCl melts (dotted line) during constant current electrolysis. $c_{M^{n+}}^*$ is the initial concentration in the electrolyte, and c_M^* is the initial concentration in the liquid metal [84].

$$2I\sqrt{\tau} = nFAc_M^*\sqrt{\pi D}, \quad (2.26)$$

which they used to calculate the chemical diffusivity because the electrode potential would deviate drastically at τ (fig. 2-6). Equation 2.25 is also known as the *Sand equation* [21], and there are several practical issues one needs to consider when measuring the transition time τ . If a significant double-layer is present, then it will charge proportional to dE/dt and the Faradaic current will be slightly different than the applied one. This effect is mostly dominant during the beginning and end of the pulse, which makes short pulses unreliable. This capacitive effect will increase with surface area, therefore it is imperative to minimize the area of contact between the electrode and electrolyte. These transition time problems have historically discouraged the use of controlled-current techniques compared to controlled-potential methods [21]. Besides issues with measuring the transition time, the authors did not use a true reference electrode, instead they utilized a pseudo-reference electrode and did not mention any potential issues regarding polarization effects. They also did not

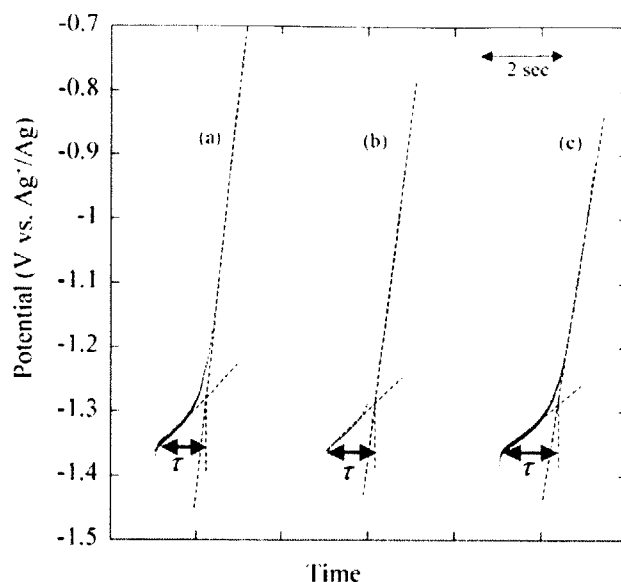


Figure 2-6: Typical chronopotentiograms using a liquid Cd electrode containing La in LiCl-KCl-2.0 wt % LaCl₃ melts at 723 K. The applied current was (a) 65 mA, (b) 60 mA, (c) 55 mA [84].

account for convection, which they should at least briefly mentioned because of the relatively large cell surface areas used of roughly 5 cm².

Capillary Methods

Most of experimental values for diffusion in liquid metals reported in literature have been measured using capillary techniques [39, 52, 58, 60–71, 71–77]. Anderson and Saddington [101] first proposed the capillary-reservoir method in 1949. It consisted of a 1 mm diameter, 2-10 cm long capillary containing a radioactive liquid metal that is immersed in a bath of the same liquid metal that is of ordinary composition (nonradioactive), shown in figure 2-7.

The capillary is immersed just above the surface of the liquid, the experimental time begins once the capillary is completely covered. The boundary conditions to solve Fick's second law, $\partial c / \partial t = D(\partial^2 c / \partial x^2)$, at $t = 0$ are

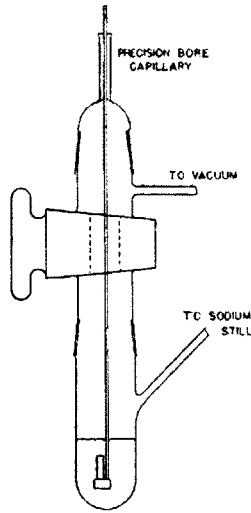


Figure 2-7: Schematic of capillary-reservoir apparatus used by Meyer [60] to measure the diffusion of liquid sodium.

$$c = c_0 \quad \text{for } 0 < x < l \quad (2.27)$$

$$c = 0 \quad \text{for } x > l, \quad (2.28)$$

and for $t > 0$

$$c = f(x, t) \quad \text{for } 0 < x < l \quad (2.29)$$

$$c = 0 \quad \text{for } x > l. \quad (2.30)$$

c_0 is the initial tracer concentration in the capillary, l is the capillary length, and x is the distance from the side of the capillary in contact with the reservoir. Solving Fick's law gives the following solution of the average tracer concentration in the capillary

$$\frac{c_{av}}{c_0} = \frac{8}{\pi^2} \sum_{n=0}^{\infty} \frac{\exp\left(\frac{-(2n+1)^2\pi^2 Dt}{4l^2}\right)}{(2n+1)^2} \quad (2.31)$$

The series solution (eq. 2.31) converges rapidly as the number of terms grow, so only

the first couple of terms are necessary to compute the diffusivity.

The capillary techniques do offer ways to measure the diffusion of liquid metals, but it does so at the expense of errors that are impossible to eliminate. The main source of error, as you might have guessed, is convection. Convection can become a very serious issue under the influence of temperature gradients, and simulations are needed to estimate such conditions. Unfortunately, the majority of the work published in liquid alloy diffusion was done before powerful computers existed, so authors only speculate on the onset of convection, which led to large discrepancies between reported values. In some experiments, the capillary was manually rotated to maintain $c = 0$ at the open boundary, which could deplete the tracer concentration if the rotation is too rapid [52]. Buell's [68] work on the interdiffusion of tin in bismuth used a 10 cm capillary, and although the work was elegant, there are too many sources of error to ignore. For example, due to the large volume required to fill the capillary, there was significant volume change upon melting adding a constant source of error. Their method of calculating the diffusion coefficient was to measure the resistivity *in-situ* of the alloy by placing tungsten electrodes along the capillary, 1 cm apart. This required a significant amount of current (due to the accuracy of their equipment) to measure a reliable voltage drop, which led to Joule heating (convection) and electrotransport. After collecting data for weeks, the resistances were converted to concentrations using the work of an unpublished masters thesis [68], which inherently incorporated the sources of the author's errors into the diffusion coefficient calculations.

Convection is a dominant source of error for these methods because of the need to use long capillaries to carry on these experiments. The longer the capillary, the more difficult it will be to maintain it at constant temperature with a furnace, specially for weeks at a time. The error is clearly seen on the concentration-penetration profiles for the interdiffusion [76] of tin in bismuth (fig. 2-8). One notices significant scatter in the data as the capillary size increases, which they attributed to the influence of convection. There is no doubt the scatter in the data could be a result of convection, but to make the claim that convective transport increases with increasing capillary diameter is merely a speculation because no effort was made to explain the effect

solidification has on the concentration profile. Other authors [62] believe the opposite, that small-diameter capillaries will experience ‘wall-effects’ near the wall because of the no-slip boundary condition, so more reliable results could be obtained with larger diameters.

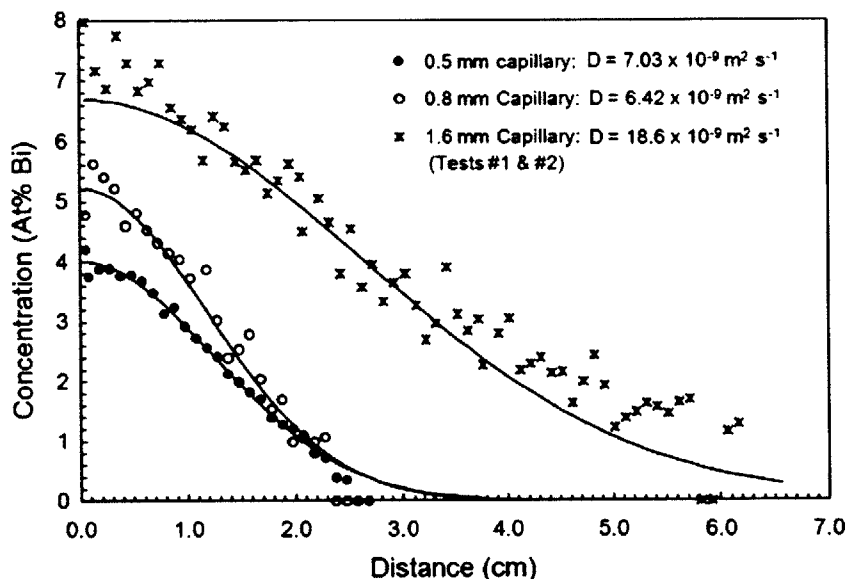


Figure 2-8: Effect of capillary diameter on concentration-penetration profiles for the interdiffusion of Bi in liquid Sn at 700 °C [76]

In the long capillary technique, the radioactive metal is brought in contact with the nonradioactive metal (fig. 2-9(a)) then heated until it melts and allowed to diffuse (fig. 2-9(b)). After some time (days), the liquid metal is solidified so that it can be analyzed. The issue, as briefly mentioned above, arises when the alloy solidifies. Freezing will more than likely start from the bottom of the capillary and proceed up the walls as shown in figure 2-9(c). This will create a flux of tracer diffusion from the center of the capillary to the wall, driven by solidification turbulence, effectively creating a parabolic-shaped interface which will vary depending on the thermal conductivities of the solidified metal and capillary wall. This will cause the tracer diffusion concentration to be greater at the wall compared to the center which can be seen in figure 2-9(d).

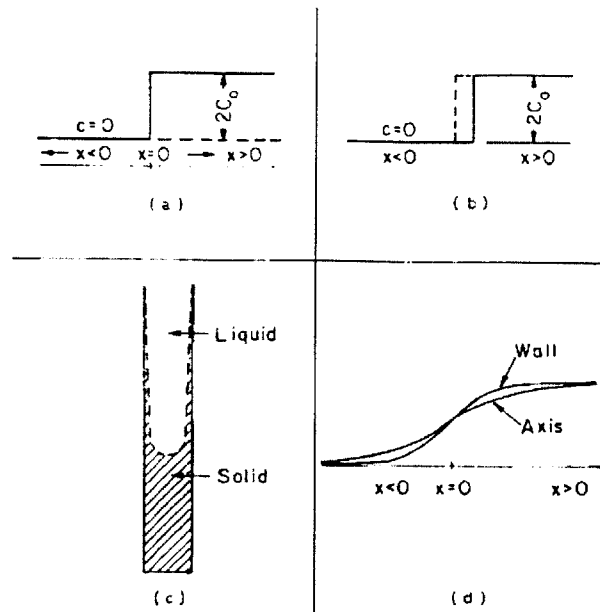


Figure 2-9: (a) Initial concentration profile. (b) Concentration profile after melting. (c) Freezing interface of metal thread. (d) Concentration profiles at capillary axis and wall. [52]

Shear Cell Method

The shear cell method [50–59] is similar to the capillary method, the main difference being that it is sectioned before the liquid metal is solidified for analysis. This method was created to eliminate the dominating sources of error in the capillary-reservoir method which are solute diffusion during solidification, convection from thermal gradients, length corrections, and segregation due to nonuniform solidification [102]. Figure 2-10 is a schematic representation of the shear cell used by Bruson [102] to measure the interdiffusion coefficients of antimony, tin, and silver in molten copper.

The cell used by Bruson is made from stacking 20 disks that are 4 mm thick and 42 mm in diameter. Two 1.5 mm diameter holes are drilled, one is filled with copper spanning the length of the stacked disks, and the other is the height of one disk (fig. 2-10(1)) filled with the radioactive species. The shear cell is then heated in a furnace to the operating temperature, while keeping the liquid metals separated. Once at temperature, the experiment clock starts ticking when the disks are rotated (sheared) until the radioactive metal is perfectly sandwiched between liquid copper. At the end of the experiment, the disks are rotated to segregate the capillary into

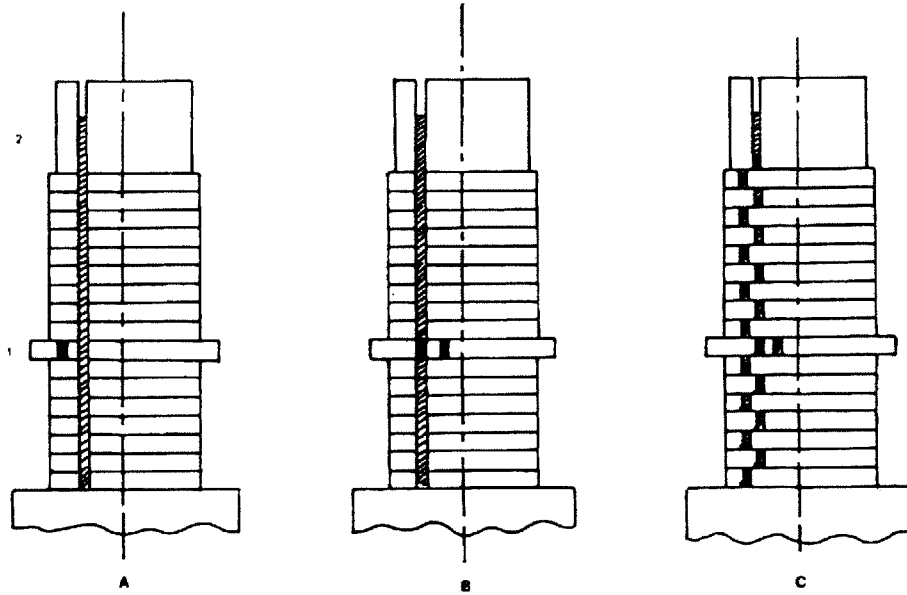


Figure 2-10: Schematic representation of the shear cell: (1) intermediate disk with-radioactive alloy; (2) filling reservoir: **A**, configuration of the cell during the heating of the system; **B**, the radioactive isotope is put into contact with the long capillary; **C**, at the end of the diffusion run, each capillary is sectioned into 20 beads. [102]

the 20 parts (fig. 2-10C) before cooling it down. This eliminates the turbulent effect solidification has on the transport within a capillary, as described in the section before.

To calculate the chemical diffusion coefficient, Fick's second law must be solved with unique boundary conditions. Assuming the capillary length is infinite within the time scale of the experiment, the initial concentration is given by

$$c(x, 0) = c_0 \Theta(x + h) [1 - \Theta(x - h)], \quad (2.32)$$

where c_0 is the initial alloy concentration, $2h$ is the thickness of the center disk containing the radioactive species, and $\Theta(x)$ is a step function. With this, one can derive the following concentration solution

$$c(x, t) = \frac{c_0}{2} \left[\operatorname{erf} \left(\frac{h - x}{2\sqrt{Dt}} \right) + \operatorname{erf} \left(\frac{h + x}{2\sqrt{Dt}} \right) \right], \quad (2.33)$$

and then perform a least-squares fit of the equation to the data so the the diffusion coefficient can be extrapolated.

This technique was created to counter the sources of error of the capillary-reservoir and long capillary method, but large discrepancies in the reported literature suggests that other sources of error are at play. Convection can be induced when the cells are sheared [103], which simulations show it affecting the initial concentration distribution the most. Also, the materials used to contain the liquid metals must be inert and stable during thermal cycling because the metals can leak if the disks expand asymmetrically over time.

Other Methods

Other methods that have been used in the past to measure liquid diffusion include neutron radiography [80], melting point experiments [74, 104–106], and laser techniques [107, 108].

2.3 Conclusion

The current methods available for measuring the diffusion in liquid metals are not reliable, require long operation times, and include many inherited errors from the experimental setups caused by convection. Most of the work was done in the 1960s and 1970s before powerful computers could help calculate the effect of convection, which is probably why reported values do not agree with each other. Convection can be minimized if one uses small capillaries. Unfortunately the experimental methods require the use of large capillaries because diffusion is orders of magnitude faster in liquid alloys compared to solids.

Chapter 3

Theoretical Derivation of Chemical Diffusivity in Liquid Alloys

In 1977, W. Weppner and R. A. Huggins [109] created the galvanostatic intermittent titration technique (GITT), an experimental method used to accurately measure the chemical diffusion of lithium in the intermetallic compound Li_3Sb . GITT combines the use of both kinetic and thermodynamic measurements on solid electrodes, which are measured with respect to a stable reference electrode with minimal polarization effects. This is possible because the electrode potential is a direct measure of the lithium activity in Li_3Sb at the electrode-electrolyte interface. The electrode potential can be related to the surface concentration using the Nernst equation. This is the key enabler for calculating the chemical diffusion coefficient in liquid alloys. Fick's laws can be solved with specific boundary conditions to derive a relation between concentration and diffusivity. This chapter describes this process, but re-derived for the purpose of studying diffusion in binary liquid alloys, which is proven to be fundamentally different than the solid-state equation when compared.

3.1 Chemical Diffusivity of A in the A||B Binary Liquid Alloy

In order to measure the chemical diffusivity of component A (\tilde{D}_A) in a liquid alloy A||B as a function of mole fraction x_A and temperature T , the surface concentration of the electrode has to be related to its potential. Figure 3-1 is an illustration of the electrochemical setup used in the experiments. While in equilibrium, the cell potential is given by the Nernst equation,

$$E = \frac{RT}{z_A F} \ln \frac{a_A(\text{RE})}{a_A(\text{A}_x\text{B}_{1-x})} \quad (3.1)$$

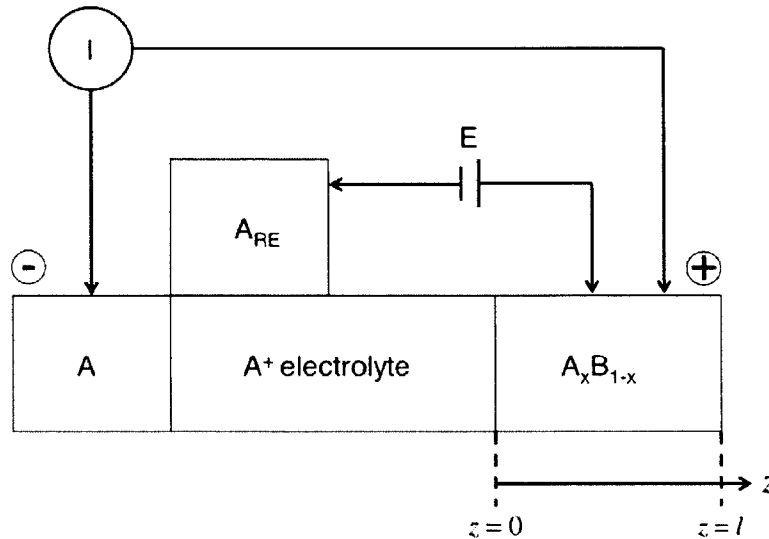


Figure 3-1: Schematic of alloying cell. Current is passed between the negative electrode and positive electrode, while the potential is measured versus the reference electrode A_{RE}. The electrode-electrolyte interface is at $z = 0$ and the bottom of the electrode is $z = l$.

To show how the chemical diffusivity can be measured electrochemically, a mathematical description for the electrode surface concentration is needed which is acquired by solving Fick's laws of diffusion.

3.1.1 Surface Concentration Solution

Let's assume an electrode of length $z = l$ (fig. 3-2(a)) and at time $t = 0$ has an initial molar concentration

$$c_A(z, 0) = c_A^0. \quad (3.2)$$

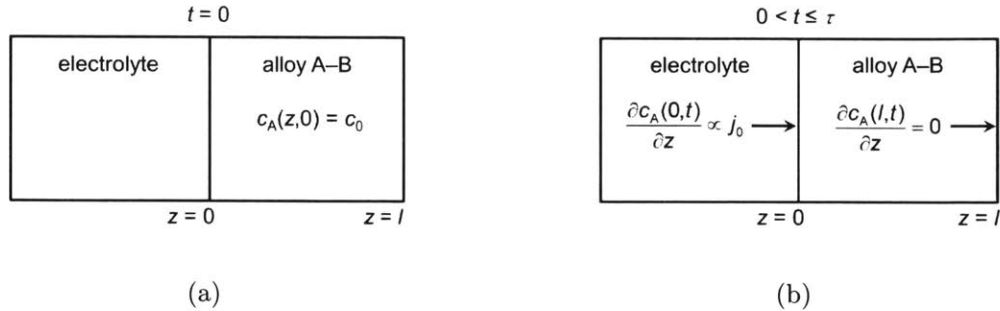


Figure 3-2: Boundary conditions, (a) initial molar concentration at $t = 0$, and (b) fluxes during galvanostatic pulse.

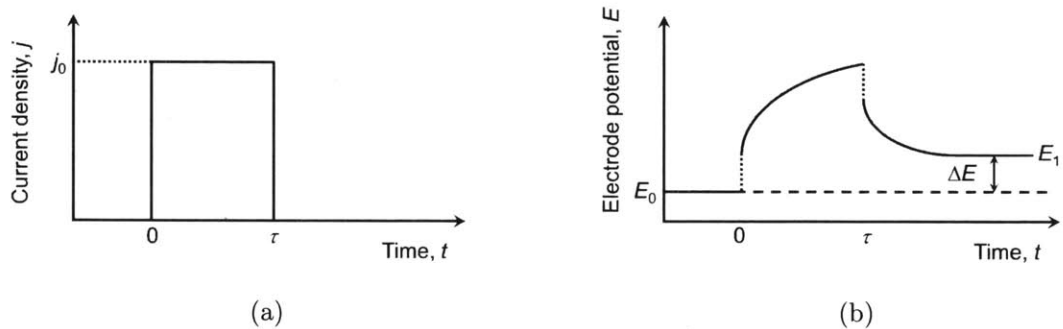


Figure 3-3: GITT pulse (a) Applied current density j_0 at $t = 0$. (b) Evolution of electrode potential.

Then a constant current density pulse j_0 is applied externally at $z = 0$ (fig. 3-2(b)) for a time $t = \tau$ (fig. 3-3(a)), and the transient evolution of the electrode potential¹ E is recorded versus a reference electrode (fig. 3-3(b)). The resulting electrode-electrolyte interface flux $J = j_0/z_A F$ from the applied current is related to the chemical diffusivity by Fick's first law

¹Since the electrode potential gives us the surface activity, it will change under any external applied current that induces a Faradaic reaction at the electrode surface in contact with the electrolyte.

$$\frac{dc(0, t)}{dz} = \frac{j_0}{z_A F \tilde{D}_A}, \quad (3.3)$$

where z_A is the number of electrons and F the Faraday constant. Since the liquid electrode has a fixed length l , there will be no flux through the end of the electrode, so the following boundary condition at $z = l$ must be satisfied

$$\frac{dc(l, t)}{dz} = 0. \quad (3.4)$$

Using the previous boundary conditions² (eqn. 3.2—3.4) to solve Fick's second law

$$\frac{\partial c_A(z, t)}{\partial t} = \tilde{D}_A \frac{\partial^2 c_A(z, t)}{\partial z^2} \quad (3.5)$$

yields an infinite series solution at $z = 0$ [109, 110]

$$c_A(z = 0, t) = c_A^0 + \frac{2j_0\sqrt{t}}{z_A F \sqrt{\tilde{D}_A}} \sum_{n=0}^{\infty} \left[\text{ierfc} \left(\frac{nl}{\sqrt{\tilde{D}_A t}} \right) + \text{ierfc} \left(\frac{(n+1)l}{\sqrt{\tilde{D}_A t}} \right) \right], \quad (3.6)$$

which is valid at all times. The infinite series makes it difficult to apply to a finite system, but we can get around this by taking a closer look at the arguments of the integral of the complimentary error function³ in eq. 3.6. Let's consider only the $n = 0$ term in the concentration solution

$$c_A(z = 0, t) = c_A^0 + \frac{2j_0\sqrt{t}}{z_A F \sqrt{\tilde{D}_A}} \left[\text{ierfc}(0) + \text{ierfc} \left(\frac{l}{\sqrt{\tilde{D}_A t}} \right) \right]. \quad (3.7)$$

The first term is easily evaluated since $\text{ierfc}(0) = 1/\sqrt{\pi}$ (see Appendix B). The second term, $\text{ierfc}(l/\sqrt{\tilde{D}_A t})$ is what complicates the solution, so modifications are needed to approximate it to zero. This is achieved by comparing the characteristic time scale for diffusion, $\tau_D = l^2/\tilde{D}_A$ to the experiment time $t = \tau$. It has to be such that it

²The solution assumes no boundary motion at the interface, which is a correct approximation when the overall change in composition for the electrode is minimal, so the average volume V during a coulometric pulse is considered constant.

³Appendix B show the error function related equations.

makes the limit of the argument approach infinity⁴ ($l/\sqrt{\tilde{D}_A t} \rightarrow \infty$). This is possible only when the experiment pulse time (τ) is much much smaller than the characteristic diffusion time scale (τ_D).

Assuming the pulse time is indeed much shorter than the characteristic diffusion time ($\tau \ll l^2/\tilde{D}_A$), equation 3.7 becomes

$$c_A(0, t) = c_A^0 + \frac{2j_0\sqrt{t}}{z_A F \sqrt{\pi \tilde{D}_A}}, \quad (3.8)$$

and if the electrode volume V remains constant, it can be written as

$$c_A(0, t) = \frac{n_A(0, t)}{V} = \frac{n_A^0}{V} + \frac{2j_0\sqrt{t}}{z_A F \sqrt{\pi \tilde{D}_A}}, \quad (3.9)$$

where n_A is the moles of component A at the electrode surface.

3.1.2 Composition Relation to Potential

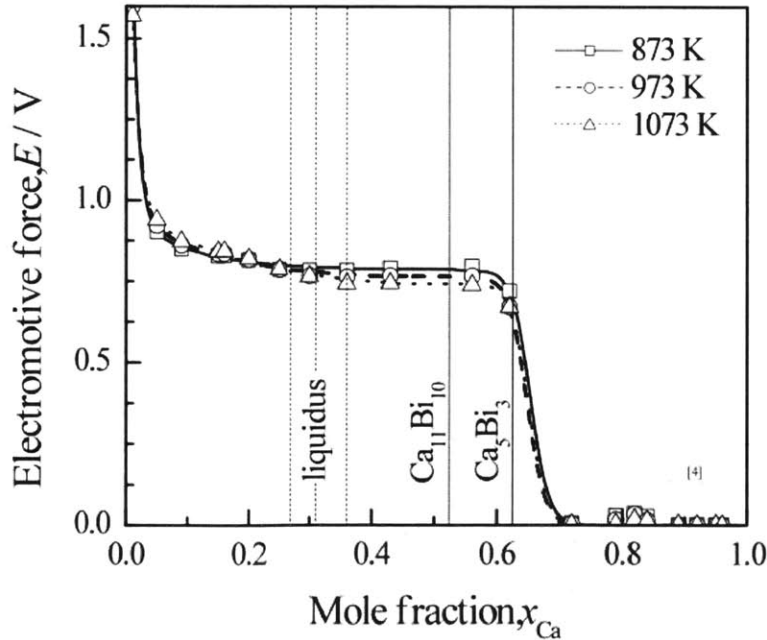


Figure 3-4: EMF data of calcium in bismuth between 600-800°C [17].

⁴This will inherently make all the other higher terms in the series ($n = 1 \dots \infty$) reach zero faster than the initial $n = 0$.

E.m.f. diagrams show how the electrode potential varies with mole fraction under constant temperature and pressure, see figure 3-4 for example. The Nernst equation (eq. 3.1) is heavily used in these thermodynamic measurements because it describes quantitatively how potential varies with composition, so it is safe to assume the electrode potential varies only with surface mole fraction $E(x_A)$ if the temperature fluctuations are small. Therefore, with equation 3.9 we can write the mole fraction of A as a function of the surface concentration

$$x_A(c_A(t)) = \frac{c_A(t)}{c_A(t) + c_B} = \frac{n_A^0 + \frac{2j_0V\sqrt{t}}{z_A F \sqrt{\pi \bar{D}_A}}}{n_B + n_A^0 + \frac{2j_0V\sqrt{t}}{z_A F \sqrt{\pi \bar{D}_A}}} \quad (3.10)$$

We are interested in how a small change ($\leq 0.25\%$) in mole fraction of A transiently affects the electrode potential. This is achieved by writing the electrode potential as

$$E(x_A(c_A(\sqrt{t}))), \quad (3.11)$$

with the assumption that the electrode potential is only a function of composition ($E = f(x_A)$) and concentration only a function of time ($c_A = g(t)$) at the electrode-electrolyte interface ($z = 0$). Note that this equation was derived assuming very small fractional mole changes of the active species with the titration time constrained, so the chain-rule was applied to equation 3.11 to get the potential dependence on time

$$\left. \frac{dE}{d\sqrt{t}} \right|_t = \left. \frac{dE}{dx_A} \right|_{g(t)} \cdot \left. \frac{dx_A}{d\sqrt{t}} \right|_t \quad (0 < t \leq \tau). \quad (3.12)$$

The exact form of how the electrode potential evolves with surface concentration (dE/dx_A) is unknown, but it can be approximated to a good degree from steady-state bulk measurements because the induced changes in composition are very small. In fact, if it's linear over the range in composition studied then it is indeed a good linear approximation, and we can write it as

$$\left. \frac{dE}{dx_A} \right|_{g(t)} \approx \frac{\Delta E}{\Delta x_A}, \quad (3.13)$$

which is approximated from open circuit voltage measurements induced from the small changes in composition.

$dx_A/d\sqrt{t}$ is computed by differentiating equation 3.10

$$\frac{dx_A}{d\sqrt{t}} = \frac{2n_B j_0 V}{z_A F \sqrt{\pi \tilde{D}_A} \left(n_B + n_A^0 + \frac{2j_0 V \sqrt{t}}{z_A F \sqrt{\pi \tilde{D}_A}} \right)^2} \quad (3.14)$$

In theory, the surface concentration is constant with square root of time, but the mole fraction is not, therefore it is important to examine how it deviates. The chemical diffusivity appears twice in equation 3.14, and if the time-dependent factor $\left(\frac{2j_0 V \sqrt{t}}{z_A F \sqrt{\pi \tilde{D}_A}} \right)$ changes the value drastically during pulsing, then it can only be solved numerically. On the other hand, if it can be approximated to be constant, then we can simply solve for the chemical diffusivity. To see whether or not $dx_A/d\sqrt{t}$ can be treated as a constant, sensitivity analysis has to be done on the current density j_0 , volume V , and the square root of the pulse time \sqrt{t} . This was done (shown in Appendix C) with the variables used in the experiments, and can conclude that for our experimental system the following approximation is valid

$$\frac{2j_0 V \sqrt{t}}{z_A F \sqrt{\pi \tilde{D}_A}} \approx 0 \quad (3.15)$$

because equation 3.14 is virtually constant during the entire pulse sequence. With the use of the approximation it is safe to write the surface mole fraction as

$$\frac{dx_A}{d\sqrt{t}} = \frac{2n_B j_0 V}{z_A F \sqrt{\pi \tilde{D}_A} (n_B + n_A^0)^2} \quad (3.16)$$

3.1.3 Chemical Diffusivity Equation

Substituting equations (3.13), and (3.16) into (3.12) yields the complete time-dependent potential equation

$$\frac{dE}{d\sqrt{t}} = \frac{\Delta E}{\Delta x_A} \frac{2n_B j_0 V}{z_A F \sqrt{\pi \tilde{D}_A} (n_B + n_A^0)^2}. \quad (3.17)$$

Now we can solve for \tilde{D}_A in (3.17) to get the chemical diffusivity

$$\tilde{D}_A = \frac{1}{\pi} \left[\frac{2n_B j_0 V \left(\frac{\Delta E}{\Delta x_A} \right)}{z_A F (n_B + n_A^0)^2 \left(\frac{dE}{d\sqrt{t}} \right)} \right]^2 \quad (3.18)$$

3.2 Chemical Diffusivity Derivation of A in the $A_{y+\delta}B$ Binary Solid Intermetallic Compound

Weppner and Huggins [109] proposed GITT as a method for determining kinetic parameters in intermetallic compounds $A_{y+\delta}B$. Their coulometric titrations consisted of small current pulses (I_0) to induce the following change in stoichiometry

$$\Delta\delta = \frac{I_0 \tau M_B}{z_A m_B F} \quad (3.19)$$

where τ is the pulse time, M_B is the atomic mass of B, m_B is mass of B, and F is the Faraday constant. Dimensional analysis shows this is just the ratio of A moles titrated during the pulse to that of component B present. The Fickian concentration used by the authors has units of particles per volume with a surface rate

$$\frac{dc_i}{d\sqrt{t}} = \frac{2I_0}{S z_i q \sqrt{\tilde{D}} \pi} \quad (t \ll l^2 / \tilde{D}). \quad (3.20)$$

If the molar volume (V_M) of the intermetallic compound remains constant during the galvanostatic pulse, the concentration c_i can be related to the change in stoichiometry by

$$dc_i = \frac{N_A}{V_M} d\delta, \quad (3.21)$$

where N_A is Avogadro's number.

Equation 3.21 is used to write the concentration differential (eq. 3.20) as a stoichiometry differential

$$\frac{d\delta}{d\sqrt{t}} = \frac{d\delta}{dc_i} \frac{dc_i}{d\sqrt{t}} = \frac{2I_0V_M}{Sz_iN_Aq\sqrt{\tilde{D}}\pi}, \quad (3.22)$$

and since the changes in stoichiometry are very small, they expand it by dE to get the cell voltage dependence on time

$$\frac{dE}{d\sqrt{t}} = \frac{2I_0V_M}{SFz_i\sqrt{\tilde{D}}\pi} \frac{dE}{d\delta}. \quad (3.23)$$

$dE/d\delta$ is the difference in open circuit voltage divided by the change in stoichiometry (eq. 3.19) measured at equilibrium.

They then solve for the chemical diffusion coefficient (\tilde{D}) to get

$$\tilde{D} = \frac{4}{\pi} \left(\frac{V_M}{SFz_i} \right)^2 \left[\frac{I_0 \frac{dE}{d\delta}}{\frac{dE}{d\sqrt{t}}} \right]^2 \quad (t \ll l^2/\tilde{D}) \quad (3.24)$$

3.3 Difference Between Liquid and Solid-State Diffusivity Equations

Let's compare the chemical diffusivity equation for liquid alloys (eq. 3.18) to solid intermetallic compounds (eq. 3.24). Equation 3.18 can be rewritten to closely resemble equation 3.24

$$\tilde{D}_A = \frac{1}{\pi} \left[\frac{2n_B j_0 V \left(\frac{\Delta E}{\Delta x_A} \right)}{z_A F (n_B + n_A^0)^2 \left(\frac{dE}{d\sqrt{t}} \right)} \right]^2 = \frac{4}{\pi} \left(\frac{V_M}{SFz_A} \right)^2 \left[\frac{I_0 x_B \frac{\Delta E}{\Delta x_A}}{\frac{dE}{d\sqrt{t}}} \right]^2 \quad (3.25)$$

The difference between the two arises from the definition of how the electrode potential changes with the corresponding change in activity. For solid electrodes, $dE/d\delta$ is the change in electrode potential ΔE due to the change in stoichiometry $\Delta\delta$ (eq. 3.19) measured at equilibrium, given by

$$\frac{dE}{d\delta} = \frac{\Delta E}{\Delta\delta} = \frac{\Delta E z_A F m_B}{I_0 M_B \tau} = \frac{\Delta E z_A F}{I_0 \tau} n_B = \frac{\Delta E}{n_A^{\tau}} n_B \quad (3.26)$$

where $n_B = m_B/M_B$ is the moles of B and $n_A^\tau = I_0\tau/z_A F$ is the added moles of A. The equivalent of equation 3.26 for liquid alloys derived in this thesis is

$$x_B \frac{\Delta E}{\Delta x_A}. \quad (3.27)$$

In the limit of very small changes in composition of A in the liquid A||B alloy, the change in mole fraction of A is approximated as

$$\Delta x_A = \frac{n_A^\tau n_B}{(n_A^0 + n_B + n_A^\tau)(n_A^0 + n_B)} \cong \frac{n_A^\tau n_B}{(n_A^0 + n_B)^2}, \quad (3.28)$$

so equation 3.27 is written as

$$x_B \frac{\Delta E}{\Delta x_A} = \frac{\Delta E}{n_A^\tau} (n_B + n_A^0) \quad (3.29)$$

The fundamental difference between the two chemical diffusivity equations can be seen in the new derivation (eq. 3.29), which incorporates to total number of moles for the binary system, not just that of component B (eq. 3.26). Equation 3.29 can be rewritten as

$$x_B \frac{\Delta E}{\Delta x_A} = \frac{\Delta E}{\frac{n_A^\tau}{(n_B + n_A^0)}} \quad (3.30)$$

and interpreted as the change in electrode (ΔE) potential due to an infinitesimal change in mole fraction ($n_A^\tau/(n_B + n_A^0)$). This is more applicable to our electrochemical system because we apply very small pulses ($\Delta x_A \leq 0.25\%$), and the electrode potentials we measure are directly related to the surface activity which is a measure of the surface mole fraction.

3.4 Conclusion

The diffusion equation for liquid alloys derived in this thesis (eq 3.18) can be applied to any molten-salt electrochemical system by using a suitable electrolyte that minimizes self-discharge currents along with a stable, non-polarizable reference electrode. A

great amount of effort has been invested at MIT to find candidates that meet the above requirements, one being calcium-bismuth due to its high voltage. Results are presented in chapter 5 using such couple, in the liquid range between 500 °C and 700 °C at 5%, 10%, and 15% calcium atomic percent.

A close inspection of the chemical diffusivity equation 3.18 reveals what needs to be experimentally measured. Besides a couple of constants, we have full control of the sample volume, pulse time, and electrode surface area, but must measure the change in open circuit voltage at equilibrium and the electrode response during the applied galvanostatic pulse. A three-electrode setup is used where the working electrode potential is measured vs. a two-phase 35% - mol Ca-Bi reference electrode proven to be stable during the time scale of these experiments [17].

Chapter 4

Electrochemical Experiments and Procedure for Measuring the Chemical Diffusivity in Liquid Alloys

The experimental procedure for calculating the chemical diffusivity values consists of two parts. The first is the initial galvanostatic titration to the desired composition (fig. 4-6), and the second is a sequence of constant current pulses (fig. 4-7) designed to determine the chemical diffusivity. But first, the electrochemical system of interest is described.

4.1 Experimental Setup

4.1.1 Materials Selection

It is of extreme importance to use the most inert, cost effective, materials that can withstand months in contact with molten salts and liquid metals without corrosion degrading the mechanical integrity. With this in mind, we aimed to select the the most stable materials in the temperature range of operation, which is between 550 °C - 700

°C. Figure 4-1 is the test vessel, along with the materials used. The electrical leads were made from 99.9% pure tungsten wire and had a diameter of 1 mm. The leads were sanded with 600 grit sandpaper and rinsed with ethanol to eliminate impurities.

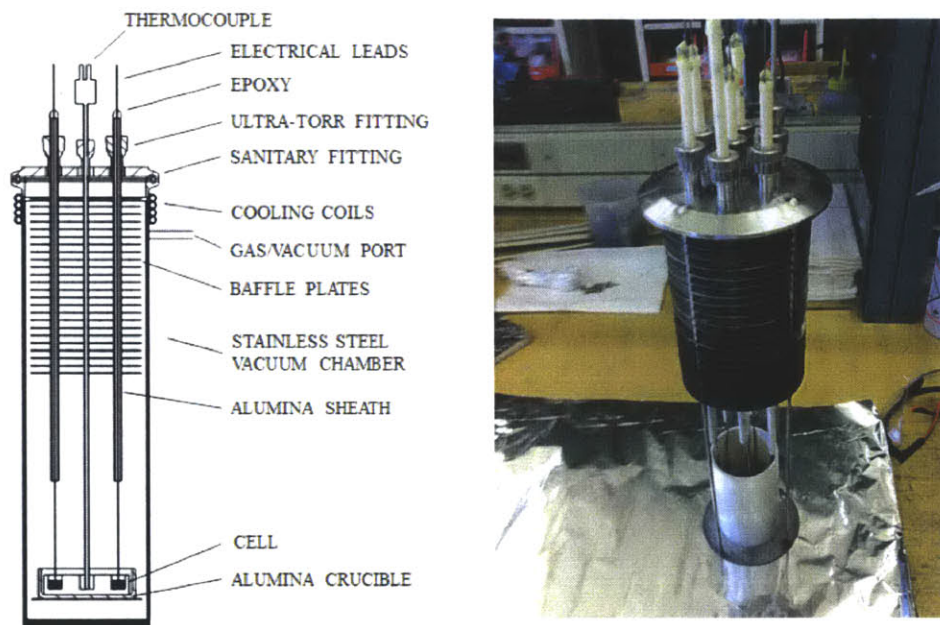


Figure 4-1: Experiment test vessel.

High purity boron nitride crucibles¹ were used to contain the liquid alloy electrodes with the dimensions shown in table 4.1. Figure 4-2 shows how the electrochemical cell was spatially organized inside the test vessel. The main crucible containing the electrodes/electrolyte and electrode sheaths were made from alumina due to its inertness with the molten salt electrolyte.

	Radius (cm)	Height (cm)	Thickness (cm)	Sample height (cm)
WE	0.3	1.2	0.2	0.5
RE 1	0.4	1.2	0.2	0.9
RE 2	0.4	1.2	0.2	0.9
CE	1.5	1.2	0.2	0.9

Table 4.1: Electrode dimensions.

¹The MIT machine shop precision made the electrodes used in the GITT experiment.

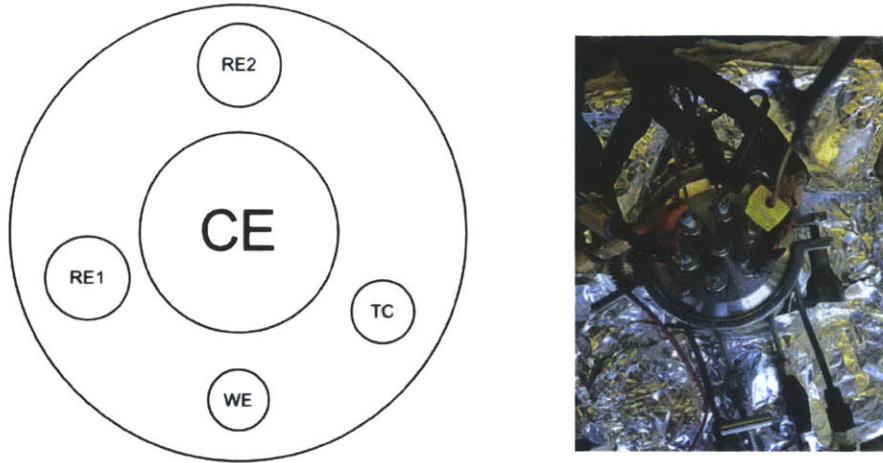


Figure 4-2: Cell layout. The outer perimeter is the alumina crucible, and it is not drawn to scale.

4.1.2 Electrochemical System

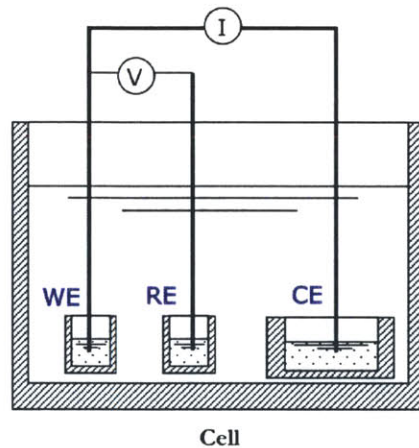


Figure 4-3: Three-electrode cell schematic. Current is passed between the counter electrode and working electrode, while the working electrode potential is measured with respect to the reference electrode.

Our system of interest is the Ca-Bi alloy couple, and the goal is to apply the newly derived equation for liquid alloys to measure the chemical diffusivity of calcium in liquid bismuth. This new method offers a new way to measure kinetic properties of super reactive liquid metals no possible before. The counter electrode is the source of calcium, and is composed of a 17% - mol Ca-Bi alloy. It was chosen because it is a liquid during the entire temperature range of operation. It also ensures that there will

be no kinetic limitations from the counter electrode which is imperative for these type of electrochemical measurements. A 35% - mol Ca-Bi biphasic reference electrode was used because of its stability [17] due to the electrochemical potential being constant in the two-phase regime. This ensures the voltage will not drift with any small deviations in concentration over time, so it provides a true reference point. The electrolyte, a mixture of 38.5% LiCl - 26.5% NaCl - 35% CaCl₂, was pre-melted to maximize homogeneity². This electrolyte composition was heavily studied by Kim [2], and it proved to work well while minimizing calcium solubility. The entire electrochemical cell was assembled inside an argon glovebox with oxygen and water ppm levels less than 0.1 to minimize contamination, and oxide formation.

Due to the affinity for the Ca-Bi couple to form high temperature intermetallic compounds, the reference electrode alloy was first pre-melted using an arc-melter under argon atmosphere. All the electrodes were then melted in the BN crucibles using an induction-melter that was custom-added to the glovebox. This procedure is explained in more detail in appendix D.2. The test vessel was slowly heated from room temperature to operating temperature using a procedure aimed at drying the electrolyte². The furnace was covered with aluminum foil and a copper mesh, and was grounded along with the vessel to minimize the noise from the furnace or any spurious electromagnetic noise that can affect the signal. The data was collected using a Metrohm Autolab potentiostat and a National Instruments[®] data acquisition card (fig. 4-4).

²The premelting procedure can be found in appendix D.

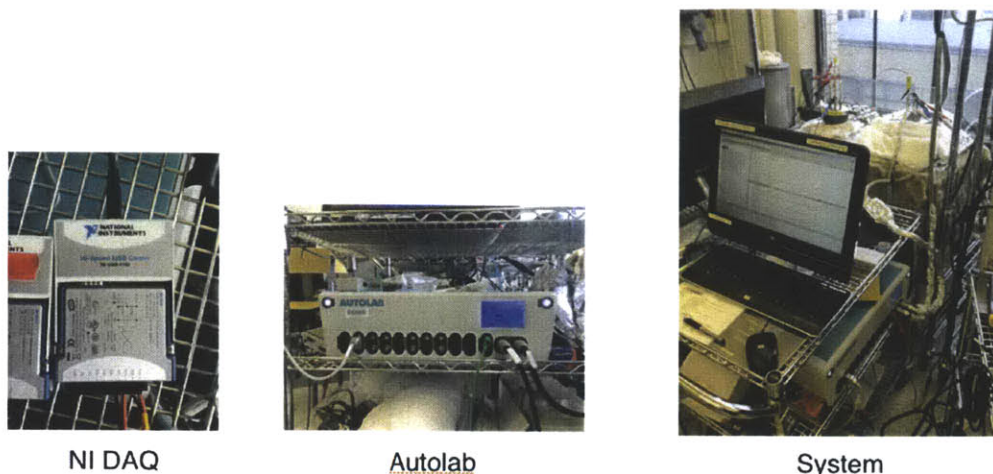


Figure 4-4: Experiment setup

4.2 Electrochemical Pulse Sequences

4.2.1 Initial Composition Titration

Figure 4-5 is the Ca-Bi phase diagram with labels, and it provides a good visual where the system stands during operation. Figure 4-6 part A shows the working electrode being held constant at 0.7 V vs reference electrode for around 6000 seconds to remove the calcium from the previous test. A titration to composition, either 5%, 10%, or 15%, as shown in part B, followed by relaxation to the open circuit voltage (part C).

4.2.2 Determination of \tilde{D}

After the system relaxes, the pulse sequence shown in Figure 4-7 is applied to calculate the chemical diffusivity at the composition of interest. A single pulse consists of three parts: an initial open circuit voltage measurement, the galvanostatic pulse, and relaxation to open circuit voltage. The four applied pulses have one thing in common, they all change the working electrode composition by $0.25\% x_{\text{Ca}}$. Besides this, the applied current density ranged from $5 - 20\text{ mA/cm}^2$, incremented by 5 mA/cm^2 each time since in theory the diffusion coefficients should be invariant with respect to the applied current. The pulse time τ was adjusted to meet the common restriction of equivalent mole fraction change. The procedure shown in table 4.2 was used, and the

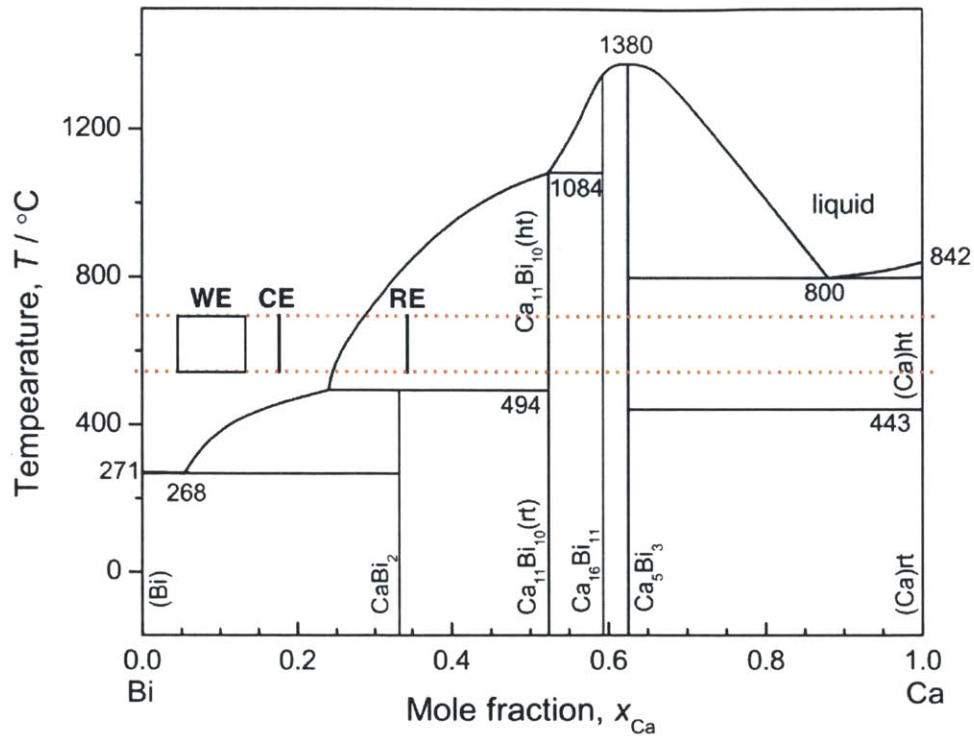


Figure 4-5: Calcium-Bismuth phase diagram [17].

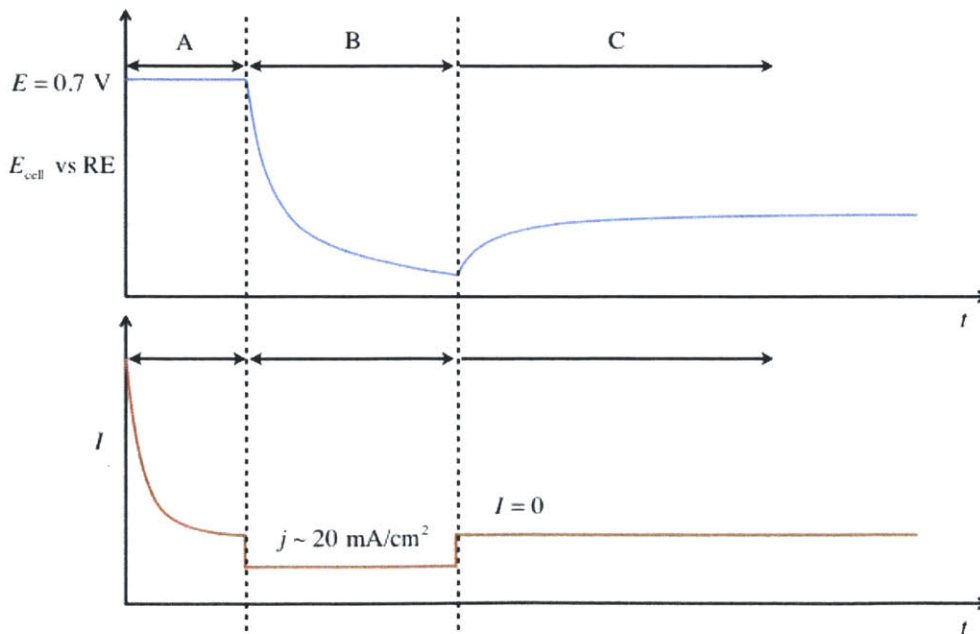


Figure 4-6: Titration to composition. A) Potentiostatic cleaning of working electrode. B) Coulometric titration to composition. C) Open circuit relaxation.

average diffusivity value was calculated (see chapter 5).

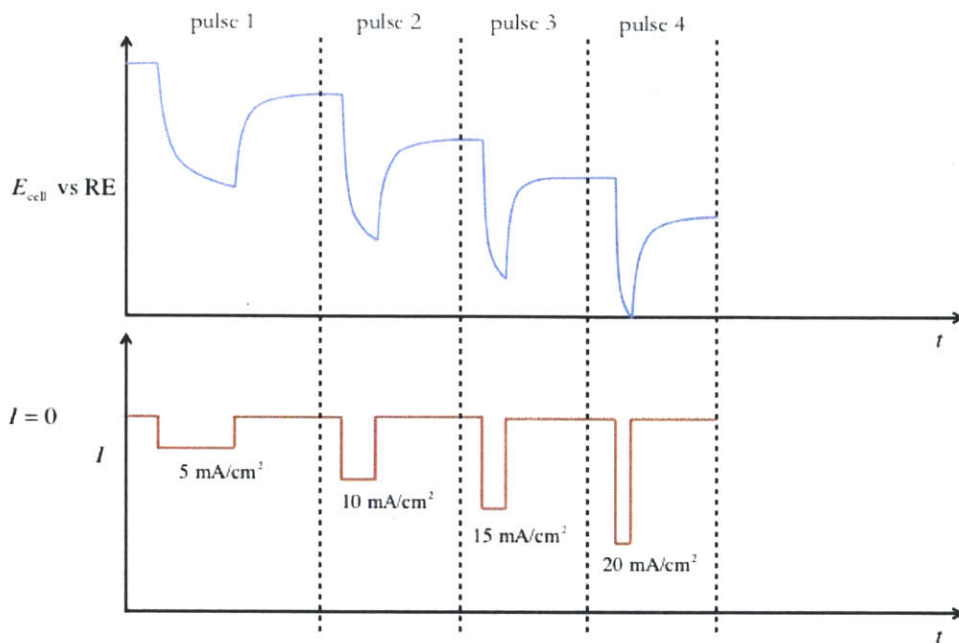


Figure 4-7: Custom four pulse sequence used for determining chemical diffusivity. Each individual pulse changes the calcium composition by 0.25% x_{Ca} .

% Ca	Pulse (#)	j (mA/cm ²)	Time (s)	Rate (mol/s)	$\Delta\%Ca$
5	1	5	2029	7.123×10^{-9}	0.25
5.25	2	10	1020	1.425×10^{-8}	0.25
5.5	3	15	683	2.136×10^{-8}	0.25
5.75	4	20	515	2.848×10^{-8}	0.25
10	1	5	2261	7.123×10^{-9}	0.25
10.25	2	10	1137	1.425×10^{-8}	0.25
10.5	3	15	762	2.136×10^{-8}	0.25
10.75	4	20	575	2.848×10^{-8}	0.25
15	1	5	2535	7.123×10^{-9}	0.25
15.25	2	10	1275	1.425×10^{-8}	0.25
15.5	3	15	855	2.136×10^{-8}	0.25
15.75	4	20	645	2.848×10^{-8}	0.25

Table 4.2: Pulse sequence parameters at 5%, 10%, and 15% Ca-Bi.

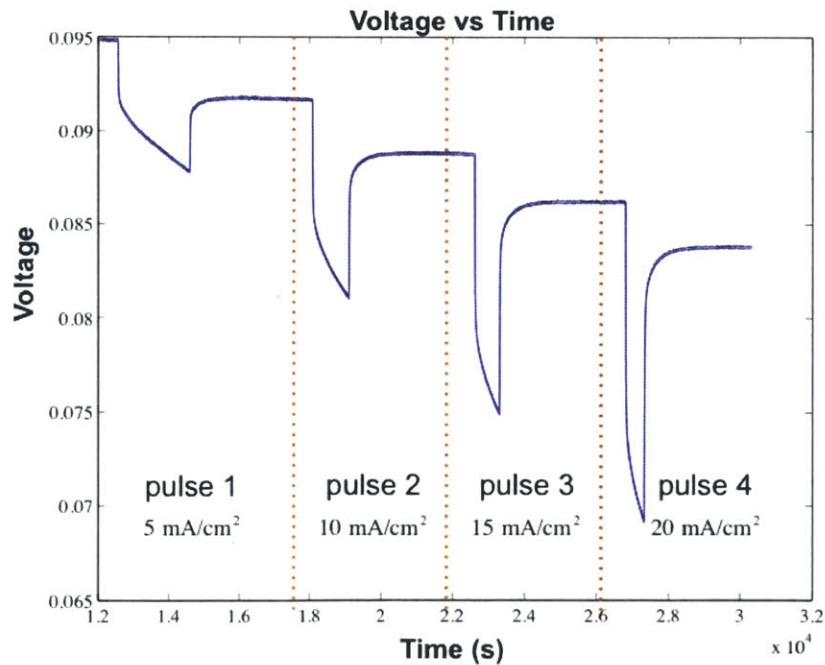


Figure 4-8: Typical pulse sequence applied at 5%, 10%, and 15% - mol Ca-Bi. Each individual pulse changes the calcium composition by 0.25% x_{Ca} .

4.3 Conclusion

Two separate pulse sequences were used to gather the data used to calculate the chemical diffusion coefficient. The first sequence consists of titrating the electrode to a composition between 5% - 15% Ca-Bi. A four-pulse sequence consisting of different current densities was applied after the open circuit voltage stabilized. Different current densities between 5-20 mA/cm² were used because in theory \tilde{D} is invariant to the applied current, so it provided a method for comparison. Natural convection has to be minimized during the time-scale of the experiments to eliminate scatter in the data from enhanced values affected by the flow. Extra insulation was added to the experiment furnace to prevent the temperature from drifting. The hot-zone was located near the center of the electrolyte rather than the bottom which in theory will minimize any buoyancy-driven convection affecting the system. Careful consideration was also made so that no vibrations perturb the liquid, which can come from the use of mechanical equipment such as vacuum pumps. Also, since convection is governed by the dimensionless Rayleigh number which scales with size, the electrode of interest should be made as small as possible which is explained in section 6.4.

Chapter 5

Results and Data Analysis

This chapter will present the electrochemical data and the analysis done to calculate the chemical diffusivity of calcium in liquid bismuth. MATLAB[®] was the software used to analyze all the data generated for each diffusivity value which consisted of four files (two Autolab, two Labview) containing all the experiment information. A lot of effort went into writing the scripts, but was well worth it given how much time was saved analyzing such a complicated data set. Please refer to Appendix F for more information regarding the scripts.

5.1 Application of the Chemical Diffusion Equation (eq. 3.18)

Let's take a closer look at the chemical diffusivity equation derived in chapter 3 to see which variables need to be experimentally measured:

$$\tilde{D}_A = \frac{1}{\pi} \left[\frac{2n_B j_0 V \left(\frac{\Delta E}{\Delta x_A} \right)}{z_A F (n_B + n_A^0)^2 \left(\frac{dE}{d\sqrt{t}} \right)} \right]^2 \quad (5.1)$$

Equation 5.1 requires two voltage rates that need to be extrapolated from the data; the difference in equilibrium potential caused by the titration pulse $\frac{\Delta E}{\Delta x_{Ca}}$, and the square root dependence of the transient potential $\frac{dE}{d\sqrt{t}}$. The other variables do not

change because of the constant volume¹ assumption, a fundamental basis used in the derivation of the concentration solution, but nevertheless there are associated errors with these assumptions that need to be propagated.

5.2 Sources of Error

5.2.1 Uncertainty in Voltage Measurements

Figure 5-1 is an example of the pulse sequence used to calculate the chemical diffusivity of calcium in the 5% Ca-Bi liquid alloy, which is shown along with the temperature variations at 575 °C. The change in equilibrium voltage after each pulse is clearly seen in the same figure, which are the five constant potential asymptotes. At the end of each pulse, the change in calcium mole fraction was $\Delta x_{\text{Ca}} = 0.25\%$, so we can plot the electrode's potential dependence on the change in composition to examine its linear behavior between 5-6% Ca. This open circuit voltage is calculated by averaging the last 250 data points (fig. 5-1), and the standard deviation was taken as the error (5-2).

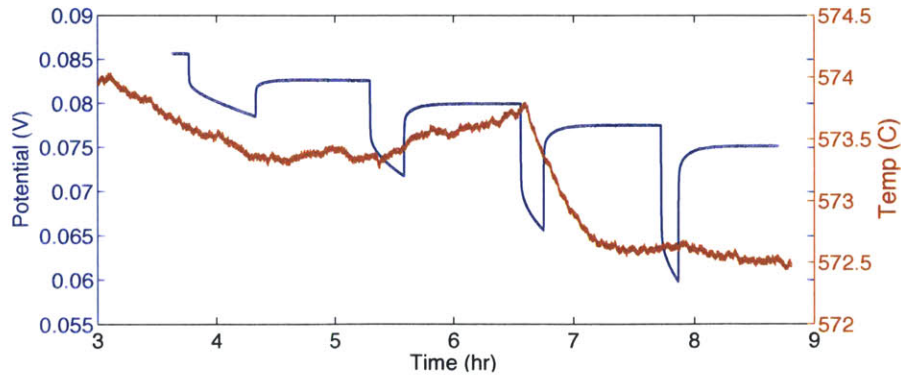


Figure 5-1: Four-pulse sequence used in determining the chemical diffusivity of calcium in bismuth at roughly 575 °C. The temperature fluctuations during the pulse sequence are superimposed to aid in the analysis.

¹One can calculate how much the volume changes with the extra calcium added during titration, assuming a linear relationship, and it changes by less than 0.3% which can be safely assumed to be constant.

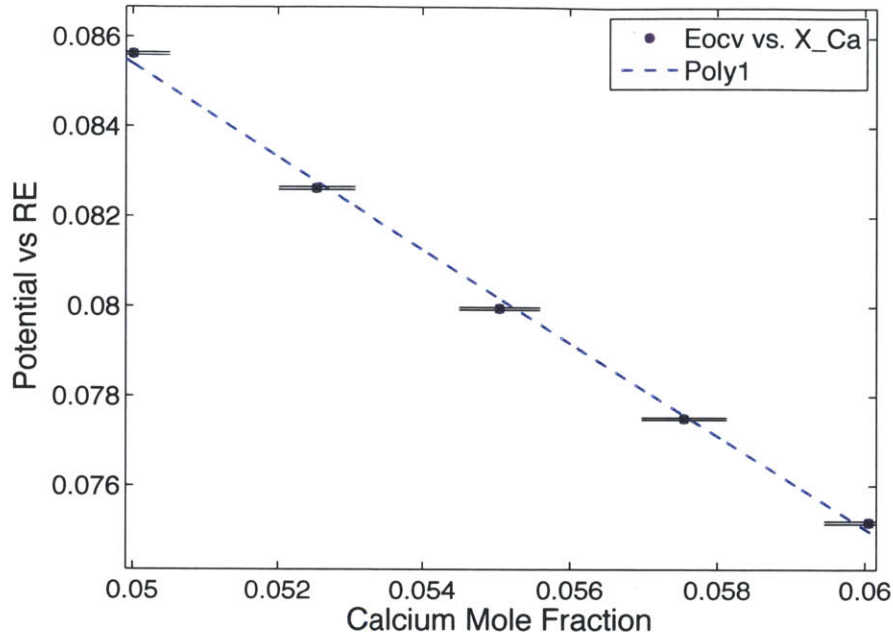


Figure 5-2: Potential versus calcium mole fraction. 5% Ca-Bi, 575°C.

The uncertainty in the potential difference between the potentials E_1 and E_2 were added in quadrature (equation 5.13). The results are shown in figure 5-3.

In theory, the rate of change in potential with composition should be constant if the compositional changes are infinitesimal. Their variation could be associated with the temperature fluctuation experienced during data collection, or influenced by a small leakage current, so it makes sense to assume the value to be constant and the error to be the standard deviation of the four rates. If we treat this as the dominant source of error, then the new propagated error grows, and can be seen in figure 5-4.

5.2.2 Differential Error Analysis

There are five fundamental sources of error that need to be taken into account when calculating the chemical diffusivity. The errors can be added in quadrature and propagated to the individual data points. In order to do so, the chemical diffusivity equation is written as

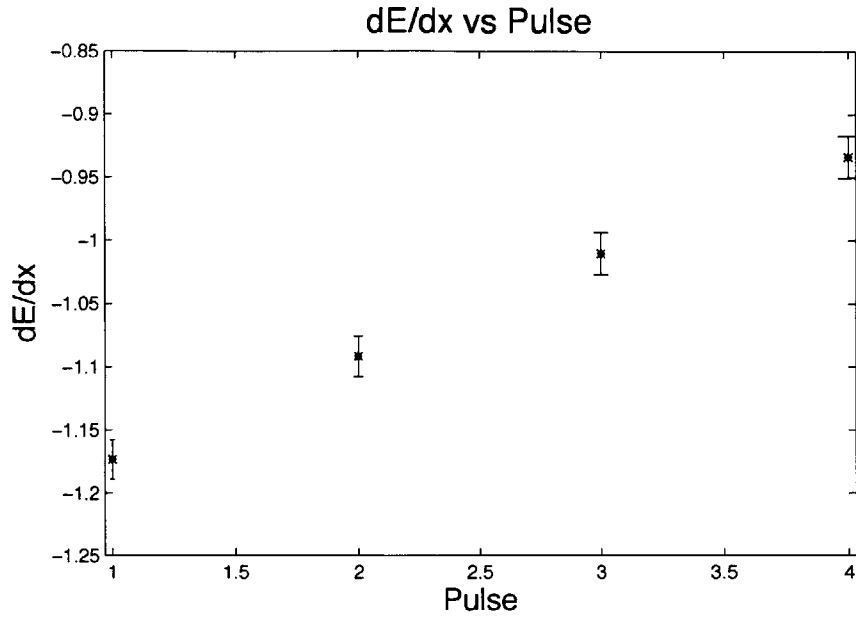


Figure 5-3: $\frac{dE_i}{dx_{Ca}}$ plotted for each pulse. In theory these values should be the same, but deviations in temperature and other environmental changes will induce small deviations.

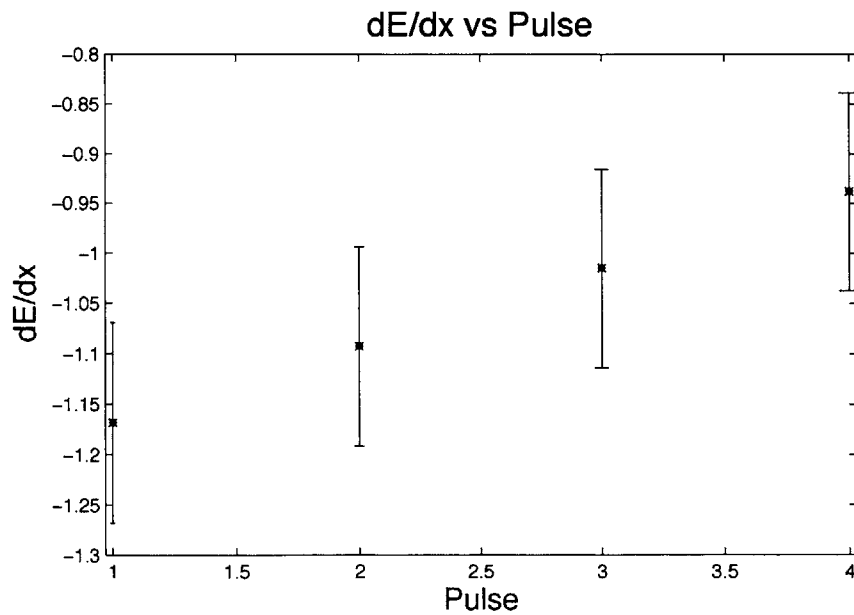


Figure 5-4: $\frac{dE_i}{dx_{Ca}}$ error bars are the standard deviation of the four values. This is assumed valid because in theory they should be equal.

$$\tilde{D}_i = \frac{4}{\pi} \left(\frac{dE}{dx_{\text{Ca}}} \frac{n_{\text{Bi}} V}{(n_{\text{Bi}} + n_{\text{Ca}}^0)^2} \frac{j_0}{z_{\text{Ca}} F \frac{dE}{d\sqrt{t}}} \right)^2 = \frac{4n_{\text{Bi}}^2}{\pi z_{\text{Ca}}^2 F^2} \left(\frac{abc}{fg} \right)^2 \quad (5.2)$$

where the variables are defined as

$$a = \frac{dE}{dx_{\text{Ca}}} \quad (5.3)$$

$$b = V \quad (5.4)$$

$$c = j_0 \quad (5.5)$$

$$f = (n_{\text{Bi}} + n_{\text{Ca}}^0)^{-2} \quad (5.6)$$

$$g = \frac{dE}{d\sqrt{t}}, \quad (5.7)$$

and have the following associated uncertainty:

$$\Delta a = \text{std}(dE/dx_{\text{Ca}}) \quad (5.8)$$

$$\Delta b = V_{\text{Ca}}^{\tau} \quad (5.9)$$

$$\Delta c = \sigma_S \quad (5.10)$$

$$\Delta f = n_{\text{Ca}}^{\tau} \quad (5.11)$$

$$\Delta g = \frac{\sigma_{\Delta E_i}}{\sqrt{\tau_i}}. \quad (5.12)$$

a is the average of the four values shown in figure 5-4, and Δa is the standard deviation calculated from the four dE/dx values, which varies depending on concentration. At 5% Ca, it is around 0.1, but decreases in magnitude at higher concentrations to take a value between 0.002 and 0.01.

b is the initial volume of the alloy. It is assumed to be the linear sum of the individual component volumes calculated using the measured masses and densities at the operating temperature, which is around 0.1 cm³. Δb is assumed to be the added volume during the calcium titration, V_{Ca}^{τ} , which is roughly 10⁻⁴.

c is the current density, but the dominant uncertainty lies in the surface area for the

electrode. The electrodes were machined at the MIT machine shop, and the diameter was assumed to have a 1% relative error. Δc is then the propagated uncertainty in the surface area, calculated to be 10^{-3} .

f is the inverse square of the total number of moles initially present in the alloy. The error is introduced assuming no change in f , so Δf becomes the moles of calcium added, which is typically around 10^{-5} ($\Delta x_{\text{Ca}} \leq 0.25\%$).

Δg is a complicated source of error because it is what ultimately affects the deviation of the four values, sometimes beyond the error bars calculated from the propagated errors. This is because it is heavily dependent on the bounds separating the linear component of the potential's response as a function of square root of time. It is also sensitive to temperature fluctuations. In order to propagate this error, it was defined to be the uncertainty from the standard deviation of the open circuit voltage measurements

$$\sigma_{\Delta E_i} = \sqrt{\sigma_{E_1}^2 + \sigma_{E_2}^2}, \quad (5.13)$$

divided by the square root of the pulse time $\sigma_{\Delta E_i}/\sqrt{tau}$. Now that we have all the variables defined, we can compute the error in the chemical diffusivity by applying the following equation:

$$\sigma_{\tilde{D}_i} = \sqrt{\left(\frac{\partial \tilde{D}_i}{\partial a} \Delta a\right)^2 + \left(\frac{\partial \tilde{D}_i}{\partial b} \Delta b\right)^2 + \left(\frac{\partial \tilde{D}_i}{\partial c} \Delta c\right)^2 + \left(\frac{\partial \tilde{D}_i}{\partial f} \Delta f\right)^2 + \left(\frac{\partial \tilde{D}_i}{\partial g} \Delta g\right)^2} \quad (5.14)$$

5.3 Calculated Chemical Diffusivities of Calcium in Bismuth

In section 5.1 we analyzed how the derived chemical diffusion equation for liquid alloys is used to calculate the chemical diffusivity at 5% Ca-Bi, 575 °C. We also demonstrated how the calculated chemical diffusivities are independent of the applied current density, which has to hold true in order to have confidence on the diffusivity

values. This section will show all the calculated chemical diffusivities of calcium in bismuth at 5%, 10%, 15% Ca-Bi between 550 °C and 700 °C.

The data was collected over a period of two months, and the electrochemical system used was very stable after it equilibrated. The system was left at 650 °C overnight before starting any coulometric titrations. Unfortunately this was not enough time to allow the system to equilibrate even though the electrode potential response seemed normal. This was discovered after the computed chemical diffusivities deviated greatly from the overall trend shown when plotting all the calculated values together, seen in figure 5-5. The error was due to the reference electrodes drifting (see E-7) during electrolysis because the system was still equilibrating. There error analysis is clear to point out the values which deviate greatly, and also gives us confidence the technique works.

5.3.1 5% Calcium in Bismuth

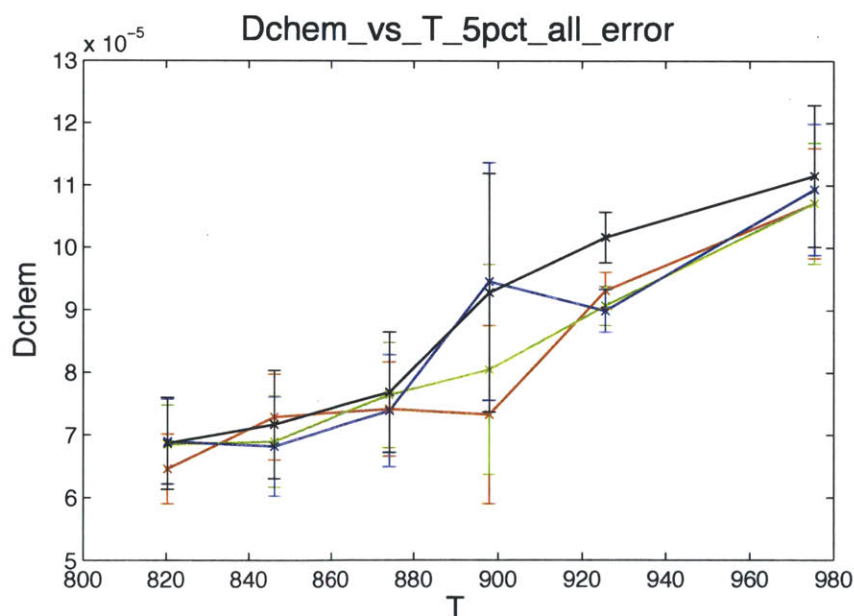


Figure 5-5: Chemical diffusion coefficients at 5% Ca-Bi.

Figure 5-5 are the chemical diffusivity values calculated using the data collected at 5% calcium in liquid bismuth. There is a noticeable trend of the value increasing with

T (K)	\tilde{D}_{chem1} (cm ² /s)	\tilde{D}_{chem2} (cm ² /s)	\tilde{D}_{chem3} (cm ² /s)	\tilde{D}_{chem4} (cm ² /s)
820.3	(6.46 ± 0.56)x10 ⁻⁵	(6.85 ± 0.63)x10 ⁻⁵	(6.89 ± 0.68)x10 ⁻⁵	(6.87 ± 0.73)x10 ⁻⁵
846.2	(7.29 ± 0.68)x10 ⁻⁵	(6.90 ± 0.73)x10 ⁻⁵	(6.82 ± 0.79)x10 ⁻⁵	(7.17 ± 0.86)x10 ⁻⁵
874.2	(7.41 ± 0.75)x10 ⁻⁵	(7.64 ± 0.84)x10 ⁻⁵	(7.39 ± 0.90)x10 ⁻⁵	(7.69 ± 0.96)x10 ⁻⁵
897.9	(7.33 ± 1.14)x10 ⁻⁵	(8.05 ± 1.7)x10 ⁻⁵	(9.46 ± 1.9)x10 ⁻⁵	(9.28 ± 1.9)x10 ⁻⁵
925.6	(9.32 ± 0.29)x10 ⁻⁵	(9.07 ± 0.31)x10 ⁻⁵	(9.0 ± 0.34)x10 ⁻⁵	(10.2 ± 0.40)x10 ⁻⁵
975.4	(10.7 ± 0.88)x10 ⁻⁵	(10.7 ± 0.97)x10 ⁻⁵	(10.9 ± 1.1)x10 ⁻⁵	(11.2 ± 1.1)x10 ⁻⁵

Table 5.1: Chemical diffusion coefficients of Ca in 5% a Ca-Bi liquid alloy. Errors are shown to one significant figure.

temperature, which is expected under the assumption that diffusion is an activated process.

5.3.2 10% Calcium in Bismuth

Figure 5-6 is the plotted chemical diffusivity data shown in table 5.2. These values were calculated using the same method described above for the 5% Ca-Bi liquid alloy. The propagated relative errors are also shown to one significant figure.

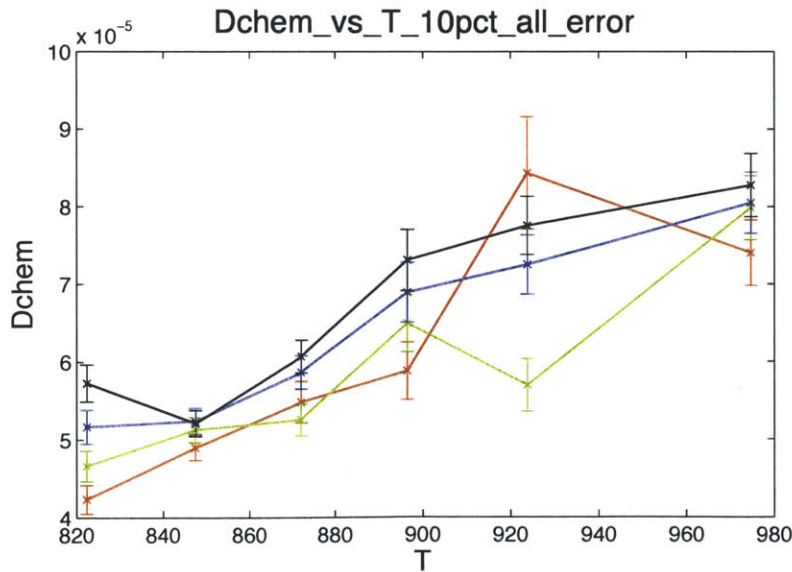


Figure 5-6: Chemical diffusion coefficients at 10% Ca-Bi.

T (K)	\tilde{D}_1 (cm ² /s)	\tilde{D}_2 (cm ² /s)	\tilde{D}_3 (cm ² /s)	\tilde{D}_4 (cm ² /s)
822.3	$(4.23 \pm 0.19) \times 10^{-5}$	$(4.66 \pm 0.20) \times 10^{-5}$	$(5.16 \pm 0.22) \times 10^{-5}$	$(5.73 \pm 0.24) \times 10^{-5}$
847.5	$(4.89 \pm 0.16) \times 10^{-5}$	$(5.12 \pm 0.16) \times 10^{-5}$	$(5.24 \pm 0.17) \times 10^{-5}$	$(5.21 \pm 0.17) \times 10^{-5}$
872.1	$(5.48 \pm 0.27) \times 10^{-5}$	$(5.25 \pm 0.21) \times 10^{-5}$	$(5.86 \pm 0.22) \times 10^{-5}$	$(6.07 \pm 0.21) \times 10^{-5}$
896.5	$(5.88 \pm 0.37) \times 10^{-5}$	$(6.50 \pm 0.37) \times 10^{-5}$	$(6.89 \pm 0.39) \times 10^{-5}$	$(7.31 \pm 0.39) \times 10^{-5}$
924.1	$(8.43 \pm 0.72) \times 10^{-5}$	$(5.70 \pm 0.34) \times 10^{-5}$	$(7.25 \pm 0.38) \times 10^{-5}$	$(7.76 \pm 0.38) \times 10^{-5}$
974.7	$(7.40 \pm 0.43) \times 10^{-5}$	$(7.98 \pm 0.41) \times 10^{-5}$	$(8.05 \pm 0.40) \times 10^{-5}$	$(8.28 \pm 0.41) \times 10^{-5}$

Table 5.2: Chemical diffusion coefficients of Ca in 10% Ca-Bi. Errors are shown to one significant figure.

5.3.3 15% Calcium in Bismuth

Figure 5-7 is the chemical diffusivity data for 15% Ca-Bi, which is shown in table 5.3. These values were calculated along with their uncertainties to show their true reliability. At this composition, some of the values differ beyond their calculated errors, more noticeable at 700°C.

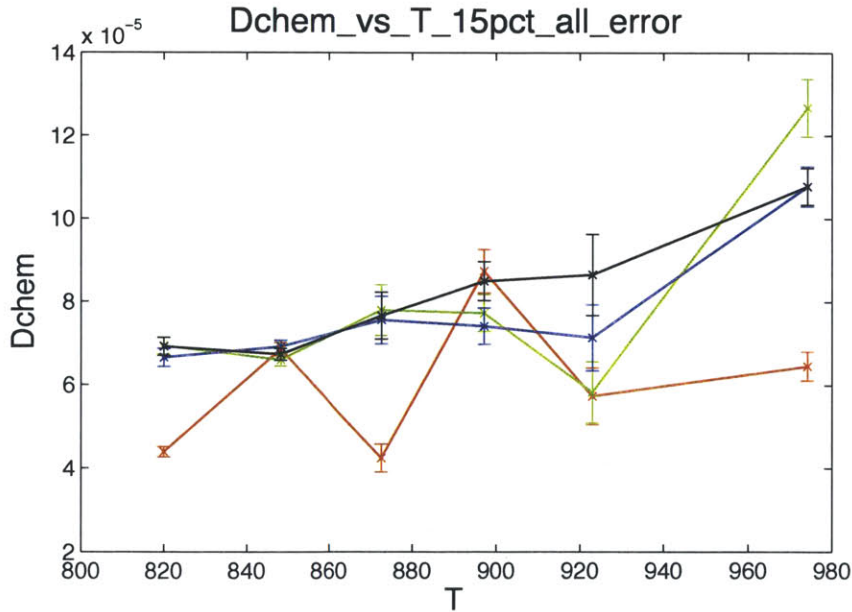


Figure 5-7: Chemical diffusion coefficients at 15% Ca-Bi.

This implies there are other sources of error inherited in the system. The uncertainty is introduced when analyzing the transient potential variation with square root of time $\frac{dE}{d\sqrt{t}}$, which is discussed comprehensively in the section below.

T (K)	\tilde{D}_1 (cm ² /s)	\tilde{D}_2 (cm ² /s)	\tilde{D}_3 (cm ² /s)	\tilde{D}_4 (cm ² /s)
820.0	$(4.39 \pm 0.13) \times 10^{-5}$	$(6.93 \pm 0.20) \times 10^{-5}$	$(6.65 \pm 0.22) \times 10^{-5}$	$(6.92 \pm 0.22) \times 10^{-5}$
848.2	$(6.85 \pm 0.16) \times 10^{-5}$	$(6.59 \pm 0.15) \times 10^{-5}$	$(6.91 \pm 0.15) \times 10^{-5}$	$(6.73 \pm 0.15) \times 10^{-5}$
872.7	$(4.24 \pm 0.34) \times 10^{-5}$	$(7.80 \pm 0.61) \times 10^{-5}$	$(7.56 \pm 0.57) \times 10^{-5}$	$(7.66 \pm 0.56) \times 10^{-5}$
897.2	$(8.73 \pm 0.52) \times 10^{-5}$	$(7.73 \pm 0.45) \times 10^{-5}$	$(7.41 \pm 0.44) \times 10^{-5}$	$(8.49 \pm 0.47) \times 10^{-5}$
923.0	$(5.74 \pm 0.68) \times 10^{-5}$	$(5.83 \pm 0.74) \times 10^{-5}$	$(7.14 \pm 0.79) \times 10^{-5}$	$(8.65 \pm 0.98) \times 10^{-5}$
974.1	$(6.46 \pm 0.35) \times 10^{-5}$	$(12.7 \pm 0.70) \times 10^{-5}$	$(10.8 \pm 0.48) \times 10^{-5}$	$(10.8 \pm 0.44) \times 10^{-5}$

Table 5.3: Chemical diffusion coefficients of Ca in 15%Ca-Bi. Errors are shown to one significant figure.

5.4 $\frac{dE_j}{d\sqrt{t}}$ vs Temperature

The theoretical derivation of the chemical diffusion equation (eq. 3.18) for liquid alloys in chapter 3 states the rate of change in electrode potential with respect to the square root of time should be linear during the time scales of the experiments. Our liquid electrodes do show the same behavior, but only after an initial nonlinearity, which is observed within the first 50-100 seconds of each pulse. The nonlinear behavior seems to be independent of temperature because the calculated rates are very similar (fig. 5-13). The nonlinearity is clearly seen in figure 5-8, which is a plot of the electrode potential variation with square root of time during the applied galvanostatic pulses.

We initially believed the nonlinear behavior was due to either a kinetic limitation from the electrolyte, or a local thermodynamic effect such as joule heating. We also thought about the possibility that a surface passivation layer could be causing the initial nonlinear behavior, but this is unlikely because we can still draw large current densities without the potential deviating drastically. If a solid interface is present, then solid calcium would be deposited onto the surface faster than it could diffuse causing the voltage to exponentially shift, which is not observed. We now believe this effect is a result from the electrode design. Recent work involving a new electrode design shows the potential to be entirely linear with the square root of time, so we now think that the nonlinearity is a mixed potential effect from the tungsten lead being in contact with the electrolyte. The new electrode design isolates the tungsten

lead from the electrolyte, effectively eliminating the mix potential problem. We are confident this initial nonlinear behavior does not affect the diffusivity measurements, which should prove true if the different diffusivity values calculated from the four current densities are the same.

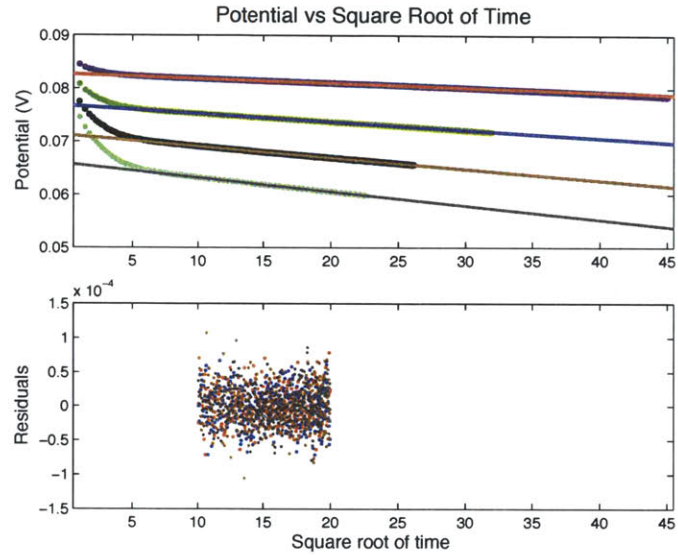


Figure 5-8: Electrode potential dependence with the square root of time. The longer pulse shown in blue corresponds to the smallest applied current density which was 5 mA/cm².

Figure 5-9 is a plot of linear $\frac{dE_i}{d\sqrt{t}}$ fits to the data. The fits had a lower bound to exclude the initial nonlinearity, and an upper bound. The upper bound might be a little confusing, but it will make more sense if we look at the entire residual (fig. 5-10) after excluding the initial nonlinearity from the pulses. One can see the residual fit is linear between $\sqrt{t} = 10$ and $\sqrt{t} = 25$, then falls off nonlinearly until the end of the pulse, which is why the upper bound limit was imposed.

The nonlinearity observed at later times is caused by the 'end-effects' of the cell because the titration pulses were applied for times longer than what the constraint time $\tau \ll l^2/\tilde{D}_{Ca}$ allows. To show this, we ran finite element simulations² (which will be the focus of next chapter) to solve for the transient surface composition using the calculated \tilde{D}_{Ca} values. The surface concentration was then mapped to the electrode

²Simulations used the full numerical form of the solution to solve for the surface composition, unlike the simplified version used in the experiments.

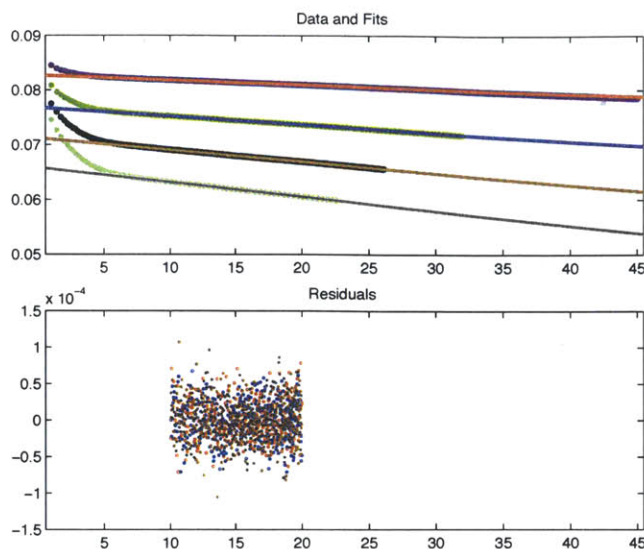


Figure 5-9: Top: Linear fits to electrode potential variation with square root of time. Bottom: Residual plot from the fits and data showing random scatter averaged at zero, signifying good fits.

potential by using a linear polynomial fitted to the equilibrium voltage variation with composition (5-2). The results are in excellent agreement with each other and can be seen in figure 5-11.

The next step is to compare the slope values inside the bounded region, so fitting a linear polynomial with the same bounds used in the analysis (red fit and residual in fig. 5-12) of the experimental data to the simulated $\frac{dE_j}{d\sqrt{t}}$ rate gives a value of $-8.56 \times 10^{-5} \text{ V s}^{-1/2}$, which is less than 1% difference when compared to the experimental value, $-8.48 \times 10^{-5} \text{ V s}^{-1/2}$ (table 5.4). This validates the assumption that we can use bulk-average equilibrium potentials ($\Delta E / \Delta x_{Ca}$) in the diffusivity equation when relating it to the transient potential that evolves during the application of a galvanostatic pulse.

The analysis using the experimental value $\frac{dE_j}{dx_{Ca}}$ was carried to demonstrate how the nonlinearity affected the rate. The simulated $\frac{dE_j}{d\sqrt{t}}$ result did not exhibit an initial nonlinear behavior, and was within 1% of the measured value, allowing us to conclude that it had no effect.

The diffusion data shows an overall trend of increasing diffusivity with temperature, but looks scattered at times because of the reference electrode drifting during

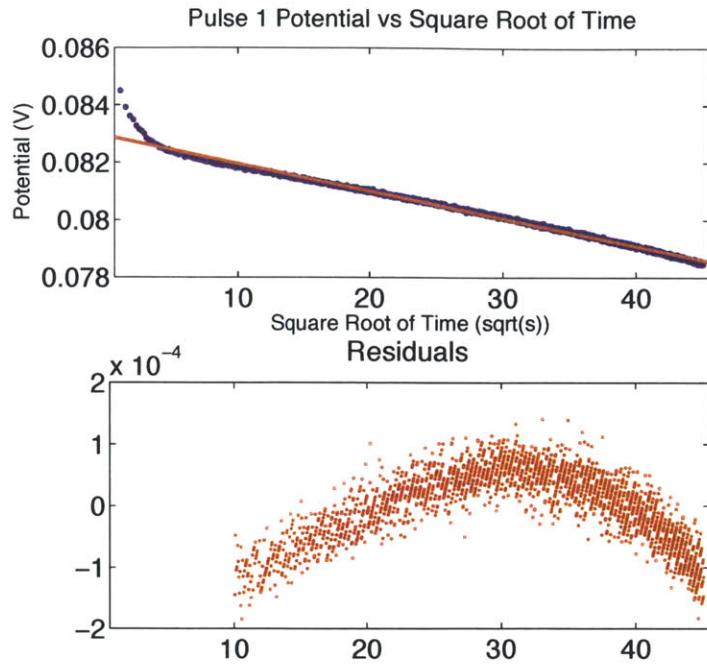


Figure 5-10: Top: Linear fits to electrode potential variation of pulse 1 with square root of time. Bottom: Residual plot from the linear fit and data.

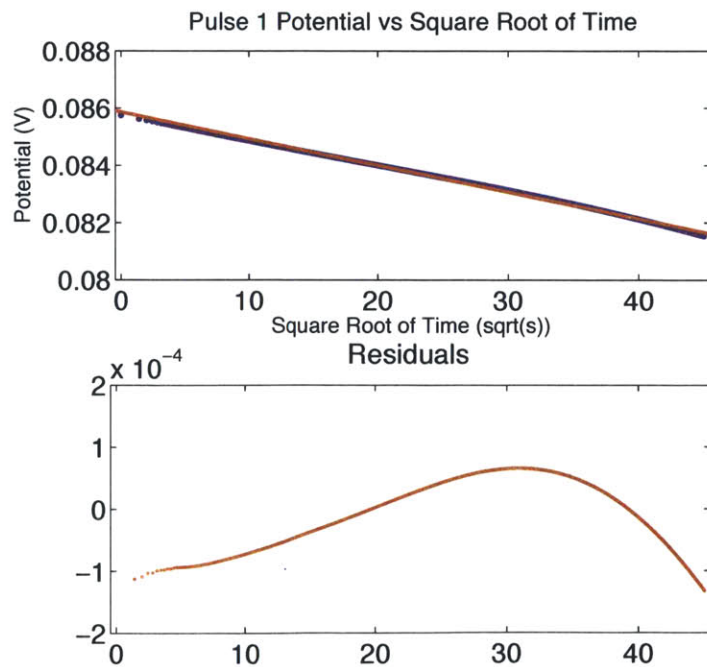


Figure 5-11: Top: Linear fit to simulated electrode potential variation of pulse 1 with square root of time. Bottom: Residual plot from the linear fit and data.

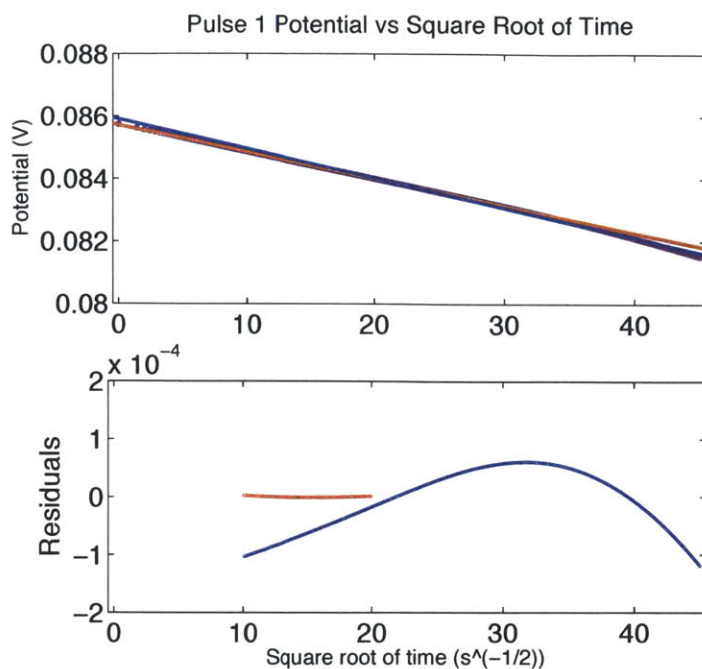


Figure 5-12: Top: Linear fits to simulated electrode potential variation of pulse 1 with square root of time. Bottom: Residual plot from the linear fit and data. The residual fit in red has both upper and lower bounds, and the slope in that region is $\frac{dE_i}{d\sqrt{t}} = -8.56 \times 10^{-5} \text{ V s}^{-1/2}$.

electrolysis. The $\frac{dE_i}{d\sqrt{t}}$ dependance on temperature and electromagnetic noise also contributed to the scatter in the data, and is more evident at 10% and 15% Ca-Bi. This does not necessarily make the data flawed because we can do corrections to it by examining the entire data set as a whole. This requires to examine how the chemical diffusivity will vary collectively over the entire range of temperature.

There is no way to predict how $\frac{dE_i}{d\sqrt{t}}$ will vary with temperature, and it seem to trend in a way that are constant with temperature and only vary with applied current. This trend can be true because the e.m.f. data (fig. 3-4 of Ca-Bi shows the electrode potential curves to be virtually the same between 500 °C-700 °C, so one would expect the transient electrode potential rate to be constant with temperature. In fact, the $\frac{dE_i}{d\sqrt{t}}$ values get closer to each other as current pulse (p1 = 5, p2 = 10, p3 = 15, p4 = 20 (mA/cm²)) increases³ independent of temperature. A reason for this could be due to a much faster rate of change in surface potential, so variations in temperature and

³The percent differences are 19.1%, 9.3%, 4.4%, and 3.7% for pulse 1, pulse 2, pulse 3, and pulse 4 respectively.

electromagnetic noise do not affect the rate as much when compared to the smaller current density pulses.

The $\frac{dE_j}{d\sqrt{t}}$ rates at 10% Ca-Bi are roughly half the value measured at 5% Ca-Bi. This intuitively makes sense because at 10% Ca-Bi, the e.m.f. curve is not as steep as it is for 5%. Also, the rate of change in surface mole fraction under a constant current is technically smaller at 10% Ca-Bi than at 5% Ca-Bi. This makes the electrode potential more vulnerable to environmental changes such as temperature drift, and can be seen by how the data in table 5.5 varies slightly more compared to the 5% Ca-Bi data in table 5.4. These small variations in the $\frac{dE_j}{d\sqrt{t}}$ rate at 10% are indeed affected by the temperature drift, and can be seen in the 10% Ca-Bi-potential and temperature variation data in Appendix E.

T (K)	$\frac{dE_{p1}}{d\sqrt{t}} \left(\frac{V}{\sqrt{s}} \right)$	$\frac{dE_{p2}}{d\sqrt{t}} \left(\frac{V}{\sqrt{s}} \right)$	$\frac{dE_{p3}}{d\sqrt{t}} \left(\frac{V}{\sqrt{s}} \right)$	$\frac{dE_{p4}}{d\sqrt{t}} \left(\frac{V}{\sqrt{s}} \right)$
820.3	-8.74×10^{-5}	-1.608×10^{-4}	-2.24×10^{-4}	-2.74×10^{-4}
846.1	-8.480×10^{-5}	-1.55×10^{-4}	-2.143×10^{-4}	-2.65×10^{-4}
874.1	-8.92×10^{-5}	-1.604×10^{-4}	-2.207×10^{-4}	-2.748×10^{-4}
897.8	-9.58×10^{-5}	-1.64×10^{-4}	-2.177×10^{-4}	-2.70×10^{-4}
925.6	-7.91×10^{-5}	-1.494×10^{-4}	x	-2.71×10^{-4}
975.4	-8.42×10^{-5}	-1.55×10^{-4}	-2.16×10^{-4}	-2.721×10^{-4}

Table 5.4: Rate of change of electrode potential versus square root of time at 5% Ca-Bi.

T (K)	$\frac{dE_{p1}}{d\sqrt{t}} \left(\frac{V}{\sqrt{s}} \right)$	$\frac{dE_{p2}}{d\sqrt{t}} \left(\frac{V}{\sqrt{s}} \right)$	$\frac{dE_{p3}}{d\sqrt{t}} \left(\frac{V}{\sqrt{s}} \right)$	$\frac{dE_{p4}}{d\sqrt{t}} \left(\frac{V}{\sqrt{s}} \right)$
822.3	-4.24×10^{-5}	-8.26×10^{-5}	-1.17×10^{-4}	-1.52×10^{-4}
847.4	-4.46×10^{-5}	-8.70×10^{-5}	-1.25×10^{-4}	-1.67×10^{-4}
872.1	-4.42×10^{-5}	-8.83×10^{-5}	-1.25×10^{-4}	-1.61×10^{-4}
896.4	-4.37×10^{-5}	-8.51×10^{-5}	-1.21×10^{-4}	-1.53×10^{-4}
924.1	-4.26×10^{-5}	-8.35×10^{-5}	x	-1.62×10^{-4}
974.7	-4.47×10^{-5}	-8.43×10^{-5}	-1.23×10^{-4}	-1.58×10^{-4}

Table 5.5: Rate of change of electrode potential versus square root of time at 10% Ca-Bi.

T (K)	$\frac{dE_{p1}}{d\sqrt{t}}$ ($\frac{V}{\sqrt{s}}$)	$\frac{dE_{p2}}{d\sqrt{t}}$ ($\frac{V}{\sqrt{s}}$)	$\frac{dE_{p3}}{d\sqrt{t}}$ ($\frac{V}{\sqrt{s}}$)	$\frac{dE_{p4}}{d\sqrt{t}}$ ($\frac{V}{\sqrt{s}}$)
822.3	-3.35×10^{-5}	-5.59×10^{-5}	-7.68×10^{-5}	-10.1×10^{-5}
847.5	-3.21×10^{-5}	-5.67×10^{-5}	-8.59×10^{-5}	-11.08×10^{-5}
872.1	-3.75×10^{-5}	-6.39×10^{-5}	-9.07×10^{-5}	-11.29×10^{-5}
896.5	-3.08×10^{-5}	-5.22×10^{-5}	-7.71×10^{-5}	-10.06×10^{-5}
924.1	-3.16×10^{-5}	-6.21×10^{-5}	x	-11.69×10^{-5}
974.7	-3.60×10^{-5}	-5.70×10^{-5}	-7.82×10^{-5}	-10.27×10^{-5}

Table 5.6: Rate of change of electrode potential versus square root of time at 15% Ca-Bi.

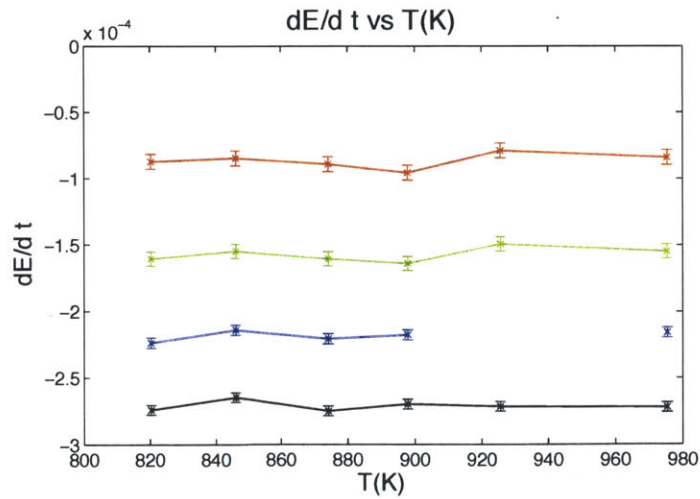


Figure 5-13: Potential variation with square root of time plotted as a function of temperature. The error bars is the standard deviation of the values assuming they only rely on current density.

5.5 Average Diffusion Coefficients

To incorporate the error associated with the deviation in $\frac{dE_i}{d\sqrt{t}}$, the chemical diffusion coefficients were averaged and their standard deviation used as the uncertainty (table 5.7). The diffusion coefficients are not dependent on current density, and their variation has been shown to be heavily rely on the potential dependence with composition and temperature. Therefore, the standard deviation of the average value provides a good way to see the uncertainty in the values.

The chemical diffusivities, along with their standard deviations are plotted together as a function of composition in figure 5-17. The data agrees with the work of Buell [68], which shows the same trend for the diffusion of tin in liquid bismuth. The phase diagrams for Ca-Bi and Sn-Bi are not similar, so it is difficult to associate the trend having to deal with atomic ordering of the interacting species. The one similarity between calcium and tin is that both have been measured to have roughly 11 nearest neighbors in the liquid state [111]. Bismuth has 8.8 nearest neighbors when liquid, so this trend in the diffusivity could potentially be due to the atomic properties of liquid bismuth.

T (K)	$\tilde{D}_{5\%}$ (cm ² /s)	$\tilde{D}_{10\%}$ (cm ² /s)	$\tilde{D}_{15\%}$ (cm ² /s)
820.0	$(6.77 \pm 0.21) \times 10^{-5}$	$(4.95 \pm 0.65) \times 10^{-5}$	$(6.22 \pm 0.12) \times 10^{-5}$
848.2	$(7.04 \pm 0.22) \times 10^{-5}$	$(5.12 \pm 0.16) \times 10^{-5}$	$(6.77 \pm 0.14) \times 10^{-5}$
872.7	$(7.53 \pm 0.15) \times 10^{-5}$	$(5.67 \pm 0.37) \times 10^{-5}$	$(6.82 \pm 0.17) \times 10^{-5}$
897.2	$(8.53 \pm 1.0) \times 10^{-5}$	$(6.65 \pm 0.61) \times 10^{-5}$	$(8.09 \pm 0.62) \times 10^{-5}$
923.0	$(9.39 \pm 0.54) \times 10^{-5}$	$(7.28 \pm 1.2) \times 10^{-5}$	$(6.84 \pm 0.14) \times 10^{-5}$
974.1	$(10.9 \pm 0.21) \times 10^{-5}$	$(7.93 \pm 0.37) \times 10^{-5}$	$(10.2 \pm 0.26) \times 10^{-5}$

Table 5.7: Averaged chemical diffusion coefficients. Errors are shown to one significant figure and are the standard deviation of the averaged values.

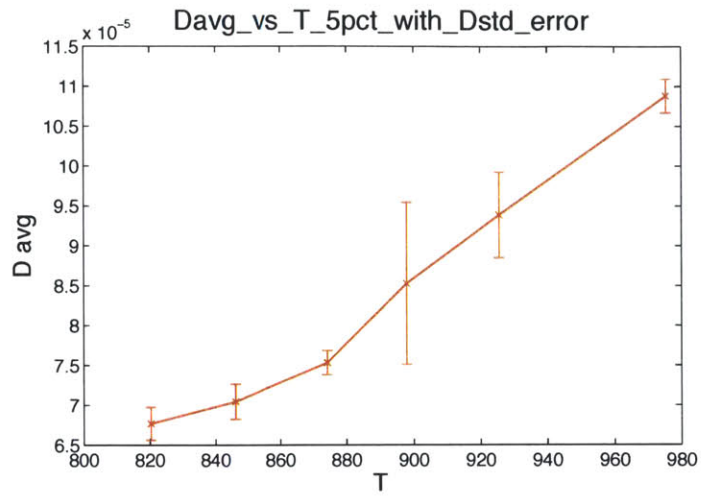


Figure 5-14: Average chemical diffusion coefficient at 5% Ca-Bi.

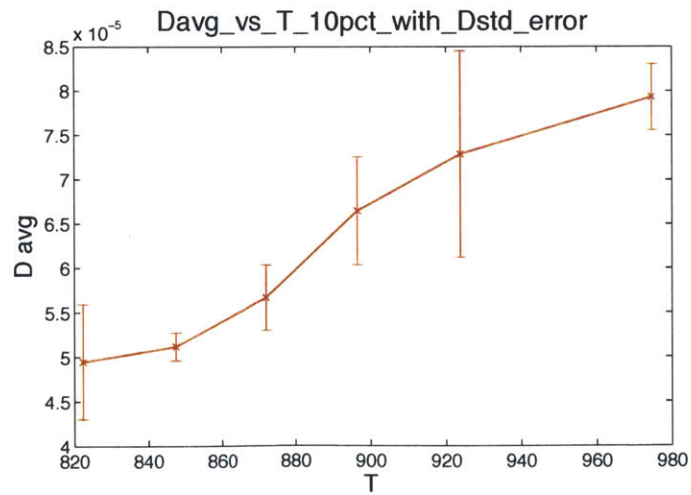


Figure 5-15: Average chemical diffusion coefficient at 10% Ca-Bi.

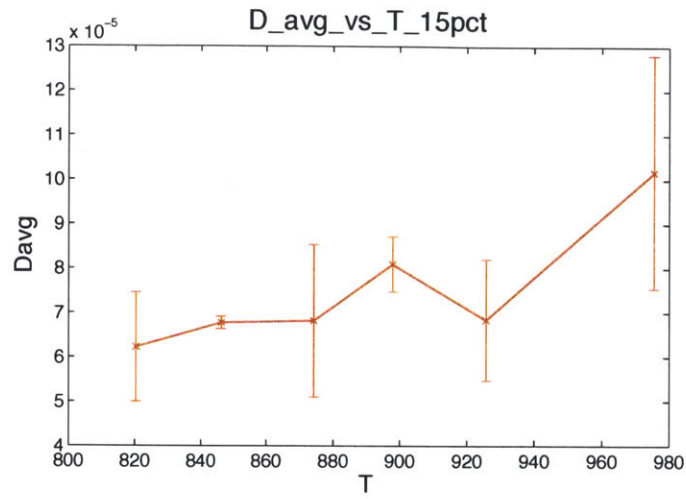


Figure 5-16: Average chemical diffusion coefficient at 15% Ca-Bi.

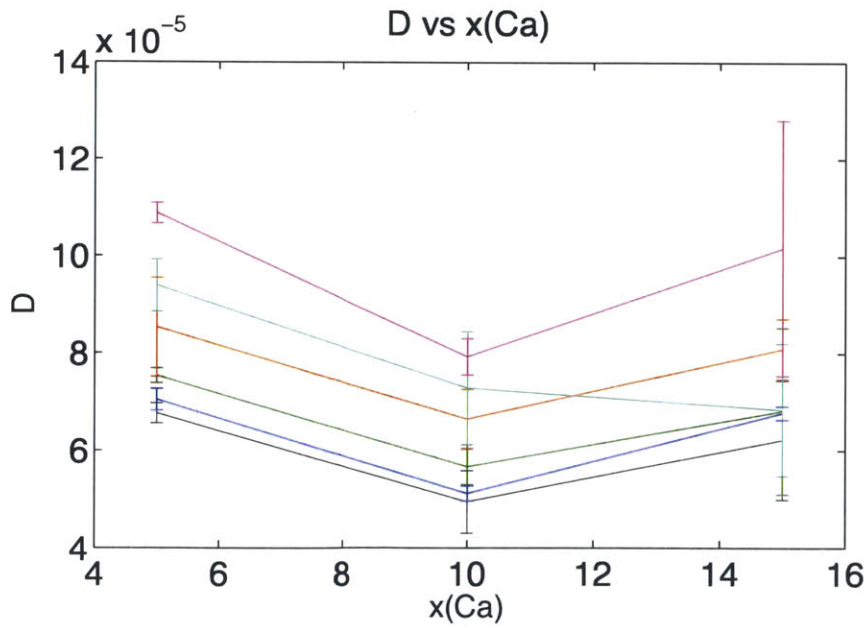


Figure 5-17: Averaged chemical diffusivity values.

5.6 Diffusion Activation Energies

We calculate the activation energy, $H_{D,j}$, for diffusion as a function of composition j by treating the system as Arrhenius using the following equation,

$$\tilde{D}_{Ca,j} = \tilde{D}_j^0 \exp\left(-\frac{H_{D,j}}{RT}\right), \quad (5.15)$$

where \tilde{D}_j^0 is the frequency factor, R is the gas constant, and T is the Temperature. For convenience we rewrite it as

$$\ln\left(\tilde{D}_{Ca,j}\right) = \ln\left(\tilde{D}_j^0\right) - \frac{H_{D,j}}{R} \frac{1}{T} \quad (5.16)$$

by taking the natural log of the equation. We then calculate the activation energy for diffusion ($H_{D,j}$) from the slope ($H_{D,j}/R$) in equation 5.16. To use this method, the natural log of the chemical diffusivity values is plotted versus the inverse temperature (in Kelvin), and a least-squares regression is then fitted. The data is shown in table 5.8 and plotted in figure 5-18.

Chemical Diffusion Frequency Factor \tilde{D}_j^0

By treating the system as Arrhenius, we assume the dominant mode of diffusion in liquid alloys is analogous to solute diffusion via the vacancy method for solids. This allows us to write the frequency factor as [18]

$$\tilde{D}_j^0 = gfv_D a^2 \exp\left(\frac{\Delta S}{R}\right) \quad (5.17)$$

where g is a geometrical factor⁴, f is the correlation factor (assume $f = 1$), v_D the attempt frequency, a is the lattice parameter, and ΔS is the diffusion entropy. \tilde{D}_j^0 contains the information related to entropy, so if liquid diffusion is to be described by equation 5.15, then ΔS in equation 5.17 has to be positive. The difficulty lies in knowing g , f , v_D , and a . The geometrical factor g is equal to $Z/6$ [112] for cubic structures, so for a first order approximation we will assume g is the same in liquid

⁴Usually g is of order one, e.g., $g = 1$ in cubic metals.

alloys, and that a is equal to the mean distance of nearest neighbors. Bismuth has an average of $Z = 8$ nearest neighbors [37] at an average distance of $a = 3.36 \text{ \AA}$, which makes $g \approx 1.3$. The only variable left to analyze is the attempt frequency ν_D , which deserves a little attention. For solids, it is usually customary to set the attempt frequency equal to the Debye frequency⁵ $\nu_D = \frac{k_B T_D}{h}$. The Debye temperature [113] itself is $T_D = \left(\frac{h \nu_s}{2\pi k_B} \right) \left(\frac{6\pi^2 N}{V} \right)^{1/3}$, where $\frac{N}{V}$ is the number density, and ν_s is the speed of sound through the material, so substituting it into ν_D gives

$$\nu_D = \left(\frac{\nu_s}{2\pi} \right) \left(\frac{6\pi^2 N}{V} \right)^{1/3}. \quad (5.18)$$

We see the Debye frequency is proportional to the speed of sound within the material, and since the speed of sound in a liquid [114–117] is less than that of solids, it is reasonable we approximate the value smaller than that of solids. Typical values of ν_D for solids reported in literature [118–120] range between $10^{12} \text{ (s}^{-1}\text{)}$ and $10^{14} \text{ (s}^{-1}\text{)}$, so we decided to use the lower value of $\nu_D = 10^{12} \text{ (s}^{-1}\text{)}$ in our first order approximation of the activation entropy for diffusion.

We can now solve for ΔS using the average value of \tilde{D}^0 from table 5.11 to get a sense of its magnitude and sign:

$$\tilde{D}^0 = (1.3)(1)(1 \times 10^{12})(3.36 \times 10^{-10})^2 \exp\left(\frac{\Delta S}{R}\right) = 1.45 \times 10^{-7} \quad (5.19)$$

$$\rightarrow \exp\left(\frac{\Delta S}{R}\right) = 1.02 \rightarrow \Delta S \approx 0.02R \quad (5.20)$$

So, for a first approximation, the activation entropy for liquid diffusion is indeed positive and around $0.2 \text{ J/mol}\cdot\text{K}$ which is very small. This gives us confidence that we can describe diffusion in liquid alloys as an activated process, and assume the chemical diffusivities conform to Arrhenius behavior.

⁵ k_B is Boltzmann's constant, T_D is the Debye temperature, and h is Planck's constant.

5.6.1 Diffusion Activation Energies

The calculated activation energies at 5%, 10%, and 15% Ca-Bi ($H_{D,j}$) are in excellent agreement with reported activation energies of similar metals [58, 66, 121, 122]. Table 5.11 shows the tabulated activation energies along with the diffusion pre-factor (\tilde{D}_j^0). Tables 5.8, 5.9, and 5.10 are used to calculate the chemical diffusion coefficients by fitting a least-squares regression to the data, for which the calculated uncertainty in the slope is computed from the regression.

$\frac{1}{T}$ (K ⁻¹)	$\ln(\tilde{D}_1)$
1.22×10^{-3}	-9.60 ± 0.03
1.18×10^{-3}	-9.53 ± 0.03
1.14×10^{-3}	-9.43 ± 0.02
1.11×10^{-3}	-9.36 ± 0.12
1.08×10^{-3}	-9.28 ± 0.06
1.03×10^{-3}	-9.13 ± 0.02

Table 5.8: Natural log of averaged chemical diffusivity for 5% Ca-Bi liquid alloy.

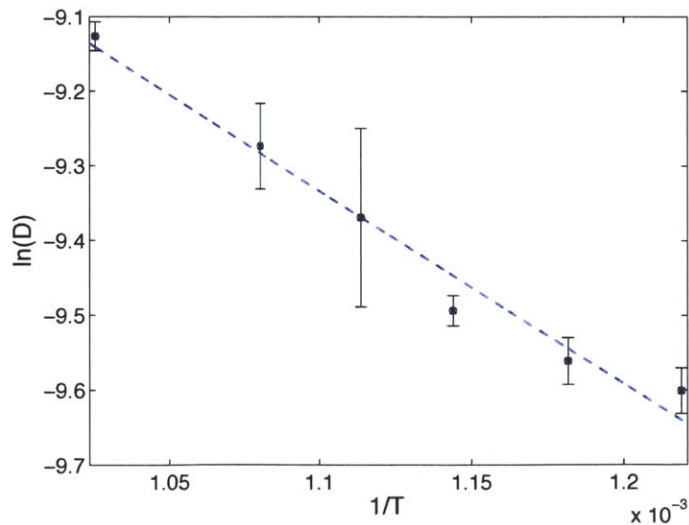


Figure 5-18: Natural log of chemical diffusivity versus inverse temperature for 5% Ca-Bi.

The activation energy values for calcium diffusion in the Ca-Bi liquid alloy are shown in table 5.11. The values are all around 20 kJ/mol, and show the activation

$\frac{1}{T}$ (K ⁻¹)	$\ln(\tilde{D}_1)$
1.22×10^{-3}	-9.91 ± 0.13
1.18×10^{-3}	-9.88 ± 0.03
1.14×10^{-3}	-9.77 ± 0.06
1.11×10^{-3}	-9.62 ± 0.09
1.08×10^{-3}	-9.53 ± 0.16
1.03×10^{-3}	-9.44 ± 0.05

Table 5.9: Natural log of averaged chemical diffusivity for 10% Ca-Bi liquid alloy.

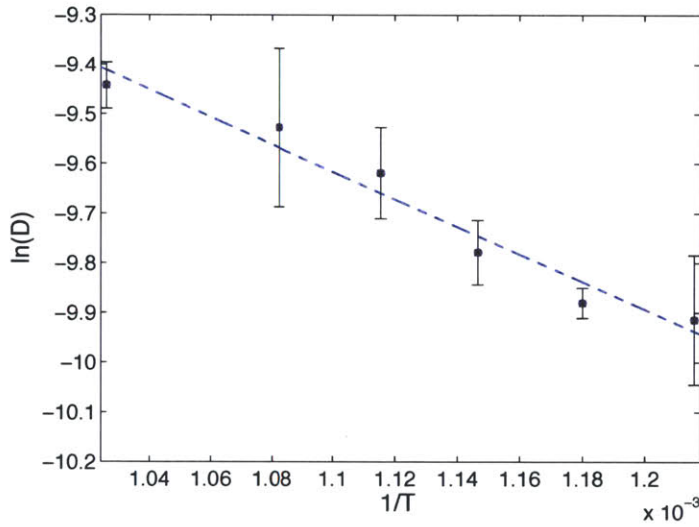


Figure 5-19: Natural log of chemical diffusivity versus inverse temperature for 10% Ca-Bi.

$\frac{1}{T}$ (K ⁻¹)	$\ln(\tilde{D}_1)$
1.22×10^{-3}	-9.69 ± 0.20
1.18×10^{-3}	-9.60 ± 0.03
1.14×10^{-3}	-9.59 ± 0.25
1.11×10^{-3}	-9.42 ± 0.08
1.08×10^{-3}	-9.59 ± 0.20
1.03×10^{-3}	-9.19 ± 0.26

Table 5.10: Natural log of averaged chemical diffusivity for 15% Ca-Bi liquid alloy.

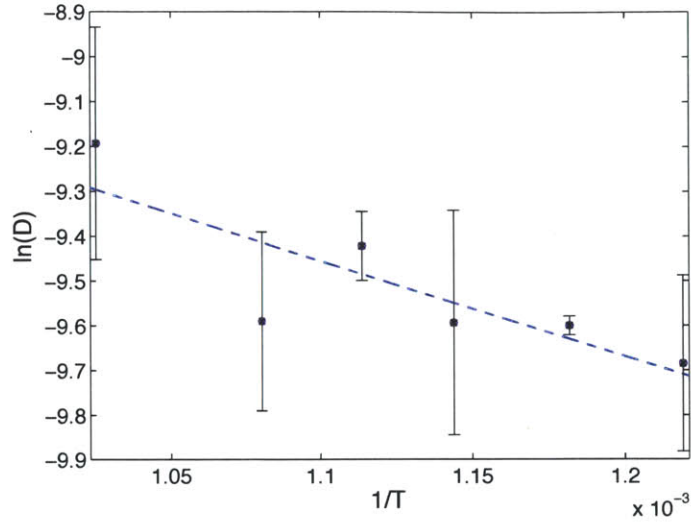


Figure 5-20: Natural log of chemical diffusivity versus inverse temperature for 15% Ca-Bi.

x_{Ca}	Slope [$H_{D,j}/R$]	$H_{D,j}$ [$\frac{\text{kJ}}{\text{mol}\cdot\text{K}}$]	$\ln(\tilde{D}_j^0)$	\tilde{D}_j^0 [$\frac{\text{cm}^2}{\text{s}}$]
5	2578 ± 210	21.4 ± 1.7	-6.50 ± 0.23	$1.51 \pm 0.05 \times 10^{-3}$
10	2767 ± 287	23.0 ± 2.4	-6.7 ± 0.32	$1.40 \pm 0.06 \times 10^{-3}$
15	2130 ± 708	17.7 ± 5.9	-7.11 ± 0.8	$1.47 \pm 0.9 \times 10^{-3}$

Table 5.11: Activation energy for diffusion of Ca in Ca-Bi liquid alloy along with the diffusion prefactor values and propagated uncertainties.

energy to be higher at 10% Ca-Bi. This is not too surprising because the diffusion coefficients calculated at 10% Ca-Bi seem to be lower than the other two compositions. This by itself is rather remarkable because the dominant variables we have been describing ($\frac{dE_j}{d\sqrt{t}}$, $\frac{dE}{dx_{Ca}}$) really influence the chemical diffusivity value, and differ greatly between compositions, and yet the calculated chemical diffusivities are very close to each other with the activation energies virtually indistinguishable.

5.7 Conclusion

The diffusion coefficient of calcium in liquid bismuth has been measured for the first time ever. No literature data exists on the diffusivity of liquid calcium because of the extreme difficulty involved in dealing with super reactive metals. The new technique presented in this thesis does show reliable results that are in agreement with published values of similar metals, therefore this method will open new opportunities for studying the kinetic properties of highly reactive liquid metals.

Also, the activation energy as a function of composition was calculated from the diffusivity data, which shows to range between 17.7 kJ/mol and 23.0 kJ/mol. We can try to reason such values using the theoretical work of Takamichi [123] which focused on predicting self-diffusion properties of liquid metals using a modified Stokes-Einstein relation. Takamichi had predicted the self-diffusion of calcium to be 7.21×10^{-5} cm²/s with an activation energy of 29.2 kJ/mol, and the diffusion of bismuth to be 2.72×10^{-5} cm²/s with an activation energy of 12.5 kJ/mol. The activation energies calculated from the diffusivity data are very close to these values, which is the right trend predicted by Takamichi's work.

Chapter 6

Transport Phenomena Simulations

Transport simulations of liquid metal batteries will be presented in this chapter. Some of the work focuses on the effect convection has on the liquid electrode under a thermal gradient. Ideally, a battery with liquid electrodes that can be more homogeneously mixed at the end of a discharge is preferred because it will allow for a higher electrode capacity, and also be energy efficient in the process. Therefore, it is imperative to numerically model the induced velocity field in a LMB as a function of material properties, geometry, and most importantly temperature gradients. Also, as a LMB cycles, the Joule heating generated by the current passing through the electrolyte needs to keep the cell at its liquid temperature, so thermal energy balance simulations were also done on two cell geometries. We cannot simply do back of the envelope calculations to estimate how the flow will vary because of how complex this system is. The last section of this chapter focuses on the earlier simulation work done using phase field to model the two electrode-electrolyte liquid interface kinetics simultaneously during cell cycling.

Before we present and discuss the simulation results, we will first do a brief introduction of the numerical method used, followed by the derivation of the governing partial differential equations that are solved in order to obtain useful information about the system of interest.

6.1 Brief Introduction to Finite Element Analysis (FEA)

Extremely complex physics needs to be coupled in order to obtain solutions to this problem sought after in this thesis. To ease the numerical pain, finite element analysis (FEA) was chosen as the method and COMSOL Multiphysics as the software. Since the output of a simulation will only be as good as the input provided, it is important to build a malleable model whose material properties can be quickly adjusted. Below is a list of questions we set to answer via simulations:

- How does the magnitude of thermal gradients affect mixing inside a LMB cell?
- How does the fluid flow vary under the same thermal gradient for liquid metals with significant different densities, thermal conductivities, etc?
- What is the difference in fluid motion for a bottom electrode if the electrolyte is liquid vs solid?
- How does the velocity profile change in the bottom electrode as a function of the liquid electrolyte's material properties?
- How does mixing vary if we change the size of the top current collector?
- How does the Joule heat generated in the electrolyte affect the mixing and how does it vary as a function of electrolyte thickness?
- What are the optimal dimensions for a self-heated cell?

Here I will briefly explain how FEA works, a more detailed discussion on the subject can be found here [124]. FEA is also known as the finite element method (FEM) and has been widely used in the design and interpretation of engineering problems, particularly with fluids, solids, and complex structures. It is a powerful computational tool aimed at predicting physical phenomena. A good understanding of the physical laws governing the system is required to generate useful solutions

related to specific boundary conditions. FEA works by breaking down a physical geometry into multiple elements, and then connecting these elements at nodes as shown in Figure 6-1.

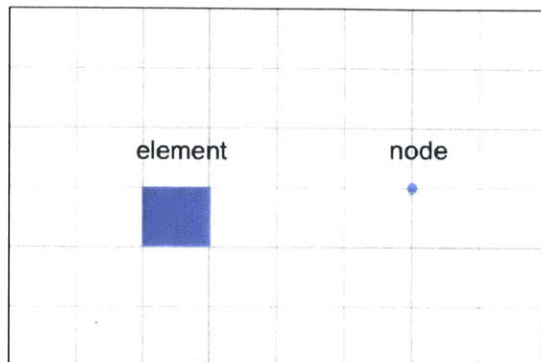


Figure 6-1: Simple quadratic mesh on a rectangular geometry. Each square is called an element, 48 elements make up this geometry. Each point of intersection makes up a node, so there are 63 nodes on the geometry.

This process of connecting the nodes yields a simultaneous set of algebraic equations that are then solved within the elements and nodes of the geometry [125]. The set of simultaneous equations can be written in matrix notation

$$[\mathbf{K}]\{\mathbf{v}\} = \{\mathbf{f}\} \quad (6.1)$$

where \mathbf{K} is a material property, \mathbf{v} the material behavior, and \mathbf{f} the action or force on the system. In Table 6.1 below are examples of these variables.

	Property $[\mathbf{K}]$	Behavior $\{\mathbf{u}\}$	Action $\{\mathbf{f}\}$
Thermal	conductivity	temperature	heat source
Fluid	viscosity	velocity	body force
Electrostatic	dielectric permittivity	electric potential	charge

Table 6.1: Physical examples of common FEA matrix variables.

With FEA, the interest lies in the behavior $\{\mathbf{u}\}$ of a system, therefore equation 6.1 is transformed to

$$\{\mathbf{v}\} = [\mathbf{K}]^{-1}\{\mathbf{f}\}. \quad (6.2)$$

It is impossible to account for all the physical behavior observed in real systems using FEA models, even with the most refined mathematical algorithms. Therefore, it is necessary to validate the physical limitations of a FEA computational model. To accomplish this, models were developed in the following order:

1. Presenting a physical problem.
2. Deriving a mathematical model for the problem using differential equations with assumptions on geometry, material laws, boundary conditions, etc.
3. Solving a system using finite element software with optimal choice of mesh density, finite elements, solution parameters, etc.
4. Verifying the accuracy of the FEA solution by comparing to a closed-form solution.
5. Resolving inaccuracy in the solution through refining.
6. Interpreting the results in terms of real physical behavior and adjusting the model accordingly.

6.2 Conservation Equations

There are two universal requirements to be able to mathematically describe transport phenomena. The first is knowing the *constitutive equation* applicable to the transport of interest. A constitutive equation is derived from material properties and measured experimentally, which is merely the systems response to external forces. An example of a constitutive equation is Fourier's law of heat conduction given by

$$\mathbf{q} = -k\nabla T \quad (6.3)$$

where \mathbf{q} is the heat response to the applied thermal gradient ∇T , and k is the materials thermal conductivity which will be a function of the material properties and can vary spatially.

The other requirement is a conservation equation for the system, which stems from first principles. Appendix G describes the general derivation of a conservation equation, below we discuss the ones applicable to LMBs used in simulations.

Conservation of Mass

We all know that mass is conserved, and it can be proved by letting¹ $c(\mathbf{r}, t) = \rho(\mathbf{r}, t)$, where ρ is the mass per unit volume. If the material is moving with a velocity \mathbf{v} through the control volume, then the flux is simply $\mathbf{J} = \rho\mathbf{v}$. A quick check in dimensional analysis shows $\mathbf{J} \left[\frac{\text{mol}}{\text{s}\cdot\text{cm}^2} \right] = \rho \left[\frac{\text{mol}}{\text{cm}^3} \right] \mathbf{v} \left[\frac{\text{cm}}{\text{s}} \right]$, and since mass can't be created nor destroyed in the control volume of interest, we set $R_V = 0$. Plugging it all in gives

$$\frac{\partial \rho}{\partial t} = \nabla \cdot (\rho\mathbf{v}) \quad (6.4)$$

which is commonly known as the *continuity equation*. If the density is constant, then equation 6.4 deduces to

$$\nabla \cdot (\rho\mathbf{v}) = \nabla \cdot \mathbf{v} = 0 \quad (6.5)$$

which proves that the material of interest is incompressible, therefore the material volume will not dilate. In other words, the material enters and leaves the control volume at the same rate. We use the continuity equation extensively when solving for fluid motion. The law of conservation of mass allows us to make use of the *material derivative*

$$\frac{D}{Dt} = \frac{\partial}{\partial t} + \mathbf{v} \cdot \nabla \quad (6.6)$$

¹ $c(\mathbf{r}, t)$ is defined in Appendix G.

which describes the rate of motion being observed from the reference point of the fluid for scalar quantities. With this, the general conservation equation (G.7) is written as

$$\frac{Dc}{Dt} = -\nabla \cdot \mathbf{j} + R_V, \quad (6.7)$$

where \mathbf{j} is the diffusive flux component of the total flux.

Fick's second law of diffusion is derived from equation 6.7, which is the partial differential equation solved in COMSOL when describing the conservation of atomic species. This is achieved by inserting the constitutive equation which describes atomic diffusion (Fick's first law of diffusion²)

$$\mathbf{j} = -D_i \nabla c \quad (6.8)$$

into equation 6.7 to get

$$\frac{Dc}{Dt} = -D_i \nabla^2 c + R_V. \quad (6.9)$$

Conservation of Energy

Conservation of energy, also known as the second law of thermodynamics, is a universal law describing how energy cannot be created nor destroyed, only transferred. If a local energy density u (energy per unit volume) is assumed to exist with an energy flux \mathbf{q} , then it can be written as

$$\frac{\partial u}{\partial t} = -\nabla \cdot \mathbf{q}. \quad (6.10)$$

In COMSOL, the energy density conserved is that of heat and it is related to the heat capacity with $c = u = \rho c_p T$. The diffusive heat flux then becomes $\mathbf{j} = \mathbf{q} = -\mathbf{k} \cdot \nabla T$. The constitutive equation comes into play as the heat flux, which is simply Fourier's law of heat conduction. Since current is being passed through LMBs, Joule Heating will be generated and the heat can be expressed by $R_V = Q_h$. Inserting these relations

² D_i is the diffusion coefficient not the material derivative, and it's assume constant.

into equation 6.7 and assuming ρ , c_p , and \mathbf{k} are constant, gives

$$\rho c_p \frac{DT}{Dt} = k \nabla^2 T + Q_h. \quad (6.11)$$

Conservation of Momentum

Newton's second law of motion, $\mathbf{F} = m \frac{d\mathbf{v}}{dt}$, states that the rate of change of momentum equals the force acting on a body. If the control volume contains a fluid with constant material properties, Newton's second law becomes

$$\mathbf{F} = \frac{d}{dt} \int_{V(t)} \rho \mathbf{v} dV. \quad (6.12)$$

This introduces the time derivative of the velocity vector, so the Leibniz rule for differentiation (equation G.2) can be applied, and after a little bit of math we can write the force as a function of the material derivative

$$\mathbf{F} = \int_{V(t)} \rho \frac{D\mathbf{v}}{Dt} dV. \quad (6.13)$$

The next question to be answered is what constitutes the force \mathbf{F} . There are two types of forces that can act on a fluid. The first acts on the body of the fluid, which are known as *body forces* (\mathbf{F}_B), and the second are *surface stresses* (\mathbf{F}_S). The body force used in COMSOL is the effect of gravity on the fluid,

$$\mathbf{F}_B = \int_{V(t)} \rho \mathbf{g} dV. \quad (6.14)$$

because it plays a major role in the onset of convection under thermal gradients. Stresses on a surface are given by the stress vector $\mathbf{s}(\mathbf{n})$, which is the force per unit area perpendicular to the fluid's surface. It is related to the total stress tensor ($\boldsymbol{\sigma}$) by $\mathbf{s}(\mathbf{n}) = \hat{\mathbf{n}} \cdot \boldsymbol{\sigma}$, so \mathbf{F}_S is simply

$$\mathbf{F}_S = \int_{S(t)} \mathbf{s}(\mathbf{n}) dS = \int_{S(t)} \hat{\mathbf{n}} \cdot \boldsymbol{\sigma} dS. \quad (6.15)$$

Balancing the forces results in

$$\int_{V(t)} \rho \frac{D\mathbf{v}}{Dt} dV = \int_{V(t)} \rho \mathbf{g} dV + \int_{S(t)} \hat{\mathbf{n}} \cdot \boldsymbol{\sigma} dS, \quad (6.16)$$

and applying Green's theorem to the surface integral yields the wanted differential form

$$\int_{V(t)} \left(\rho \frac{D\mathbf{v}}{Dt} - \rho \mathbf{g} - \nabla \cdot \boldsymbol{\sigma} \right) dV = 0. \quad (6.17)$$

It can then be expressed as

$$\rho \frac{D\mathbf{v}}{Dt} = \rho \mathbf{g} + \nabla \cdot \boldsymbol{\sigma}. \quad (6.18)$$

Equation 6.18 is the general form of the conservation of linear momentum for a fluid. To model fluid motion, the Navier-Stokes equations are required. To derive them, the stress tensor is expressed as the sum of the rest pressure (P) and viscous stress ($\boldsymbol{\tau}$)

$$\boldsymbol{\sigma} = -P\boldsymbol{\delta} + \boldsymbol{\tau}, \quad (6.19)$$

where $\boldsymbol{\delta}$ is the identity tensor which ensures the rest pressure only acts perpendicular to the surface of the fluid. Applying the divergence to the stress tensor ($\nabla \cdot \boldsymbol{\sigma} = -\nabla P + \nabla \cdot \boldsymbol{\tau}$) yields the *Cauchy momentum equation*

$$\rho \frac{D\mathbf{v}}{Dt} = \rho \mathbf{g} + -\nabla P + \nabla \cdot \boldsymbol{\tau}. \quad (6.20)$$

For an incompressible Newtonian fluid, the viscous stress is given by

$$\boldsymbol{\tau} = \mu[\nabla \mathbf{v} + (\nabla \mathbf{v})^t] = \mu \nabla^2 \mathbf{v}. \quad (6.21)$$

Taking the divergence of the viscous stress and inserting it in equation 6.20 gives the Navier-Stokes equations in vector form:

$$\rho \frac{D\mathbf{v}}{Dt} = \rho \mathbf{g} + -\nabla P + \mu \nabla^2 \mathbf{v}. \quad (6.22)$$

Equations 6.5, 6.7, 6.11, and 6.22 are all that are needed to describe the physics

behind LMBs.

6.3 Thermal Simulation Results

Thermal energy balance calculations are critical for calculating optimal operation conditions for liquid metal batteries. It will be important to have high operating energy efficiencies that produce usable electricity, rather than just using the energy to keep a cell at temperature as LMBs are scaled-up in size. To simulate the best results, the model requires accurate temperature and composition-dependent thermal conductivities, densities, heat capacities, and electrical/ionic resistivities of all the materials in the cell. Since accurate values are not readily available in the literature, published data of similar materials was used and linearized for alloy compositions.

A top priority in scaling a LMB is to optimize the cell geometry and current density maintaining a constant temperature at around 630 °C while having a high round-trip energy efficiency. Our objective was to create a model that would serve as a basis for optimizing a self-heated cells geometry, starting with two different geometries. The first geometry was similar to that used by Cairns (fig. 1-6) at Argonne National Laboratory, shown schematically in figure 6-2. The second cell geometry studied is the one currently being used at MIT shown in figure 6-6 because it allows for better thermal management, which is proven in the simulations results.

6.3.1 Argonne National Laboratory Cell Geometry

The first step was to create simple thermal models using heaters as the heat source, so a 2-D radial numerical model was created to compute the power required to keep a cell at a temperature. A radial cross-section of the 20-Ah Argonne National Laboratory cell geometry used in the simulation is shown in figure 6-3, and the cell dimensions on table 6.2. The thermal boundary conditions are shown in figure 6-4. The heaters (shown in red) had a power density of $q = 5.4 \text{ W/cm}^3$. The boundary condition at the top and bottom of the insulation was set to simulate a stacked cell, and the rest of the boundaries were set to lose heat by convection, except for the cooling lines which

were set to room temperature. The cooling lines are necessary because it prevents the rubber seal from melting, but are detrimental to the systems efficiency because of the huge thermal gradient induced.

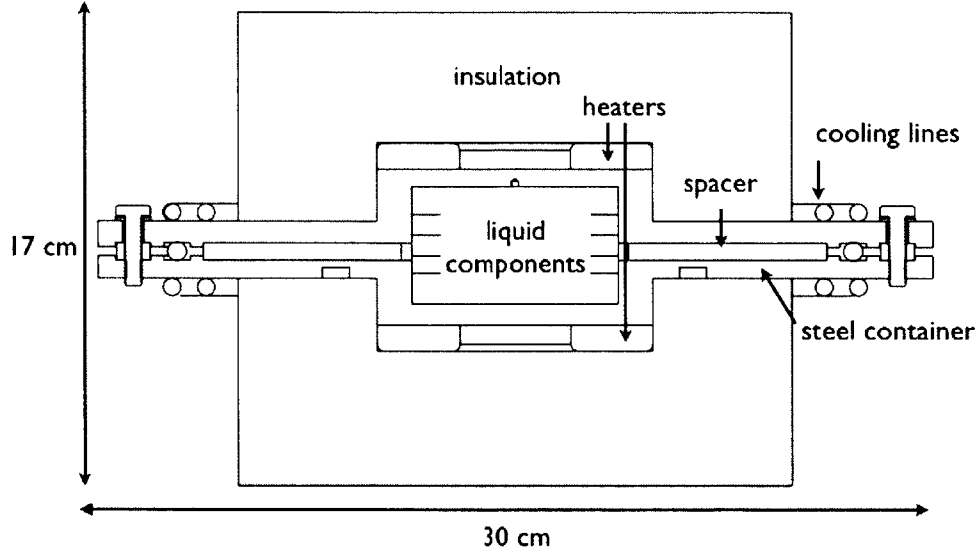


Figure 6-2: Cell schematic of the geometry used at Argonne National Laboratory by Cairns [10].

To maintain this cell at a constant temperature of 630 °C, our simulations show that 1,054 W of power are required. This value is in excellent agreement with the experimental power measured by Dr Brice Chung for this geometry, but unfortunately this power requirement is too high for the cell to be self-heated. Matching the simulated and experimental power gave us confidence to run simulations using cells with bigger diameters in order to find the critical size self-heating size. This was achieved by simulating the power required to keep the cell at temperature, and comparing this to the Joule heating power generated by a current passing through the electrolyte for three different cell sizes of $r_{AC} = 50$ cm, 100 cm, and 200 cm. The simulated power requirements to keep the cell around 600 °C is shown in table 6.3. Now we need to compare this simulated value to the Joule heating power generated in the electrolyte.

This is achieved by assuming the power generated is given by the relation $P = I^2 R$ where I is the applied current, and R is the electrolyte resistance. Using the relations $I = jA$, $R = \frac{L}{\sigma A}$, and $A = \pi r_{AC}^2$, the power is expressed as $P = \frac{j^2 L \pi r^2}{\sigma}$, where L is

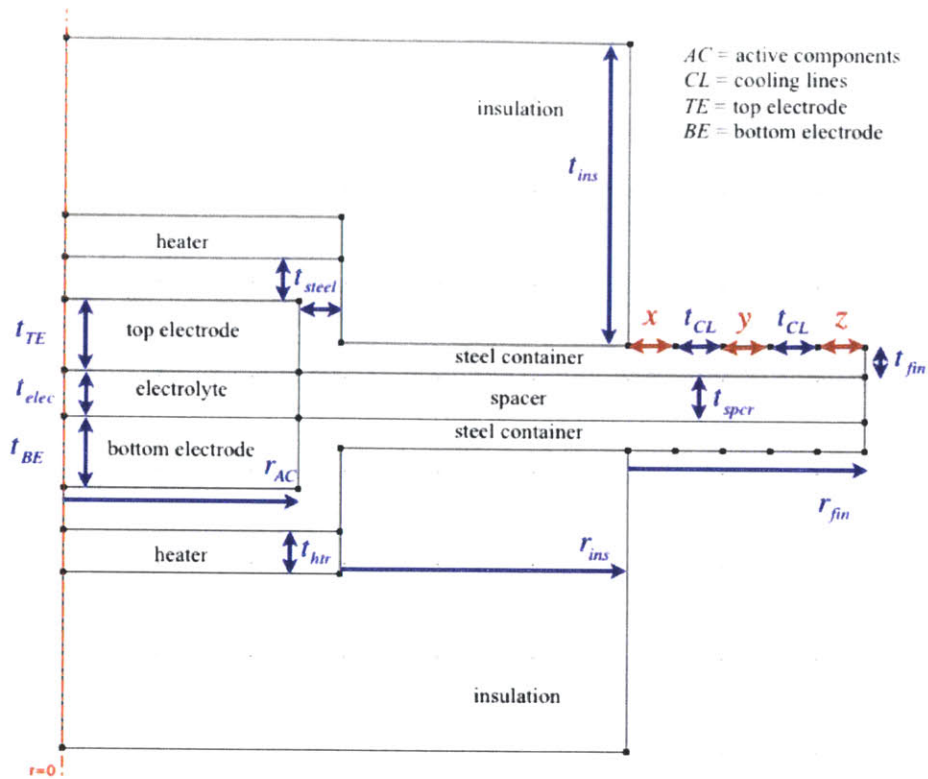


Figure 6-3: Radial cross-section of simplified Argonne National Laboratory cell design used in the simulations.

Dimension #	(cm)
r_AC	5
t_steel	0.9
t_elec	1
t_BE	1.5
t_htr	0.9
t_ins	6.5
t_CL	1
t_spcr	1
x	1
y	1
z	1
r_AC	5
r_ins	6.1
r_fin	0.63

Table 6.2: Cell dimensions used in the thermal simulation of the cell design shown in figure 6-3.

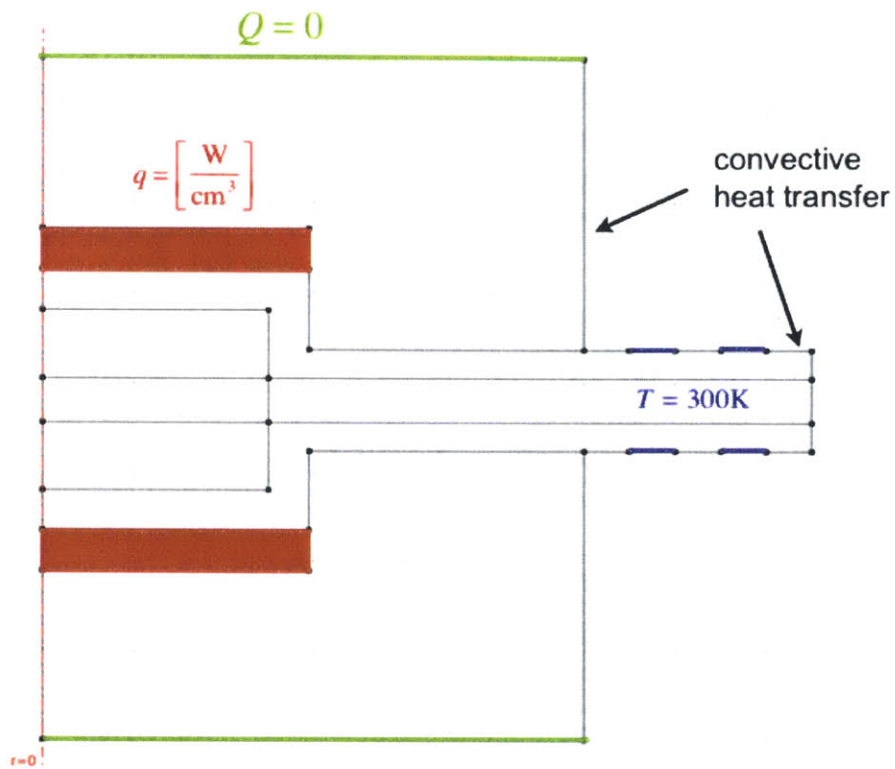


Figure 6-4: Thermal boundary conditions for the 20Ah Argonne National Laboratory cell geometry.

r_{AC} [cm]	P[W]
25	6,600
100	8,600
200	15,300

Table 6.3: Simulated power for the three radii of interest.

the electrolyte thickness, and σ the electrolyte conductivity. By setting the thickness L to be 1 cm, and the conductivity 2 S/cm, we plotted the joule heating power P (fig. 6-5) as a function of cell radius r_{AC} for three different current densities $j = 250, 500, 1000$ mA/cm².

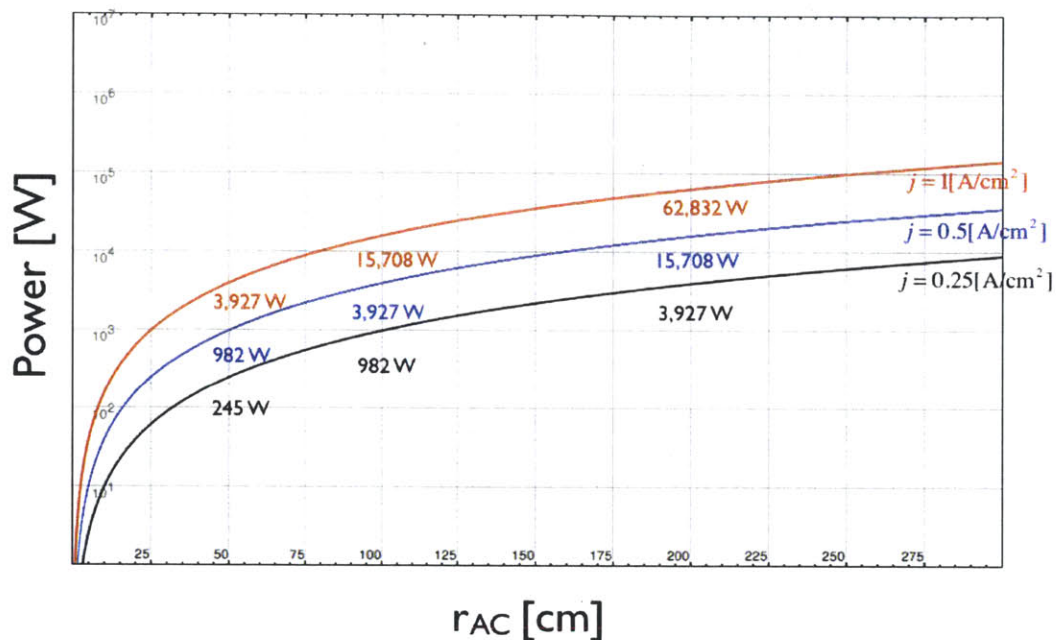


Figure 6-5: Joule heating generated as a function of cell radius for three different current densities.

Comparing the simulated values in table 6.3 with figure 6-5, we see that the 100 cm radius cell can start reaching a self-heated size if the current density is operated between 500 and 1000 mA/cm². This is too high of a current density for a Ca-Bi chemistry, which we saw from the chemical diffusivity sensitivity analysis in figure 1-23. This, along with thermal expansion issues³, added to the confidence of abandoning such cell geometry.

6.3.2 MIT Cell Geometry

To counter the deleterious issues presented with the Argonne National Laboratory cell geometry, a new cell (fig. 6-6) design was created. The new design, which I am

³The thermal gradients required for this geometry caused the 20-Ah cells to bow outward, which made the cell unstable over time.

calling the MIT cell geometry in this thesis, was engineered to minimize thermal gradients in the cell. The cell dimensions were similar to those in table 6.2 with the exception of the top insulation being 2.5 cm thick, and the bottom and side insulation 5 cm. At this point in time we were testing chemistries whose operating temperature was 450 °C. To keep it at this temperature, the power requirement was calculated to be roughly 36 W, again being in excellent agreement with the power measured in the laboratory. This new power requirement is an order of magnitude smaller, and allows for the possibility of a self-heated cell with convenient dimensions, which are currently being investigated.

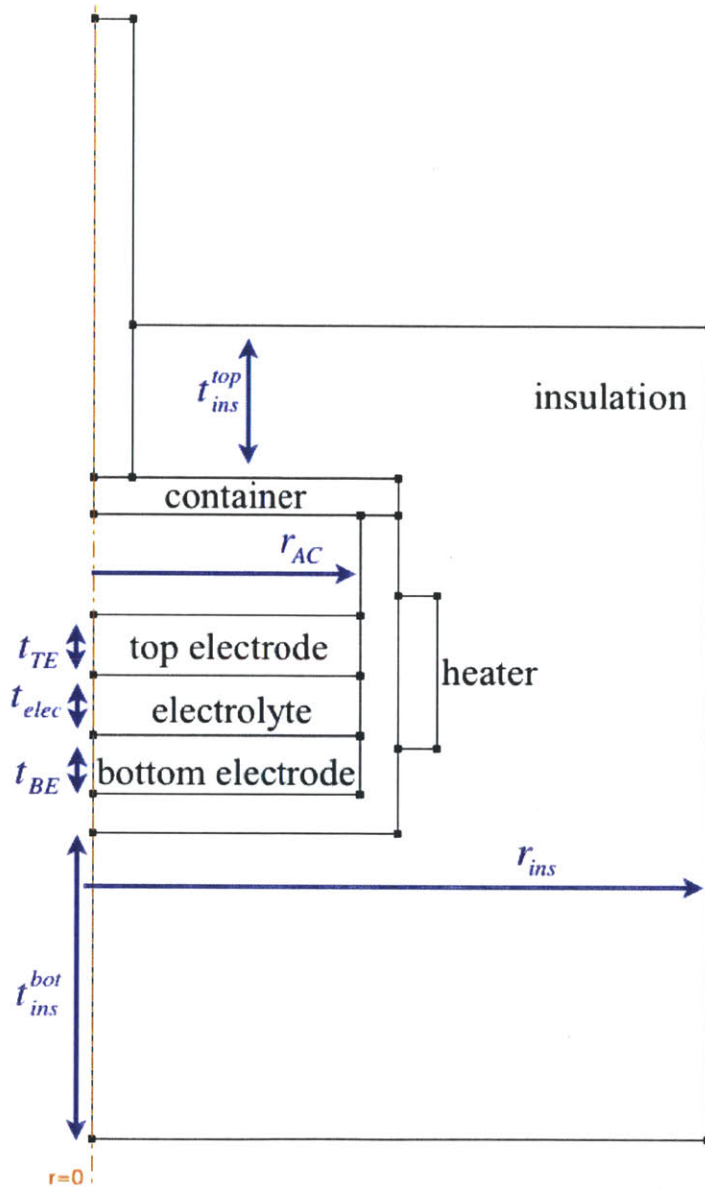


Figure 6-6: Radial cross-section of simplified MIT cell design used in the simulations.

6.4 Electrode Mixing Simulations

To optimize the performance and gain insight on the transport properties of these liquid electrodes, the governing heat, momentum, and mass transport conservation equations derived in section 6.2 were solved using the boundary conditions mentioned below. The calculated diffusion coefficients were used in two separate convection-diffusion 2D radial simulations using Ca-Bi. These simulations are imperative to understanding the mixing behavior of the electrodes under thermal gradients, which can ultimately lead to increasing the electrode capacity.

6.4.1 Uniform Temperature Gradient

Figure 6-7 is a radial cross section of a simple liquid electrode interest along with the thermal boundary conditions required to induce convection. The boundary conditions for fluid flow are no slip ($v = 0$) on the bottom and side of the cell, and slip on top with the characteristics of a liquid-liquid interface.

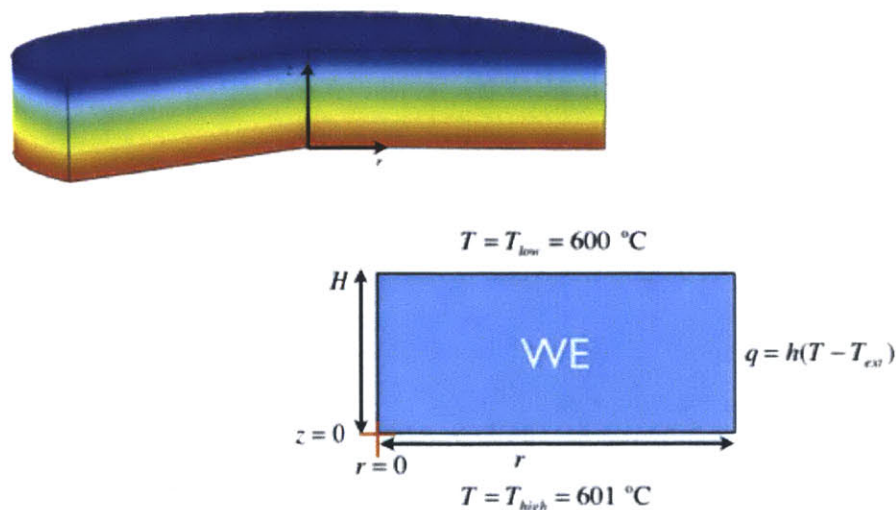


Figure 6-7: Radial schematic with thermal boundary conditions for liquid electrode.

A chemical diffusion coefficient of $6 \times 10^{-5} \text{ cm}^2/\text{s}$ and a current density of $200 \text{ mA}/\text{cm}^2$ was used in the simulation. The flow was allowed to stabilize for the first 500 seconds. Calcium was then introduced uniformly through the top for an hour to observe the

mixing behavior enhanced by convection. Figure 6-8 are the simulated results after the hour, and it shows how the induced Rayleigh-Bénard cells had a maximum velocity of 1.4×10^{-3} cm/s, and affected the overall composition profile in the electrode. The flow forced the concentration of calcium to increase at the top of the cell, preferentially near the center and next to the wall. The maximum composition of $x_{\text{Ca}} = 16\%$ was attained at the center, which is not far from the liquidus composition. We want to limit the formation of any intermetallic compound because they will hinder the kinetics of the system, so it's essential to be able to find conditions that will enhance the mixing if we are to operate at these current densities.

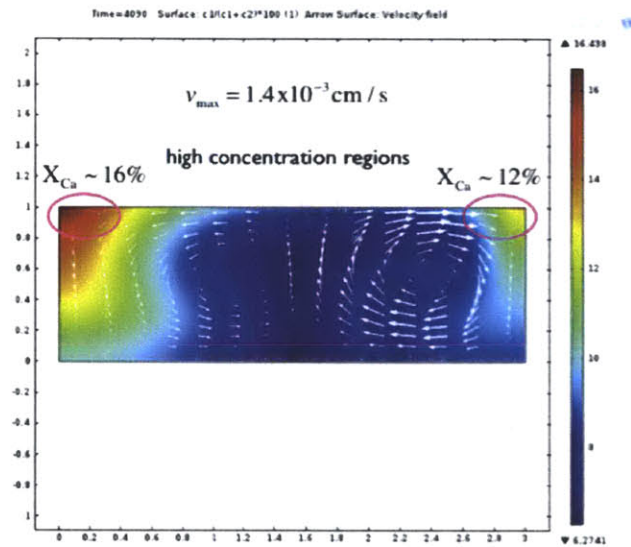


Figure 6-8: Concentration and fluid velocity profile after titrating calcium for an hour into a liquid electrode with a one degree per centimeter thermal gradient.

6.4.2 Nonuniform Temperature Gradient

We decided to change the boundary conditions slightly by adding the equivalent of a cooling line to the bottom of the electrode, and set it to the same temperature as the top of the electrode (600 °C). It was added because it made intuitive sense that fluid flow would be perturbed because the results in figure 6-8 showed that to be the region where the fluid was flowing dominantly upwards. The new numerical results show a significant different concentration profile, this time with the maximum

concentration occurring near the side wall as a consequence of the different induced flow. This time the maximum velocity was 0.19 cm/s, two orders of magnitude faster resulting in the highest concentration being $x_{Ca} = 11\%$, which is 5% less than the first simulation. Also, the concentration range at the end of the pulse for this simulation was 3.6%, significantly less than the first simulation (10.1%) resulting in better mixing. Therefore, we can effectively increase the electrodes capacity by tuning the thermal environment of the cell.

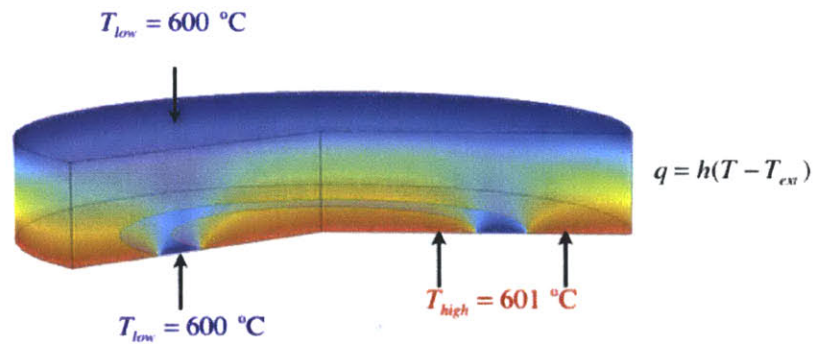


Figure 6-9: New boundary conditions to compare the mixing behavior.

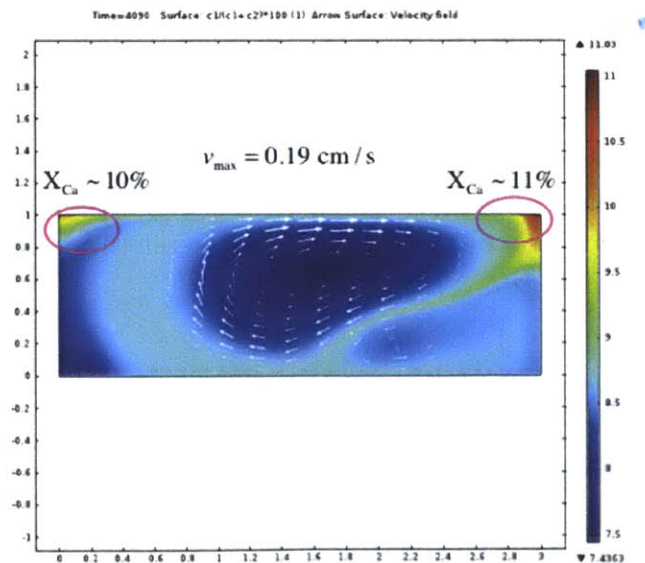


Figure 6-10: Concentration and fluid velocity profile after titrating calcium for an hour into a liquid electrode with the modified boundary conditions seen in figure 6-9.

6.4.3 Dimensionless Numbers

It is no surprise that such a small change in the temperature boundary conditions would generate very different result in the composition profiles. This is because the dominant form of heat transfer in liquid metals is by conduction due to their uniquely high thermal conductivities. As a result, liquid metals tend to have relatively small Prandtl ($\text{Pr} = \frac{\nu}{\alpha}$) numbers, usually ranging between 10^{-3} and 10^{-2} [20], which is a dimensionless number relating the modes of heat transfer by convection to that of conduction. This makes the thermal boundary layer thickness greater than the momentum boundary layer, causing heat to diffuse faster by means of conduction rather than convection. The Schmidt ($\text{Sc} = \frac{\nu}{D}$) number for liquid metals, which relates momentum mass transfer to diffusion mass transfer, is usually in the 10 to 10^2 range [10]. This is considered high for liquids, but it's a property of liquid metals stemming from their high kinematic viscosity, so transport by convection will dominate over diffusion if simultaneous momentum and mass diffusion convection processes are happening. If convection is to dominate diffusion, the liquid metal has to be flowing under an appropriate gradient, which will rely on other parameters.

One of those parameters is the Rayleigh number (eq. 6.23), a dimensionless variable associated with the heat transfer within a liquid. It is the product of the Grashof number, which relates buoyant and viscous forces, and the Prandtl number. Convection will trump conduction as a transport mode if the Rayleigh number

$$\text{Ra} = \text{Gr} \cdot \text{Pr} = \frac{g\beta}{\nu\alpha}\Delta TL^3, \quad (6.23)$$

of a fluid surpasses a critical value (≈ 1100). g is gravity, β is the thermal expansion coefficient, ΔT is the difference in temperature along the characteristic length L , ν is the kinematic viscosity, and α the thermal diffusivity of the fluid. An order of magnitude estimate for the Ra number applicable to for our system can be computed if the characteristic length L is known. This can be difficult to define depending on the gradient's direction that is driving the flow. Nonetheless, we can write an expression for the Ra number generalized to our system using appropriate values for

the material properties of liquid bismuth.

Literature values for the variables in equation 6.23 are needed to derive a Ra number equation for a bismuth liquid electrode. The thermal expansion coefficient of liquid bismuth [126] can be taken to be approximately $k = 10^{-5} \text{ K}^{-1}$, but can vary with other liquid metals [127–129]. Sobolev [130] recently published a scientific report with values for the thermal diffusivity of liquid bismuth to be $\alpha = 10^{-2} \text{ cm}^2/\text{s}$, and the dynamic viscosity $\mu = 10^{-3} \text{ Pa}\cdot\text{s}$ for our temperature of interest. The density of liquid bismuth is roughly $10 \text{ g}/\text{cm}^3$, so the kinematic viscosity was taken to be $\nu = 10^{-3} \text{ cm}^2/\text{s}$. Plugging all these values into equation 6.23 gives the Rayleigh equation specific to liquid electrodes

$$\text{Ra} \approx 10[\text{cm}^{-3}\text{K}^{-1}]\Delta TL^3 \quad (6.24)$$

Equation 6.24 defines whether or not a thermal gradient ΔT across a bismuth liquid electrode of length L will induce convection. The electrodes used in the simulations are 1 cm in thickness, but one cannot assume this to be the characteristic length because the convective boundary condition along the side wall along is a function of its aspect ratio and will enhance it. This was evident in the simulations. For a thermal difference of $\Delta T = 1 \text{ K}$ and $L = 5 \text{ cm}$, the Ra numbers begin to reach the critical area where the onset of natural convection starts to dominate transport [131–133]. Once convection dominates, there will be simultaneous momentum and diffusive transport mechanisms active, which will make the Schmidt number important.

We can also use equation 6.24 to predict if the electrodes used in the liquid experiments (table 4.1) will experience convective issues. Assuming the same temperature gradient for the length $L = 1 \text{ cm}$, the calculated Ra number is 10, hence convection is negligible. This was also confirmed with FEA simulations using the same boundary conditions shown in figure 6-7 on the small electrode geometry, which show the maximum velocity attained from convection was on the order of $10^{-6} \text{ cm}^2/\text{s}$. We can take this value and do an order of magnitude estimate of the relative impact convection has on transport compared to diffusion. To do this, let's imagine a small

infinitesimal volume originating from the electrode-electrolyte interface that travels away in the liquid bismuth at the velocity equal to the numerical value of 10^{-6} cm²/s for a time $t = 10^3$ s. After the time is over, the infinitesimal volume has traveled a linear distance of $L_c = v_c t_p = 10^{-3}$ cm. The equivalent diffusive characteristic length is the penetration depth equation, $L_d = \sqrt{6Dt_p}$. If we use a chemical diffusivity⁴ value of $D = 10^{-4}$, we get a diffusive distance of $x_p = 0.8$ cm. So, we can conclude from this order of magnitude analysis and simulation results that diffusion transport overwhelmingly dominates convection within our timescale t_p of interest.

Through simulation we can predict fluid velocity magnitudes associated with different boundary conditions, therefore we can check to what degree convection affects the overall transport by defining the following ratio:

$$\psi \equiv \frac{L_c}{L_d} = \frac{v_c t_p}{\sqrt{6Dt_p}} = \frac{v_c}{\sqrt{6D}} t_p^{1/2}. \quad (6.25)$$

If $\psi \ll 1$, convection can be neglected, but if $\psi \gg 1$, then convection dominates the mode of transport displacing a fluid during the time t_p . Equation 6.25 can also be used to estimate the time when convective transport becomes important, by assuming this occurs when $\psi = 0.1$ and solving for t_p . Doing so gives us a time

$$t_p = \frac{6D}{v_c^2} \psi^2, \quad (6.26)$$

and solving it gives us a time of 2.5×10^6 s, which is around 70 days. This time is too long for convection to be of any real influence on the transport properties of the electrodes used to measure the chemical diffusivity of calcium in liquid Ca-Bi.

The same analysis can be done using the calculated velocities of the two MIT 20-Ah simulations, which were $v_{c1} = 1.4 \times 10^{-3}$ cm/s first simulation (fig. 6-7), and $v_{c2} = 0.19$ cm/s for the second (fig. 6-9). For the operating time of an hour, the calculated ψ values were 3.4, and 465 respectively which are much greater than one signifying convection will drastically affect the overall transport. This is clearly evident when the concentration difference of both simulations at the end of the hour run are compared.

⁴The experimental chemical diffusivity values measured range between 510^{-5} and 110^{-4}

The model with the modified thermal boundary conditions resulted in a faster velocity, and the electrode was indeed better mixed.

6.4.4 Induced Velocity as a Function of Geometry

6.5 Phase Field Simulations

Phase field was the first simulation work I did when I first started working on modeling LMBs. This last section describes the transport work done using the phase field method to model the simultaneous motion of three liquid layers of a LMB during cycling. To the best of our knowledge, this has never been done before and was achieved with the use of Heaviside step functions.

6.5.1 Phase Field Theory

There are a handful of numerical algorithms within FEA one can use to model the motion of an interface, one of those being phase field. The phase field method indirectly tracks the boundary between two phases by solving the evolution of the conserved order parameter ϕ , which is governed by the Cahn-Hilliard [134] differential equation. In order to do so, the free energy density at a position ($f(r)$) is written as a function of ϕ , $f(r) = f(\phi(r), \nabla\phi(r))$. In the absence of gradients, the homogeneous free energy density⁵ is $f^{\text{hom}}(\phi) = f(\phi, \nabla\phi = 0)$. Expanding the free energy density about the order parameter and its gradient, and integrating it over the entire system gives the following approximation for the molar free energy [18, 135–137]

$$F(\phi) = N_o \int_V f(\phi, \nabla\phi) dV = N_o \int_V \left[\xi f^{\text{hom}}(\phi) + \frac{\epsilon}{2} |\nabla\phi|^2 \right] dV. \quad (6.27)$$

ξ and ϵ are phase field variables that are adjusted to control the interface thickness ($\delta \sim \sqrt{\epsilon/\xi}$) and surface energy ($\gamma \sim \sqrt{\epsilon\xi}$). The first term in equation 6.27 is the homogeneous free energy, and the second term is the energy contribution from gra-

⁵The molar free energy $F(\phi)$ is calculated from $F(\phi) = N_o \bar{V} f^{\text{hom}}(\phi)$, where N_o is the number of atoms in the local volume \bar{V}

dients in ϕ . The field variable ϕ in the homogeneous free energy evolves to take the value of either +1 or -1, which differentiates the two phases of interest continuously across the interphase.

In order to model an electrochemical system consisting of three phases, the free energy functional in equation 6.27 had to be modified to include the electrostatic contribution to the free energy ($\sum_i Fz_i c_i \Phi$) of species c_i having charge z_i that is influenced by the electric potential Φ . Doing so gives us the free energy functional

$$F(\phi) = N_o \int_V \left[\xi f^{\text{hom}}(\phi) + \frac{\epsilon}{2} |\nabla \phi|^2 + \sum_i Fz_i c_i \Phi \right] dV \quad (6.28)$$

which is valid throughout the entire electrochemical system assuming the electrostatic contribution is a function of the order parameter ϕ .

The electrostatic energy contribution is dominant in the electrolyte because ions are influenced by the electrochemical potential difference between the two electrodes, therefore the ionic properties must be written as functions of the evolved field variables, the same way Wanida [138] did for the analysis of Fe-FeO. For simplicity, the electrolyte was assumed to be pure molten CaCl_2 . Defining $\phi = 1$ to be in the electrolyte, we can write the calcium and chlorine atomic fractions as $x_{\text{Ca}^{2+}} = \frac{1}{3}(2 - \phi)$ and $x_{\text{Cl}^-} = \frac{1}{3}(\phi + 1)$. Assuming the molar mass of the molten salt⁶ M is linear, we can write the ionic concentrations in the electrolyte as⁷

$$c_{\text{Ca}} = \frac{\rho}{3M}(2 - \phi) \quad (6.29)$$

$$c_{\text{Cl}} = \frac{\rho}{3M}(\phi + 1) \quad (6.30)$$

These concentrations are substituted in equation 6.28 to obtain the free energy functional

⁶ $M = M_{\text{Ca}}x_{\text{Ca}} + M_{\text{Cl}}x_{\text{Cl}}$, where M_{Ca} and M_{Cl} are the atomic masses of calcium and chlorine.

⁷For simplicity, we will omit the ionic charge number in the variable.

$$F(\phi) = N_o \int_V \left[\xi f^{\text{hom}}(\phi) + \frac{\epsilon}{2} |\nabla\phi|^2 + \frac{F z_{\text{Ca}} \rho \Phi}{3M} (2 - \phi) + \frac{F z_{\text{Cl}} \rho \Phi}{3M} (\phi + 1) \right] dV, \quad (6.31)$$

which is specific for the CaCl₂ molten salt system.

Since the field variable ϕ is a measure of particle number, the variational derivative of $F(\phi)$ with respect to ϕ is the chemical potential for the system:

$$\mu = \frac{\delta F}{\delta \phi} = N_o \left[\xi \frac{\partial f^{\text{hom}}}{\partial \phi} - \epsilon^2 \nabla^2 \phi - \frac{F \rho \Phi}{3M} (z_{\text{Cl}} - z_{\text{Ca}}) \right] \quad (6.32)$$

Letting $z_{\text{Ca}} = +2z$ and $z_{\text{Cl}} = -z$, the chemical potential simplifies to

$$\mu = \frac{\delta F}{\delta \phi} = N_o \left[\xi \frac{\partial f^{\text{hom}}}{\partial \phi} - \epsilon^2 \nabla^2 \phi - \frac{z F \rho \Phi}{M} \right], \quad (6.33)$$

with z being a dummy variable that allows the differentiation between the molten salt electrolyte and liquid metal. z takes the value of one in the electrolyte, and zero in the metal, so to do this the principle of electroneutrality is invoked:

$$\sum_i z_i c_i = z_{\text{Ca}} c_{\text{Ca}} + z_{\text{Cl}} c_{\text{Cl}} = 0 \rightarrow z_{\text{Ca}} = -z_{\text{Cl}} \left(\frac{1 + \phi}{2 - \phi} \right). \quad (6.34)$$

One can assume $z_{\text{Cl}} = -1$ through the entire system because it only exists in the electrolyte, and since $z_{\text{Ca}} = +2z$, we can write z as

$$z = \frac{1 + \phi}{2(2 - \phi)}. \quad (6.35)$$

Substituting equation 6.35 into equation 6.33 yields the full chemical potential

$$\mu = N_o \left[\xi \frac{\partial f^{\text{hom}}}{\partial \phi} - \epsilon^2 \nabla^2 \phi - \frac{F \rho \Phi}{2M} \left(\frac{1 + \phi}{2 - \phi} \right) \right], \quad (6.36)$$

which is valid in both electrolyte and metal.

6.5.2 Derivation of Custom Source Term

The electrostatic term in the chemical potential in equation 6.36 was added as a source modification to the governing equations in COMSOL. We did this by rewriting the chemical potential as $\mu = \mu^\circ + \mu_{el}$, where

$$\mu_{el} = \frac{N_o F \rho \Phi}{2M} \left(\frac{1 + \phi}{2 - \phi} \right). \quad (6.37)$$

We can compute the added flux using the relation $J_{el} = \gamma_m \nabla \mu_{el}$ where γ_m is the mobility. Taking the divergence of J_{el} gives

$$\frac{\partial \phi}{\partial t} + \nabla \cdot J = 0 = \frac{\partial \phi}{\partial t} + \nabla \cdot (J^\circ + J_{el}) \Rightarrow \frac{\partial \phi}{\partial t} + \nabla \cdot J^\circ = -\nabla \cdot J_{el} = R_{PF}, \quad (6.38)$$

where R_{PF} is the source term contribution from the electrostatic free energy term added as a modification to COMSOL. The final result is shown below in equation 6.39:

$$\begin{aligned} R_{PF} = & \frac{2\Phi \frac{\partial \phi^2}{\partial r}}{(\phi - 2)^2} - \frac{(\phi + 1) \frac{\partial^2 \Phi}{\partial r^2}}{(\phi - 2)} - \frac{2 \frac{\partial \phi}{\partial r} \frac{\partial \Phi}{\partial r}}{(\phi - 2)} - \frac{(\phi + 1) \frac{\partial^2 \Phi}{\partial z^2}}{(\phi - 2)} - \frac{2 \frac{\partial \phi}{\partial z} \frac{\partial \Phi}{\partial z}}{(\phi - 2)} - \\ & \frac{\left(\frac{\Phi \frac{\partial \phi}{\partial r}}{(\phi - 2)} + \frac{(\phi + 1) \frac{\partial \phi}{\partial r}}{(\phi - 2)} - \frac{\Phi(\phi + 1) \frac{\partial \phi}{\partial r}}{(\phi - 2)^2} \right)}{r} + \frac{2\Phi \frac{\partial \phi^2}{\partial z}}{(\phi - 2)^2} - \frac{\Phi \frac{\partial^2 \Phi}{\partial r^2}}{(\phi - 2)} - \frac{\Phi \frac{\partial^2 \Phi}{\partial z^2}}{(\phi - 2)} - \\ & \frac{2\Phi (\phi + 1) \frac{\partial \phi^2}{\partial r}}{(\phi - 2)^3} - \frac{2\Phi (\phi + 1) \frac{\partial \phi^2}{\partial z}}{(\phi - 2)^3} + \frac{\Phi (\phi + 1) \frac{\partial^2 \Phi}{\partial r^2}}{(\phi - 2)^2} + \frac{\Phi (\phi + 1) \frac{\partial^2 \Phi}{\partial z^2}}{(\phi - 2)^2} + \\ & \frac{2(\phi + 1) \frac{\partial \Phi}{\partial r} \frac{\partial \phi}{\partial r}}{(\phi - 2)^2} + \frac{2(\phi + 1) \frac{\partial \Phi}{\partial z} \frac{\partial \phi}{\partial z}}{(\phi - 2)^2} \end{aligned} \quad (6.39)$$

The surface tension γ is added to the Navier-Stokes equations as a body force, defined as the product of the chemical potential and the gradient of the phase field variable.

6.5.3 Phase Field Modification for Three Phases

The phase field method is only applicable using two phases, but we were still able to use the theory to model the motion of two boundaries simultaneously, corresponding to three coexisting phases. Figure 6-11 is a radial cross-section of the three phases of interest in modeling. To do so, two separate phase field partial differential equations were solved; one for the Ca-Mg and electrolyte, and the other for the bismuth and electrolyte. The use of Heaviside step functions were employed to distinguish between the two volume fractions

$$V_{f1} = flc2hs(\phi) \quad (6.40)$$

$$V_{f2} = flc2hs(-\phi), \quad (6.41)$$

which have the property shown in figure 6-12; it's zero for negative values of the phase field variable ϕ , and one for positive values. It's basically a step function, but special because the first two derivatives are continuous. The trick allowing the use of two separate phase field governing equations lies in writing the density of the three phases as a function of volume fractions, which requires the use of a third Heaviside step function that is dependent on geometry. The density was then written as

$$\rho = \rho_{\text{salt}} \cdot V_{f1} + [\rho_{\text{Bi}} + (\rho_{\text{Ca-Mg}} - \rho_{\text{Bi}}) \cdot flc2hs(z - a)] \cdot V_{f2}. \quad (6.42)$$

A quick check confirms the density is indeed differentiated by the Heaviside step functions (fig. 6-13).

6.5.4 Results

Ohm's law and Fourier's law of heat conduction were also coupled with the phase field equations. The wetting angle was fixed at 45° , and the surface tension was chosen to be $0.5 \text{ N}\cdot\text{m}^2$. Figure 6-14 shows the three coexisting phases as the simulation starts. After 50 seconds, the bottom electrode has grown at the expense of the top electrode

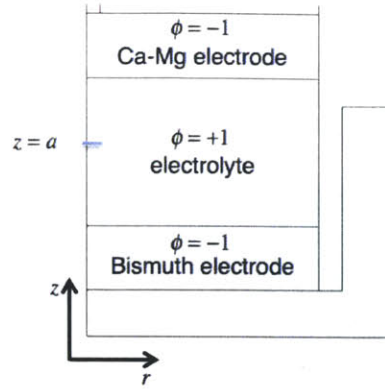


Figure 6-11: Cell schematic used in the phase field model with the appropriate conserved order parameter values.

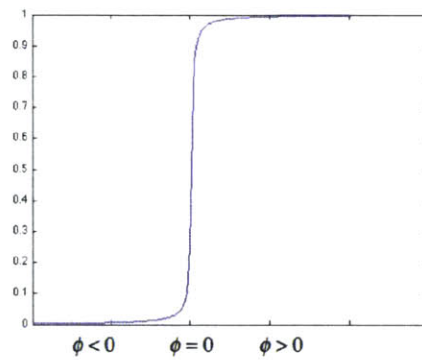


Figure 6-12: Heaviside function used to differentiate the volume fractions of the different phases.

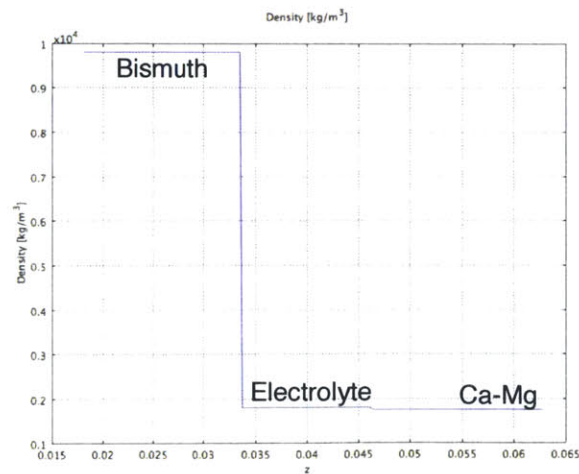


Figure 6-13: The density from equation 6.42 self-segregates with the help of Heaviside step functions.

as seen in figure 6-15, with the two interfaces moving coherently. The trick with Heaviside functions has proven to be successful, and to our knowledge it was the first time phase field has been used to model the kinetics of three different phases.

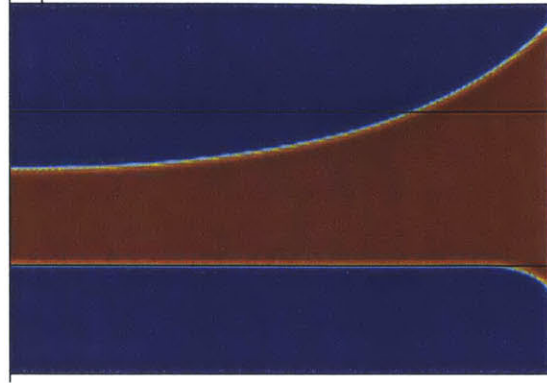


Figure 6-14: Simulation of three phases and two boundaries simultaneous moving at a time $t = 2$ s.

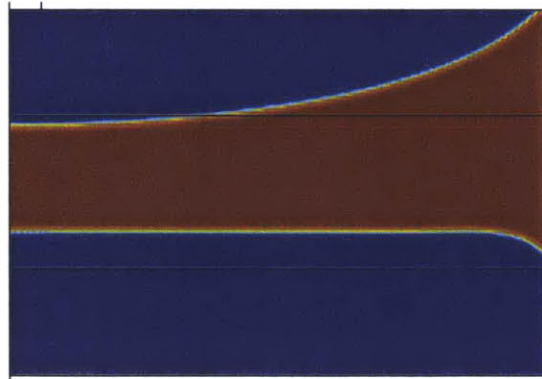


Figure 6-15: Simulation of three phases and two boundaries simultaneous moving at a time $t = 50$ s. Compared to figure 6-14, the bismuth electrode has grown at the expense of the calcium-magnesium.

Mass has to be conserved, so an integration coupling variable was used to calculate the stability of the mass as it evolves in the entire system. Figure 6-16 shows that mass was indeed conserved during the run of the simulation since the percent difference of its variation was less than 1%.

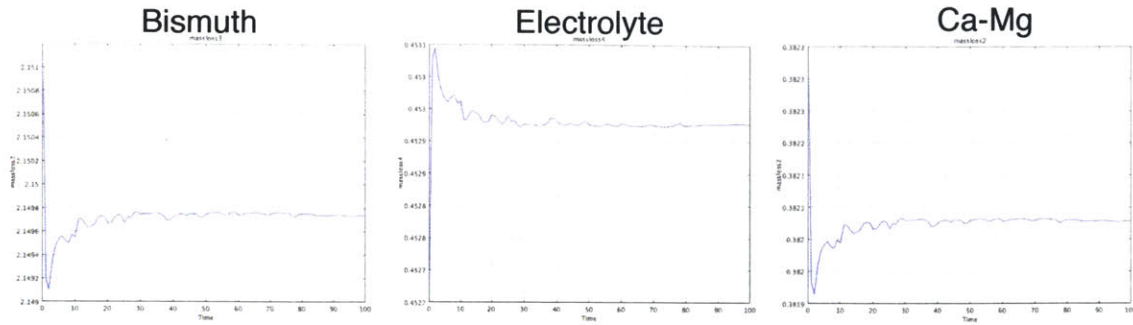


Figure 6-16: Mass loss of each component as a function of time calculated using an integration coupling variable over the entire system. The variation was less than 1% signifying mass conservation.

6.6 Conclusion

The finite element method is a great tool for better understanding the kinetics of LMBs. Phase field is only applicable to two phases because the phase field variable ϕ can only evolve to two values, unless you can utilize the geometry to write out the density as a function of the three phases. This is exactly what was done in order to use the phase field method to model the three coexisting phases inside a LMB during cycling. The thermal model using the Argonne National Laboratory cell schematic was far from being able to self-heat because of the huge thermal gradients that arose from its design. Thermal cycling also caused the cell container to mechanically expand over time, changing the overall structure of the cell. On the other hand, the MIT cell design proved to be more energy efficient because it requires a power density that is an order of magnitude less than the previous design to maintain it at temperature. The mixing results show how one can begin to engineer the insulation surrounding the cell in order to change the temperature profile, which will directly change the flow pattern. Under the same gradient, the velocity increased with electrode height and was more distinct at larger radii. The increase of convection as the system scales up in size is good for LMBs, but not for doing sensitive experiments such as measuring the chemical diffusivity. To measure the chemical diffusion coefficient, we need very small capillaries as predicted by the simulation results. The key is to have full control of the temperature gradients, so one can then control the flow inside a cell.

Chapter 7

Conclusion

This thesis outlines the derivation of a new technique that was created to measure the chemical diffusivity in liquid alloys. It was created because the previous techniques used to measure such phenomena contain many sources of error. The main source of error is primarily the effect of natural convection arising from thermal gradients that are unavoidable. Besides the inherent errors, the other methods require the liquid metal to be quenched in order to examine the composition profile, and cannot be applied to extremely reactive metals. This new electrochemical method offers the possibility to do kinetic measurements on reactive metals. This was demonstrated in this thesis by calculating the chemical diffusivity of calcium in liquid bismuth from the electrochemical data collected specifically for this purpose. This is the first time such measurements have been performed, and we are pleased to report the first diffusivity values of calcium in the liquid state. The chemical diffusion coefficient has been shown to be extremely important in the optimization of LMBs. Depending on the value, LMBs can be operated under very different kinetic conditions. In LMBs, convection is not necessarily an issue because it helps increase the capacity of the liquid electrodes. If one can fully control the thermal gradients inside a LMB, then convection can be optimized to enhance the mixing behavior. This will keep the surface concentration from reaching the liquidus concentration, which will in return increase the operating times of these liquid batteries.

Appendix A

Energy Storage Technologies

A.1 Pumped-Hydro Storage

Pumped-hydro storage is the most mature and economical energy storage technology, costing roughly \$100/kWh [11]. In pumped-hydro, water is pumped up to a higher elevation reservoir during off-peak hours, and allowed to flow back down through a turbine generator during peak hours. The main disadvantage of this technology is geographical limitation; huge reservoirs at higher elevations are needed. Because of this, the capital cost can vary depending on the location.

A.2 Sodium-Sulfur (NaS) Battery

First researched by Ford Motor Co., the NaS battery is composed of a sodium anode, sulfur cathode, and a solid beta-alumina electrolyte/separator [139]. It can achieve an open circuit voltage (OCV) of 2.075 V at 350 °C, but the grid-scale limitation is the high capital cost, more than \$400/kWh [3] which makes this system economically unsuitable for large scale storage.

A.3 Lead-Acid Battery

Lead-acid batteries are the most mature electrochemical technology for energy storage. Limitations in using this battery chemistry for large scale storage applications lie in the relative low specific energy density, the short life (~ 1000 cycles) when deeply discharged, unstable performance at low temperatures (< 0 °C), and the high capital cost comparable to NaS [3].

A.4 Lithium-Ion Battery

Although lithium-ion batteries have high energy and power densities, their high capital costs (greater than \$1000/kWh), potential for thermal-runaway, and need for specialized charging electronics make them unsuitable for large-scale energy storage [140].

A.5 Flywheels

Flywheels store mechanical energy in the rotational inertia of a disk. Flywheels boast high power densities and fast response times, but lack the energy density for the long charge-discharge cycles required by grid-scale energy storage. [140].

Appendix B

Error Function Related Equations

Error Function - erf(x)

$$\operatorname{erf}(x) = \frac{2}{\sqrt{\pi}} \int_0^x e^{-s^2} ds \quad (\text{B.1})$$

$\operatorname{erf}(x)$ is a gaussian integral with the limits $\operatorname{erf}(0)=0$ and $\operatorname{erf}(\infty)=1$

Complimentary Error Function - erfc(x)

$$\operatorname{erfc}(x) = 1 - \operatorname{erf}(x) = 1 - \frac{2}{\sqrt{\pi}} \int_0^x e^{-s^2} ds \quad (\text{B.2})$$

$\operatorname{erfc}(x)$ has the limits $\operatorname{erfc}(0)=1$ and $\operatorname{erfc}(\infty)=0$

Integral of Complimentary Error Function ierfc(x)

$$\operatorname{ierfc}(x) = \frac{2}{\sqrt{\pi}} \int_{\infty}^x \operatorname{erfc}(s) ds = \frac{1}{\sqrt{\pi}} \exp(-x^2) - x[1 - \operatorname{erf}(x)] \quad (\text{B.3})$$

In the limit as $x \rightarrow 0$, $\operatorname{ierfc}(x) \rightarrow \frac{1}{\sqrt{\pi}}$

Appendix C

Sensitivity Analysis on $\frac{dx_A}{d\sqrt{t}}$

$$\frac{dx_A}{d\sqrt{t}} = \frac{2n_B j_0 V}{z_A F \sqrt{\pi \tilde{D}_A} \left(n_B + n_A^0 + \frac{2j_0 V \sqrt{t}}{z_A F \sqrt{\pi \tilde{D}_A}} \right)^2} \quad (\text{C.1})$$

To show how this differential will vary, we will use the experimental variables for 5% calcium (A=Ca) in bismuth (B=Bi) at 575 °C.

They are: $n_{\text{Bi}} = 5.2 \times 10^{-3}$ [mol], $n_{\text{Ca}}^0 = 2.74 \times 10^{-4}$ [mol], $z_{\text{Ca}} = 2$, $V = 0.1198$ [cm³], $F = 96485$ [C/mol], $\tilde{D}_{\text{Ca}} = 7 \times 10^{-5}$ [cm²/s], and $j_0 = 5, 10, 15, 20$ [mA/cm²].

Figure C-1 shows how the rate varies over the duration of the pulse, the longest time corresponding to the smallest current density. The percent differences were 0.68%, 0.98%, 1.21%, 1.37%, for $j_0 = 5, 10, 15, 20$ [mA/cm²] respectively. We can conclude that this value is indeed negligible and we can further approximate equation C.1 to be

$$\frac{dx_A}{d\sqrt{t}} = \frac{2n_B j_0 V}{z_A F \sqrt{\pi \tilde{D}_A} (n_B + n_A^0)^2} \quad (\text{C.2})$$

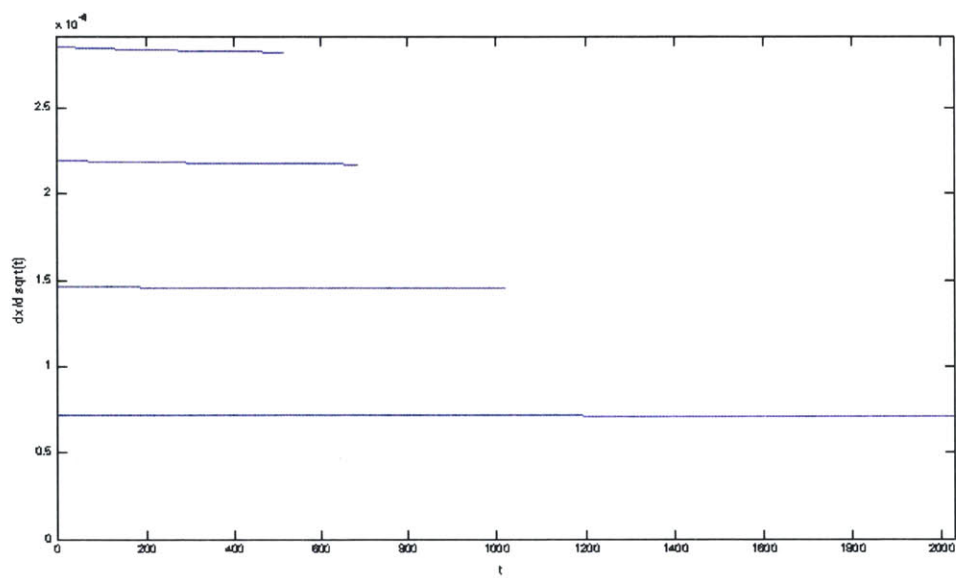


Figure C-1: Sensitivity analysis at various current densities $j_0 = 5, 10, 15, 20$ [mA/cm²].

Appendix D

Experiment Preparation

D.1 Electrolyte

The primary electrolyte used in the experiment was the 38.5% LiCl - 26.5% NaCl - 35% CaCl₂ ternary system. The following salts were used: LiCl (99.995%, Alfa Aesar, Stock No. 13684), NaCl (99.99%, Alfa Aesar, Stock No. 35716), CaCl₂ (99.99%, Alfa Aesar, Stock No. 44280). The salts were mixed together inside an argon glovebox, and placed inside quartz crucibles that were then loaded inside the same stainless steel vessel used in the titration experiments. The vessel was removed from the glovebox and placed inside a 5" Thermo Scientific[®] crucible furnace (max 1200 °C). A vacuum was pulled on the vessel and when the pressure dropped below 10 mTorr, the temperature was ramped to 80 °C at a rate of 1 °C/min and held for 12 hours. The temperature was then ramped to 230 °C using the same rate, and held for another 12 hours under vacuum. Argon was then introduced inside the vessel at a steady flow rate of 25 c.c., and the temperature was ramped up to 700 °C and held for three hours to ensure the electrolyte was melted. The vessel was then cooled to room temperature, and brought inside the glovebox. Inside the glovebox, the electrolyte was broken down to small pieces then blended and stored inside a plastic bottle for future use. Figure D-1 shows the pre-melted salts inside the glovebox.



Figure D-1: Pre-melted salts inside quartz crucibles before

D.2 Electrodes

D.2.1 Reference Electrodes

The reference electrodes used were composed of 35-mol% Ca in Bi, and were prepared by first arc-melting the metals together using an Edmund Bühler GmbH arc melter (figure D-2). The alloy was placed inside the arc-melter as seen in figure D-3, pumped under vacuum for five minutes before introducing argon inside. This was done three times to ensure the alloy was in an inert environment before melting. The RE alloy was melted (figure D-4), and turned over three times and remelted each time, then it was broken up into four small pieces, and remelted again while turning it over another three times to ensure maximum homogeneity.

The alloy was then broken into small pieces. 1.8 g of it was induction melted inside an 8 mm inner diameter boron nitride crucible that was 14 mm in height, along with the tungsten lead to facilitate the cell assembly. Two of these electrodes were made.



Figure D-2: Arcmelter used to prepare the reference electrodes.



Figure D-3: Calcium and bismuth metals inside arc-melter.

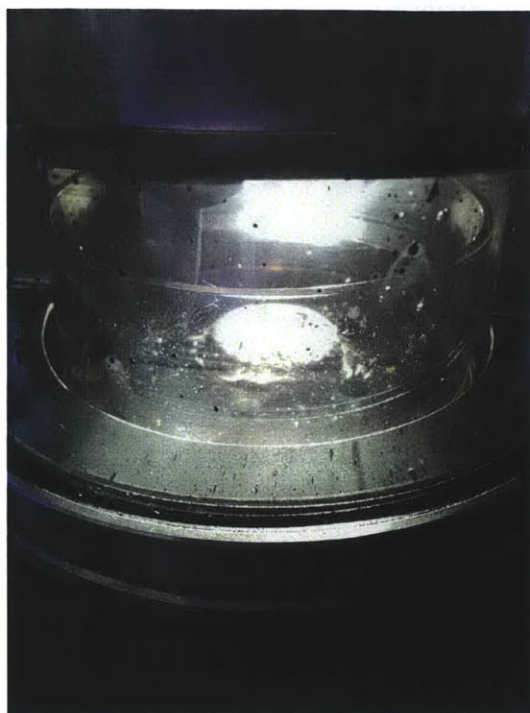


Figure D-4: 35-mol% Ca-Bi alloy premelted inside the arc-melter.

D.2.2 Working Electrode

The working electrode was made of high purity bismuth, and was also induction melted inside a 6 mm inner diameter boron nitride crucible.

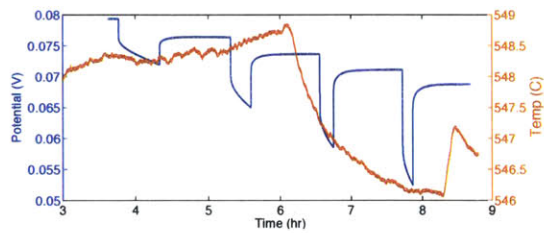
D.2.3 Counter Electrode

The counter electrode was a 15-mol% Ca in Bi, also induction melted inside the glovebox in a boron nitride crucible.

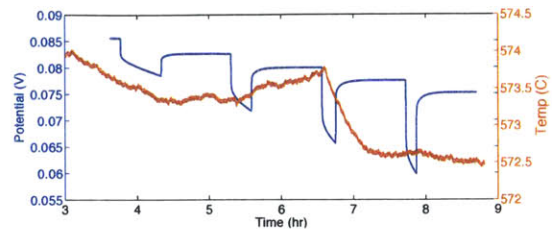
Appendix E

Supplementary Data

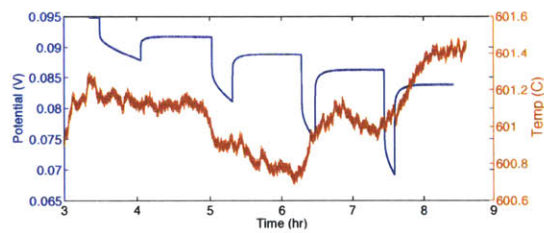
E.1 5% Ca-Bi: Electrode Potential Pulse Sequence and Temperature



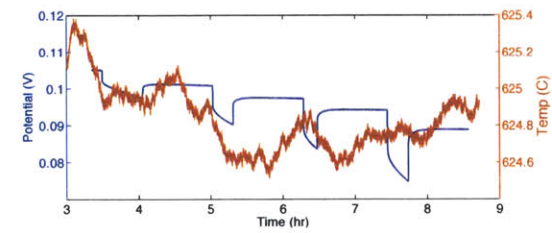
(a) 550 °C



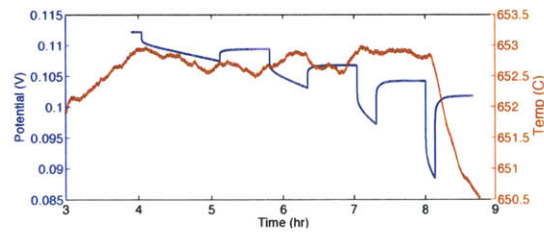
(b) 575 °C



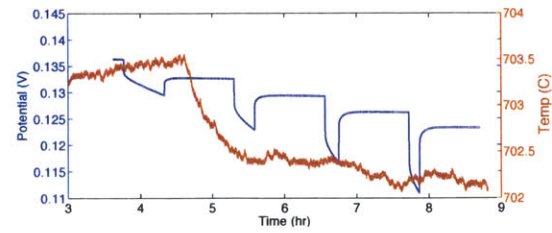
(c) 600 °C



(d) 625 °C



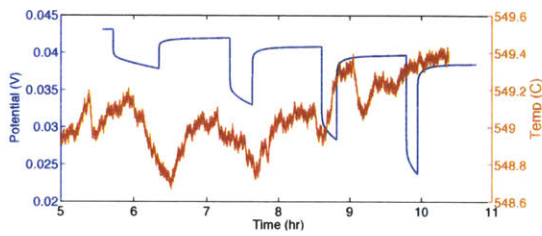
(e) 650 °C



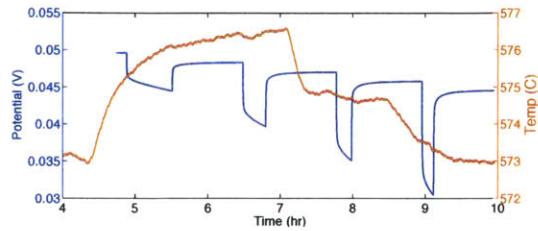
(f) 700 °C

Figure E-1: 5%: Electrode potential and temperature with time.

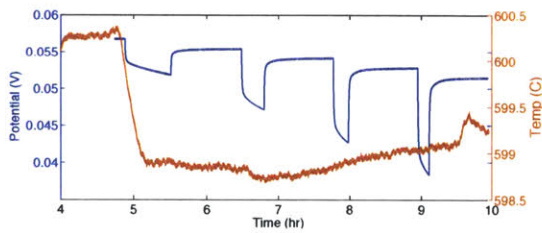
E.2 10% Ca-Bi: Electrode Potential Pulse Sequence and Temperature



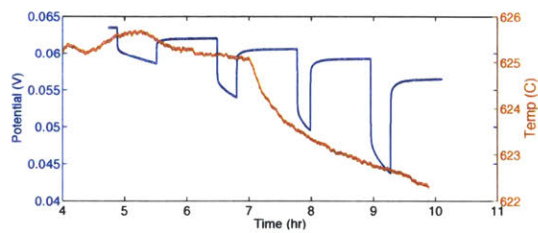
(a) 550 °C



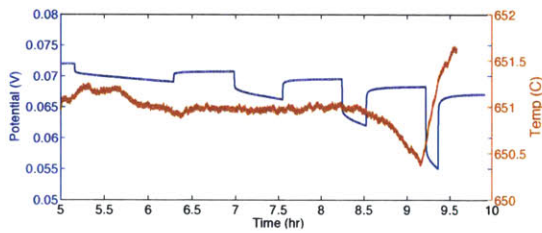
(b) 575 °C



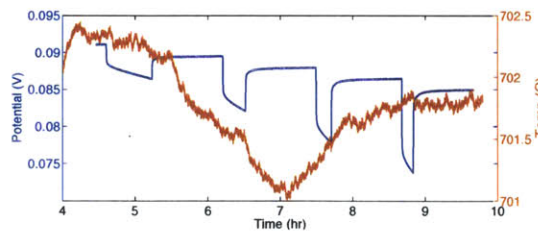
(c) 600 °C



(d) 625 °C



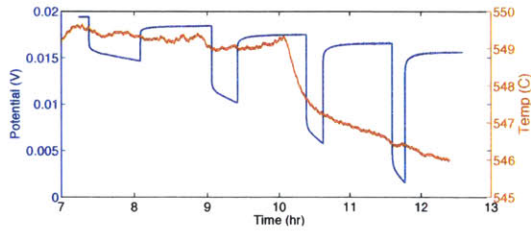
(e) 650 °C



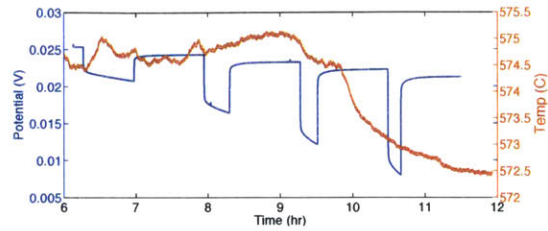
(f) 700 °C

Figure E-2: 10%: Electrode potential and temperature with time.

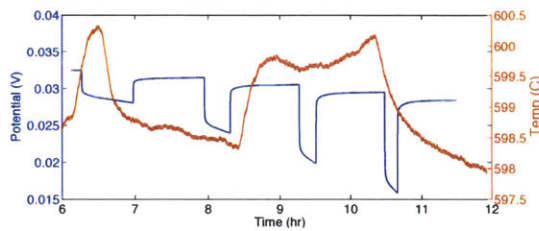
E.3 15% Ca-Bi: Electrode Potential Pulse Sequence and Temperature



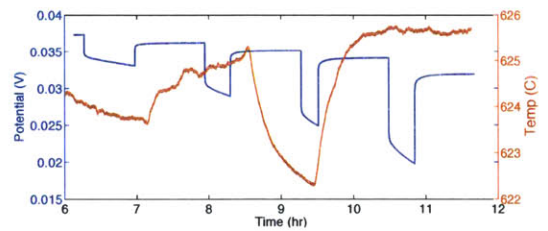
(a) 550 °C



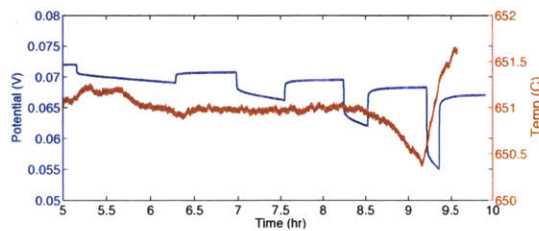
(b) 575 °C



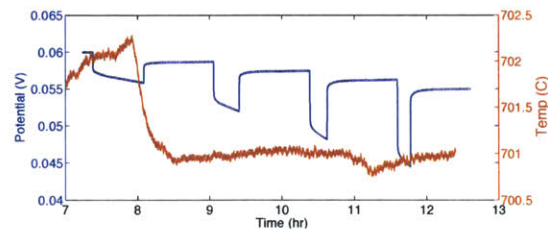
(c) 600 °C



(d) 625 °C



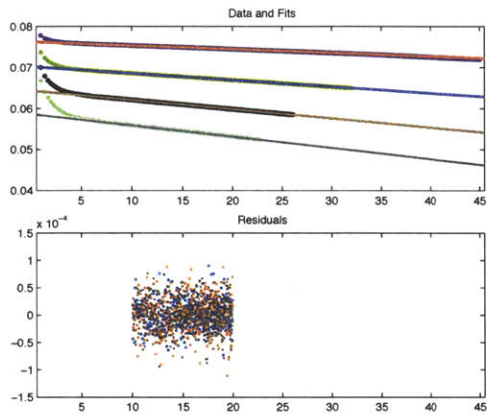
(e) 650 °C



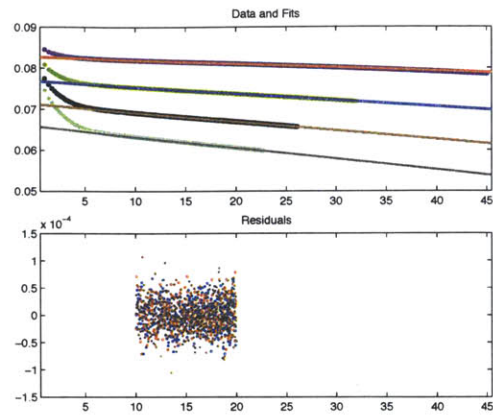
(f) 700 °C

Figure E-3: 15%: Electrode potential and temperature with time.

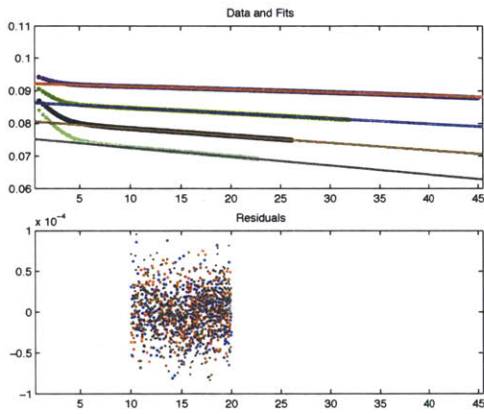
E.4 5% Ca-Bi: Potential Variation With Time



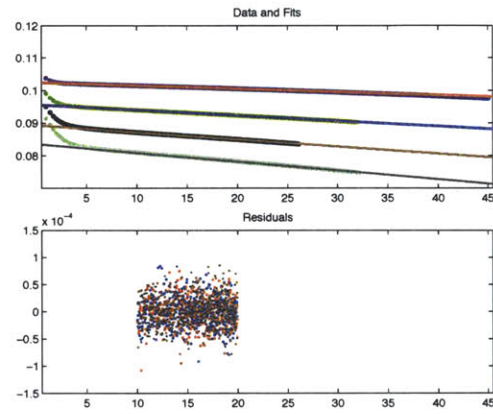
(a) 550 °C



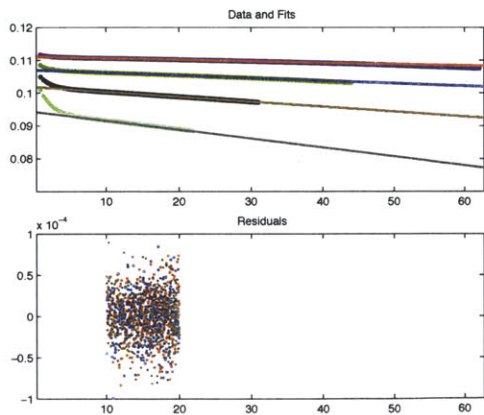
(b) 575 °C



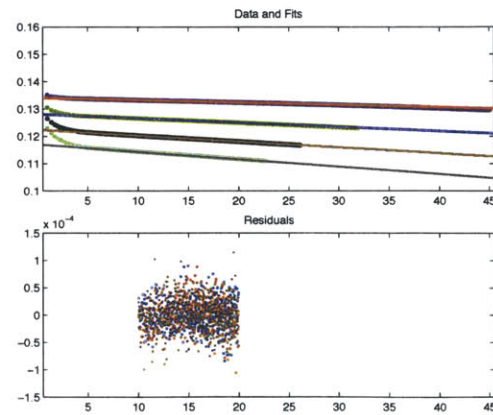
(c) 600 °C



(d) 625 °C



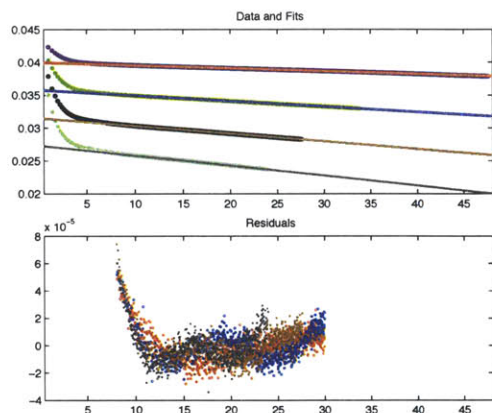
(e) 650 °C



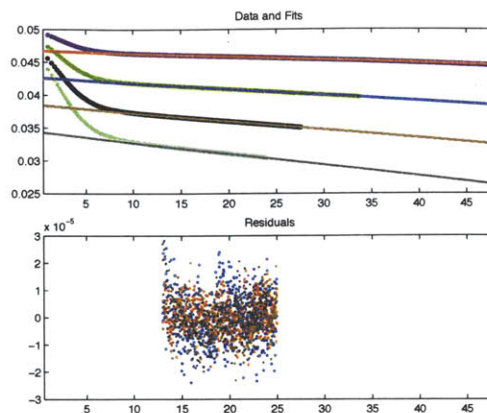
(f) 700 °C

Figure E-4: 5%: Potential versus square root of time.

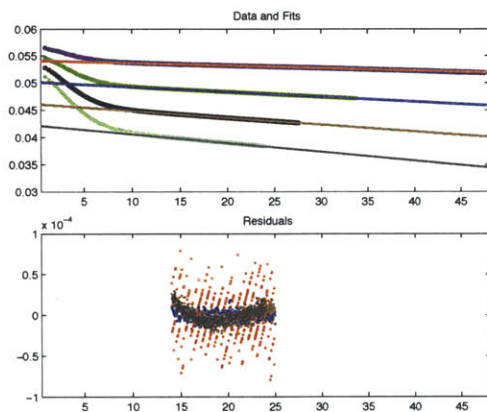
E.5 10% Ca-Bi: Potential Variation With Time



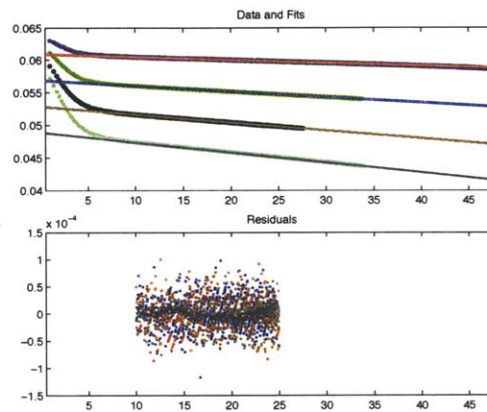
(a) 550 °C



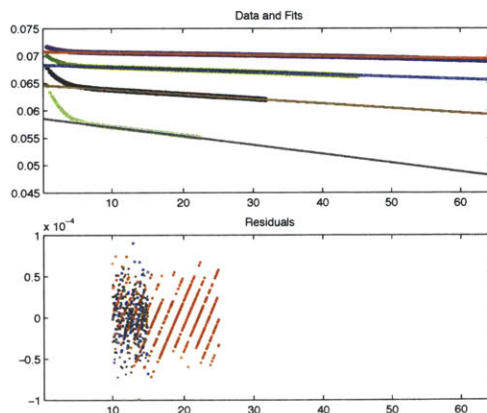
(b) 575 °C



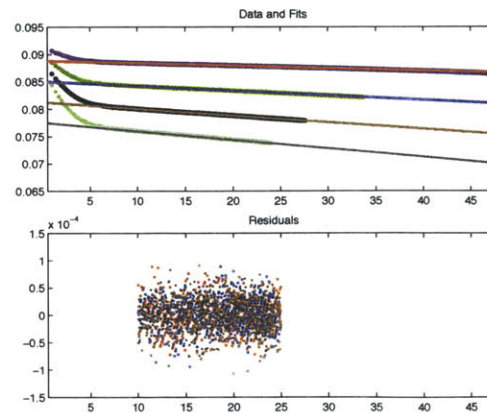
(c) 600 °C



(d) 625 °C



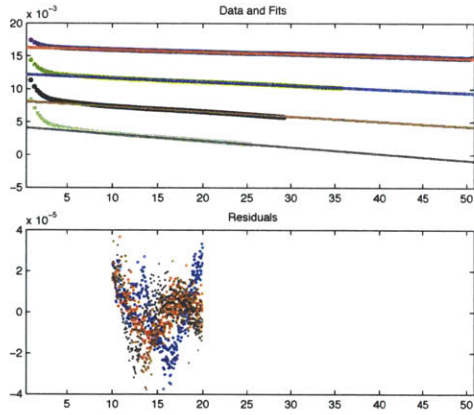
(e) 650 °C



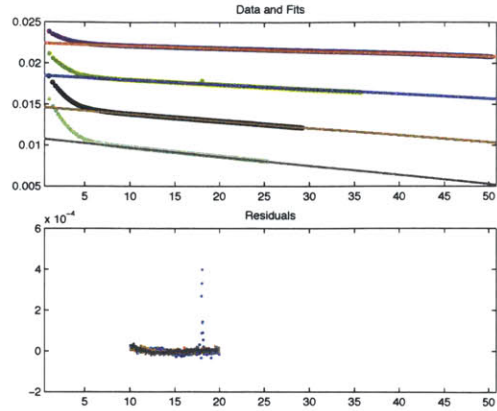
(f) 700 °C

Figure E-5: 10%: Potential versus square root of time.

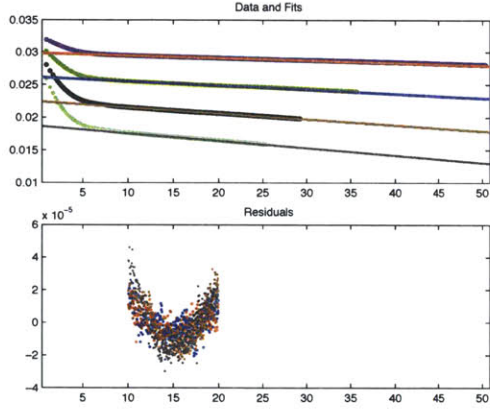
E.6 15% Ca-Bi: Potential Variation With Time



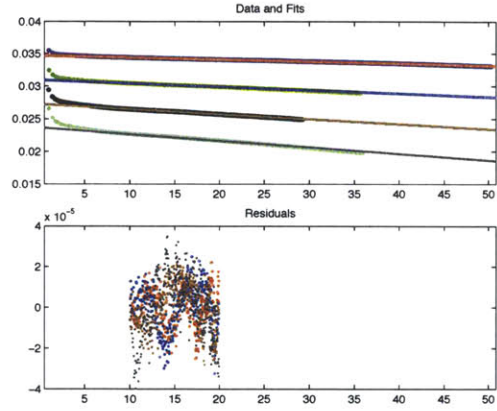
(a) 550 °C



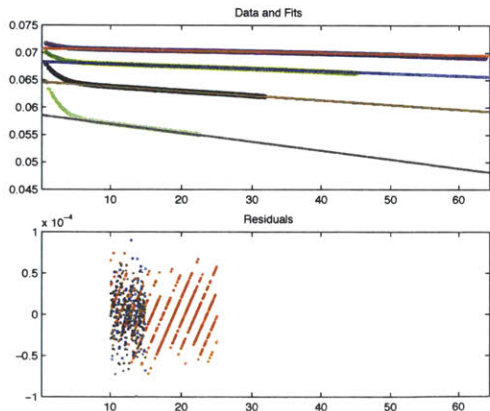
(b) 575 °C



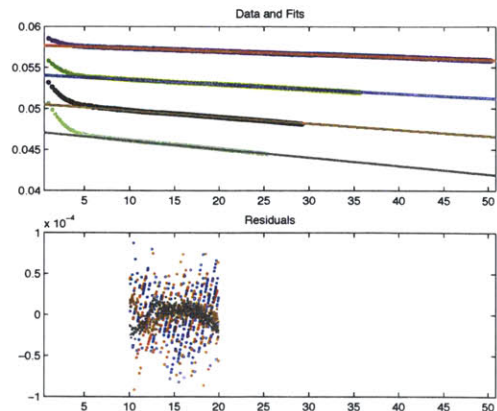
(c) 600 °C



(d) 625 °C



(e) 650 °C



(f) 700 °C

Figure E-6: 15%: Potential versus square root of time.

E.7 5% Ca-Bi: Reference Electrode

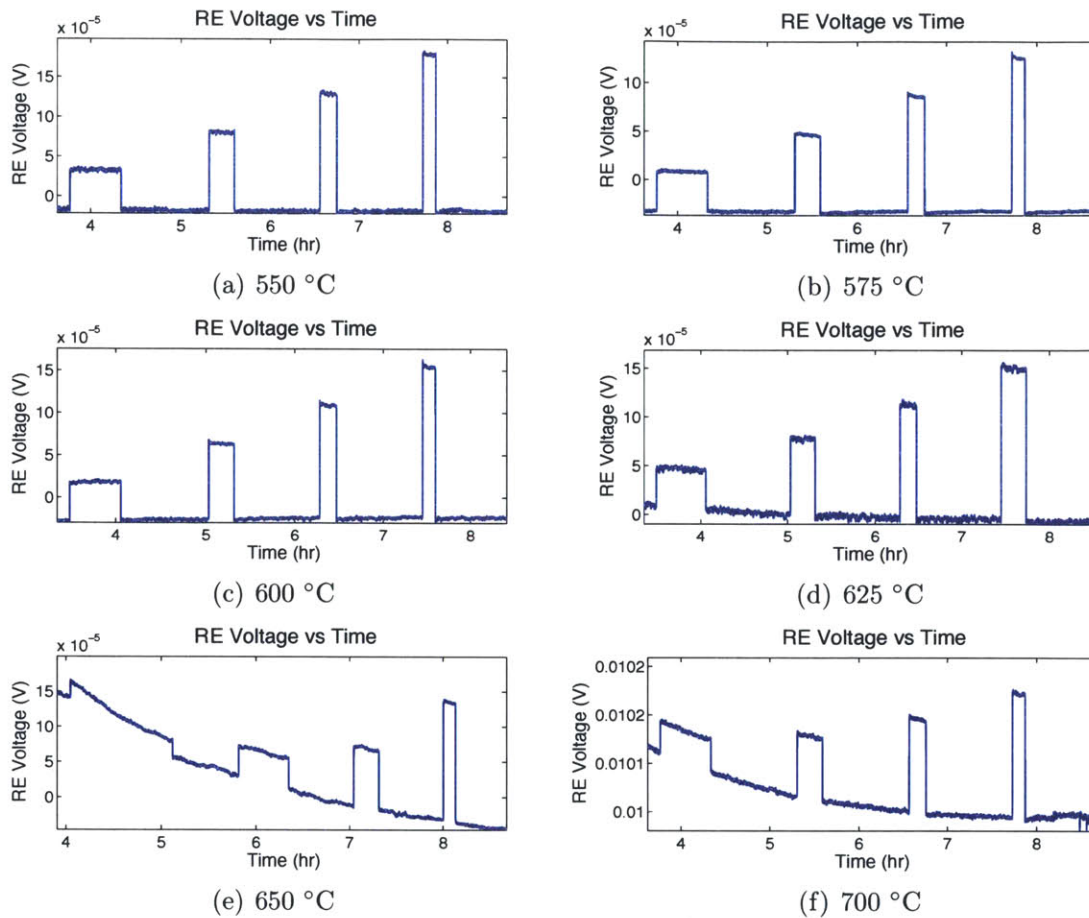


Figure E-7: 5%: Reference electrode stability.

E.8 10% Ca-Bi: Reference Electrode

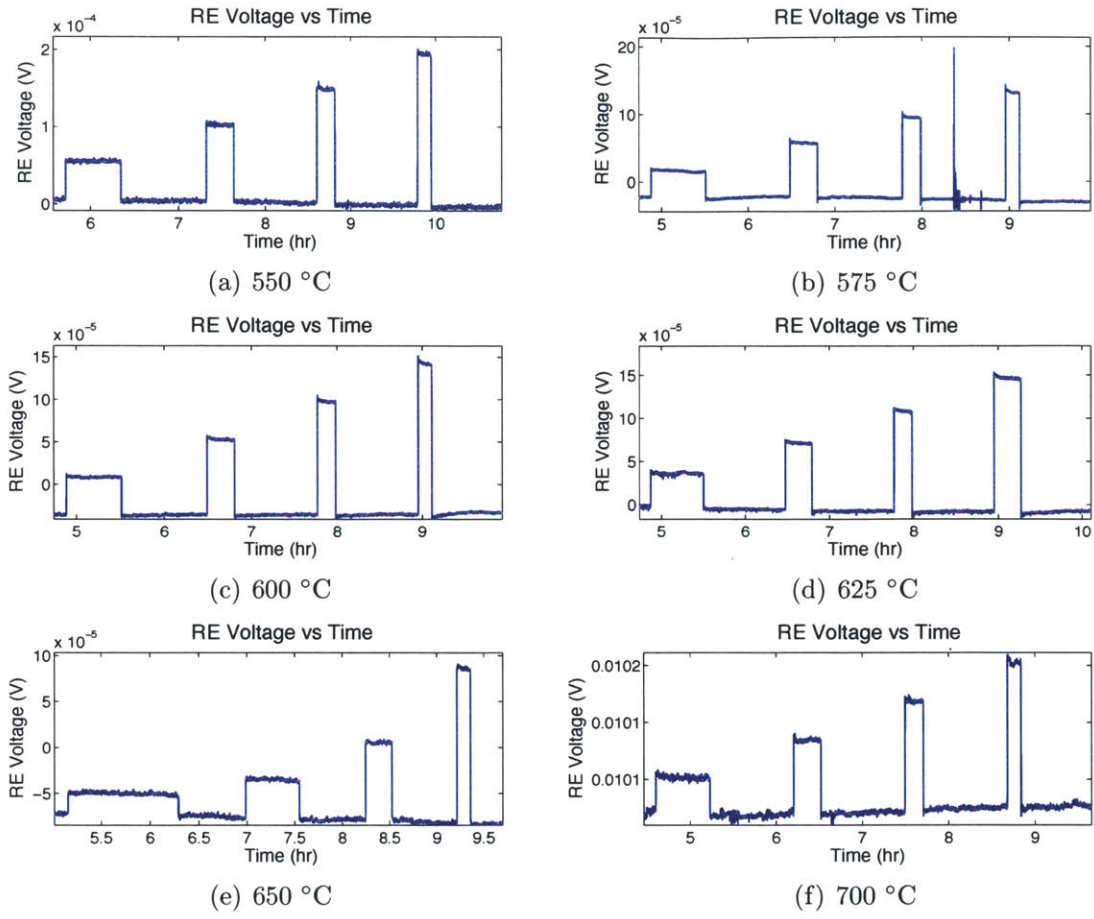


Figure E-8: 10%: Reference electrode stability.

E.9 15% Ca-Bi: Reference Electrode

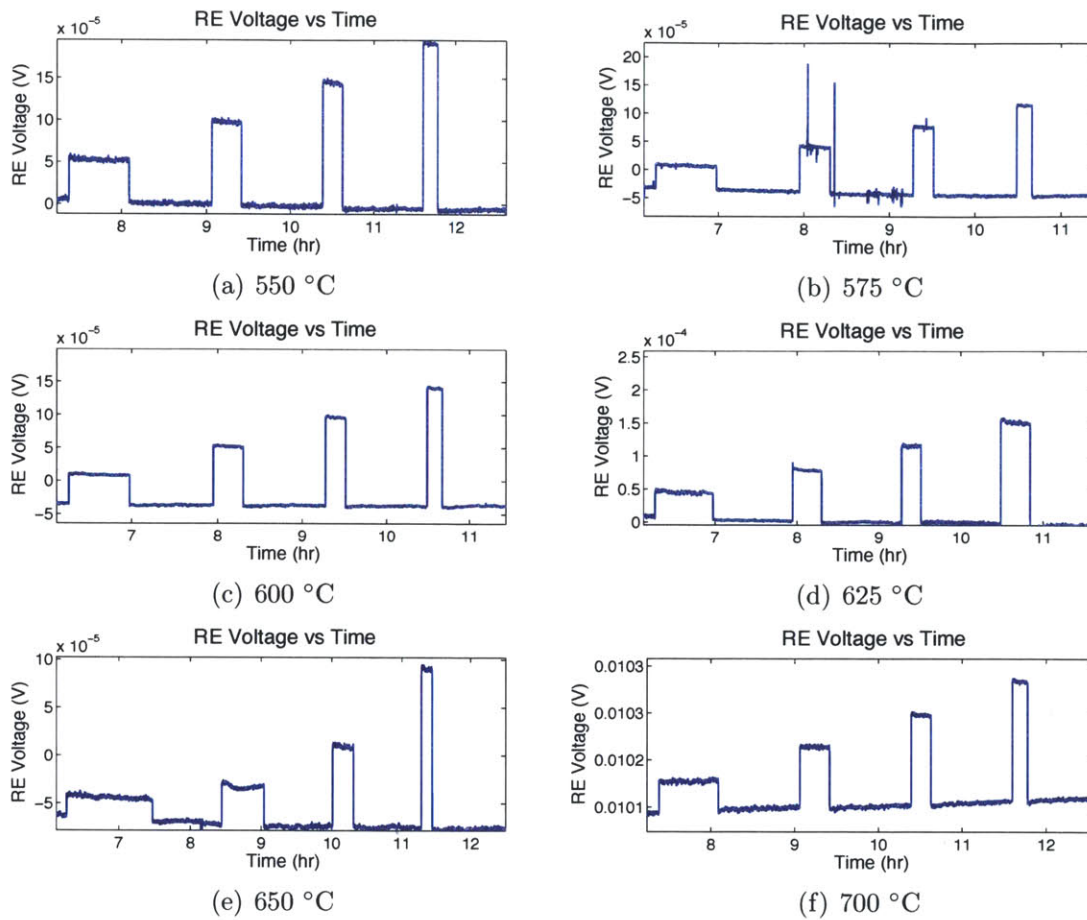


Figure E-9: 15%: Reference electrode stability.

E.10 5% Ca-Bi: Counter Electrode

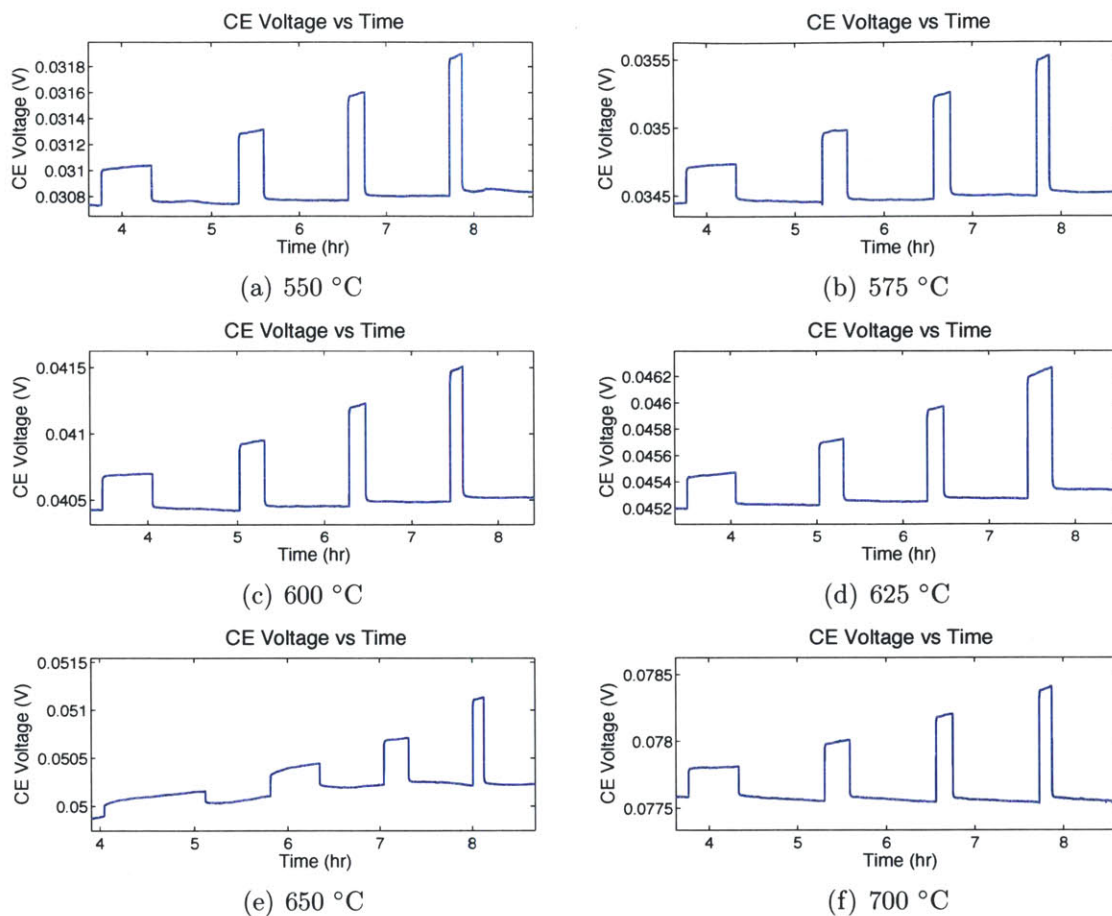


Figure E-10: 5%: Counter electrode stability.

E.11 10% Ca-Bi: Counter Electrode

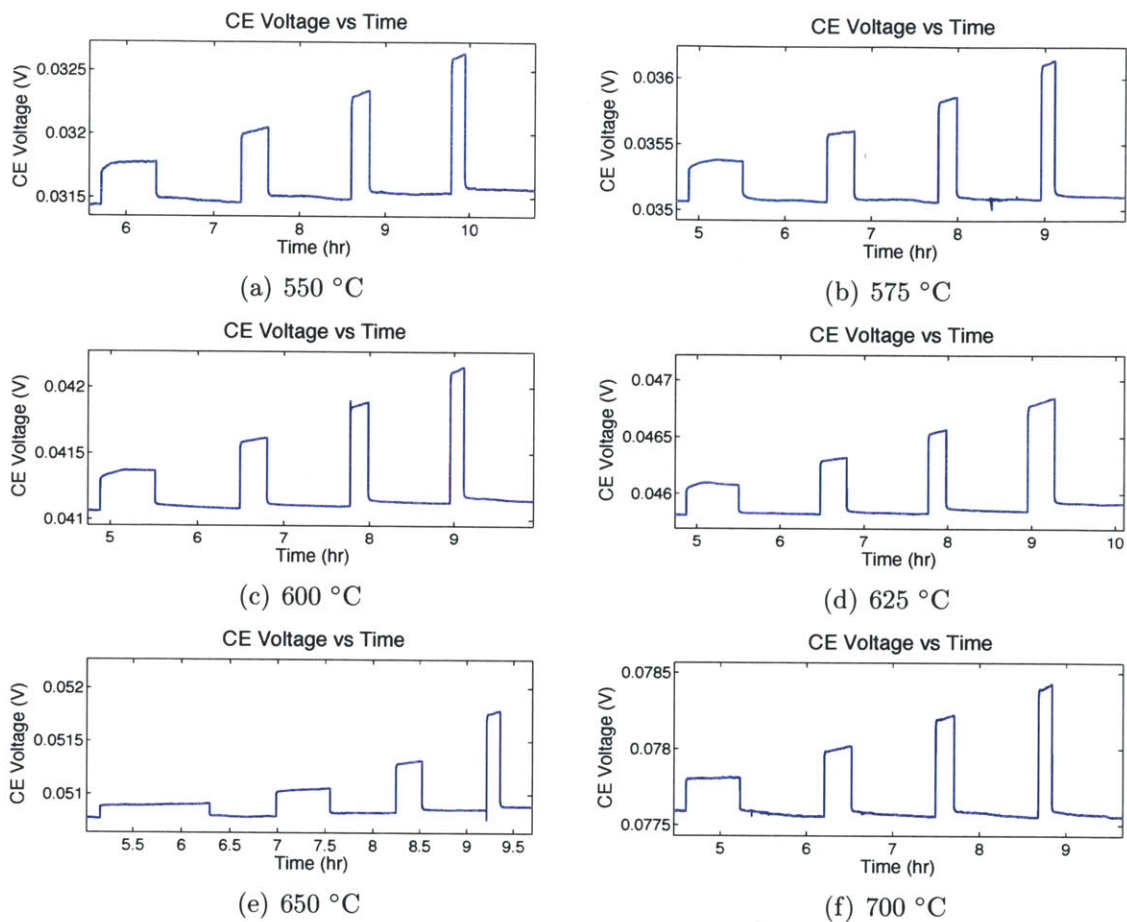


Figure E-11: 10%: Counter electrode stability.

E.12 15% Ca-Bi: Counter Electrode

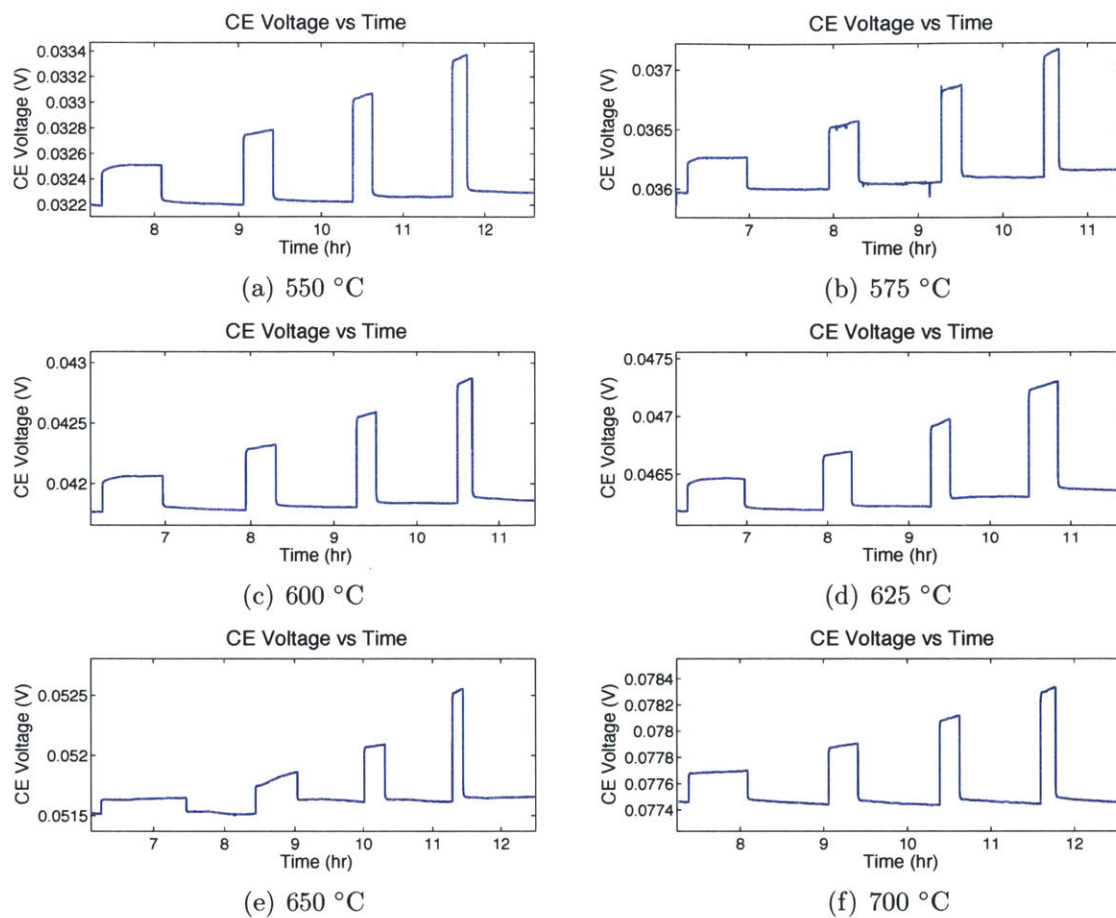


Figure E-12: 15%: Counter electrode stability.

Appendix F

MATLAB Data Analysis Scripts

```
1 clear
2 global I_pulse1
3 cd ~/Dropbox/MATLAB/scripts/
4 Z = 0
5
6 global pct_diff; %% Parameters
7 rad = .3; %WE1 radius
8 % rad = .35; %WE2 radius
9 % rad = .4; %WE3 radius
10
11 % m_Bi = 1.08904; %WE1 GITT4 mass
12 %m_Bi = 1.4817; %WE2 GITT4 mass
13 %m_Bi = 1.92968 %WE3 GITT4 mass
14
15 m_Bi = 1.08716; %WE1 GITT5 mass
16 % m_Bi = 1.47417 %WE2 GITT5 mass
17 % m_Bi = 1.93145 %WE3 GITT5 mass
18
19 %% Start of code
20 cd ~/Dropbox/MATLAB/GITT_Data_DP_2/GITT5_DP/Temp_DP/WE1/
21 Temp_labview
```

```

22 Volt_labview
23 cd ~/Dropbox/MATLAB/GITT_Data_DP_2/GITT5_DP/
24 GITT_composition_data
25 GITT_pulse_data
26 GITT_Calculations_DP
27 percent_titration
28
29 cd(file_path)
30 mkdir = num2str(round(Ca_mole_percent_start))
31 mkdir(mkdir)
32 cd(mkdir)
33
34 D_differentiation
35 D_numerical
36 D_difference
37 plotALL_DP

1 % 20111027 SalB: This script inputs the data from the autolab
   text file,
2 % concatenates the data arrays, and plots voltage vs time for
   the pulse
3 % sequences. The generic value of 40 should only be changed
   if you have
4 % more than 40 data sequences with headers written to it in
   the file.
5 format long
6
7
8 %% code below asks the user to select the input file
9 [file_name, file_path] = uigetfile('*.txt','Select Temperature
   Data File');
10 cd(file_path);

```



```

11 fid = fopen(file_name);
12
13 %% the for loop below writes each data sequence (according to
    the headers)
14 % to its own column in a cell array.
15
16 headers = textscan(fid, '%s', 39);
17 data = textscan(fid, '%f %f %f %f');
18
19
20
21 fclose(fid);
22 T_bulk = data{1,1};
23 T_WE1 = data{1,2};
24 T_WE2 = data{1,3};
25 T_WE3 = data{1,4};
26
27
28 TimeT = 0:1:numel(T_bulk)-1;
29 TimeT = TimeT';
30
31 Temp = T_bulk;
32 T_avg = mean(T_bulk);
33 T_range = range(T_bulk);
34 T_std = std(T_bulk);

```

1 % 20111027 SalB: This script inputs the data from the autolab
text file,
2 % concatenates the data arrays, and plots voltage vs time for
the pulse
3 % sequences. The generic value of 40 should only be changed
if you have

```

4  % more than 40 data sequences with headers written to it in
    the file.
5
6  format long
7
8  %% code below asks the user to select the input file
9  [file_name, file_path] = uigetfile('*.txt','Select Voltage
    File');
10 cd(file_path);
11 fid = fopen(file_name);
12
13 %% the for loop below writes each data sequence (according to
    the headers)
14 % to its own column in a cell array.
15 for m = 1
16 headers = textscan(fid,'%s',21); %#ok<NASGU>
17 data = textscan(fid,'%f %f');
18 V1 = data{1,1};
19 volt1{:,m} = V1;
20 V2 = data{1,2};
21 volt2{:,m} = V2; %#ok<SAGROW>
22 end
23
24 fclose(fid);
25
26 VoltRE = volt1{1,:};
27 VoltCE = volt2{1,:};
28 TimeV = 1:1:numel(VoltCE);
29 TimeV = TimeV';

1  % 20111027 SalB: This script inputs the data from the autolab
    text file,

```

```

2  % concatenates the data arrays, and plots voltage vs time for
   the pulse
3  % sequences
4  format long
5  %% code below asks the user to select the input file
6  [file_name, file_path] = uigetfile('*.txt','Select X_Ca
   Titration File');
7  cd(file_path);
8  fid = fopen(file_name);
9
10 for m = 1:40
11 headersc= textscan(fid,'%s',6); %#ok<NASGU>
12 datac = textscan(fid,'%f %f %f');
13 t1 = datac{1,1};
14 timec{:,m} = t1;
15 V = datac{1,2};
16 voltc{:,m} = V;
17 A = datac{1,3};
18 currentc{:,m} = A; %#ok<SAGROW>
19 end
20
21 fclose(fid);
22
23 %% finds empty cell arrays and deletes them
24 test = cellfun('isempty', voltc);
25 test1 = find(test<1);
26 voltc = voltc(1:numel(test1));
27 currentc = currentc(1:numel(test1));
28 timec = timec(1:numel(test1));

1  % 20111027 SalB: This script inputs the data from the autolab
   text file,

```

```

2  % concatenates the data arrays, and plots voltage vs time for
    the pulse
3  % sequences
4  format long
5  %% code below asks the user to select the input file
6  [file_name, file_path] = uigetfile('*.txt','Select Pulse Data
    File');
7  cd(file_path);
8  fid = fopen(file_name);
9
10 for m = 1:40
11 headers = textscan(fid,'%s',6); %#ok<NASGU>
12 data = textscan(fid,'%f %f %f');
13 t1 = data{1,1};
14 timep{:,m} = t1;
15 V = data{1,2};
16 voltp{:,m} = V;
17 A = data{1,3};
18 currentp{:,m} = A; %#ok<SAGROW>
19 end
20
21 fclose(fid);
22 %% finds empty cell arrays and deletes them
23 test = cellfun('isempty', voltp);
24 test1 = find(test<1);
25 voltp = voltp(1:numel(test1));
26 currentp = currentp(1:numel(test1));
27 timep = timep(1:numel(test1));
28
29 %% averages the the voltages
30 for n = 1:numel(test1)
31 Vm = voltp{:,n};

```

```

32 Im = mean(abs(currentp{:,n}));
33
34     if Im < 0.00001
35         Em = mean(Vm(numel(Vm)-250:numel(Vm)));
36         Eavg{:,n} = Em;
37         E_ocv(n) = Em;
38     else
39         Em = mean(Vm(numel(Vm)-2:numel(Vm)));
40         Eavg{:,n} = Em;
41         E_ocv(n) = Em;
42     end
43 end

1 %% Fundamental constants
2 q = 1.602176565e-19;
3 k = 1.3806488e-23;
4 NA = 6.0221415e23;
5 R = 8.3144621;
6 z = 2;
7 F = 96485.3415;
8 S = pi*(rad^2-.05^2);
9
10 for n = 1:numel(test1)
11     Vm = voltp{:,n};
12     Im = mean(abs(currentp{:,n}));
13
14     if Im < 0.00001
15         Em = mean(Vm(numel(Vm)-250:numel(Vm)));
16         Eavg{:,n} = Em;
17         E_ocv(n) = Em;
18     else
19         Em = mean(Vm(numel(Vm)-2:numel(Vm)));

```

```

20         Eavg{:,n} = Em;
21         E_ocv(n) = Em;
22     end
23 end
24
25 OCVp1_1 = voltp{:,1};
26 OCVp1_2 = voltp{:,3};
27 OCVp2_1 = voltp{:,4}; %ocv before second pulse, 500s
28 OCVp2_2 = voltp{:,6}; %ocv after pulse, relaxation. Typically
    ~3000s
29 OCVp3_1 = voltp{:,7};
30 OCVp3_2 = voltp{:,9};
31 OCVp4_1 = voltp{:,10};
32 OCVp4_2 = voltp{:,12};
33 ocv1p13 = [OCVp1_1 OCVp3_1];
34 ocv1p24 = [OCVp2_1 OCVp4_1];
35 ocv2p13 = [OCVp1_2 OCVp3_2];
36 ocv2p24 = [OCVp2_2 OCVp4_2];
37
38 E_ocv1 = ocv2p13(:,1);
39 E_ocv2 = ocv2p24(:,1);
40 E_ocv3 = ocv2p13(:,2);
41 E_ocv4 = ocv2p24(:,2);
42 E_ocv_avg1 = mean(E_ocv1(numel(E_ocv1)*2/3:numel(E_ocv1)))
43 E_ocv_avg2 = mean(E_ocv2(numel(E_ocv2)*2/3:numel(E_ocv2)))
44 E_ocv_avg3 = mean(E_ocv3(numel(E_ocv3)*2/3:numel(E_ocv3)))
45 E_ocv_avg4 = mean(E_ocv4(numel(E_ocv4)*2/3:numel(E_ocv4)))
46
47
48 %% variables
49 Time_pulse = vertcat(timep{1,1:numel(test1)});
50 Volt_pulse = vertcat(voltp{1,1:numel(test1)});

```

```

51 Current_pulse = vertcat(currentp{1,1:numel(test1)});
52
53 Time1 = vertcat(timec{1,:});
54 Volt1 = vertcat(voltc{1,:});
55 Current1 = vertcat(currentc{1,:});
56 %
57 Time_titrate = timec{1,3};
58 Volt_titrate = voltc{1,3};
59 Current_titrate = currentc{1,3};
60 Current_clean = currentc{1,2};
61 Time_clean = timec{1,2};
62
63 Time_exp = vertcat(Time1,Time_pulse);
64 Volt_exp = vertcat(Volt1, Volt_pulse);
65
66 x1 = round(timep{1,1}(1)); %initial time before pulsing
    20120731
67 x2 = round(max(Time_pulse));
68 x2 = round(max(Time_pulse))-abs(x2-numel(T_bulk));% final time
    after pulsing
69 maxV_CE = max(VoltCE(x1:x2)) + 0.05*max(VoltCE(x1:x2));
70 minV_CE = min(VoltCE(x1:x2)) - 0.05*min(VoltCE(x1:x2));
71 maxV_RE = max(VoltRE(x1:x2)) + 0.2*max(VoltRE(x1:x2));
72 minV_RE = min(VoltRE(x1:x2)) - 0.2*min(VoltRE(x1:x2));
73 T_pulse = T_bulk(round(x1):round(x2));
74 T_avg = mean(T_pulse);
75 T = 273.15+T_avg;
76
77 rho_Bi = (10811-(1320*T/1000))/1000; %density at temperature
78 rho_Ca = 1.378-0.00023*(T_avg - 842);%Ca density vs Temp
79
80 %% calculation for Ca mole deposition and mass addition

```

```

81 I_ti = abs(mean(currentc{: ,3})); %Titration current
82 M_Ca = 40.078; %Ca atomic mass (g/mol)
83 Ca_mol = I_ti*round(range(timec{: ,3}))/z/F; %Ca mole deposition
    during titration
84 m_Ca = M_Ca*Ca_mol; % Ca mass deposition from titration
85 V_Ca = M_Ca/rho_Ca; %Ca molar volume
86 Vol_Ca = V_Ca*Ca_mol; %Ca sample volume
87
88 %% bismuth WE variables
89 M_Bi = 208.9804; %Bi atomic mass
90 V_Bi = M_Bi/rho_Bi; %Bi molar volume
91 Bi_mol = m_Bi/M_Bi; %Bi moles
92 Vol_Bi = m_Bi/rho_Bi; % Bi sample volume
93
94 %% Alloy mixture calculation
95 m_tot = m_Bi+m_Ca; %total mass
96 Vol = Vol_Bi+Vol_Ca; %total volume
97 c_Ca_i = (Ca_mol)/Vol; %initial calcium concentration
98 amu = (m_tot)/(Bi_mol+Ca_mol); %effective atomic mass
99 MV = Vol/(Bi_mol+Ca_mol); %effective molar volume
100
101 % OCV_current_1 = mean(current{: ,1});
102 % Cleaning_current_avg = mean(current{: ,2});
103 % Titration_current_avg = mean(current{: ,3});
104 % OCV_current_2 = mean(current{: ,4});
105
106 %% Pulsing data
107 Volt_pulse1 = vertcat(voltp{1,1:3});
108 Volt_pulse2 = vertcat(voltp{1,4:6});
109
110 if n > 10
111     Volt_pulse3 = vertcat(voltp{1,7:9});

```



```

112     Volt_pulse4 = vertcat(voltp{1,10:12});
113 end
114
115 %% pulse 1
116 tau1 = round(range(timep{: ,2}));
117 I_pulse1 = (mean(currentp{: ,2}));%current during first GITT
    pulse
118 IR1 = Z*I_pulse1;% IR from ACI
119 vv1 = voltp{: ,2};
120 tt1 = 1:1:numel(vv1);
121 tt1 = tt1';
122 sqtt1 = sqrt(tt1);
123 Esp1 = E_ocv_avg1 - E_ocv(1);
124 Etp1 = E_ocv(2) - E_ocv(1);
125
126 Ca_ti_p1 = abs(I_pulse1*tau1/z/F);%Ca moles added during 1st
    GITT pulse
127 m_Ca_p1 = M_Ca*Ca_ti_p1;% Ca mass deposition from 1st pulse (g
    )
128 Vol_Ca_p1 = m_Ca_p1/rho_Ca;%Ca sample volume
129 Vol1 = Vol+Vol_Ca_p1;
130 c_Ca_i2 = (Ca_mol+Ca_ti_p1)/Vol1;%new Ca concentration after 1
    st GITT pulse
131 X_Ca1 = Ca_mol/(Ca_mol+Bi_mol); % initial Ca mole fraction
132 X_Bi1 = 1-X_Ca1;
133 X_Ca_pulse1 = (Ca_ti_p1+Ca_mol)/(Ca_mol+Bi_mol+Ca_ti_p1); %
    final Ca mole fraction
134 Delta_X1 = X_Ca_pulse1 - X_Ca1; % Ca mole fraction titrated
    during pulse1
135 dEdx(1) = Esp1/Delta_X1;% delta ocv divided by Ca mole
    fraction titrate

```

```

136 L1 = (Vol+Vol1)/2/S; %average height of sample after 1st
      titration
137 dlna_dlnx_1 = -(z*F*X_Ca1*Esp1)/(R*T*Delta_X1); %thermodynamic
      enhancement factor
138 dlna_dlnx(1) = dlna_dlnx_1;
139 Volt_pulse1 = vertcat(voltp{1,1:3});
140 Time_pulse1 = 1:1:numel(Volt_pulse1);
141 Time_pulse1 = Time_pulse1';
142
143
144 Time_OCVp1_1 = 0:1:numel(OCVp1_1)-1;
145 Time_OCVp1_1 = Time_OCVp1_1';
146 global Time_OCVp1_2;
147 Time_OCVp1_2 = 0:1:numel(OCVp1_2)-1;
148
149 Time_OCVp1_2 = Time_OCVp1_2';
150
151 %% pulse 2
152 tau2 = round(range(timep{: ,5}));
153 I_pulse2 = (mean(currentp{: ,5})); %current during second GITT
      pulse
154 IR2 = Z*I_pulse2;
155 vv2 = voltp{: ,5};
156 tt2 = 1:1:numel(vv2);
157 tt2 = tt2';
158 sqtt2 = sqrt(tt2);
159 Esp2 = E_ocv_avg2 - E_ocv(4);
160 Etp2 = E_ocv(5) - E_ocv(4);
161
162 Ca_ti_p2 = abs(I_pulse2*tau2/z/F); %Ca moles added during 2nd
      GITT pulse

```

```

163 m_Ca_p2 = M_Ca*Ca_ti_p2;% Ca mass deposition from 2nd pulse (g
    )
164 Vol_Ca_p2 = m_Ca_p2/rho_Ca; % Vol of Ca added during 2nd pulse
165 Vol2 = Vol1+Vol_Ca_p2;
166 c_Ca_i3 = (Ca_mol+Ca_ti_p1+Ca_ti_p2)/Vol2;%new Ca
    concentration after 2nd GITT pulse
167 X_Ca2 = (Ca_mol+Ca_ti_p1)/(Ca_mol+Bi_mol + Ca_ti_p1);
168 X_Bi2 = 1-X_Ca2;
169 X_Ca_pulse2 = (Ca_ti_p1+Ca_mol+Ca_ti_p2)/(Ca_mol+Bi_mol+
    Ca_ti_p1+Ca_ti_p2);
170 Delta_X2 = X_Ca_pulse2 - X_Ca2;
171 dEdx(2) = Esp2/Delta_X2;
172 L2 = (Vol1+Vol2)/2/S; %average height of sample after 2nd
    titration
173 dlna_dlnx_2 = -(z*F*X_Ca2*Esp2)/(R*T*Delta_X2); %thermodynamic
    enhancement factor
174 dlna_dlnx(2) = dlna_dlnx_2;
175 Volt_pulse2 = vertcat(voltp{1,4:6});
176 Time_pulse2 = 1:1:numel(Volt_pulse2);
177 Time_pulse2 = Time_pulse2';
178
179
180 Time_OCVp2_1 = 0:1:numel(OCVp2_1)-1;
181 Time_OCVp2_1 = Time_OCVp2_1';
182 Time_OCVp2_2 = 0:1:numel(OCVp2_2)-1;
183 Time_OCVp2_2 = Time_OCVp2_2';
184
185 if n > 10
186     %% pulse 3
187     tau3 = round(range(timep{: ,8}));
188     I_pulse3 = mean(currentp{: ,8});
189     IR3 = Z*I_pulse3;

```

```

190     vv3 = voltp{:,8};
191     tt3 = 1:1:numel(vv3);
192     tt3 = tt3';
193     sqtt3 = sqrt(tt3);
194     Esp3 = E_ocv_avg3 - E_ocv(7);
195     Etp3 = E_ocv(8) - E_ocv(7);
196     Ca_ti_p3 = abs(I_pulse3*tau3/z/F);%Ca moles added during 3
        rd GITT pulse
197     m_Ca_p3 = M_Ca*Ca_ti_p3;% Ca mass deposition from 2nd
        pulse (g)
198     Vol_Ca_p3 = m_Ca_p3/rho_Ca; % Vol of Ca added during 2nd
        pulse
199     Vol3 = Vol2+Vol_Ca_p3;
200     Ca_mol_endp3 = Ca_mol + Ca_ti_p1 + Ca_ti_p2 + Ca_ti_p3;
201     c_Ca_i4 = (Ca_mol_endp3)/Vol3;%new Ca concentration after
        4th GITT pulse
202     X_Ca3 = (Ca_mol + Ca_ti_p1 + Ca_ti_p2)/(Ca_mol + Ca_ti_p1
        + Ca_ti_p2 + Bi_mol);
203     X_Bi3 = 1-X_Ca3;
204     X_Ca_pulse3 = (Ca_ti_p1+Ca_mol+Ca_ti_p2+Ca_ti_p3)/(Ca_mol+
        Bi_mol+Ca_ti_p1+Ca_ti_p2 + Ca_ti_p3);
205     Delta_X3 = X_Ca_pulse3 - X_Ca3;
206     dEdx(3) = Esp3/Delta_X3;
207     L3 = (Vol2+Vol3)/2/S; %average height of sample after 3rd
        titration
208     dlنا_dlnx_3 = -(z*F*X_Ca3*Esp3)/(R*T*Delta_X3); %
        thermodynamic enhancement factor
209     dlنا_dlnx(3) = dlنا_dlnx_3;
210     Volt_pulse3 = vertcat(voltp{1,7:9});
211     Time_pulse3 = 1:1:numel(Volt_pulse3);
212     Time_pulse3 = Time_pulse3' ;
213

```

```

214
215 Time_OCVp3_1 = 0:1:numel(OCVp3_1)-1;
216 Time_OCVp3_1 = Time_OCVp3_1';
217 Time_OCVp3_2 = 0:1:numel(OCVp3_2)-1;
218 Time_OCVp3_2 = Time_OCVp3_2';
219
220 %% pulse 4
221 tau4 = round(range(timep{: ,11}));
222 I_pulse4 = mean(currentp{: ,11});
223 IR4 = Z*I_pulse4;
224 vv4 = voltp{: ,11};
225 tt4 = 1:1:numel(vv4);
226 tt4 = tt4';
227 sqtt4 = sqrt(tt4);
228 Esp4 = E_ocv_avg4 - E_ocv(10);
229 Etp4 = E_ocv(11) - E_ocv(10);
230
231 Ca_ti_p4 = abs(I_pulse4*tau4/z/F); %Ca moles added during 4
    rd GITT pulse
232 m_Ca_p4 = M_Ca*Ca_ti_p4; % Ca mass deposition from 4th
    pulse (g)
233 Vol_Ca_p4 = m_Ca_p4/rho_Ca; % Vol of Ca added during 4th
    pulse
234 Vol4 = Vol3+Vol_Ca_p4;
235 Ca_mol_endp4 = Ca_mol + Ca_ti_p1 + Ca_ti_p2 + Ca_ti_p3 +
    Ca_ti_p4;
236 c_Ca_i5 = (Ca_mol_endp4)/Vol4;
237 X_Ca4 = (Ca_mol + Ca_ti_p1 + Ca_ti_p2 + Ca_ti_p3)/(Ca_mol
    + Ca_ti_p1 + Ca_ti_p2+Ca_ti_p3 + Bi_mol);
238 X_Bi4 = 1-X_Ca4;
239 X_Ca_pulse4 = (Ca_ti_p1+Ca_mol+Ca_ti_p2+Ca_ti_p3 +
    Ca_ti_p4)/(Ca_mol+Bi_mol+ ...

```

```

240 Ca_ti_p1+Ca_ti_p2 + Ca_ti_p3 + Ca_ti_p4);
241 Delta_X4 = X_Ca_pulse4 - X_Ca4;
242 dEdx(4) = Esp4/Delta_X4;
243 L4 = (Vol3+Vol4)/2/S; %average height of sample after 4th
      titration
244 dlna_dlnx_4 = -(z*F*X_Ca4*Esp4)/(R*T*Delta_X4); %
      thermodynamic enhancement factor
245 dlna_dlnx(4) = dlna_dlnx_4;
246 Volt_pulse4 = vertcat(voltp{1,10:12});
247 Time_pulse4 = 1:1:numel(Volt_pulse4);
248 Time_pulse4 = Time_pulse4';
249
250 % vvp13 = [vv1 vv3];
251 % vvp24 = [vv2 vv4];
252 % VP13 = [Volt_pulse1 Volt_pulse3];
253 % VP24 = [Volt_pulse2 Volt_pulse4];
254
255
256 Time_OCVp4_1 = 0:1:numel(OCVp4_1)-1;
257 Time_OCVp4_1 = Time_OCVp4_1';
258 Time_OCVp4_2 = 0:1:numel(OCVp4_2)-1;
259 Time_OCVp4_2 = Time_OCVp4_2';
260
261
262
263 OCV1 = [OCVp1_1 OCVp2_1 OCVp3_1 OCVp4_1];
264
265
266 I_pulse = -[I_pulse1 I_pulse2 I_pulse3 I_pulse4];
267
268 J_pulse1 = abs(I_pulse1/S)*1000;
269 J_pulse2 = abs(I_pulse2/S)*1000;

```

```

270     J_pulse3 = abs(I_pulse3/S)*1000;
271     J_pulse4 = abs(I_pulse4/S)*1000;
272     J_pulse = [J_pulse1 J_pulse2 J_pulse3 J_pulse4];
273     Esp = [Esp1 Esp2 Esp3 Esp4];
274     tau = [tau1 tau2 tau3 tau4];
275
276 end
277
278 Ca_mole_end = Ca_mol+Ca_ti_p1+Ca_ti_p2+Ca_ti_p3+Ca_ti_p4;
279 Ca_mole_percent_start = Ca_mol/(Ca_mol+Bi_mol)*100
280 Ca_mole_percent_end = Ca_mole_end/(Ca_mole_end+Bi_mol)*100
281
282 pctdiff(dEdx); % pct diff of dEdx
283 dEdx_pct_diff = pct_diff;
284
285 pctdiff(dlna_dlnx); %pct diff of enhancement factor
286 dlna_dlnx_pct_diff = pct_diff;
287
288 %%
289
290
291 global ocv1Ymax ocv1Ymin ocv2Ymax ocv2Ymin
292 ocv1Ymax = E_ocv(1)+0.1*(E_ocv(1) - E_ocv(9));
293 ocv1Ymin = E_ocv(9)-0.1*(E_ocv(1) - E_ocv(9));
294 ocv2Ymax = E_ocv(3)+0.1*(E_ocv(3) - E_ocv(12));
295 ocv2Ymin = E_ocv(12)-0.1*(E_ocv(3) - E_ocv(12));

```

1 %% Calculates the percent titration by integrating the current

2

```

3 b = Current_titrate;
4 c = Time1;
5 charge_titrated = round(c(2)-c(1))*trapz(b);

```

```

6 Ca_mole_titrated = abs(charge_titrated/2)/F;
7
8 Ca_mole_percent_titration = Ca_mole_titrated/(Ca_mole_titrated
+Bi_mol)*100

1 % fits slope to selected data and calculated D based on dEdsqt
from slope
2 % of fit assuming constant volume...but using average volume
3 global pct_diff cf_1 cf_2 cf_3 cf_4;
4 global t_long1 t_long2 t_long3 t_long4
5 createFit2(sqtt1,vv1,sqtt2,vv2,sqtt3,vv3,sqtt4,vv4);
6 dE_dsqt1 = cf_1.p1;
7 dE_dsqt2 = cf_2.p1;
8 dE_dsqt3 = cf_3.p1;
9 dE_dsqt4 = cf_4.p1;
10 dE_dsqzero1 = cf_1.p2;
11 dE_dsqzero2 = cf_2.p2;
12 dE_dsqzero3 = cf_3.p2;
13 dE_dsqzero4 = cf_4.p2;
14 dE_dsqt = [dE_dsqt1 dE_dsqt2 dE_dsqt3 dE_dsqt4];
15
16 D_diff1 = (1/pi)*((2*L1*(Bi_mol+Ca_mol+Ca_ti_p1)*(Bi_mol+
Ca_mol)*Esp1)/(tau1*(Ca_mol+Bi_mol+0.5*Ca_ti_p1)^2*dE_dsqt1
))^2; %chemical D of pulse1
17 D_diff2 = (1/pi)*((2*L2*(Bi_mol+Ca_mol+Ca_ti_p1+Ca_ti_p2)*(
Bi_mol+Ca_mol+Ca_ti_p1)*Esp2)/(tau2*(Ca_mol+Bi_mol+Ca_ti_p1
+0.5*Ca_ti_p2)^2*dE_dsqt2))^2;
18 D_diff3 = (1/pi)*((2*L3*(Bi_mol+Ca_mol+Ca_ti_p1+Ca_ti_p2+
Ca_ti_p3)*(Bi_mol+Ca_mol+Ca_ti_p1+Ca_ti_p2)*Esp3)/(tau3*(
Ca_mol+Bi_mol+Ca_ti_p1+Ca_ti_p2+0.5*Ca_ti_p3)^2*dE_dsqt3))
^2;

```



```

19 D_diff4 = (1/pi)*((2*L4*(Bi_mol+Ca_mol+Ca_ti_p1+Ca_ti_p2+
    Ca_ti_p3+Ca_ti_p4)*(Bi_mol+Ca_mol+Ca_ti_p1+Ca_ti_p2+
    Ca_ti_p3)*Esp4)/(tau4*(Ca_mol+Bi_mol+Ca_ti_p1+Ca_ti_p2+
    Ca_ti_p3+0.5*Ca_ti_p4)^2*dE_dsqt4))^2;
20 D_diff = [D_diff1 D_diff2 D_diff3 D_diff4];
21 D_diff_avg = mean(D_diff)
22
23 pctdiff(D_diff);
24 D_diff_pct_diff = pct_diff;
25
26 D_Ca_diff1 = D_diff1/dlna_dlnx_1; %component D of pulse1
27 D_Ca_diff2 = D_diff2/dlna_dlnx_2;
28 D_Ca_diff3 = D_diff3/dlna_dlnx_3;
29 D_Ca_diff4 = D_diff4/dlna_dlnx_4;
30 D_Ca_diff = [D_Ca_diff1 D_Ca_diff2 D_Ca_diff3 D_Ca_diff4];
31 D_Ca_diff_avg = mean(D_Ca_diff)
32
33 pctdiff(D_Ca_diff);
34 D_Ca_diff_pct_diff = pct_diff;

1
2
3 figure
4 fitOCV1(Time_OCVp1_1,OCVp1_1,Time_OCVp2_1,OCVp2_1,Time_OCVp3_1
    ,OCVp3_1,Time_OCVp4_1,OCVp4_1);
5 close
6 dVocv_dt1 = cf_1.p1; %first 500s ocv before pulsing
7 dVocv_dt2 = cf_2.p1;
8 dVocv_dt3 = cf_3.p1;
9 dVocv_dt4 = cf_4.p1;
10 V01 = cf_1.p2;
11 V02 = cf_2.p2;

```

```

12 V03 = cf_3.p2;
13 V04 = cf_4.p2;
14
15 V1fit = V01+dVocv_dt1*Time_OCVp1_1;
16 V2fit = V02+dVocv_dt2*Time_OCVp2_1;
17 V3fit = V03+dVocv_dt3*Time_OCVp3_1;
18 V4fit = V04+dVocv_dt4*Time_OCVp4_1;
19
20 Vfit = [V1fit V2fit V3fit V4fit];
21 OCVdatawfit = [OCVp1_1 OCVp2_1 OCVp3_1 OCVp4_1 V1fit V2fit
                V3fit V4fit];
22
23 xt2 = numel(Time_OCVp1_2);
24 xt1 = xt2-500;
25
26
27 fitOCV2(Time_OCVp1_2,OCVp1_2,Time_OCVp2_2,OCVp2_2,Time_OCVp3_2
          ,OCVp3_2,Time_OCVp4_2,OCVp4_2);
28 close
29 dVocv2_dt1 = cf_1.p1;%last ocv after pulse
30 dVocv2_dt2 = cf_2.p1;
31 dVocv2_dt3 = cf_3.p1;
32 dVocv2_dt4 = cf_4.p1;
33
34 %% percent differences
35
36 DeltaV_vv_fit1 = vv1(1) - dE_dsqzero1;
37 DeltaV_vv_fit2 = vv2(1) - dE_dsqzero2;
38 DeltaV_vv_fit3 = vv3(1) - dE_dsqzero3;
39 DeltaV_vv_fit4 = vv4(1) - dE_dsqzero4;
40

```

```

41 DVvvf = [DeltaV_vv_fit1 DeltaV_vv_fit2 DeltaV_vv_fit3
           DeltaV_vv_fit4];
42
43 % Eocv minus the zero point extrapolation of dE/dsqt(t)
44 DeltaV_ocv_fit1 = E_ocv(1) - dE_dsqzero1;
45 DeltaV_ocv_fit2 = E_ocv(4) - dE_dsqzero2;
46 DeltaV_ocv_fit3 = E_ocv(7) - dE_dsqzero3;
47 DeltaV_ocv_fit4 = E_ocv(10) - dE_dsqzero4;
48
49 DVocvf = [DeltaV_ocv_fit1 DeltaV_ocv_fit2 DeltaV_ocv_fit3
           DeltaV_ocv_fit4];
50 figure
51 fitVvvocv(I_pulse, DVocvf)
52 close
53 dVvocf_dJ = cf_1.p1
54 Vvoc0 = cf_1.p2;
55 figure
56 FIT1_res(sqtt1,vv1)
57 figure
58 FIT2_res(sqtt2,vv2)
59 figure
60 FIT3_res(sqtt3,vv3)
61 figure
62 FIT4_res(sqtt4,vv4)

1
2 D_delta1 = (1/pi)*((2*L1*Esp1)/(tau1*dE_dsqt1))^2; %chemical D
           of pulse1
3 D_delta2 = (1/pi)*((2*L2*Esp2)/(tau2*dE_dsqt2))^2; %chemical D
           of pulse2
4 D_delta3 = (1/pi)*((2*L3*Esp3)/(tau3*dE_dsqt3))^2; %chemical D
           of pulse3

```

```

5 D_delta4 = (1/pi)*((2*L4*Esp4)/(tau4*dE_dsqt4))^2; %chemical
   D of pulse4
6 D_delta = [D_delta1 D_delta2 D_delta3 D_delta4];
7 D_delta_avg = mean(D_delta)
8
9 pctdiff(D_delta);
10 D_delta_pct_diff = pct_diff;
11
12 D_Ca_delta1 = D_delta1/dlna_dlnx_1; %component D of pulse1
13 D_Ca_delta2 = D_delta2/dlna_dlnx_2;
14 D_Ca_delta3 = D_delta3/dlna_dlnx_3;
15 D_Ca_delta4 = D_delta4/dlna_dlnx_4;
16 D_Ca_delta = [D_Ca_delta1 D_Ca_delta2 D_Ca_delta3 D_Ca_delta4
   ];
17 D_Ca_delta_avg = mean(D_Ca_delta)
18
19 pctdiff(D_Ca_delta);
20 D_Ca_delta_pct_diff = pct_diff;

1 global tp1_low tp1_high tp2_low tp2_high tp3_low tp3_high
   tp4_low tp4_high
2 global cf_1 cf_2 cf_3 cf_4 pct_diff;
3
4 a1 = 10;
5 a2 = 20;
6 tp1_low = a1;
7 tp1_high = a2;
8
9 tp2_low = a1;
10 tp2_high = a2;
11
12 tp3_low = a1;

```

```

13 tp3_high = a2;
14
15 tp4_low = a1;
16 tp4_high = a2;
17
18 createFit_bounded(sqtt1,vv1,sqtt2,vv2,sqtt3,vv3,sqtt4,vv4);
19
20 dE_dsqt_bnd1 = cf_1.p1;
21 dE_dsqt_bnd2 = cf_2.p1;
22 dE_dsqt_bnd3 = cf_3.p1;
23 dE_dsqt_bnd4 = cf_4.p1;
24
25 dE_dsqt_bnd = [dE_dsqt_bnd1 dE_dsqt_bnd2 dE_dsqt_bnd3
                dE_dsqt_bnd4];
26
27 Dchem_fixed1 = (1/pi)*((2*dEdx(1)*L1*Bi_mol*Ca_ti_p1)/((Bi_mol
                +Ca_mol)^2*tau1*dE_dsqt_bnd1))^2; %chemical D of pulse1
28 Dchem_fixed2 = (1/pi)*((2*dEdx(2)*L1*Bi_mol*Ca_ti_p2)/((Bi_mol
                +Ca_mol+Ca_ti_p1)^2*tau2*dE_dsqt_bnd2))^2;%chemical D of
                pulse2
29 Dchem_fixed3 = (1/pi)*((2*dEdx(3)*L1*Bi_mol*Ca_ti_p3)/((Bi_mol
                +Ca_mol+Ca_ti_p1+Ca_ti_p2)^2*tau3*dE_dsqt_bnd3))^2; %
                chemical D of pulse3
30 Dchem_fixed4 = (1/pi)*((2*dEdx(4)*L1*Bi_mol*Ca_ti_p4)/((Bi_mol
                +Ca_mol+Ca_ti_p1+Ca_ti_p2+Ca_ti_p3)^2*tau4*dE_dsqt_bnd4))
                ^2;%chemical D of pulse4
31 Dchem_fixed = [Dchem_fixed1 Dchem_fixed2 Dchem_fixed3
                Dchem_fixed4];
32
33 pctdiff(Dchem_fixed);
34 Dchmfxd_diff_pct_diff = pct_diff;
35 Dchem_fxd_avg = mean(Dchem_fixed);

```

```

36 D_fixed_poly_exp;

1 function createFit_bounded(sqtt1,vv1,sqtt2,vv2,sqtt3,vv3,sqtt4
   ,vv4)
2 global tp1_low tp1_high tp2_low tp2_high tp3_low tp3_high
   tp4_low tp4_high
3 global cf_1 cf_2 cf_3 cf_4
4
5 %CREATEFIT Create plot of data sets and fits
6 % CREATEFIT(SQTT1,VV1,SQTT2,VV2,SQTT3,VV3,SQTT4,VV4)
7 % Creates a plot, similar to the plot in the main Curve
   Fitting Tool,
8 % using the data that you provide as input. You can
9 % use this function with the same data you used with CFTOOL
10 % or with different data. You may want to edit the function
   to
11 % customize the code and this help message.
12 %
13 % Number of data sets: 4
14 % Number of fits: 4
15
16 % Data from data set "vv1 vs. sqtt1":
17 % X = sqtt1:
18 % Y = vv1:
19 % Unweighted
20
21 % Data from data set "vv2 vs. sqtt2":
22 % X = sqtt2:
23 % Y = vv2:
24 % Unweighted
25
26 % Data from data set "vv3 vs. sqtt3":

```

```

27 %      X = sqtt3:
28 %      Y = vv3:
29 %      Unweighted
30
31 % Data from data set "vv4 vs. sqtt4":
32 %      X = sqtt4:
33 %      Y = vv4:
34 %      Unweighted
35
36 % Auto-generated by MATLAB on 04-Feb-2013 18:25:37
37
38 %% Set up figure to receive data sets and fits
39 f_ = clf;
40 figure(f_);
41 set(f_,'Units','Pixels','Position',[905 1 672 481]);
42 % Line handles and text for the legend.
43 legh_ = [];
44 legt_ = {};
45 % Limits of the x-axis.
46 xlim_ = [Inf -Inf];
47 % Axes for the main plot.
48 ax_ = axes;
49 set(ax_,'Units','normalized','OuterPosition',[0 .5 1 .5]);
50 % Axes for the residuals plot.
51 ax2_ = axes;
52 set(ax2_,'Units','normalized','OuterPosition',[0 0 1 .5]);
53 set(ax2_,'Box','on');
54 % Line handles and text for the residuals plot legend.
55 legrh_ = [];
56 legrt_ = {};
57 set(ax_,'Box','on');
58 axes(ax_);

```

```

59 hold on;
60
61 %% --- Plot data that was originally in data set "vv1 vs.
      sqtt1"
62 sqtt1 = sqtt1(:);
63 vv1 = vv1(:);
64 h_ = line(sqtt1,vv1,'Parent',ax_,'Color',[0.333333 0
      0.666667],...
65         'LineStyle','none', 'LineWidth',1,...
66         'Marker','.', 'MarkerSize',12);
67 xlim_(1) = min(xlim_(1),min(sqtt1));
68 xlim_(2) = max(xlim_(2),max(sqtt1));
69 legh_(end+1) = h_;
70 legt_{end+1} = 'vv1 vs. sqtt1';
71
72 % --- Plot data that was originally in data set "vv2 vs. sqtt2
      "
73 sqtt2 = sqtt2(:);
74 vv2 = vv2(:);
75 h_ = line(sqtt2,vv2,'Parent',ax_,'Color',[0.333333 0.666667
      0],...
76         'LineStyle','none', 'LineWidth',1,...
77         'Marker','.', 'MarkerSize',12);
78 xlim_(1) = min(xlim_(1),min(sqtt2));
79 xlim_(2) = max(xlim_(2),max(sqtt2));
80 legh_(end+1) = h_;
81 legt_{end+1} = 'vv2 vs. sqtt2';
82
83 % --- Plot data that was originally in data set "vv3 vs. sqtt3
      "
84 sqtt3 = sqtt3(:);
85 vv3 = vv3(:);

```



```

86 h_ = line(sqtt3,vv3,'Parent',ax_,'Color',[0 0 0],...
87     'LineStyle','none', 'LineWidth',1,...
88     'Marker','.', 'MarkerSize',12);
89 xlim_(1) = min(xlim_(1),min(sqtt3));
90 xlim_(2) = max(xlim_(2),max(sqtt3));
91 legh_(end+1) = h_;
92 legtf_{end+1} = 'vv3 vs. sqtt3';
93
94 % --- Plot data that was originally in data set "vv4 vs. sqtt4
    "
95 sqtt4 = sqtt4(:);
96 vv4 = vv4(:);
97 h_ = line(sqtt4,vv4,'Parent',ax_,'Color',[0.333333 1
    0.666667],...
98     'LineStyle','none', 'LineWidth',1,...
99     'Marker','.', 'MarkerSize',12);
100 xlim_(1) = min(xlim_(1),min(sqtt4));
101 xlim_(2) = max(xlim_(2),max(sqtt4));
102 legh_(end+1) = h_;
103 legtf_{end+1} = 'vv4 vs. sqtt4';
104
105 %% Nudge axis limits beyond data limits
106 if all(isfinite(xlim_))
107     xlim_ = xlim_ + [-1 1] * 0.01 * diff(xlim_);
108     set(ax_,'XLim',xlim_)
109     set(ax2_,'XLim',xlim_)
110 else
111     set(ax_,'XLim',[-0.75173133498611055536,
        75.924864833597155211]);
112     set(ax2_,'XLim',[-0.75173133498611055536,
        75.924864833597155211]);
113 end

```

```

114
115 %% --- Create fit "fit 1"
116
117 % Apply exclusion rule "bound"
118 ex_ = (sqtt1 <= tp1_low | sqtt1 >= tp1_high);
119 ok_ = isfinite(sqtt1) & isfinite(vv1);
120 if ~all( ok_ )
121     warning( 'GenerateMFile:IgnoringNansAndInfs',...
122             'Ignoring NaNs and Infs in data.' );
123 end
124 ft_ = fittype('poly1');
125
126 % Fit this model using new data
127 if sum(~ex_(ok_))<2
128     % Too many points excluded.
129     error( 'GenerateMFile:NotEnoughDataAfterExclusionRule',...
130           'Not enough data left to fit ''s'' after applying
131           exclusion rule ''s''.',...
132           'fit 1', 'bound' );
133 else
134     cf_1 = fit(sqtt1(ok_),vv1(ok_),ft_,'Exclude',ex_(ok_));
135 end
136 % Alternatively uncomment the following lines to use
137 % coefficients from the
138 % original fit. You can use this choice to plot the original
139 % fit against new
140 % data.
141 %     cv_ = { -1.8926162002725882002e-05,
142 %           0.062601823024445474308};
143 %     cf_ = cfit(ft_,cv_{:});
144
145 % Plot this fit

```

```

142 h_ = plot(cf_1,'fit',0.95);
143 set(h_(1),'Color',[1 0 0],...
144     'LineStyle','-','LineWidth',2,...
145     'Marker','none','MarkerSize',6);
146 % Turn off legend created by plot method.
147 legend off;
148 % Store line handle and fit name for legend.
149 legh_(end+1) = h_(1);
150 legt_{end+1} = 'fit 1';
151
152 % Compute and plot residuals.
153 res_ = vv1(~ex_) - cf_1(sqtt1(~ex_));
154 [x_,i_] = sort(sqtt1(~ex_));
155 axes(ax2_);
156 hold on;
157 h_ = line(x_,res_(i_), 'Parent',ax2_,'Color',[1 0 0],...
158     'LineStyle','none','LineWidth',1,...
159     'Marker','.', 'MarkerSize',6);
160 axes(ax_);
161 hold on;
162 legrh_(end+1) = h_;
163 legrt_{end+1} = 'fit 1';
164
165 %% --- Create fit "fit 2"
166
167 % Apply exclusion rule "bound2"
168 ex_ = (sqtt2 <= tp2_low | sqtt2 >= tp2_high);
169 ok_ = isfinite(sqtt2) & isfinite(vv2);
170 if ~all( ok_ )
171     warning( 'GenerateMFile:IgnoringNansAndInfs',...
172             'Ignoring NaNs and Infs in data.' );
173 end

```

```

174 ft_ = fittype('poly1');
175
176 % Fit this model using new data
177 if sum(~ex_(ok_))<2
178     % Too many points excluded.
179     error( 'GenerateMFile:NotEnoughDataAfterExclusionRule',...
180         'Not enough data left to fit ''s'' after applying
181         exclusion rule ''s''.',...
182         'fit 2', 'bound2' );
183 else
184     cf_2 = fit(sqtt2(ok_),vv2(ok_),ft_,'Exclude',ex_(ok_));
185 end
186 % Alternatively uncomment the following lines to use
187 % coefficients from the
188 % original fit. You can use this choice to plot the original
189 % fit against new
190 % data.
191 % cv_ = { -2.7446888792954034127e-05,
192 %         0.060715683994276063717};
193 % cf_ = cfit(ft_,cv_{:});
194
195 % Plot this fit
196 h_ = plot(cf_2,'fit',0.95);
197 set(h_(1),'Color',[0 0 1],...
198     'LineStyle','-','LineWidth',2,...
199     'Marker','none','MarkerSize',6);
200 % Turn off legend created by plot method.
201 legend off;
202 % Store line handle and fit name for legend.
203 legh_(end+1) = h_(1);
204 legt_{end+1} = 'fit 2';
205

```

```

202 % Compute and plot residuals.
203 res_ = vv2(~ex_) - cf_2(sqtt2(~ex_));
204 [x_,i_] = sort(sqtt2(~ex_));
205 axes(ax2_);
206 hold on;
207 h_ = line(x_,res_(i_), 'Parent',ax2_,'Color',[0 0 1],...
208         'LineStyle','none', 'LineWidth',1,...
209         'Marker','.', 'MarkerSize',6);
210 axes(ax_);
211 hold on;
212 legrh_(end+1) = h_;
213 legrt_{end+1} = 'fit 2';
214
215 %% --- Create fit "fit 3"
216
217 % Apply exclusion rule "bound3"
218 ex_ = (sqtt3 <= tp3_low | sqtt3 >= tp3_high);
219 ok_ = isfinite(sqtt3) & isfinite(vv3);
220 if ~all( ok_ )
221     warning( 'GenerateMFile:IgnoringNansAndInfs',...
222             'Ignoring NaNs and Infs in data.' );
223 end
224 ft_ = fittype('poly1');
225
226 % Fit this model using new data
227 if sum(~ex_(ok_))<2
228     % Too many points excluded.
229     error( 'GenerateMFile:NotEnoughDataAfterExclusionRule',...
230           'Not enough data left to fit ''s'' after applying
231           exclusion rule ''s''.',...
232           'fit 3', 'bound3' );
233 else

```

```

233     cf_3 = fit(sqrtt3(ok_),vv3(ok_),ft_,'Exclude',ex_(ok_));
234 end
235 % Alternatively uncomment the following lines to use
      coefficients from the
236 % original fit. You can use this choice to plot the original
      fit against new
237 % data.
238 %     cv_ = { -3.5146749800720710193e-05,
      0.058798706315903385977};
239 %     cf_ = cfit(ft_,cv_{:});
240
241 % Plot this fit
242 h_ = plot(cf_3,'fit',0.95);
243 set(h_(1),'Color',[0.666667 0.333333 0],...
244     'LineStyle','-','LineWidth',2,...
245     'Marker','none','MarkerSize',6);
246 % Turn off legend created by plot method.
247 legend off;
248 % Store line handle and fit name for legend.
249 legh_(end+1) = h_(1);
250 legt_{end+1} = 'fit 3';
251
252 % Compute and plot residuals.
253 res_ = vv3(~ex_) - cf_3(sqrtt3(~ex_));
254 [x_,i_] = sort(sqrtt3(~ex_));
255 axes(ax2_);
256 hold on;
257 h_ = line(x_,res_(i_), 'Parent',ax2_,'Color',[0.666667 0.333333
      0],...
258     'LineStyle','none','LineWidth',1,...
259     'Marker','.', 'MarkerSize',6);
260 axes(ax_);

```

```

261 hold on;
262 legrh_(end+1) = h_;
263 legrt_{end+1} = 'fit 3';
264
265 %% --- Create fit "fit 4"
266
267 % Apply exclusion rule "bound4"
268 ex_ = (sqtt4 <= tp4_low | sqtt4 >= tp4_high);
269 ok_ = isfinite(sqtt4) & isfinite(vv4);
270 if ~all( ok_ )
271     warning( 'GenerateMFile:IgnoringNansAndInfs',...
272             'Ignoring NaNs and Infs in data.' );
273 end
274 ft_ = fittype('poly1');
275
276 % Fit this model using new data
277 if sum(~ex_(ok_))<2
278     % Too many points excluded.
279     error( 'GenerateMFile:NotEnoughDataAfterExclusionRule',...
280           'Not enough data left to fit ''s'' after applying
281           exclusion rule ''s''.',...
282           'fit 4', 'bound4' );
283 else
284     cf_4 = fit(sqtt4(ok_),vv4(ok_),ft_,'Exclude',ex_(ok_));
285 end
286 % Alternatively uncomment the following lines to use
287 % coefficients from the
288 % original fit. You can use this choice to plot the original
289 % fit against new
290 % data.
291 % cv_ = { -4.1313451369437088673e-05,
292          0.056886936326529982666};

```

```

289 %   cf_ = cfit(ft_,cv_{:});
290
291 % Plot this fit
292 h_ = plot(cf_4,'fit',0.95);
293 set(h_(1),'Color',[0.333333 0.333333 0.333333],...
294     'LineStyle','-','LineWidth',2,...
295     'Marker','none','MarkerSize',6);
296 % Turn off legend created by plot method.
297 legend off;
298 % Store line handle and fit name for legend.
299 legh_(end+1) = h_(1);
300 legt_{end+1} = 'fit 4';
301
302 % Compute and plot residuals.
303 res_ = vv4(~ex_) - cf_4(sqtt4(~ex_));
304 [x_,i_] = sort(sqtt4(~ex_));
305 axes(ax2_);
306 hold on;
307 h_ = line(x_,res_(i_), 'Parent',ax2_,'Color',[0.333333 0.333333
308     0.333333],...
309     'LineStyle','none','LineWidth',1,...
310     'Marker','.', 'MarkerSize',6);
311 axes(ax_);
312 hold on;
313 legrh_(end+1) = h_;
314 legrt_{end+1} = 'fit 4';
315
316 %% --- Finished fitting and plotting data. Clean up.
317 hold off;
318 % % Display legend
319 % leginfo_ = {'Orientation','vertical','Location','NorthEast'};

```



```

319 % h_ = legend(ax_, legh_, legt_, leginfo_{:});
320 % set(h_, 'Interpreter', 'none');
321 % leginfo_ = {'Orientation', 'vertical', 'Location', '
      NorthEast'}; % properties of resid legend
322 % h_ = legend(ax2_, legrh_, legrt_, leginfo_{:});
323 % set(h_, 'Interpreter', 'none');
324 % Remove labels from x- and y-axes.
325 xlabel(ax_, '');
326 ylabel(ax_, '');
327 xlabel(ax2_, '');
328 ylabel(ax2_, '');
329 % Add titles to the plots.
330 title(ax_, 'Data and Fits');
331 title(ax2_, 'Residuals');
332 set(f_, 'PaperSize', [7 5]); %Set the paper to have width 5
      and height 5.
333 set(f_, 'PaperPosition', [0 0 7 5]);
334 saveas(f_, '@@FIXED_Fit_pulses_vs_sqttime', 'pdf')
335 saveas(f_, '@@FIXED_Fit_pulses_vs_sqttime', 'fig')

1 %%Takes into account the shape of the E vs XCa curve
2 global pct_diff cf_1 cf_2 E_ocv
3 X_Ca = [X_Ca1 X_Ca2 X_Ca3 X_Ca4 X_Ca_pulse4];
4 Eocv = [E_ocv(1) E_ocv(3) E_ocv(6) E_ocv(9) E_ocv(12)];
5 createFit_dEdX_exp(X_Ca, Eocv);
6 createFit_dEdX_poly(X_Ca, Eocv);
7 createFit_dEdX_exp_poly(X_Ca, Eocv);
8 var_a = cf_1.a;
9 var_b = cf_1.b;
10 var_c = cf_1.c;
11 var_d = cf_1.d;
12 %slope of linear fit E(XCa) = cf_2.p1*XCa+cf_2.p2

```

```

13 var_p1 = cf_2.p1;
14 var_p2 = cf_2.p2;
15 syms XCa
16 E = var_a*exp(var_b*XCa)+var_c*exp(var_d*XCa);
17 E_lin = var_p1*XCa+var_p2;
18 dEdXCa = diff(E);
19 delta = .00125;
20 dEdX_fixe1 = subs(dEdXCa,X_Ca1+delta);
21 dEdX_fixe2 = subs(dEdXCa,X_Ca2+delta);
22 dEdX_fixe3 = subs(dEdXCa,X_Ca3+delta);
23 dEdX_fixe4 = subs(dEdXCa,X_Ca4+delta);
24 dEdX_fixe5 = subs(dEdXCa,X_Ca_pulse4+delta);
25 D_fixe1 = (1/pi)*((2*dEdX_fixe1*L1*Bi_mol*Ca_ti_p1)/((Bi_mol+
    Ca_mol)^2*tau1*dE_dsqt_bnd1))^2; %chemical D of pulse1
26 D_fixe2 = (1/pi)*((2*dEdX_fixe2*L1*Bi_mol*Ca_ti_p2)/((Bi_mol+
    Ca_mol+Ca_ti_p1)^2*tau2*dE_dsqt_bnd2))^2; %chemical D of
    pulse2
27 D_fixe3 = (1/pi)*((2*dEdX_fixe3*L1*Bi_mol*Ca_ti_p3)/((Bi_mol+
    Ca_mol+Ca_ti_p1+Ca_ti_p2)^2*tau3*dE_dsqt_bnd3))^2; %
    chemical D of pulse3
28 D_fixe4 = (1/pi)*((2*dEdX_fixe4*L1*Bi_mol*Ca_ti_p4)/((Bi_mol+
    Ca_mol+Ca_ti_p1+Ca_ti_p2+Ca_ti_p3)^2*tau4*dE_dsqt_bnd4))^2;
    %chemical D of pulse4
29 D_fixe = [D_fixe1 D_fixe2 D_fixe3 D_fixe4];
30 D_fixe_avg = mean(D_fixe)
31 pctdiff(D_fixe);
32 D_fixe_pct_diff = pct_diff;
33 %% Linear Fit
34 dEdXCa_lin = diff(E_lin);
35 D_fixp1 = (1/pi)*((2*subs(dEdXCa_lin,X_Ca1)*L1*Bi_mol*Ca_ti_p1
    )/((Bi_mol+Ca_mol)^2*tau1*dE_dsqt_bnd1))^2; %chemical D of
    pulse1

```

```

36 D_fixp2 = (1/pi)*((2*subs(dEdXCa_lin,X_Ca2)*L1*Bi_mol*Ca_ti_p2
    )/((Bi_mol+Ca_mol+Ca_ti_p1)^2*tau2*dE_dsqt_bnd2))^2; %
    chemical D of pulse2
37 D_fixp3 = (1/pi)*((2*subs(dEdXCa_lin,X_Ca3)*L1*Bi_mol*Ca_ti_p3
    )/((Bi_mol+Ca_mol+Ca_ti_p1+Ca_ti_p2)^2*tau3*dE_dsqt_bnd3))
    ^2; %chemical D of pulse3
38 D_fixp4 = (1/pi)*((2*subs(dEdXCa_lin,X_Ca4)*L1*Bi_mol*Ca_ti_p4
    )/((Bi_mol+Ca_mol+Ca_ti_p1+Ca_ti_p2+Ca_ti_p3)^2*tau4*
    dE_dsqt_bnd4))^2;%chemical D of pulse4
39 D_fixp = [D_fixp1 D_fixp2 D_fixp3 D_fixp4];
40 D_fixp_avg = mean(D_fixp)
41 pctdiff(D_fixp);
42 D_fixp_pct_diff = pct_diff;
43 plotPulseSeq_Temp(Time_pulse./3600,Volt_pulse,TimeT./3600,Temp
    );
44 figure
45 plotD_ALL(J_pulse, Dchem_fixed,J_pulse, D_fixe,J_pulse, D_fixp
    );
46 GITT_linear_nonlinear_sep;

1 global V_ocv_std sigma_E1 sigma_E2 sigma_E3 sigma_E4
    D_chem_unc1 D_chem_unc2 D_chem_unc3 D_chem_unc4 D_sigEav
    Eo_std
2
3 V_relax1 = voltp{:,1};
4 V_relax2 = voltp{:,3};
5 V_relax3 = voltp{:,6};
6 V_relax4 = voltp{:,9};
7 V_relax5 = voltp{:,12};
8
9

```

```

10 V_ocv_mean1 = mean(V_relax1(numel(V_relax1)-250:numel(V_relax1
    )));
11 V_ocv_mean2 = mean(V_relax2(numel(V_relax2)-250:numel(V_relax2
    )));
12 V_ocv_mean3 = mean(V_relax3(numel(V_relax3)-250:numel(V_relax3
    )));
13 V_ocv_mean4 = mean(V_relax4(numel(V_relax4)-250:numel(V_relax4
    )));
14 V_ocv_mean5 = mean(V_relax5(numel(V_relax5)-250:numel(V_relax5
    )));
15
16 V_ocv_mean = [V_ocv_mean1 V_ocv_mean2 V_ocv_mean3 V_ocv_mean4
    V_ocv_mean5];
17
18
19 V_ocv_std1 = std(V_relax1(numel(V_relax1)-250:numel(V_relax1))
    );
20 V_ocv_std2 = std(V_relax2(numel(V_relax2)-250:numel(V_relax2))
    );
21 V_ocv_std3 = std(V_relax3(numel(V_relax3)-250:numel(V_relax3))
    );
22 V_ocv_std4 = std(V_relax4(numel(V_relax4)-250:numel(V_relax4))
    );
23 V_ocv_std5 = std(V_relax5(numel(V_relax5)-250:numel(V_relax5))
    );
24
25 V_ocv_std = [V_ocv_std1 V_ocv_std2 V_ocv_std3 V_ocv_std4
    V_ocv_std5];
26
27 V_ocv_frac_unc = V_ocv_std./V_ocv_mean;
28
29 sigma_E1 = sqrt(V_ocv_std1^2+V_ocv_std2^2);

```

```

30 sigma_E2 = sqrt(V_ocv_std2^2+V_ocv_std3^2);
31 sigma_E3 = sqrt(V_ocv_std3^2+V_ocv_std4^2);
32 sigma_E4 = sqrt(V_ocv_std4^2+V_ocv_std5^2);
33
34 sigma_E = [sigma_E1 sigma_E2 sigma_E3 sigma_E4];
35
36 pulse_num = [1 2 3 4];
37
38 E_sq_unc = 2*sigma_E./abs(Esp);
39
40 a= 0.1193;
41 del_a = 4e-4;
42
43 % b1 = abs(Esp1);
44 % b2 = abs(Esp2);
45 % b3 = abs(Esp3);
46 % b4 = abs(Esp4);
47 %
48 % del_b1 = sigma_E1;
49 % del_b2 = sigma_E2;
50 % del_b3 = sigma_E3;
51 % del_b4 = sigma_E4;
52
53 b1 = abs(dEdx(1));
54 b2 = abs(dEdx(2));
55 b3 = abs(dEdx(3));
56 b4 = abs(dEdx(4));
57
58 del_b1 = std(dEdx);
59 del_b2 = std(dEdx);
60 del_b3 = std(dEdx);
61 del_b4 = std(dEdx);

```

```

62 c = .275;
63 del_c = .002;
64 d = tau1;
65 del_d = 1e-6;
66 f1 = dE_dsqt_bnd1;
67 del_f1 = sigma_E1/sqrt(tau1);
68 f2 = dE_dsqt_bnd2;
69 del_f2 = sigma_E2/sqrt(tau2);
70 f3 = dE_dsqt_bnd3;
71 del_f3 = sigma_E3/sqrt(tau3);
72 f4 = dE_dsqt_bnd4;
73 del_f4 = sigma_E4/sqrt(tau4);
74
75 sigma_D1 = 2*sqrt((del_a/a)^2+(del_b1/b1)^2+(del_c/c)^2+(del_d
    /d)^2+(del_f1/f1)^2);
76 sigma_D2 = 2*sqrt((del_a/a)^2+(del_b2/b2)^2+(del_c/c)^2+(del_d
    /d)^2+(del_f2/f2)^2);
77 sigma_D3 = 2*sqrt((del_a/a)^2+(del_b3/b3)^2+(del_c/c)^2+(del_d
    /d)^2+(del_f3/f3)^2);
78 sigma_D4 = 2*sqrt((del_a/a)^2+(del_b4/b4)^2+(del_c/c)^2+(del_d
    /d)^2+(del_f4/f4)^2);
79
80 sigma_D =[sigma_D1 sigma_D2 sigma_D3 sigma_D4];
81
82 D_chem_unc = sigma_D.*Dchem_fixed;
83 D_chem_unc1 = D_chem_unc(1);
84 D_chem_unc2 = D_chem_unc(2);
85 D_chem_unc3 = D_chem_unc(3);
86 D_chem_unc4 = D_chem_unc(4);
87
88 Eoav = mean(abs(dEdx));
89 Eo_std = std(dEdx);

```

```
90 sigma_Eavg = 2*Eo_std/Eoav
91 D_sigEav = sigma_Eavg*Dchem_fxd_avg
92
93
94
95 createFit_ocv_poly(pulse_num,dEdx)
```


Appendix G

Conservation Equations

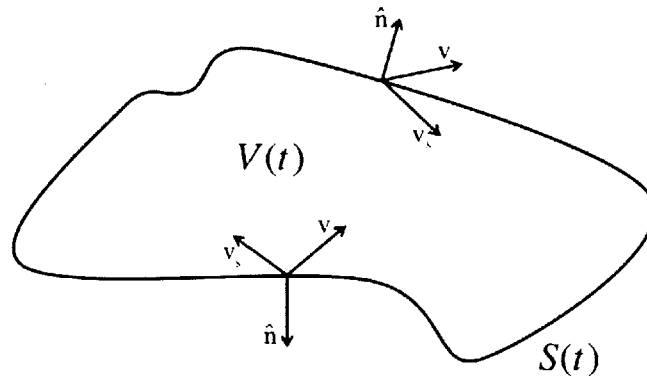


Figure G-1: Control volume $V(t)$ with surface area $S(t)$ that can change with time. The surface normal vector ($\hat{\mathbf{n}}$), surface velocity \mathbf{v}_S , and fluid velocity (\mathbf{v}) all vary with surface position and time.

It is extremely important to know very well how these fundamental equations are derived and applied to specific systems when doing multi-physics modeling. Conservation equations are derived from the basis of continuum mechanics under the assumption that a conserved quantity cannot be created or destroyed, it can only be transported between places in a continuous motion. In elementary physics one learns about the types of conserved quantities that exist such as mass, energy, and momentum, and how to convert between one form to another. For example, we've all heard of Einstein's famous $E = mc^2$ equation to which most can recite without even knowing that it's actually a conservation statement. So how does one begin to con-

serve physical quantities? Imagine a *control volume* $V(t)$ exists in a region of space with the surface area $S(t)$ and can evolve with time (fig. G-1). Also, imagine there's a concentration $c(\mathbf{r}, t)$ of stuff with a corresponding flux $\mathbf{J}(\mathbf{r}, t)$ within the control volume, and that this "stuff" can be added at a volumetric rate $R_V(\mathbf{r}, t)$ ¹. Note that since the control volume is not static, the surface area can sweep regions at a rate proportional to the surface velocity given by $\mathbf{v}_S \cdot \hat{\mathbf{n}} dS$. Now if we add up all the components mentioned above to account for the total amount of stuff accumulated per unit time inside the control volume, we arrive at the following conservation of "stuff":

$$\frac{d}{dt} \int_{V(t)} c(\mathbf{r}, t) dV = - \int_{S(t)} \mathbf{J}(\mathbf{r}, t) \cdot \hat{\mathbf{n}} dS + \int_{V(t)} R_V(\mathbf{r}, t) dV + \int_{S(t)} c(\mathbf{r}, t) \mathbf{v}_S \cdot \hat{\mathbf{n}} dS. \quad (\text{G.1})$$

Equation G.1 can be further simplified by invoking the *Leibniz rule* for differentiating Integrals which states that integrals with variable limits of integration can be written as:

$$\frac{d}{dt} \int_{V(t)} f(\mathbf{r}, t) dV = \int_{V(t)} \frac{\partial f}{\partial t} dV + \int_{S(t)} (\hat{\mathbf{n}} \cdot \mathbf{v}_S) f dS. \quad (\text{G.2})$$

Substituting equation G.2 appropriately into G.1 yields a more simplified version that does not depend on the surface velocity \mathbf{v}_S given by:

$$\int_{V(t)} \frac{\partial c}{\partial t} dV = - \int_{S(t)} \mathbf{J}(\mathbf{r}, t) \cdot \hat{\mathbf{n}} dS + \int_{V(t)} R_V(\mathbf{r}, t) dV. \quad (\text{G.3})$$

Now, what equation G.3 is really saying is that as long as the concentration variable $c(\mathbf{r}, t)$ remains continuous throughout the control volume, this general conservation equation will always hold.

If we apply *Gauss's theorem*, which states that the volume integral of the divergence of a vector field is equal to flux of the field across the surface enclosing the volume,

¹If its removal rather than accumulation, the volumetric rate of production switches signs to $-R_V(\mathbf{r}, t)$

$$\int_V (\nabla \cdot \mathbf{J}) dV = \int_S (\mathbf{J} \cdot \hat{\mathbf{n}}) dS, \quad (\text{G.4})$$

to the surface integral in equation G.3, then we can rewrite the integral equation as

$$\int_{V(t)} \frac{\partial c}{\partial t} dV = - \int_{V(t)} (\nabla \cdot \mathbf{J}) dV + \int_{V(t)} R_V(\mathbf{r}, t) dV \quad (\text{G.5})$$

which can be further rewritten down to

$$\int_{V(t)} \left(\frac{\partial c}{\partial t} + (\nabla \cdot \mathbf{J}) - R_V \right) dV = 0. \quad (\text{G.6})$$

This is a powerful statement. In the limit the control volume goes to zero ($V \rightarrow 0$), the argument inside the integral of equation G.6 remains constant making it a valid general conservation equation down to a point in space. So with this, we can write the general conservation equation in differential form²

$$\frac{\partial c}{\partial t} = -\nabla \cdot \mathbf{J} + R_V \quad (\text{G.7})$$

which yields the partial differential equations (PDE's) needed to describe the transient evolution of the conserved quantity of interest.

We can then solve the PDE's to obtain solutions for the desired extensive property that contains all the information regarding the history in time and position of how it evolved. Since we are on the topic of conserved entities, we would like to show how we can use equation G.7 to derive the conservation equations for mass, energy, and momentum. One thing to note is that the total flux \mathbf{J} can be written as the sum of diffusive (\mathbf{j}) and convective ($c\mathbf{u}$) fluxes ($\mathbf{J} = \mathbf{j} + c\mathbf{u}$) so, before continuing with the derivations we rewrite equation G.7 as

$$\frac{\partial c}{\partial t} = -\nabla \cdot (\mathbf{j} + c\mathbf{u}) + R_V. \quad (\text{G.8})$$

²For simplicity, let $c(\mathbf{r}, t) = c$, $\mathbf{J}(\mathbf{r}, t) = \mathbf{J}$, and $R_V(\mathbf{r}, t) = R_V$

Bibliography

- [1] P. Denholm and R. M. Margolis, "Evaluating the limits of solar photovoltaics (PV) in traditional electric power systems," *Energy Policy*, vol. 35, no. 5, pp. 2852–2861, 2007.
- [2] H. Kim, D. A. Boysen, J. M. Newhouse, B. L. Spatocco, B. Chung, P. J. Burke, D. J. Bradwell, K. Jiang, A. A. Tomaszowska, K. Wang, W. Wei, L. A. Ortiz, S. A. Barriga, S. M. Poizeau, and D. R. Sadoway, "Liquid Metal Batteries: Past, Present, and Future," *Chemical Reviews*, p. 121127124032006, Nov. 2012.
- [3] I. Gyuk, *Energy Storage for Grid Connected Wind Generation Applications*. US. DOE, 1000 Independence Ave., S.W. Washington, DC 20585: EPRI PAEC Corporation, Dec. 2004.
- [4] D. J. Bradwell, *Liquid metal batteries : ambipolar electrolysis and alkaline earth electroalloying cells*. PhD thesis, Massachusetts Institute of Technology, Feb. 2011.
- [5] G. Survey, *Mineral Commodity Summaries*. 2012, Geological Survey, Apr. 2012.
- [6] K. Grjotheim and H. Kvande, *Introduction to Aluminum Electrolysis*. Aluminum-Verlag, 2 ed., 1993.
- [7] A.-M. popescu and V. Constantin, "The influence of interelectrode distance on current efficiency in aluminum electrolysis with an inert anode," *Bulgarian Chemical Communications*, vol. 32, no. 2, pp. 140–149, 2000.
- [8] H. Kvande, "Introduction to Aluminium Electrolysis," 1993.
- [9] D. J. Bradwell, H. Kim, A. H. C. Sirk, and D. R. Sadoway, "Magnesium–Antimony Liquid Metal Battery for Stationary Energy Storage," *Journal of the American Chemical Society*, vol. 134, pp. 1895–1897, Feb. 2012.
- [10] E. J. Cairns, C. E. Crouthamel, A. K. Fischer, M. S. Foster, J. C. Hesson, C. E. Johnson, H. Shimotake, and A. D. Tevebaugh, "GALVANIC CELLS WITH FUSED-SALT ELECTROLYTES.," tech. rep., Argonne National Laboratory (ANL), Argonne, IL (United States), Jan. 1967.

- [11] D. Bradwell, “Technical and Economical Feasibility of a High-Temperature Self-Assembling Battery,” Master’s thesis, Massachusetts Institute of Technology, 77 Massachusetts Ave, Cambridge, MA 02139, Sept. 2006.
- [12] W. H. Woodford, Y.-M. Chiang, and W. C. Carter, ““Electrochemical Shock” of Intercalation Electrodes: A Fracture Mechanics Analysis,” *Journal of the Electrochemical . . .*, 2010.
- [13] W. H. Woodford, Y.-M. Chiang, and W. C. Carter, “Electrochemical Shock of Polycrystalline Lithium Battery Materials,” *Meeting Abstracts*, 2011.
- [14] W. H. Woodford, W. C. Carter, and Y.-M. Chiang, “Design criteria for electrochemical shock resistant battery electrodes ,” *Energy & Environmental Science*, vol. 5, no. 7, pp. 8014–8024, 2012.
- [15] D. J. Bradwell, S. Osswald, W. Wei, S. A. Barriga, G. Ceder, and D. R. Sadoway, “Recycling ZnTe, CdTe, and Other Compound Semiconductors by Ambipolar Electrolysis,” *Journal of the American Chemical Society*, vol. 133, pp. 19971–19975, Dec. 2011.
- [16] H. Okamoto, “Ca-Sb (Calcium-Antimony),” *Journal of Phase Equilibria*, vol. 18, pp. 313–313, June 1997.
- [17] H. Kim, D. A. Boysen, D. J. Bradwell, B. Chung, K. Jiang, A. A. Tomaszowska, K. Wang, W. Wei, and D. R. Sadoway, “Thermodynamic properties of calcium–bismuth alloys determined by emf measurements,” *Electrochimica Acta*, vol. 60, pp. 154–162, Jan. 2012.
- [18] R. W. Balluffi, S. M. Allen, W. C. Carter, and R. A. Kemper, *Kinetics of Materials*. J. Wiley and Sons, 2005.
- [19] T. B. Reed, “Free Energy of Formation of Binary Compounds,” 2000.
- [20] W. M. Deen, *Analysis of Transport Phenomena*. Oxford University Press, USA, Mar. 1998.
- [21] A. J. Bard and L. R. Faulkner, *Electrochemical Methods*. Fundamentals and Applications, Wiley, Dec. 2000.
- [22] G. J. Janz and N. P. Bansal, “Molten Salts Data: Diffusion Coefficients in Single and Multi-Component Salt Systems,” 1982.
- [23] R. W. Laity, “Ion Mobility in Molten Salts,” Aug. 1971.
- [24] M. ROVERE and M. TOSI, “STRUCTURE AND DYNAMICS OF MOLTEN-SALTS,” *Reports On Progress In Physics*, vol. 49, no. 9, pp. 1001–1081, 1986.
- [25] D. A. Fick, “V. On liquid diffusion ,” *Philosophical Magazine*, vol. 10, no. 63, pp. 30–39, 1855.

- [26] J. C. Maxwell, "A Dynamical Theory of the Electromagnetic Field," *Philosophical Transactions of the Royal Society of London*, vol. 155, pp. 459–512, Jan. 1865.
- [27] W. C. Röntgen, "On a New Kind of Rays," *Science, New Series*, vol. 3, pp. 227–231, Feb. 1896.
- [28] P. Debye, "Zerstreuung von Röntgenstrahlen," *Annalen der Physik*, vol. 351, no. 6, pp. 809–823, 1915.
- [29] F. Zernike and J. A. Prins, "Die Beugung von Röntgenstrahlen in Flüssigkeiten als Effekt der Molekulanordnung," *Journal of Electronic Materials*, vol. 41, pp. 184–194, June 1927.
- [30] B. Frost, "The structure of liquid metals," *Progress in metal physics*, vol. 5, pp. 96–142, 1954.
- [31] F. C. Frank, "Supercooling of liquids," *Proceedings of the Royal Society of London. Series A, Mathematical and Physical Sciences*, pp. 43–46, 1952.
- [32] D. Tabor, *Gases, Liquids and Solids. And Other States of Matter*, Cambridge University Press, Nov. 1991.
- [33] B. I. Khrushchev, "Nature of the bond and change in the structure of metals during melting," *Journal of Electronic Materials*, vol. 12, no. 6, pp. 884–888, 1972.
- [34] W. D. Knight, A. G. Berger, and V. Heine, "Nuclear resonance in solid and liquid metals: A comparison of electronic structures," *Acta Metallurgica*, vol. 8, pp. 173–193, Oct. 1959.
- [35] C. C. Bradley, T. E. Faber, E. G. Wilson, and J. M. Ziman, "A theory of the electrical properties of liquid metals II. Polyvalent metals," *Philosophical Magazine*, vol. 7, pp. 865–887, May 1962.
- [36] C. Norris and J. Wotherspoon, "Photoemission measurements in liquid bismuth," *Journal of Physics F-Metal Physics*, vol. 6, no. 9, p. L263, 2001.
- [37] P. C. Sharrah, J. I. Petz, and R. F. Kruh, "Determination of Atomic Distributions in Liquid Lead-Bismuth Alloys by Neutron and X-Ray Diffraction," *The Journal of Chemical Physics*, vol. 32, no. 1, p. 241, 1960.
- [38] O. Chamberlain, "Neutron Diffraction in Liquid Sulfur, Lead, and Bismuth," *Physical Review*, vol. 77, pp. 305–313, Feb. 1950.
- [39] M. TANIGAKI, Y. TOYOTA, M. HARADA, and W. EGUCHI, "MUTUAL DIFFUSION-COEFFICIENT IN MOLTEN LEAD BISMUTH MIXTURES," *Journal of Chemical Engineering of Japan*, vol. 16, no. 2, pp. 92–98, 1983.

- [40] D. I. V. Katz, R. N. Lyon, and E. C. Miller, *Liquid-metals handbook*. Washington, D.C: Atomic Energy Comm. [u.a.], 1954.
- [41] C. Williams and F. T. Miles, "LIQUID METAL FUEL REACTOR SYSTEMS FOR POWER," *Nucleonics (U.S.) Ceased publication*, vol. Vol: 12, No. 7, July 1954.
- [42] S. Lawroski and L. J. Burris, "PROCESSING OF REACTOR FUEL MATERIALS BY PYROMETALLURGICAL METHODS," *Atomic Energy Review (Austria)*, vol. Vol: 2: No. 3, Jan. 1964.
- [43] B. N. Bhat and R. A. Swalin, "Thermotransport of cobalt in liquid silver," *Acta Metallurgica*, vol. 6, pp. 523–527, June 1972.
- [44] B. N. Bhat and R. A. Swalin, "Thermotransport of silver in liquid gold," *Acta Metallurgica*, vol. 20, pp. 1387–1396, Dec. 1972.
- [45] H. Cheng, Y. J. Lue, and M. Chen, "Interdiffusion in liquid Al-Cu and Ni-Cu alloys," *The Journal of Chemical Physics*, vol. 131, no. 4, 2009.
- [46] M. Schaefer, R. A. Fournelle, and J. Liang, "Theory for intermetallic phase growth between cu and liquid Sn-Pb solder based on grain boundary diffusion control," *Journal of Electronic Materials*, vol. 27, pp. 1167–1176, Nov. 1998.
- [47] Y. S. Kim and T. W. Eager, "Metal transfer in pulsed current gas metal arc welding," *Welding Journal (Miami):(United States)*, vol. 72, no. 7, 1993.
- [48] W. D. MacDonald and T. W. Eagar, "Isothermal solidification kinetics of diffusion brazing," *Metallurgical and Materials Transactions A*, vol. 29, no. 1, pp. 315–325, 1998.
- [49] F. Bartels, J. W. Morris, G. Dalke, and W. Gust, "Intermetallic phase formation in thin solid-liquid diffusion couples," *Journal of Electronic Materials*, vol. 23, pp. 787–790, Aug. 1994.
- [50] N. H. Nachtrieb and J. Petit, "Self-Diffusion in Liquid Mercury," *The Journal of Chemical Physics*, vol. 24, no. 4, pp. 746–750, 1956.
- [51] J. Petit and N. H. Nachtrieb, "Self-Diffusion in Liquid Gallium," *The Journal of Chemical Physics*, vol. 24, no. 5, p. 1027, 1956.
- [52] N. H. Nachtrieb, "Self-diffusion in liquid metals," *Advances in Physics*, vol. 16, pp. 309–323, Apr. 1967.
- [53] A. Bruson and M. Gerl, "Diffusion coefficient of 113-Sn, 124-Sb, 110m-Ag, and 195-Au in liquid Sn," *Physical review. B, Condensed matter*, vol. 21, pp. 5447–5454, June 1980.

- [54] G. Mathiak, A. Griesche, K. H. Kraatz, and G. Froberg, "Diffusion in liquid metals," *Journal of Non-Crystalline Solids*, vol. 205-207, pp. 412-416, Oct. 1996.
- [55] A. Griesche, K. H. Kraatz, and G. Froberg, "A modified shear cell for mass transport measurements in melts," *Review of Scientific Instruments*, vol. 69, no. 1, p. 315, 1998.
- [56] T. Masaki, T. Fukazawa, S. Matsumoto, T. Itami, and S. Yoda, "Measurements of diffusion coefficients of metallic melt under microgravity - current status of the development of shear cell technique towards JEM on ISS," *Measurement Science & Technology*, vol. 16, no. 2, pp. 327-335, 2005.
- [57] S. Suzuki, K.-H. Kraatz, and G. Froberg, "Diffusion Experiments in Liquid Sn-Bi and Al-Ni Systems with a Stable Density Layering Using the Foton Shear Cell Under 1G Conditions," *Microgravity Science and Technology*, vol. 16, pp. 120-126, 2005.
- [58] A. Griesche, B. Zhang, J. Horbach, and A. Meyer, "Interdiffusion and Thermodynamic Forces in Binary Liquid Alloys," *Materials Science Forum*, vol. 649, pp. 481-486, May 2010.
- [59] S. Suzuki, K.-H. Kraatz, G. Froberg, R. Rosu-Pflumm, and G. Mueller-Vogt, "Impurity diffusion measurements of Bi in liquid Sn using stable density layering and the shear cell technique," in *Journal of Non-Crystalline Solids*, pp. 3300-3304, Osaka Univ, Inst Sci & Ind Res, Osaka, Japan, 2007.
- [60] R. E. Meyer and N. H. Nachtrieb, "Self-Diffusion of Liquid Sodium," *The Journal of Chemical Physics*, vol. 23, no. 10, pp. 1851-1854, 1955.
- [61] R. MEYER and N. NACHTRIEB, "Self-Diffusion in Sodium Near the Melting Point," *The Journal of Chemical Physics*, vol. 23, no. 2, pp. 405-405, 1955.
- [62] G. Careri, A. PAOLETTI, and M. Vicentini, "Further experiments on liquid Indium and Tin self-diffusion," *Il Nuovo Cimento*, vol. 10, pp. 1088-1099, Dec. 1958.
- [63] D. Paoletti, G. Spagnolo, V. Bagini, and M. Santarsiero, "A new method for measuring the diffusivity of liquid binary mixtures using DSPI," *Pure and Applied Optics: Journal of the European Optical Society Part A*, vol. 2, p. 489, 1993.
- [64] M. Vicentini and A. PAOLETTI, "Self diffusion in liquid In-Sn alloys," *Il Nuovo Cimento*, vol. 14, pp. 1373-1380, Dec. 1959.
- [65] A. PAOLETTI and M. Vicentini, "Self diffusion in liquid In-Pb alloys," *Il Nuovo Cimento*, vol. 14, pp. 748-757, July 1959.

- [66] C. H. Ma and R. A. Swalin, "A study of solute diffusion in liquid tin," *Acta Metallurgica*, vol. 8, pp. 388–395, June 1960.
- [67] N. NACHTRIEB, C. WAHL, and E. FRAGA, "Self-Diffusion of Liquid Zinc," *Journal of Physical Chemistry*, vol. 67, no. 11, pp. 2353–&, 1963.
- [68] C. H. Buell and F. O. Shuck, "Diffusion in the Liquid Bi-Sn System," *Metallurgical Transactions*, vol. 1, pp. 1875–1880, July 1970.
- [69] J. Foster and R. Reynik, "Self-diffusion in liquid tin and indium over extensive temperature ranges," *Metallurgical and Materials Transactions B*, vol. 4, no. 1, pp. 207–216, 1973.
- [70] J. Verhoeven, E. Gibson, and M. Beardsley, "The diffusion coefficient of Bi in dilute liquid alloys of Bi in Sn," *Metallurgical and Materials Transactions B*, vol. 6, no. 2, pp. 349–349, 1975.
- [71] J. Verhoeven, E. Gibson, and R. Griffith, "Measurement of liquid metal diffusion coefficients from steady-state solidification experiments," *Metallurgical and Materials Transactions B*, vol. 6, no. 3, pp. 475–480, 1975.
- [72] R. E. Barras, H. A. Walls, and A. L. Hines, "Liquid thallium self-diffusion measurements," *Metallurgical Transactions*, vol. 6, pp. 347–348, June 1975.
- [73] T. Persson, "An in-situ technique for the determination of electrotransport in liquid metallic alloys," *Advances in Space Research*, vol. 4, no. 5, pp. 81–84, 1984.
- [74] J. NOWOK, "Analysis of Atomic Diffusion in Liquid-Metals at Melting Temperatures in Capillary-Like Media," *Acta Metallurgica Et Materialia*, vol. 42, no. 12, pp. 4025–4028, 1994.
- [75] M. Klassen and J. Cahoon, "Interdiffusion of Sn and Pb in liquid Pb-Sn alloys," *Metallurgical and Materials Transactions A*, vol. 31, no. 5, pp. 1343–1352, 2000.
- [76] C. B. Porth and J. R. Cahoon, "Interdiffusion of Bi in Liquid Sn," *Journal of Phase Equilibria & Diffusion*, vol. 31, no. 2, pp. 149–156, 2010.
- [77] N. Lee and J. Cahoon, "Interdiffusion of Copper and Iron in Liquid Aluminum," *Journal of Phase Equilibria & Diffusion*, vol. 32, no. 3, pp. 226–234, 2011.
- [78] U. Dahlborg, M. Besser, M. Calvo-Dahlborg, S. Janssen, F. Juranyi, M. J. Kramer, J. R. Morris, and D. J. Sordelet, "Diffusion of Cu in AlCu alloys of different composition by quasielastic neutron scattering," *Journal of Non-Crystalline Solids*, vol. 353, pp. 3295–3299, Oct. 2007.
- [79] A. Meyer, S. Stüber, D. Holland-Moritz, O. Heinen, and T. Unruh, "Determination of self-diffusion coefficients by quasielastic neutron scattering measurements of levitated Ni droplets," *Physical Review B*, vol. 77, Mar. 2008.

- [80] F. Kargl, M. Engelhardt, F. Yang, H. Weis, P. Schmakat, B. Schillinger, A. Griesche, and A. Meyer, "In situ studies of mass transport in liquid alloys by means of neutron radiography," *Journal of Physics: Condensed Matter*, vol. 23, p. 254201, June 2011.
- [81] R. Banish and L. Jalbert, "In-situ diffusivity measurement technique," in *Gravitational Effects in Materials and Fluid Sciences*, pp. 1311–1320, Univ Alabama, Ctr Micrograv & Mat Res, Huntsville, AL 35899 USA, 1999.
- [82] P. G. Sanders, M. O. Thompson, T. J. Renk, and M. J. Aziz, "Liquid titanium solute diffusion measured by pulsed ion-beam melting," *Metallurgical and Materials Transactions A*, vol. 32, pp. 2969–2974, Dec. 2001.
- [83] D. Oakeson and A. Virkar, "Determination of diffusivity of sodium in liquid tin using Na- β alumina," *Journal of materials science*, vol. 19, no. 1, pp. 213–222, 1984.
- [84] T. Murakami and T. Koyama, "Application of Electrochemical Method to Measure Diffusion Coefficient in Liquid Metal," *Journal of The Electrochemical Society*, vol. 158, no. 8, p. F147, 2011.
- [85] A. Ben Abdellah, J. G. Gasser, K. Bouziane, B. Grosdidier, and M. Busaidi, "Experimental procedure to determine the interdiffusion coefficient of miscibility gap liquid alloys: Case of GaPb system," *Physical Review B*, vol. 76, no. 17, 2007.
- [86] J. H. Zhao, R. P. Liu, M. Zhang, Z. H. Zhou, X. Y. Zhang, L. M. Cao, D. Y. Dai, Y. F. Xu, and W. K. Wang, "Design of solid/liquid–liquid/solid trilayer systems for the measurement of diffusion coefficients in liquid metals," *Review of Scientific Instruments*, vol. 69, no. 8, pp. 3002–3005, 1998.
- [87] X. Zhu and R. Smith, "Diffusion in liquid Pb–Au binary system," *Solidification and Gravity*, vol. 215, pp. 113–118, 1996.
- [88] J. Cahoon, Y. Jiao, K. Tandon, and M. Chaturvedi, "Interdiffusion in liquid tin," *Journal of Phase Equilibria & Diffusion*, vol. 27, pp. 325–332, Aug. 2006.
- [89] E. F. BROOME and H. A. WALLS, "Liquid Metals Diffusion - a Modified Shear Cell and Mercury Diffusion Measurements," *Transactions of the Metallurgical Society of Aime*, vol. 242, no. 10, pp. 2177–&, 1968.
- [90] R. R. Kapoor and T. W. Eagar, "Improving the calculation of interdiffusion coefficients," *Metallurgical and Materials Transactions A*, vol. 21, no. 12, pp. 3039–3047, 1990.
- [91] A. Einstein, *Investigations on the Theory of Brownian Movement*. Courier Dover Publications, 1956.

- [92] G. G. Stokes, "On the Effect of the Internal Friction of Fluids on the Motion of Pendulums." Transactions of the Cambridge Philosophical Society, 1851.
- [93] J. M. Harrison, *Brownian motion and stochastic flow systems*. Malabar, FL: Robert E. Krieger Publishing Co. Inc., 1990.
- [94] M. H. Cohen and D. Turnbull, "Molecular Transport in Liquids and Glasses," *The Journal of Chemical Physics*, vol. 31, no. 5, p. 1164, 1959.
- [95] R. Swalin, "On the theory of self-diffusion in liquid metals," *Acta Metallurgica*, vol. 7, no. 11, pp. 736–740, 1959.
- [96] H. Rickert and A. A. El Miligy, "ELECTROCHEMICAL INVESTIGATION OF OXYGEN DIFFUSION IN SOLID AND LIQUID METAL.," *Proc. Int. Symp. Reactiv. Solids, 6th, Schenectady, N. Y., 1968, 17- 28(1969).*, Jan. 1969.
- [97] B. Heshmatpour and D. Stevenson, "An electrochemical study of the solubility and diffusivity of oxygen in the respective liquid metals indium, gallium, antimony and bismuth," *Journal of Electroanalytical Chemistry and Interfacial Electrochemistry*, vol. 130, pp. 47–55, 1981.
- [98] H. CHOU, T. CHOW, S. TSAY, and H. CHEN, "Diffusivity of Oxygen in Liquid Sn and Ba_{0.35}Cu_{0.65} Alloys," *Journal of The Electrochemical Society*, vol. 142, no. 6, pp. 1814–1819, 1995.
- [99] R. Ganesan, T. Gnanasekaran, and R. S. Srinivasa, "Electrochemical study on determination of diffusivity, activity and solubility of oxygen in liquid bismuth," *The Journal of Chemical Thermodynamics*, vol. 38, pp. 739–747, June 2006.
- [100] B. Sears, T. Anderson, R. Narayanan, and A. Fripp, "The detection of solutal convection during electrochemical measurement of the oxygen diffusivity in liquid tin," *Metallurgical and Materials Transactions B*, vol. 24, no. 1, pp. 91–100, 1993.
- [101] J. S. Anderson and K. Saddington, "S 80. The use of radioactive isotopes in the study of the diffusion of ions in solution," *Journal of the Chemical Society (Resumed)*, no. 0, pp. S381–S386, 1949.
- [102] A. Bruson and M. Gerl, "Diffusion coefficients of ¹²⁴Sb, ¹¹³Sn, ^{110m}Ag, and ¹⁹⁵Au in liquid copper," *Physical review. B, Condensed matter*, vol. 19, pp. 6123–6129, June 1979.
- [103] B.-J. Yang and R. W. Smith, "Numerical modelling of transport in a liquid diffusion couple shear cell," *Journal of Physics: Condensed Matter*, vol. 15, pp. 3855–3865, June 2003.
- [104] C. Wagner, "Theoretical Analysis of Diffusion of Solutes During the Solidification of Alloys," *Journal of Metals*, vol. 6, no. 2, pp. 154–160, 1954.

- [105] J. D. Verhoeven, E. D. Gibson, and R. I. Griffith, "Measurement of Diffusion Coefficients from Steady-State Solidification Experiments," *Metallurgical Transactions B-Process Metallurgy*, vol. 6B, pp. 475–480, Sept. 1975.
- [106] J. H. Lee, S. Liu, H. Miyahara, and R. Trivedi, "Diffusion-coefficient measurements in liquid metallic alloys," *Metallurgical and Materials Transactions B*, vol. 35, no. 5, pp. 909–917, 2004.
- [107] N. Isono, P. M. Smith, D. Turnbull, and M. J. Aziz, "Anomalous diffusion of Fe in Liquid Al Measured by the pulsed laser technique," *Metallurgical and Materials Transactions A*, vol. 27, pp. 725–730, Mar. 1996.
- [108] N. Isono, P. M. Smith, D. Turnbull, and M. J. Aziz, "Anomalous diffusion of Fe in Liquid Al Measured by the pulsed laser technique," *Metallurgical and Materials Transactions A*, vol. 27, pp. 725–730, Mar. 1996.
- [109] W. Weppner and R. A. Huggins, "Determination of the Kinetic Parameters of Mixed-Conducting Electrodes and Application to the System Li₃Sb," *Journal of The Electrochemical Society*, vol. 124, pp. 1569–1578, Oct. 1977.
- [110] J. Crank, *The mathematics of diffusion*. Oxford University Press, USA, 1979.
- [111] A. L. Hines, H. A. Walls, and K. R. Jethani, "Determination of the coordination number of liquid metals near the melting point," *Journal of Electronic Materials*, vol. 16, pp. 267–274, Jan. 1985.
- [112] J. R. Cahoon, "The entropy factor in liquid diffusion," *Metallurgical and Materials Transactions A*, vol. 34, pp. 882–883, Mar. 2003.
- [113] U. Mizutani, *Introduction to the electron theory of metals*. Cambridge ; New York : Cambridge University Press, 2001.
- [114] O. J. Kleppa, "Ultrasonic Velocities of Sound in Some Metallic Liquids. Adiabatic and Isothermal Compressibilities of Liquid Metals at Their Melting Points," *The Journal of Chemical Physics*, vol. 18, no. 10, p. 1331, 1950.
- [115] A. B. Coppens, "Parameter of Nonlinearity in Fluids. III. Values of Sound Velocity in Liquid Metals," *The Journal of the Acoustical Society of America*, vol. 41, no. 6, pp. 1443–1448, 1967.
- [116] D. A. Yagodin, A. G. Mozgovi, and M. A. Pokrasin, "An experimental investigation of the velocity of sound in molten lead and bismuth and in their reciprocal eutectic alloy at high temperatures," *High Temperature*, vol. 48, no. 2, pp. 181–187, 2010.
- [117] S. Blairs, "Sound velocity of liquid metals and metalloids at the melting temperature," *Physics and Chemistry of Liquids*, vol. 45, pp. 399–407, Aug. 2007.

- [118] N. L. Peterson and W. K. Chen, "Mass Transport in Solids," *Annual Review of Materials Science*, vol. 3, pp. 75–109, Aug. 1973.
- [119] S. Choudhury, L. Barnard, J. D. Tucker, T. R. Allen, B. D. Wirth, M. Asta, and D. Morgan, "Ab-initio based modeling of diffusion in dilute bcc Fe–Ni and Fe–Cr alloys and implications for radiation induced segregation," *Journal of Nuclear Materials*, vol. 411, no. 1, pp. 1–14, 2011.
- [120] N. H. Nachtrieb, J. A. Weil, E. Catalano, and A. W. Lawson, "Self-Diffusion in Solid Sodium. II. The Effect of Pressure," *The Journal of Chemical Physics*, vol. 20, no. 8, p. 1189, 1952.
- [121] T. Iida, R. Guthrie, M. Isac, and N. Tripathi, "Accurate predictions for the viscosities of several liquid transition metals, plus barium and strontium," *Metallurgical and Materials Transactions B-Process Metallurgy and Materials Processing Science*, vol. 37, no. 3, pp. 403–412, 2006.
- [122] G. Careri and A. PAOLETTI, "A direct interchange mechanism in liquid tin and indium self diffusion," *Il Nuovo Cimento*, vol. 1, pp. 517–518, Mar. 1955.
- [123] T. Iida, R. Guthrie, and N. Tripathi, "A model for accurate predictions of self-diffusivities in liquid metals, semimetals, and semiconductors," *Metallurgical and Materials Transactions B-Process Metallurgy and Materials Processing Science*, vol. 37, no. 4, pp. 559–564, 2006.
- [124] K.-J. Bathe and K.-J. Bathe, *Finite element procedures*. Englewood Cliffs, N.J.: Prentice Hall, 1996.
- [125] K.-J. Bathe, *Finite Element Procedures*. Klaus-Jurgen Bathe, 2006.
- [126] S. V. Stankus, R. A. Khairulin, and A. G. Mozgovoï, "An experimental investigation of the density and thermal expansion of advanced materials and heat-transfer agents of liquid-metal systems of fusion reactor: Lead-lithium eutectic," *High Temperature*, vol. 44, no. 6, pp. 829–837, 2006.
- [127] W. D. Drotning, "Thermal expansion of the group IIb liquid metals zinc, cadmium and mercury," *Journal of the Less Common Metals*, vol. 96, pp. 223–227, Jan. 1984.
- [128] L. A. Blagonravov, O. O. Karchevskiy, P. V. Ivannikov, and A. V. Soboleva, "Application of double modulation for measurement of the thermal expansion coefficient of liquid metals," *Journal of Physics: Conference Series*, vol. 98, p. 032010, Mar. 2008.
- [129] P. M. Nasch and S. G. Steinemann, "Density and Thermal Expansion of Molten Manganese, Iron, Nickel, Copper, Aluminum and Tin by Means of the Gamma-Ray Attenuation Technique," *Physics and Chemistry of Liquids*, vol. 29, pp. 43–58, Jan. 1995.

- [130] V. Sobolev, "Database of thermophysical properties of liquid metal coolants for GEN-IV," Tech. Rep. Open Report of the Belgian Nuclear Research Centre, Dec. 2011.
- [131] U. Burr and U. Moller, "Rayleigh-Benard convection in liquid metal layers under the influence of a horizontal magnetic field," *Journal of Fluid Mechanics*, vol. 453, pp. 345–369, 2002.
- [132] T. N. Dihn, Y. Z. Yang, J. P. Tu, R. R. Nourgaliev, and T. G. Theofanous, "Rayleigh-Benard Natural Convection Heat Transfer: Pattern Formation, Complexity and Predictability," in *Rayleigh-Benard Natural Convection Heat Transfer: Pattern Formation, Complexity and Predictability*, (Pittsburgh, PA), Proceedings of ICAPP '04, June 2004.
- [133] G. Ahlers, "Experiments with Rayleigh-Benard convection." 2003.
- [134] J. W. Cahn and J. E. Hilliard, "Free Energy of a Nonuniform System. I. Interfacial Free Energy," *The Journal of Chemical Physics*, vol. 28, pp. 258–267, Feb. 1958.
- [135] D. Dassault and A. Powell, "Phase Field Modeling of Electrolysis in a Slag of Molten Salt," *Mills Symposium*, pp. 1–13, Aug. 2002.
- [136] J. Guyer, W. Boettinger, J. Warren, and G. McFadden, "Phase field modeling of electrochemistry. I. Equilibrium," *Physical Review E*, vol. 69, no. 2, 2004.
- [137] J. E. Guyer, W. J. Boettinger, and J. A. Warren, "Phase Field Modeling of Electrochemistry. II. Kinetics," *Physical Review E*, vol. 69, pp. 1–12, Feb. 2004.
- [138] W. Pongsaksawad, A. C. Powell, and D. Dussault, "Phase-Field Modeling of Transport-Limited Electrolysis in Solid and Liquid States," *Journal of The Electrochemical Society*, vol. 154, no. 6, p. F122, 2007.
- [139] Z. Wen, J. Cao, Z. Gu, X. Xu, F. Zhang, and Z. Lin, "Research on sodium sulfur battery for energy storage," *Solid State Ionics*, vol. 179, no. 27-32, pp. 1697–1701, 2008.
- [140] E. S. Association, "Electricity Storage Association-Technology Comparisons," Apr. 2009.